



UNIVERSITY OF
CAMBRIDGE

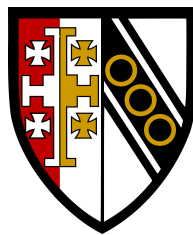
Blast Propagation and Damage in Urban Topographies

WILLIAM DRAZIN

Selwyn College

The Laboratory for Scientific Computing,
Cavendish Laboratory,
University of Cambridge

September 2017



This dissertation is submitted for the degree of Doctor of Philosophy

Abstract

For many years, terrorism has threatened life, property and business. Targets are largely in urban areas where there is a greater density of life and economic value. Governments, insurers and engineers have sought to mitigate these threats through understanding the effects of urban bombings, increasing the resilience of buildings and improving estimates of financial loss for insurance purposes. This has led to a desire for an improved approach to the prediction of blast propagation in urban cityscapes.

Urban geometry has a significant impact on blast wave propagation. Presently, only computational fluid dynamics (CFD) methods adequately simulate these effects. However, for large-scale urban domains, these methods are both challenging to use and are computationally expensive. Adaptive mesh refinement (AMR) methods alleviate the problem, but are difficult to use for the non-expert and require significant tuning. We aim to make CFD urban blast simulation a primary choice for governments, insurers and engineers through improvements to AMR and by studying the performance of CFD in relation to other methods used by the industry.

We present a new AMR flagging approach based on a second derivative error norm for compressive shocks (ENCs). This is compared with existing methods and is shown to lead to a reduction in overall refinement without affecting solution quality. Significant improvements to feature tracking over long distances are demonstrated, making the method easier to tune and less obtuse to non-experts.

In the chapter that follows, we consider blast damage in urban areas. We begin with a validation and a numerical study, investigating the effects of simple street geometry on blast resultants. We then investigate the sensitivity of their distribution to the location of the charge. We find that moving the charge by a small distance can lead to a significant change in peak overpressures and creates a highly localised damage field due to interactions between the blast wave and the geometry. We then extend the investigation to the prediction of insured losses following a large-scale bombing in London. A CFD loss model is presented and compared with simpler approaches that do not account for urban geometry. We find that the simpler models lead to significant over-predictions of loss, equivalent to several hundred million pounds for the scenario considered. We use these findings to argue for increased uptake of CFD methods by the insurance industry.

In the final chapter, we investigate the influence of urban geometry on the propagation of blast waves. An earlier study on the confinement effects of narrow streets is repeated at a converged resolution and we corroborate the findings. We repeat the study, this time introducing a variable porosity into the building façade. We observe that the effect of this porosity is as significant as the confinement effect, and we recommend to engineers that they consider porosity effects in certain cases. We conclude the study by investigating how alterations to building window layout can improve the protective effects of a façade. Maintaining the window surface area constant, we consider a range of layouts and observe how some result in significant reductions to blast strength inside the building.

Declaration

This dissertation is the result of my own work and includes nothing which is the outcome of work done in collaboration except as declared in the Preface and specified in the text. It is not substantially the same as any that I have submitted, or, is being concurrently submitted for a degree or diploma or other qualification at the University of Cambridge or any other University or similar institution except as declared in the Preface and specified in the text.

I further state that no substantial part of my dissertation has already been submitted, or, is being concurrently submitted for any such degree, diploma or other qualification at the University of Cambridge or any other University or similar institution except as declared in the Preface and specified in the text. It does not exceed the limit of sixty thousand words prescribed by the Degree Committee for Physics and Chemistry.

William Drazin,
September 2017

Acknowledgements

I would like to thank my supervisor Nikos Nikiforakis for his guidance throughout the past five years in Cambridge.

My thanks also go to my diligent and punctilious proofreaders Caroline Eveleigh, Jonathan Drazin, Lukas Wutschitz, and Oliver Strickson, whose input has had a huge impact on the thesis. This work has also benefited greatly from interactions with the members of the Laboratory for Scientific Computing. I would like to thank them all for their willingness to help me with my problems and for the fascinating, and mostly humorous discussions that ensued.

Finally, I would like to thank my friends and family for their unwavering support, remaining by my side through thick and thin.

Contents

1	Introduction	1
1.1	Thesis outline	4
2	Numerical methods for compressible gas dynamics	7
2.1	The Euler equations of gas dynamics	7
2.1.1	Stability	10
2.2	The Riemann problem for the Euler equations	10
2.3	TVD MUSCL schemes for the Euler equations	11
2.4	Mesh systems and spatial discretisation	13
2.4.1	Structured and unstructured grids	13
2.4.2	Embedded boundary methods	14
2.4.3	The Klein, Bates, Nikiforakis cut-cell method	16
2.5	Urban and topographical data	18
2.5.1	Geometry file types	19
2.5.2	Generation of a signed distance function	20
2.5.3	Examples	21
2.6	Clarification on code written for this thesis	24
3	Blast literature review and theory	25
3.1	Formation of blast waves	25
3.2	Scaling laws	27
3.3	Calculation of blast wave parameters	28
3.4	Explosion types	29
3.5	Modelling approaches	32
3.5.1	Empirical methods	32
3.5.2	Semi-empirical methods	32
3.5.3	Computational methods	33
3.6	Blast wave-structure interaction	33
3.6.1	Reflections	33
3.6.2	Clearing	35

3.6.3	Channelling and shielding	36
3.6.4	Building porosity	37
3.6.5	Blast walls	38
3.6.6	Building shape and complex geometries	39
3.6.7	Comments and conclusions	40
3.7	Numerical model	41
3.8	Numerical validation	41
3.8.1	One-dimensional shock tube problems	42
3.8.2	Shock diffraction over a sharp edge	45
3.8.3	Free-field blast	47
3.8.4	Cityscape blast experiment	47
4	Shock capturing using adaptive mesh refinement	53
4.1	Introduction	54
4.1.1	Grid hierarchy	55
4.1.2	Time stepping	57
4.1.3	Patch boundaries	58
4.1.4	Grid adaption	61
4.1.5	Shortcomings	63
4.2	Flagging	65
4.2.1	Relative difference	65
4.2.2	A modified second-derivative error norm for compressive shocks (ENCS)	69
4.3	Solution convergence	71
4.3.1	One dimensional setup	71
4.3.2	Radial resolution across the charge	74
4.4	Numerical results	75
4.4.1	One dimensional study	75
4.4.2	Two dimensional study	77
4.4.3	The Health and Safety Laboratory test case	79
4.4.4	Parameter study	82
4.5	Conclusion	86
5	Blast damage in urban cityscapes	89
5.1	Structural response to blast loading	91
5.1.1	Elastic deformation of structures	91
5.1.2	Pressure-impulse diagrams	94
5.1.3	Effects of explosive blast on buildings	96

5.1.4	Effects of explosive blast on glazing	98
5.1.5	Effects of explosive blast on the human body	99
5.2	Catastrophe modelling in the insurance industry	101
5.2.1	Insuring against loss	102
5.2.2	Understanding terrorism risk	103
5.2.3	Modelling terrorism risk	104
5.3	Blast wave clearing	108
5.3.1	Results	111
5.3.2	Comments and conclusions	115
5.4	Clearing and channelling in city streets	116
5.4.1	Results	119
5.4.2	Comments and conclusions	123
5.5	The effect of charge placement on blast wave resultants	123
5.5.1	Urban park scenario	125
5.5.2	Pressure contours	125
5.5.3	Gauge analysis	128
5.5.4	Comments and conclusions	134
5.6	A CFD-based approach to deterministic risk modelling	135
5.6.1	PRA circular terrorism loss model	135
5.6.2	Towards a CFD-based approach	135
5.6.3	Pressure prediction inside buildings	137
5.6.4	Quantifying property loss and business interruption	139
5.6.5	Quantifying human loss	140
5.7	A comparative study of a circular, hemispherical and CFD consequence model	140
5.7.1	Terrorism event on Lime Street, London	140
5.7.2	Property loss and business interruption	141
5.7.3	Human loss	146
5.8	Conclusion	150
6	The effect of urban geometry on blast resultants	153
6.1	Validation	154
6.1.1	Results	156
6.2	The effect of street width on blast propagation	158
6.2.1	Results	161
6.3	The effect of building porosity on blast propagation	167
6.3.1	Results	169
6.3.2	Comments and conclusions	173

6.4	The effect of window layout on blast propagation	175
6.4.1	Results	177
6.4.2	Comments and conclusions	180
6.5	Conclusion	183
7	Conclusions and further work	185
7.1	Further work	188
	Bibliography	203

Chapter 1

Introduction

AT 0902 hours, on April 19, 1995, a rental car containing over 2 tonnes of explosive was detonated outside the Alfred P. Murrah Federal Building in Oklahoma City, USA. The resulting explosion tore through the downtown region of the city, causing major damage to nearby structures and shattering windows in a three square-mile area [1].

The event ranks as the second most damaging terrorist attack on domestic soil, only surpassed by the September 11 World Trade Center attacks. In total, 842 people were killed or injured. Of the 168 that perished, 19 were children. The sheer power of the bomb led to significant property destruction, with 312 buildings receiving some degree of damage. Overall estimates of property loss are thought to exceed 510 million dollars [2].

The threat from these attacks was judged so serious that following the Oklahoma bombing the US government embarked on a program of security evaluation for all federal buildings. Over 600 million dollars were spent increasing blast resilience through the use of physical barriers, glazing systems and by increasing stand-off distances from vehicular traffic [3].

Today the threat from terrorism has evolved since the cataclysmic events of 9/11. The 2011 Arab Spring protests and the Syrian Civil War that followed have fuelled the rise of ISIS, surpassing Al-Qaeda as the terrorist organisation posing the greatest perceived threat to the West. The large attacks similar in style to that of 9/11 have largely been replaced by smaller 'lone wolf' events. In 2015, a total of 11 774 terrorist attacks occurred worldwide, resulting in almost 30 000 deaths, over 35 000 injuries and a total economic cost to the global economy of 90 billion dollars. Of these attacks, more than half involved a bombing [4, 5].

The impact of terrorism has led to the global 'War on Terror' and a concerted

effort to mitigate the impact of terrorism on daily life. The effects of this strategy can be seen in the changes to building and urban security that have occurred during the past twenty years.

Nowadays it is common for buildings designated as ‘at risk’ to have had some consideration of blast security during the design process. This might include upgrades to the specification of façade glazing, cladding and the structural frame. In addition, engineers may wish to increase the distance between the building and vehicular traffic to lessen the effects of the blast in the event of an attack. The categorisation of ‘at risk’ is not limited to high profile government buildings: anyone who takes a stroll through the City of London will notice the abundance of vehicle barriers that have been skilfully woven into the urban landscape.

It is not only the engineering industry that has had to adapt to the threat from terror. The multi-billion dollar insurance payouts following the World Trade Center attacks have led the global insurance industry to acknowledge that terrorism risk cannot be covered under standard insurance policies, and needs to be modelled independently. Today, insurers increasingly rely on third parties to conduct detailed catastrophe modelling of this risk.

Both the engineering and insurance industries rely on being able to predict the effects of explosions for their models to work. Engineers may need to understand how a glazing panel in a new airport building will react under loading from an improvised explosive. An insurer might need to calculate the expected financial losses to their portfolio of office buildings from the detonation of a car bomb. At the heart of each analysis is a prediction of the blast resultants arising from the detonation of an explosive in air.

There are three possible approaches to simulating these effects: *experimentation*, *empirical* or *semi-empirical* methods, and *numerical simulation*. Experimental methods record blast loads through direct measurements. This approach remains the most reliable way of measuring and studying the propagation of blast resultants. Yet it is both impractical and expensive, especially for the engineer who may wish to perform a large number of studies on a series of prospective glazing designs.

An alternate approach is to combine existing experimental data with analytic methods that form a subset of the original data (*empirical methods*) or extend the data based on simplified models of physical phenomena (*semi-empirical methods*). The most famous examples of an empirical approach are the scaled blast parameters of Kingery and Bulmash [6]. These form a polynomial fit of a number of historic blast trials and allow the prediction of blast parameters for a wide range of charge sizes and stand-off distances. These methods have been extended to semi-empirical approaches and can account for the internal and external loading of simple urban

geometries. Notable approaches are the codes `BLASTX`, `SHOCK` and `ConWep` [7–9]. A useful review of the empirical and semi-empirical approaches for predicting blast loads is given by Remennikov [10].

Empirical methods are not suitable for blast predictions that involve anything more than the simplest of geometries. In urban environments, the irregular nature of buildings means that the simulation of blast wave propagation is beyond the scope of semi-empirical methods. In this situation, numerical first-principle methods are necessary.

Numerical approaches date back to the 1940s. During this period, physicists and mathematicians attempted to model the propagation of shock waves through the air. The advent of modern computing allowed for the systems of partial differential equations governing the physics of shocks to be solved directly, giving birth to the field of computational fluid dynamics (CFD). The pioneering work of Von Neumann, Lax and Richtmyer led to the development of modern day shock capturing schemes [11,12]. At the same time, models describing spherical blast waves from point source and finite-size source explosions were developed by Brode and others [13,14].

CFD methods are more computationally expensive than empirical methods, but can implicitly capture the effects of geometry on the solution. This makes them well suited to complex cityscapes where the interactions between the blast wave and urban environment can have a substantial effect on the propagation of the blast wave. Today, blast propagation in urban environments is modelled using three-dimensional hydrocodes such as `Air3d`, `LS-DYNA` and `ANSYS Autodyn`. For a review of CFD blast modelling approaches see the work of Hao et al. [15].

Blast codes face a number of challenges. The simulation of city-scale blast scenarios involves a great range of length scales. The size of the computational domain might cover several kilometres to capture the urban zone. However, the resolution required to capture the shock could measure in centimetres. A uniform computational mesh with this cell size would result in a simulation with an enormous number of cells and would be prohibitively expensive.

To overcome this challenge, adaptive mesh refinement (AMR) methods can be used. This approach adapts the computational mesh, providing extra resolution only to regions of the solution where it is required. Their ability to judiciously allocate ‘work’ gives AMR methods the capability to dramatically reduce the computational expense of the simulation and make large-scale urban blast simulation viable.

AMR can be challenging to use correctly and requires an understanding of the numerical methods that underpin CFD. Care is required to choose parameters to ensure that refinement is distributed correctly and efficiently for the duration of the simulation. This technical challenge has, along with other factors, stifled the

attractiveness of CFD to the insurance industry who are put off by the computational expense and lack the technical ability to mitigate this cost with AMR. At present, the majority of the industry is using simple, empirical methods for predicting insured loss from terrorist attacks [16].

The aim of this thesis is to explore the benefits of a CFD approach to simulating blast propagation and damage in urban cityscapes, and to further improve the method. We aim to achieve this by demonstrating that CFD offers a superior balance of accuracy and cost when compared with simpler, empirical approaches. We also aim to improve the methods through the simplification of AMR and the inclusion of building porosity into the model. It is hoped that the research presented in this thesis benefits those with a need to understand the propagation of blast waves in urban areas, especially those in the insurance and engineering industries.

1.1 Thesis outline

In the first investigation (chapter 4), we present a novel approach to AMR with the aim of improving the ease of use and reliability of the method for urban blast simulation. A new flagging method is presented which is easier to tune and allows for more judicious selection of shock features for refinement. The aim of the chapter is to produce a flagging criterion that requires less effort to parametrise and can track important flow features over longer distances than existing methods. To test the approach, we compare it with an existing method for a range of long distance hemispherical blast scenarios.

In chapter 5 we study how CFD approaches to blast propagation in urban cityscapes can offer higher accuracy and lead to a less conservative prediction of loss than the empirical methods used in the insurance industry today. We begin the chapter with a validation study, followed by an investigation into the effect of charge placement on the outcome of an urban blast. A CFD approach is used to predict the distribution of blast resultants following two explosions in nearby locations. The change in the damage pattern is analysed and compared to the results of a simpler model which does not take geometry into account.

In the second part of the chapter, a hypothetical terrorist bombing scenario is devised and two empirical loss models are used to predict business interruption, property loss and human loss following the attack. A CFD model is presented and used to perform the same loss predictions. The results are compared to those of the empirical models to quantify the degree to which the extra accuracy of CFD changes the predictions of insured loss. We aim to demonstrate how significant improvements

in accuracy can be achieved with CFD approaches.

The investigation in chapter 6 is concerned with the effect that building façade porosity has on the street channelling of blast waves in city streets. Tall buildings create canyons which channel blast waves, maintaining their strength as they propagate away from the source. These confinement effects can increase the strength of the blast wave substantially over an equivalent free-air detonation and are a good example of how the urban environment affects the nature of blast resultants. We identify a lack of knowledge on the effect that blast ingress through building windows has on the confinement effects of street canyons. We repeat an earlier study that investigated the confinement effects of narrow streets. We integrate a porosity into the building façade with the aim of understanding whether this can mitigate the confinement effects of narrow streets.

In the second part of the chapter, we look at how window layout in buildings can be optimised to maximise the blast resilience of the structure without sacrificing light entering the building. In addition to the findings of the studies, this chapter demonstrates the important phenomena modelled by CFD methods which are impossible to capture using empirical approaches.

Chapter 2

Numerical methods for compressible gas dynamics

THERE are generally considered to be four pillars underpinning CFD: the physical problem to solve, the mathematical model, the numerical method and the computer with which the calculations are performed. In this chapter we lay the theoretical groundwork for the studies that follow by outlining the mathematical model of partial differential equations and the numerical methods with which we attempt to approximate solutions to these equations.

We begin by describing the governing equations for the dynamics of a compressible, inviscid material in section 2.1. In sections 2.2 and 2.3 we present the finite volume methods used for solving these equations. In the section that follows, the topic of mesh generation is discussed and the Klein et al. cut-cell approach is outlined. In the final section, we describe how external geometry can be used within the code to create urban cityscapes and other topologically complex domains.

2.1 The Euler equations of gas dynamics

In this section, we present the time-dependent Euler equations. These equations form a system of non-linear, hyperbolic conservation laws that govern the evolution of compressible, inviscid gases. They can be seen as a particular form of the Navier-Stokes equations where body forces, viscosity and thermal conductivity are neglected. The Euler equations are obtained through the expression of the conservation laws of mass, momentum and energy. In the present section and the one that follows, we outline this system and its relation to the Riemann problem as described in Toro [17].

The differential form of the equations can be expressed in the following form for the conservation of mass

$$\frac{\partial \rho}{\partial t} + \nabla \cdot (\rho \mathbf{v}) = 0, \quad (2.1)$$

where ρ is the material density and \mathbf{v} is the velocity. The conservation of momentum is expressed as

$$\frac{\partial \rho u}{\partial t} + \nabla \cdot (\rho u \mathbf{v}) + \frac{\partial p}{\partial x} = 0, \quad (2.2)$$

$$\frac{\partial \rho v}{\partial t} + \nabla \cdot (\rho v \mathbf{v}) + \frac{\partial p}{\partial y} = 0, \quad (2.3)$$

$$\frac{\partial \rho w}{\partial t} + \nabla \cdot (\rho w \mathbf{v}) + \frac{\partial p}{\partial z} = 0, \quad (2.4)$$

where p is the pressure and u , v and w are the components of velocity. The conservation of energy is then written in the following form:

$$\frac{\partial E}{\partial t} + \nabla \cdot ((E + p) \mathbf{v}) = 0, \quad (2.5)$$

where e is the specific internal energy and E is the total energy per unit volume

$$E = \rho \left(e + \frac{\|\mathbf{v}\|^2}{2} \right). \quad (2.6)$$

Discontinuities are a common feature of gas dynamics, where shocks are liable to occur in the solution. The differential form of the conservation laws require that the solution is differentiable and will break down in this situation. Instead, we solve the above equations using a finite-volume approach that uses the integral form of the conservation laws. This approach allows for discontinuous solutions and is inherently conservative because of the stipulation that the flux entering each control volume is identical to the flux which leaves.

We divide space into cells $[x_{i-1/2}, x_{i+1/2}]$ where $x = x_{i+1/2}$ is the cell boundary. Time is also discretised into intervals $[t^n, t^{n+1}]$. The evolution of the solution in cell i can be expressed in the following way:

$$\int_{x_{i-1/2}}^{x_{i+1/2}} [u(x, t^{n+1}) - u(x, t^n)] dx = - \int_{t^n}^{t^{n+1}} [f(u(x_{i+1/2}, t)) - f(u(x_{i-1/2}, t))] dt, \quad (2.7)$$

where $f(u(x, t))$ is the flux of the solution $u(x, t)$. This leads to the conservative update method

$$U_i^{n+1} = U_i^n - \lambda (F_{i+1/2}^n - F_{i-1/2}^n), \quad (2.8)$$

where $\lambda = \frac{\Delta t}{\Delta x}$ is the ratio of the time step and cell width. U_i^n is the cell averaged state at time t^n in cell i :

$$U_i^n = \frac{1}{\Delta x} \int_{x_{i-1/2}}^{x_{i+1/2}} u(x, t^n) dx, \quad (2.9)$$

and $F_{i+1/2}^n$ is the integral of the boundary flux in the interval $[t^n, t^{n+1}]$:

$$F_{i+1/2}^n = \frac{1}{\Delta t} \int_{t^n}^{t^{n+1}} f(u(x_{i+1/2}, t)) dt. \quad (2.10)$$

The Euler equations can be written in conservation form which is compatible with the above conservative update:

$$\partial_t \mathbf{u} + \partial_x \mathbf{f}(\mathbf{u}) + \partial_y \mathbf{g}(\mathbf{u}) + \partial_z \mathbf{h}(\mathbf{u}) = 0, \quad (2.11)$$

with

$$\mathbf{u} = \begin{bmatrix} \rho \\ \rho u \\ \rho v \\ \rho w \\ E \end{bmatrix}, \quad \mathbf{f}(\mathbf{u}) = \begin{bmatrix} \rho u \\ \rho u^2 + p \\ \rho u v \\ \rho u w \\ u(E + p) \end{bmatrix}, \quad (2.12)$$

$$\mathbf{g}(\mathbf{u}) = \begin{bmatrix} \rho v \\ \rho u v \\ \rho v^2 + p \\ \rho v w \\ v(E + p) \end{bmatrix}, \quad \mathbf{h}(\mathbf{u}) = \begin{bmatrix} \rho w \\ \rho u w \\ \rho v w \\ \rho w^2 + p \\ w(E + p) \end{bmatrix},$$

where $\mathbf{f}(\mathbf{u})$, $\mathbf{g}(\mathbf{u})$ and $\mathbf{h}(\mathbf{u})$ are the flux vectors of the conserved variables vector \mathbf{u} . The system is closed by a caloric equation of state that provides a relationship between the thermodynamic variables:

$$e = \frac{p}{(\gamma - 1)\rho}, \quad (2.13)$$

where the adiabatic index γ is the ratio of specific heats.

In situations where the flow is spherically symmetric, we can represent the above multidimensional equations as a one-dimensional equation with a cylindrical source term:

$$\partial_t \mathbf{u} + \partial_r \mathbf{f}(\mathbf{u}) = \mathbf{s}(\mathbf{u}), \quad (2.14)$$

$$\mathbf{u} = \begin{bmatrix} \rho \\ \rho u \\ E \end{bmatrix}, \quad \mathbf{f}(\mathbf{u}) = \begin{bmatrix} \rho u \\ \rho u^2 + p \\ u(E + p) \end{bmatrix}, \quad \mathbf{s}(\mathbf{u}) = -\frac{\alpha}{r} \begin{bmatrix} \rho u \\ \rho u^2 \\ u(E + p) \end{bmatrix}, \quad (2.15)$$

where r is the radial distance. When $\alpha = 0$ there exists one-dimensional flow, $\alpha = 1$ corresponds to cylindrical flow without axial variations and $\alpha = 2$ corresponds to spherically symmetric flow. This formulation can be extremely useful for simplifying the complexity of a system by taking into account its symmetry.

2.1.1 Stability

For a typical explicit scheme solving a set of hyperbolic equations to be stable, it must ensure that solution in a cell is dependent on all information that is able to affect it physically. This means that no wave can travel further than a single cell width Δx in any time step Δt . This places a restriction on the time step of the form

$$\Delta t = C_{\text{cff}} \frac{\Delta x}{S_{\text{max}}^n}, \quad (2.16)$$

where S_{max}^n is the maximum wave speed in the domain at time n . The term C_{cff} is a dimensionless quantity called the Courant number. It can be thought of as the ratio of the maximum wave speed S_{max}^n to the grid speed $\Delta x/\Delta t$ defined by the discretisation of the domain. A necessary condition for the convergence of explicit methods requires that $0 < C_{\text{cff}} \leq C_{\text{max}}$, where the upper limit C_{max} depends on the numerical scheme. For the MUSCL HANCOCK method described in section 2.3, we use $C_{\text{cff}} = 0.9$.

2.2 The Riemann problem for the Euler equations

Riemann problems occur at the discontinuities between neighbouring finite volume grid cells. They are a fundamental tool in the solution of conservation equations due to the discreteness of the grid. For the case of the one-dimensional Euler equations, the Riemann problem is the hyperbolic equation with a set of piecewise constant initial data that has a single discontinuity at $x = 0$ and $t = 0$:

$$u(x, 0) = u^{(0)}(x) = \begin{cases} u_L & \text{if } x < 0, \\ u_R & \text{if } x > 0, \end{cases} \quad (2.17)$$

where u_L and u_R are states either side of the discontinuity. The Riemann problem has an exact, self-similar analytical solution which depends on the single variable x/t .

We can consider the initial value problem as a one-dimensional tube in which two fluids are separated by a thin membrane. When this membrane is instantaneously removed, three waves are created: a central contact wave and two further waves that comprise rarefactions or shocks. This wave pattern is shown in figure 2.1 in $x-t$ space. The three waves separate the four different gas states w_L , w_{*L} , w_{*R} and w_R .

The process of solving the Riemann problem involves obtaining the star states w_{*L} and w_{*R} using the appropriate relations. For the case of a rarefaction wave, the isentropic law

$$p = C\rho^\gamma \quad (2.18)$$

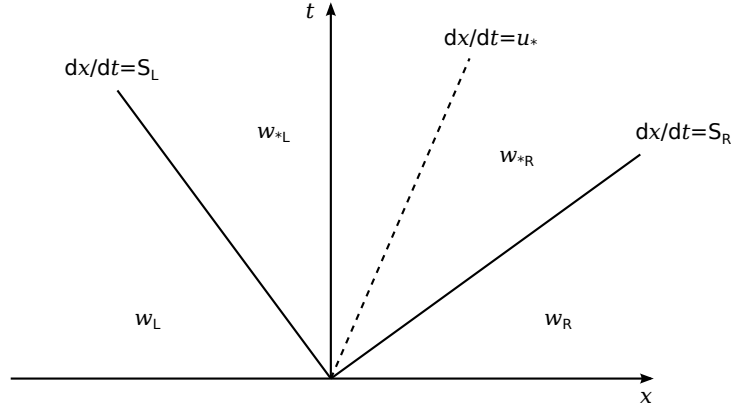


Figure 2.1: Wave patterns from a Riemann problem representing the trajectories of the different waves.

and the Generalised Riemann Invariant

$$u + \frac{2a}{\gamma - 1} = C, \quad (2.19)$$

— where u is the speed, C is a constant and a is the sound speed — are used to relate the states across the rarefaction and obtain the star state. For the case of a shock, the following Rankine-Hugoniot conditions are solved across the wave in the frame of reference of the shock:

$$\rho \hat{u} = \rho_* \hat{u}_*, \quad (2.20)$$

$$\rho \hat{u}^2 + p = \rho_* \hat{u}_*^2 + p_*, \quad (2.21)$$

$$\hat{u}(\hat{E} + p) = \hat{u}_*(\hat{E}_* + p_*), \quad (2.22)$$

where the non-starred quantities represent the left or right initial data state and $\hat{u} = u - S$, $\hat{u}_* = u_* - S$ and S is the shock speed.

2.3 TVD MUSCL schemes for the Euler equations

In order to update the solution in cell i using equation 2.8, the boundary fluxes $F_{i\pm 1/2}$ must be calculated. The calculation of a flux which does not lead to unphysical oscillations or the smearing of the shock front is a challenging task. In recent years, a number of High-Resolution Shock-Capturing (HRSC) methods have been developed. These schemes achieve second order accuracy in smooth solutions and capture the shock front with a minimum of points.

Van Leer introduced Monotone Upstream Centred Scheme for Conservation Laws (MUSCL)-type methods as an evolution of the first-order Godunov method which uses piecewise-constant data [18–20]. This approach reconstructs the data as a piecewise linear function inside the cell where the chosen slope of the state is a function of the neighbouring jumps in the piece-wise constant states. These *boundary extrapolated values* form the basis of a Generalised Riemann Problem (GRP) as a consequence of having modified the data at cell interfaces. The solution no-longer contains constant regions as in the conventional Riemann problem and must be solved appropriately. It is the boundary extrapolation of states that give MUSCL-type methods their high order status. The use of standard slope limiters with MUSCL schemes ensures that the method remains Total Variation Diminishing (TVD) and thus avoids spurious oscillations.

The MUSCL HANCOCK method [21, 22] is attributed to S. Hancock and exists as a MUSCL-type method which avoids the GRP by use of a predictor-corrector step [23]. In this method, data reconstruction is performed at each time step, leading to a piecewise linear representation of the states. For each cell-averaged state U_i^n we calculate the boundary extrapolated values

$$U_i^L = U_i^n - \frac{1}{2}\bar{\Delta}_i ; U_i^R = U_i^n + \frac{1}{2}\bar{\Delta}_i, \quad (2.23)$$

where the limited slope $\bar{\Delta}_i$ is defined as

$$\bar{\Delta}_i = \xi(\Delta_{i-1/2}, \Delta_{i+1/2})\Delta_i, \quad (2.24)$$

and $\Delta_{i-1/2} = U_i^n - U_{i-1}^n$, $\Delta_{i+1/2} = U_{i+1}^n - U_i^n$ and $\Delta_i = \frac{1}{2}(U_{i+1}^n - U_{i-1}^n)$. ξ is a scalar limiter function which applies a TVD constraint to prevent the occurrence of oscillations in the vicinity of strong gradients.

The boundary extrapolated values U_i^L, U_i^R are then evolved by half a time step using the relation

$$\bar{U}_i^L = U_i^L + \frac{1}{2} \frac{\Delta t}{\Delta x} (f(U_i^L) - f(U_i^R)), \quad (2.25)$$

$$\bar{U}_i^R = U_i^R + \frac{1}{2} \frac{\Delta t}{\Delta x} (f(U_i^L) - f(U_i^R)), \quad (2.26)$$

where $f(U_i^{L/R})$ is the numerical flux at the left or right extrapolated boundary state. These evolved states then form the initial conditions for the solution of a piece-wise constant Riemann problem

$$\partial_t U + \partial_x f(U) = 0, \quad U(x, 0) = \begin{cases} \bar{U}_i^R & \text{if } x < 0, \\ \bar{U}_{i+1}^L & \text{if } x > 0, \end{cases} \quad (2.27)$$

to obtain the similarity solution at the cell boundary $U_{i+1/2}(x/t)$. From this point onwards the method mirrors the first order Godunov method. The boundary fluxes are obtained from the similarity solution

$$F_{i+1/2} = f(U_{i+1/2}(0)), \quad (2.28)$$

and the cell states are updated using conservation equation 2.8.

2.4 Mesh systems and spatial discretisation

The computational mesh dictates how space in the domain is divided to form a discrete representation of the solution. The role of the mesh is to faithfully represent the underlying geometry while minimising the amount of information which must be stored. Meshing can be a key simulation bottleneck, especially in domains that involve complex moving topologies that require re-meshing at each time step. The mesh generation method's computational efficiency and amenability to parallelisation plays a large factor in the decision over which approach to take.

In the following section we provide a brief review of various meshing methods before outlining the Cartesian cut-cell approach used in this thesis.

2.4.1 Structured and unstructured grids

At the most fundamental level, grid systems can be categorised as either structured or unstructured. Unlike structured grids, which order nodes in a regular array, unstructured systems do not assume any regularity and must include a definition of how nodes are connected to one another in the form of connectivity arrays. Due to their unstructured nature, these meshes are particularly suited to the discretisation of complex domains involving non-regular interfaces. Meshes can be created that align to complex geometrical boundaries in the domain without the need for an immersed boundary condition.

This adaptability comes with a computational overhead that arises from the need to locate mesh vertices and define connectivity between them. Partitioning the grid for parallelisation and mesh refinement can also be a complex task.

Structured grids are the simplest of Cartesian equivalent meshes. They obey a logical relationship between nodes in which each point can be identified by one, two or three indices (i, j, k) . This regularity significantly simplifies grid implementation because connectivity arrays are no longer needed. Indexing is intuitive and corresponds to the multi-dimensional array structures of conventional computer

programming languages. Structured grids may exist in the form of a single entity or consist of a collection of meshes that form a block structured arrangement.

Due to their implicit regularity, these methods are computationally efficient and well suited to parallel processing and adaptive mesh refinement. This type of mesh is, however, not uniformly suited to the representation of complex geometries, sometimes requiring an additional approach to take these boundaries into account.

There exist a number of extensions to regular structured meshes: Curvilinear grids attempt to combine the benefits of geometry fitting associated with unstructured grids with the computational efficiency of structured grids. These grids exist as a generalised Cartesian mesh which may take the form of a non-rectangular domain whilst remaining topologically Cartesian. In essence, the system is formed using an invertible mapping from a rectilinear grid and has the advantage that the geometry of the resulting grid does not need to be stored. Despite this, the representation of complex domains using curvilinear grids may still lead to low quality grids when compared with unstructured grids which present greater flexibility in capturing features [24].

Overlapping grid methods (also known as Chimera or overset grids) [25–27] relax the requirement that neighbouring grids must align and instead merely stipulate that they must overlap [28]. These methods retain many of the generation freedoms particular to unstructured grids whilst maintaining the block-wise advantages of ordered data that structured methods enjoy. In this approach, neighbouring zones overlap and form a common zone in which the difference equations are solved twice. It is also possible for a zone to be contained within another. This is useful for capturing objects of different geometry that are features of a different geometrical object (e.g. a wing on an aircraft fuselage). In order to produce a valid solution on the chosen grid, values are interpolated from the known solution on the other sub-grid, with priority given to grids that better match the local geometry.

Difficulties with overlap methods have historically been associated with non-conservative interpolations between grids. This issue has since been rectified [29, 30]. However, achieving conservation is not straight-forward and adds extra complication to the method, especially in three dimensions. Despite this, the overlap approach is widely used for compressible flow problems where high resolution shock capturing is important [31, 32].

2.4.2 Embedded boundary methods

Embedded boundary methods aim to combine the efficiency of structured grids with the adaptability of unstructured meshes. The distinguishing feature of the

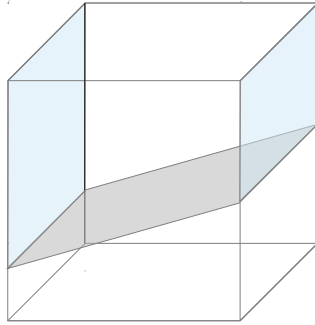


Figure 2.2: Diagram of a 3D cut-cell. Blue shaded areas indicate interfaces which lie on the same side of the cut boundary.

approach is a regular Cartesian grid which does not need to conform to the geometry. This separates the process of mesh generation from the application of boundary conditions. Today, two predominant approaches exist among others: ghost fluid and cut-cell methods.

The ghost fluid method [33, 34] was originally developed as a way to discretise a domain in which an interface separates two materials with different equations of state. Each material is assigned a band of ghost cells at the other side of the interface and an extrapolation procedure is used to initialise the states of these ghost fluid cells. Pressure and velocity are considered to be continuous across the fluid interface and are copied from the real region of the other fluid. The entropy of the ghost fluid is extrapolated across the interface to determine the ghost fluid entropy. A standard single material solver is then used for each respective material.

The method is particularly suitable for multi-material simulations because it is easier to implement than an explicit multi-material Riemann solver. It can also be modified to use moving boundaries with minimal difficulty. However, the requirement to extrapolate data into neighbouring ghost cells creates inefficiencies related to memory access and makes the scheme difficult to parallelise effectively. In addition to this, the method is not fully conservative and exhibits inaccuracies in situations where strong shocks interact with the boundary [35].

Cartesian cut-cell methods are another form of immersed boundary method. Rather than using cell edges to match the shape of the domain, the interface geometry is captured within the existing grid cells. This approach uses a single structured rectilinear grid which is then intersected by ‘cuts’ in regions which cross interfaces.

Cut-cells offer a number of advantages over conventional unstructured and overlap methods. The most obvious of which is the ability to retain the underlying logical

mesh connectivity of a regular Cartesian grid whilst achieving a good representation of the boundary. For the case of mesh generation, unstructured methods require tessellation of the domain which, especially in three dimensions, is a time-intensive process. Overlapping grids, on the other hand, require an experienced user to pick the right combination of sub-zones for the domain in question. Something that may prove to be a hindrance for a blast code run on a wide range of geometrically distinct zones. Cut-cell methods suffer from none of these problems.

The main disadvantage with cut-cell methods lies in the creation of small cells along cut boundaries, termed the *small-cell problem* [36]. A simple cut may lead to a domain with a range of cell sizes; some several orders of magnitude larger than others. This can have the unwanted effect of reducing the time step which is dependent on the cell with the smallest volume. The convergence of these methods is also linked to the size of the cell [24]. There have been several attempts by the cut-cell community to overcome the *small-cell problem*. A number of authors have proposed cell merging methods, in which small cells are identified and then merged with their neighbours [22, 37, 38]. This method has been shown to work well for a range of applications. However, cell-merging in three dimensions becomes difficult.

2.4.3 The Klein, Bates, Nikiforakis cut-cell method

In this thesis, we will follow the cut-cell approach of Klein et al. [36]. This method for solving the compressible Euler equations on cut-cell meshes overcomes the *small-cell problem* and allows for directional operator-splitting [36]. The scheme uses one-dimensional flux stabilisation to ensure that the solution remains stable for a time-step independent of cell volume. It is one of the more straightforward methods to implement and has the additional benefit of simple coupling to numerous dimensionally-split grid solvers. The fact that the scheme is inherently split is a key advantage as it renders the method more computationally efficient and allows for relatively simple extension to 3D problems. The scheme is fully conservative and first-order accurate at boundaries.

To render a strip of cells into a one-dimensional problem, each cell interface is decomposed into ‘shielded’ and ‘unshielded’ regions which each have a unique flux $F_{i-1/2,j}^{\text{shielded}}$, $F_{i-1/2,j}^{\text{unshielded}}$ respectively. This decomposition is outlined in figure 2.3. The unshielded region of the cell is treated as a conventional cell and requires no adjustment. The shielded length is affected by the boundary and is amended to produce the stabilised flux

$$F_{i-1/2}^* = F_B + \alpha_i (F_{i-1/2} - F_B) \quad (2.29)$$

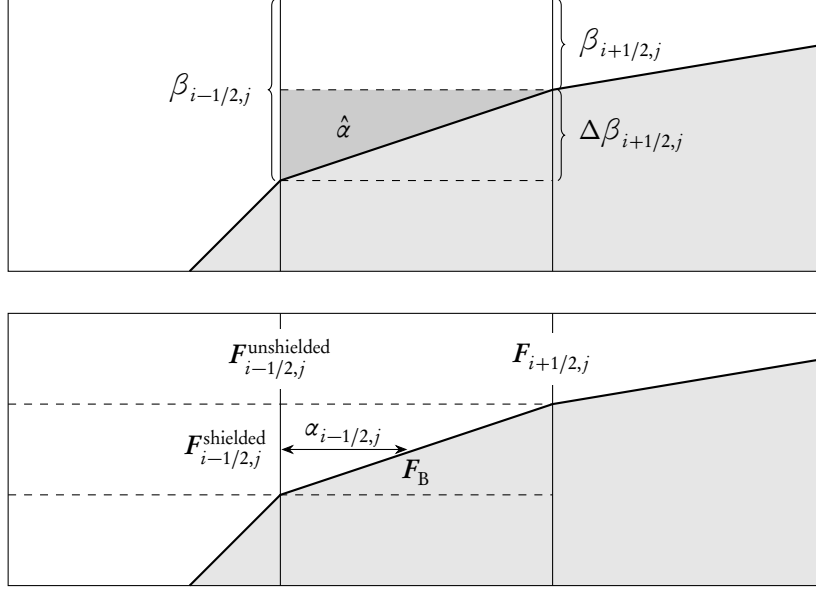


Figure 2.3: A two-dimensional zone incorporating three cut cells. Each cell is divided into shielded and non-shielded zones where the problem is reduced to a series of one dimensional relations [36].

where F_B is the boundary flux, α_i the distance of the irregular cell relative to that of the regular cell and $F_{i-1/2}$ is the regular unshielded flux. The modified flux tends to to the boundary flux as $\alpha_i \rightarrow 0$ and tends to the unshielded flux as $\alpha_i \rightarrow 1$.

In multiple dimensions, the scheme naturally decomposes into several one-dimensional problems. For the purposes of this introduction, we consider the two dimensional system. In figure 2.3 we define the unshielded portion of the cell by the symbol $\beta_{i+1/2,j}$ (the area of the cell interface in each coordinate direction relative to the regular cell interface). The total flux across the cell face at position $i-1/2,j$ may then be assembled as a weighted sum of the shielded and unshielded fluxes calculated in a one-dimensional sense:

$$\mathbf{F}_{i-1/2,j}^{2D} = \frac{1}{\beta_{i-1/2,j}} \left[\beta_{i+1/2,j} \mathbf{F}_{i-1/2,j}^{\text{unshielded}} + (\beta_{i-1/2,j} - \beta_{i+1/2,j}) \mathbf{F}_{i+1/2,j}^{\text{shielded}} \right]. \quad (2.30)$$

In certain cases, the cell may lie in a concave region in which its face is shielded from both sides. This problem may be overcome by subdividing the problem into singly and doubly-shielded zones and dealing with each individually. The unshielded flux is simply the regular cell flux

$$\mathbf{F}_{i-1/2,j}^{\text{unshielded}} = \mathbf{F}_{i-1/2,j}. \quad (2.31)$$

The shielded flux is calculated as

$$\mathbf{F}_{i-1/2,j}^{\text{shielded}} = \mathbf{F}_{i-1/2,j}^* \left(\alpha_{i-1/2,j}^{\text{shielded}} \right), \quad (2.32)$$

where

$$\alpha_{i-1/2,j}^{\text{shielded}} = \frac{\hat{\alpha}_{i-1/2,j}}{\beta_{i-1/2,j} - \beta_{i+1/2,j}}, \quad (2.33)$$

and $\hat{\alpha}_{i-1/2,j} = \alpha_{i,j} - \beta_{i+1/2,j}$ is the shielded volume fraction.

Using conventional operator splitting techniques with cut-cells can lead to distortion of cut-cell states by $\mathcal{O}(1)$ changes. This can be rectified by accumulating fluxes across all cell interfaces for each directional step of the splitting. Klein et al. define an *auxiliary flux*. During a splitting step, fluxes for faces in the direction of the splitting direction are assigned a flux as normal. Those faces which are perpendicular are assigned an auxiliary flux. For the two-dimensional case, we define the fluxes

$$\mathbf{F}_{i,j}^{\text{aux}} = \mathbf{f}(\mathbf{W}_{i,j}^0) \quad \text{and} \quad \mathbf{G}_{i,j}^{\text{aux}} = \mathbf{g}(\mathbf{W}_{i,j}^0) \quad (2.34)$$

for the x and y splitting directions respectively. Each flux is based on the reference state $\mathbf{W}_{i,j}^0 = (\rho^0, p^0, u^0, v^0)$, computed for each cut-cell prior to the first one-dimensional sweep at the beginning of the time step. This state is the tangential flow along the boundary of the cut-cell. The pressure is obtained from the solution of the Riemann problem normal to the wall and the velocity is obtained from the component tangential to the boundary. The cell update for the time step is given by:

$$\begin{aligned} \mathbf{U}_{i,j}^x &= \mathbf{U}_{i,j}^n - \frac{\Delta t}{2\Delta x \Delta y} \left(\beta_{i+1/2,j} \mathbf{F}_{i+1/2,j}^{2D} - \beta_{i-1/2,j} \mathbf{F}_{i-1/2,j}^{2D} - \Delta \beta_{i,j}^x \left(\mathbf{F}_{i,j}^B + \mathbf{F}_{i,j}^{\text{aux}} \right) \right), \\ \mathbf{U}_{i,j}^{xy} &= \mathbf{U}_{i,j}^x - \frac{\Delta t}{\Delta x \Delta y} \left(\beta_{i,j+1/2} \mathbf{G}_{i,j+1/2}^{2D} - \beta_{i,j-1/2} \mathbf{G}_{i,j-1/2}^{2D} - \Delta \beta_{i,j}^y \left(\mathbf{G}_{i,j}^B + \mathbf{G}_{i,j}^{\text{aux}} \right) \right), \\ \mathbf{U}_{i,j}^{n+1} &= \mathbf{U}_{i,j}^{xy} - \frac{\Delta t}{2\Delta x \Delta y} \left(\beta_{i+1/2,j} \mathbf{F}_{i+1/2,j}^{2D} - \beta_{i-1/2,j} \mathbf{F}_{i-1/2,j}^{2D} - \Delta \beta_{i,j}^x \left(\mathbf{F}_{i,j}^B + \mathbf{F}_{i,j}^{\text{aux}} \right) \right), \end{aligned}$$

and the total contribution of the auxiliary flux cancels over the full splitting cycle.

2.5 Urban and topographical data

The shape of the urban topography can have a significant effect on the propagation of the blast wave. For this reason, it is important to generate a cut-cell mesh that faithfully represents the underlying geometry. In this section we will describe the process by which the code generates a cut-cell mesh from an external geometry file. Figure 2.4 illustrates the three main stages of mesh generation from an external geometry. The external file is first parsed and an internal representation of the

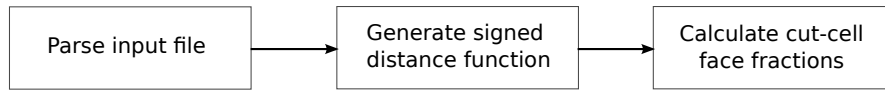


Figure 2.4: The three main stages involved in the generation of a cut-cell mesh from an external geometry file.

geometry is obtained. A signed distance function is then created which is used to calculate the cut-cell shielded face fractions. The current work is presented for three dimensional meshes. However, the method can be trivially reduced to two dimensions.

2.5.1 Geometry file types

The code accepts two types of external geometry: shapefile geospatial vector data and stereolithography (STL) formats. Shapefile data is a popular vector format for geographic information system (GIS) software and is developed and regulated by Esri as an open standard. The format can represent nontopological features in the form of points, lines and polygons. Each feature has a set of attributes which, among other properties, can describe its height above ground. The format is particularly suited to the representation of buildings, which can be stored as a 2D polygonal outline with an associated height. The Geospatial Data Abstraction Library (GDAL) is used to read the shapefile and an internal geometry is created by extruding each building outline by its associated height.

Because of its feature-based nature, the format lacks the ability to store topological information. For more general geometries, the STL format is used instead. This file type is popular and widely used by the computer-aided design (CAD) community. A geometrical surface is tessellated to form a series of connected triangular faces. Each face is described by the positions of its three vertices and the vector normal to the face. The STL format has a number of advantages including the ability to represent complex, arbitrary geometrical features, making it particularly suitable for geographical topologies and complex urban structures. The popularity of the format means that many CAD packages support the generation and modification of STL files. When working with STL files, care must be taken to insure the integrity of the file. The surface represented must be closed and completely connected, with each edge formed from two triangles without any self-intersections.

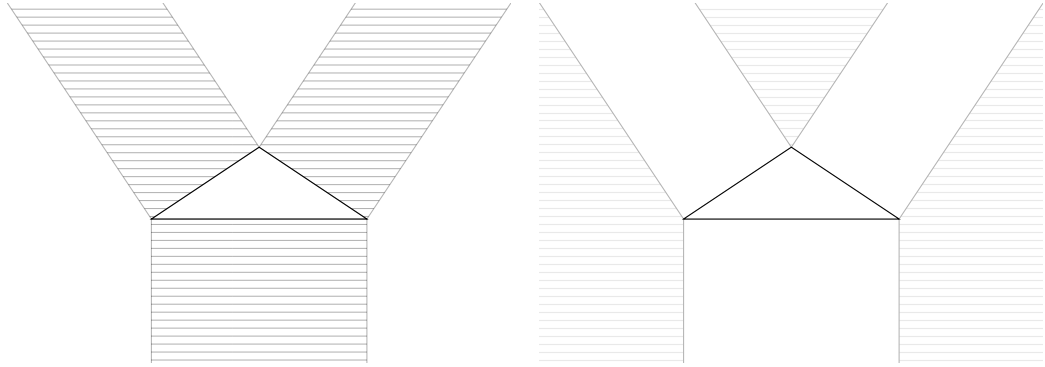


Figure 2.5: A diagram of the extrusion process around a 2D triangular object. The hatched strips show the region of points near the edges (left figure). The hatched wedges contain the points near the vertices (right figure).

2.5.2 Generation of a signed distance function

In order to generate a cut-cell mesh, we must first assign each cell vertex a distance from the interface. This distance is determined from a signed distance function $s(\mathbf{x})$. For all points \mathbf{x} in a domain \mathbb{R}^n that contains a surface $\partial\Omega$, we define this function as:

$$s(\mathbf{x}) = \min(d(\mathbf{x}, \partial\Omega)), \quad \forall \mathbf{x} \in \mathbb{R}^n, \quad (2.35)$$

which represents the smallest distance from the point \mathbf{x} to the surface $\partial\Omega$. The sign of the function dictates which side of the surface the point \mathbf{x} lies on. Points that lie on the surface have a signed distance of zero. This implies that the geometry surface is represented as the iso-surface of the value zero. In our implementation, we follow the method of Mauch to generate the signed distance function [39].

Once the parsing of the external geometry file is complete, the code obtains an internal representation of the geometry that is formed from a series of connected polygons. In three dimensions, each polygon is composed of the following features: a face, edges and vertices. For each feature f in the set of features F , an extrusion is performed creating a polygon e that contains at least the closest points to the feature. If we consider the case of a triangular feature, the extrusion of the face would produce a prism, the extrusion of the edges creates a wedge and the vertices produce a cone.

A 2D extrusion process is shown in figure 2.5 for a triangle, where extrusions are performed at edges and vertices. In 3D, extrusions would also be performed at faces. The shape is similar to a Voronoi diagram. It contains a minimum of (instead of exactly) the closest grid points to a feature.

Once the feature extrusions have been created, a scan conversion is performed to determine the cell vertices of the computational mesh that lie inside the extrusion. Scan conversions are a computer graphics technique for displaying filled polygons on raster displays. In his approach, Mauch scan converts the 3D object by slicing it with planes that coincide with mesh grid rows. For each grid row that intersects the polygon, the left and right intersection points are found and the cell vertices that lie within are marked.

The algorithm loops through each cell vertex c_{ijk} contained within the extrusion, calculating the minimum distance $s(\mathbf{x}_{ijk})$ to the feature. This process is performed for all features of the geometry that are within the computational domain, creating a signed distance function that is represented at each cell vertex. The steps for calculating the signed distance function are shown in algorithm 1.

Algorithm 1 An algorithm for computing the signed distance function at cell vertices.

```

{ $d_{ijk} = \infty$  for all  $i, j, k$ }
for all  $f \in F$  do
   $e = \text{EXTRUDE}(f)$ 
  for all  $c_{ijk} \in e$  do
     $d_{\min} = \text{distance to feature } f$ 
    if  $|d_{\min}| < |d_{ijk}|$  then
       $|d_{ijk}| = d_{\min}$ 
    end if
  end for
end for

```

It is possible to determine which cells lie on a boundary by testing for a sign change in the vertex signed distance. Cells are marked as ‘solid’ (inside the geometry) if all vertices have a negative signed distance and are marked as ‘empty’ (outside the geometry) if all vertices are positive. Cells containing vertices with both positive and negative signed distances are marked as ‘mixed’. For each mixed cell, the location of the cut and the corresponding shielded and unshielded face fractions are obtained by linearly interpolating the vertex signed distances.

2.5.3 Examples

In this section we present a number of cut-cell meshes that have been generated from a range of external geometries. Figure 2.6 shows a representation of an airport terminal. The geometry was created using the popular CAD program SketchUp and

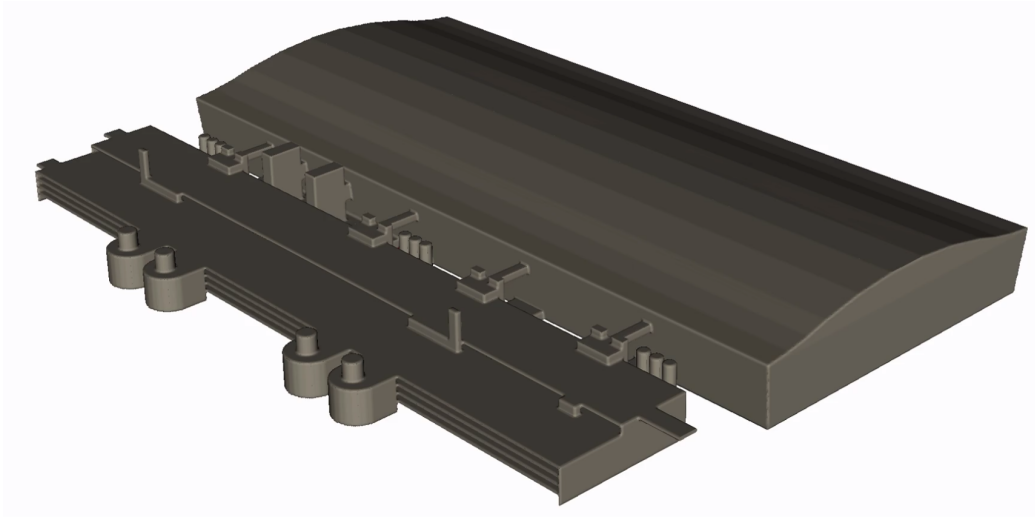


Figure 2.6: A representation of an airport terminal generated from an STL geometry.

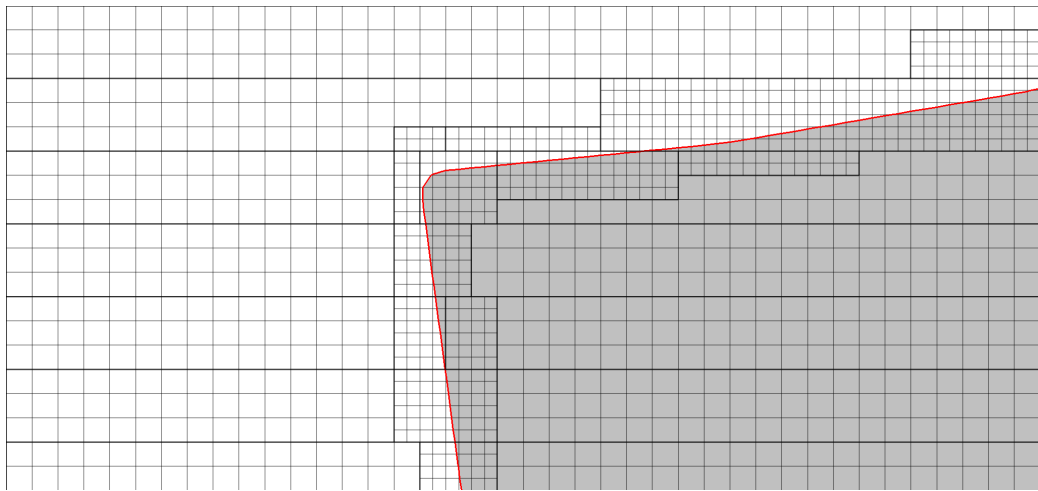


Figure 2.7: A cut-cell representation of a slice through the terminal geometry. The cuts are shown in red.



Figure 2.8: Landmap GIS data for central London [40]. The red square represents the region of the map used to generate the mesh.

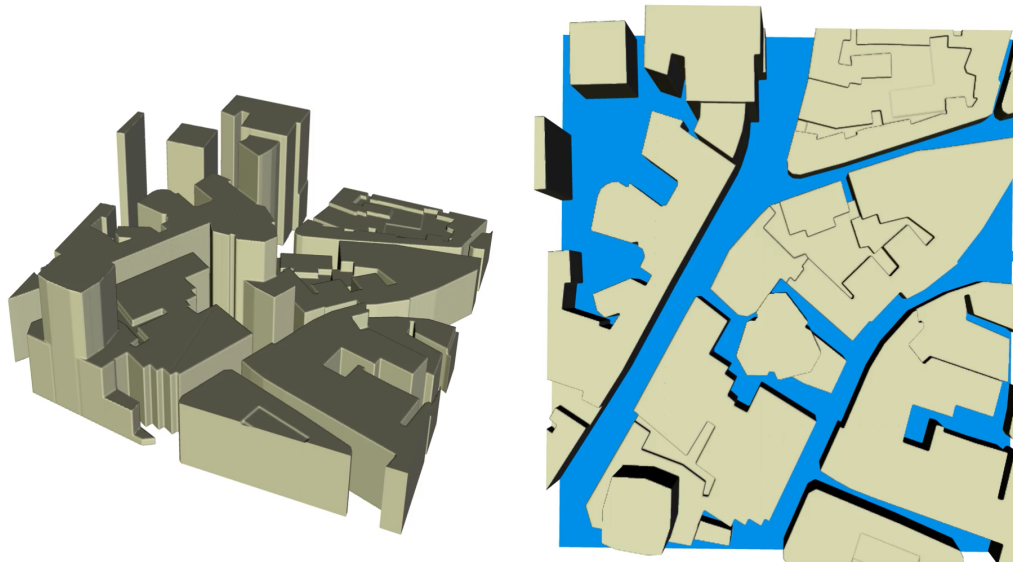


Figure 2.9: A representation of an urban business district in London, highlighted in figure 2.8 and created using GIS data.

exported as an STL file. The irregular shape of the building makes it particularly suited to this format. Figure 2.7 shows a slice taken through the roof section of the building. A cut-cell representation is shown, with cuts marking the boundary of the geometry highlighted in red.

Figure 2.8 shows an example of shapefile building outlines for central London from the Landmap project [40]. The region shown in the image is part of a larger dataset comprising nearly one million buildings in greater London. The storage efficiency of shapefiles enables this dataset to be stored in a single file of less than two hundred megabytes.

The code allows the user to specify a rectangular zone for meshing. This is shown in the figure as a red box. The resulting cut-cell mesh is shown in figure 2.9, where the building outlines have been extruded to their correct height. This example demonstrates the benefit of using shapefiles for simple, extruded geometries.

2.6 Clarification on code written for this thesis

The code that implements the numerical methods outlined in the present and following chapter was written by members of the Laboratory for Scientific Computing at the University of Cambridge and forms part of the LSC-AMR package. This code was reused by the author to conduct the studies in the chapters that follow. The code responsible for implementing the ENCS flagging module described in section 4.2.2 was written solely by the author of this thesis.

The shell tool GNU Parallel was used for managing the submission of simulation jobs [41].

Chapter 3

Blast literature review and theory

IN this chapter we introduce the theory and literature pertaining to the formation of blast waves in air and their interaction with solid obstacles. We begin by presenting the fundamental theory of blast wave formation. We then discuss the effect that urban geometry has on the blast wave. We include a review of recent work in this area, highlighting any gaps in the knowledge base that subsequent chapters in this thesis will attempt to address.

Finally, we outline the numerical model that forms the blast framework. A series of numerical tests are presented to validate each component of the model.

3.1 Formation of blast waves

An explosion is the result of a rapid expansion of gases that occurs from physical or mechanical change in a material. The phenomenon lasts for milliseconds, during which time energy is released into the surrounding air, forming a dense high pressure region. This region expands rapidly, compressing and accelerating the air outwards. An outwardly moving shock front forms, characterised by a near discontinuous increase in pressure and density. This wave contains much of the energy released by the detonation and moves faster than the speed of sound. As the blast wave propagates away from the source of the detonation, the air following the shock front is over-expanded. A cooling and contraction then occurs, reducing the pressure below atmospheric, before eventually returning to ambient conditions.

The blast wave is defined by two distinct phases: the positive phase occurs from the beginning of the wave when the pressure p is above the ambient pressure p_0 . Figure 3.1 shows the pressure history for an idealised blast wave as a function of time. Initially the pressure is equal to the ambient pressure p_0 . At the arrival time t_A the

pressure increases nearly instantaneously to the peak side-on overpressure p_{so}

$$p_{so} = p(t_A) - p_0 \quad (3.1)$$

The peak pressure decreases with distance from the detonation and inversely with the charge size.

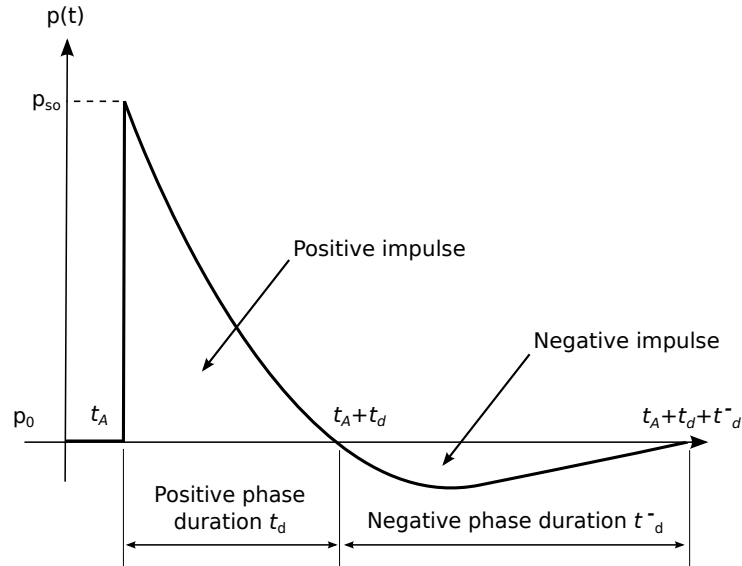


Figure 3.1: Typical blast wave pressure-time history

After reaching its peak value, the pressure decreases until reaching ambient pressure at time $t_A + t_d$, marking the end of the positive phase. The negative phase then begins, during which the pressure drops below p_0 before eventually returning to ambient at time $t_A + t_d + t_d^-$. The duration of the negative phase is t_d^- .

Obstacles that stand within the path of a blast wave experience different forces during each of the two phases. The positive phase exerts the greatest force, in the direction of the travel of the blast wave. The negative phase accounts for a suction force acting in the opposite direction. This is the reason why fragments of windows are often found in the street after the blast loading of buildings. The negative phase of the blast wave is rarely taken into account during assessments of blast loading of buildings because the main structural damage is associated with the positive phase containing the highest pressures.

The impulse is measured as the area underneath the curve and is divided between the positive phase impulse i_s and the negative phase impulse i_s^- . In addition to

pressure, impulse is a key parameter for the calculation of blast damage to buildings as it relates the total force per unit area applied to the structure.

During the 20th century a number of studies focussed on describing the formation and characteristics of blast waves. These solutions became important during the development of the nuclear bomb in the early 1940s, where the properties of strong blast waves arising from point source explosions were of particular interest. Notable contributions include the classical work of Taylor [42], Sedov [43] and von Neumann [44]. For lower energy detonations, the size of the charge has an effect on the blast wave solution and can no longer be represented as a point source. Numerical solutions in this regime were developed by Brode [13, 14] and Friedman [45], demonstrating the existence of the reflected shocks that arise from the finite size of the charge.

The simple and widely used representation of the blast wave is characterised by the Friedlander equation [46] for the overpressure $p_s(t)$. The equation describes the decay of the blast wave starting at the arrival time t_A

$$p_s(t) = p_{so} \left(1 - \frac{t}{t_d}\right) e^{-b \frac{t}{t_d}}, \quad (3.2)$$

where the parameter b is the decay coefficient for the waveform and t is the time elapsed. The decay coefficient can be obtained through the fitting of experimental pressure time curves. The positive impulse

$$i_s = \int_{t_A}^{t_A+t_d} p_s(t) dt \quad (3.3)$$

can also be analytically calculated from the Friedlander equation:

$$i_s = \frac{p_{so} t_d}{b^2} (b - 1 + e^{-b}). \quad (3.4)$$

3.2 Scaling laws

The properties of a blast wave vary with the distance from the detonation to the measuring point. The peak pressure and velocity of the blast wave diminish rapidly as the wave moves away from the source while the positive phase duration increases. This effect can be captured using scaling laws which take into account the effects of charge energy release and distance, allowing for the prediction of blast wave characteristics for a given scaled distance. The idea behind these laws is that two high explosive charges of different weights located the same scaled distance from a measurement point will produce equivalent blast waves.

The two most common forms of scaling are Sach's and Hopkinson-Cranz scaling [47]. Sach's scaling is a form of Hopkinson scaling that is concerned with high altitude explosive bursts such as nuclear bomb detonations. Since we are concerned with conventional high explosives we choose to use Hopkinson scaling. The law states that for explosions where the charges are of the same explosive material and the atmospheric conditions are identical, similar blast wave parameters are expected for a scaled distance Z , defined as

$$Z = \frac{R}{W^{1/3}}, \quad (3.5)$$

where R is the distance from detonation to source and W is the mass of the explosive.

In practice, this means that an explosive charge of mass W_1 located a distance R_1 from the measuring point will produce a blast wave with same peak overpressure p_{so} , impulse i_s , duration t_d and arrival time t_A as a second charge (W_2, R_2) if the following relationship holds:

$$\frac{R_1}{W_1^{1/3}} = \frac{R_2}{W_2^{1/3}}. \quad (3.6)$$

In reality, the composition of explosive devices varies considerably, along with the energy released during the detonation. This variation has led to the adoption of the TNT (Trinitrotoluene) equivalence standard, in which explosive weights are expressed in terms of an equivalent TNT weight. For non-TNT explosives, a TNT equivalent mass, W_{TNT} is calculated using

$$W_{TNT} = \frac{H_{exp}}{H_{TNT}} W_{exp}, \quad (3.7)$$

where H_{exp} and H_{TNT} are the specific heats released by the actual explosive and the TNT respectively. W_{exp} is the actual mass of the explosive. Values for the energetic release of common explosives are easily available and have been tabulated by Baker et al. [48] and Kinney & Graham [49].

3.3 Calculation of blast wave parameters

There are numerous empirical approaches for calculating blast wave parameters at a distance from an explosion. These methods are based on analysis of experimental data of large and small scale explosions to deduce a relationship between the peak overpressure and the scaled distance. They are valid for free-air and surface bursts as long as the correct ground reflection factor is used.

Kinney and Graham [49], basing their findings on a large volume of experimental data, produced the following relationship for the peak overpressure,

$$p_{so}(Z) = p_0 \frac{8.08 \times 10^7 \left[1 + \left(\frac{Z}{4.5} \right)^2 \right]}{\sqrt{\left(1 + \frac{Z}{0.048} \right)^2 \left(1 + \frac{Z}{0.32} \right)^2 \left(1 + \frac{Z}{1.35} \right)^2}}, \quad (3.8)$$

where Z is the scaled distance and p_0 is the ambient pressure.

We also consider Needham's 1 kt nuclear blast standard which is a set of equations for describing the detonation of a 1 kt nuclear device in an infinite sea level atmosphere [50]. The model is a fit to the results of first principles numerical calculations, supplemented by nuclear air blast data for above ground tests. The model is valid from 4.5 m to 20 km for nuclear and non-nuclear tests. The peak overpressure predicted by the model is of the following form

$$p_{so}(R) = \frac{A}{R^3} + \frac{B}{R^2} + \frac{C}{R \sqrt{\ln \left(\frac{R}{R_0} + 3 \exp \left[-\frac{1}{3} \left(\frac{R}{R_0} \right)^{1/2} \right] \right)}} \quad (3.9)$$

and is expressed in CGS units. The constants are $R_0 = 4.454 \times 10^4$, $A = 3.04 \times 10^{18}$, $B = 1.13 \times 10^{14}$, $C = 7.9 \times 10^9$.

The third approach that we consider are the Kingery-Bulmash polynomial fits [6, 51] which represent the most widely used and accepted of all the empirical approaches. Their work provides polynomial fits for incident and reflected pressures including a range of other parameters for free-air and surface bursts. The results are presented in the form of tabulated data in [6] and are valid for scaled distances in the range $Z = 0.05 \text{ m/kg}^{1/3}$ to $Z = 40 \text{ m/kg}^{1/3}$.

Figure 3.2 shows a comparison of these three approaches to compute the peak overpressure. It can be observed that, for small scaled distances ($Z < 1 \text{ m/kg}^{1/3}$), there exists a significant variation in the predicted pressure. The reason for this disagreement is the poor quality of experimental data in this region where instrumentation usually exhibits a large degree of error. It is therefore important to take care when predicting blast characteristics at short scaled distances.

Other empirical relationships have been developed by Brode [13], Henrych [52], Held [53], Bajić and Sadvovskiy [54]. For the sake of brevity, we leave the further study of these to the reader.

3.4 Explosion types

Unconfined, external explosions can be categorised into three basic types depending on the height above ground of the charge (H) and the radial distance from the

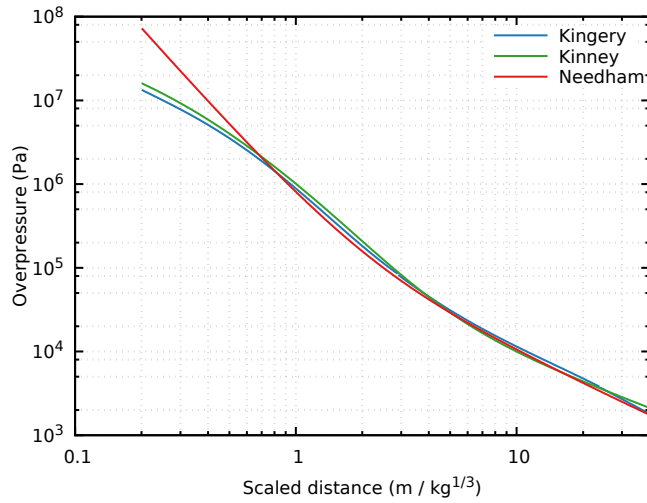


Figure 3.2: A comparison of peak overpressure against scaled distance for three scaling laws.

blast-loaded object (R). Figure 3.3 illustrates these three types.

When the height above ground is sufficiently large the blast waves propagate spherically outwards, reaching the structure before any interaction with the ground. This is known as a free-air burst. At lower altitudes, the blast wave is able to interact with the ground, reflecting and forming a secondary shock wave which travels behind the first. The reflected wave passes through heated, compressed air faster than the incident wave. Eventually the secondary wave catches up with the first, merging and forming a Mach stem.

Figure 3.4 shows this process schematically, where the incident and reflected waves are labelled I and R respectively. When the angle of incidence α_1 reaches the critical angle ($\alpha_c \simeq 40^\circ$ [55]) the Mach stem M begins to form. This phenomenon is of particular interest when studying the blast loading of structures because the peak pressure and impulse of the Mach stem can be considerably higher than the incident value.

When the charge is located on the ground, the blast waves immediately reflect and propagate hemispherically outwards before impinging on the structure. Surface bursts can be modelled as a free-air burst with double the charge mass because the ground acts as a plane of symmetry. In reality, the ground absorbs some of the incident waves and a factor of 1.8 is used instead [48].

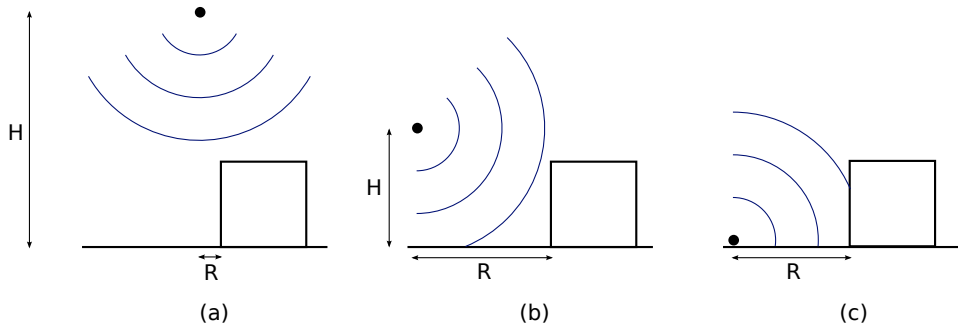


Figure 3.3: Types of external explosions; (a) free-air burst, (b) air burst, (c) surface burst.

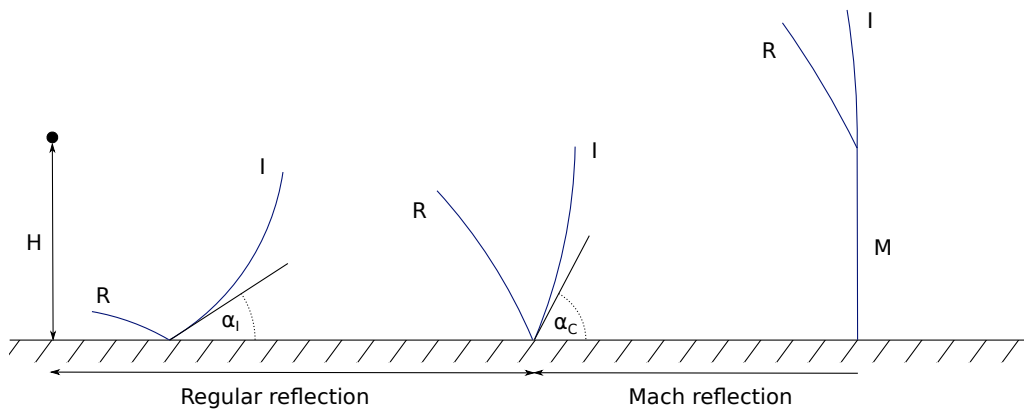


Figure 3.4: Mach stem formation from an air burst explosion.

3.5 Modelling approaches

A range of different approaches exist for the prediction of blast loads and vary in their ratio of accuracy to computational expense. Broadly, three categories exist: empirical methods, semi-empirical methods and computational methods.

3.5.1 Empirical methods

Empirical methods make up the simplest and most widely used approach. They are derived from correlations found in experimental data. The scaled distance curves outlined in section 3.3 are one particular example of such a method. The ConWep tool [9] is another practical example. The program allows the user to input the explosive parameters before calculating the blast wave solution based on empirical data.

Empirical methods are fast and relatively simple. This is their major advantage. However, such methods are severely limited by the fact that they do not take into account any geometry or terrain effects on the blast wave. They are also bounded by the experimental data. The Kingery & Bulmash curves are limited to scaled distances between $0.05 \text{ m/kg}^{1/3}$ and $40 \text{ m/kg}^{1/3}$. Anything outside this range is not validated. These shortcomings make this type of approach unsuitable for urban blast or any other application in which the geometry has a significant effect on the solution.

3.5.2 Semi-empirical methods

Semi-empirical methods attempt to address the shortcomings of empirical methods by considering limited geometrical aspects without attempting to solve any underlying conservation equations. Experimental data is used and manipulated to account for different geometrical cases.

One such approach is the use of ray-tracing techniques to approximate the effects of enclosed or partially enclosed explosions. Data from free-field explosions is used and reflected shocks are added to provide a reasonable approximation of the maximum average pressure and impulse. Contributions by Wager [8] and Britt & Lunsden [56] are of note. Other methods are capable of predicting quasi-static gas pressures that are the result of vented, internal explosions. Given the internal volume, charge size and venting characteristics, these models are able to predict a pressure time history for the blast [57]. The ray-tracing and quasi-static histories can be combined to give a full pressure history. This has been shown to match experiment with reasonable accuracy in limited circumstances [57].

These methods allow the user to improve the predictive ability of empirical methods without any additional computational expense. However, the validity of these methods is limited to confined or partially confined scenarios involving simple geometries. As is the case with empirical methods, complex urban scenarios remain largely out of reach.

3.5.3 Computational methods

The third and most complex method involves the use of computational fluid dynamics (CFD) codes to solve the underlying continuity equations of fluid flow. The Navier-Stokes or Euler equations of mass, momentum and energy are typically used. An Eulerian formulation, in which the mesh remains stationary, is the most popular approach. The problem is discretised and the three equations are solved over computational cells, with the cell size being held sufficiently small that the variation in conserved variables across each cell can be assumed to be constant.

These methods can be combined with an immersed boundary condition to enable the user to capture the effects of arbitrarily complex geometry on the problem. This is a key advantage of computational models and makes them particularly suited to the simulation of explosions in urban scenarios or regions of complex topology. However, this improved accuracy comes at the expense of computational cost. The constraints on the cell size can sometimes mean that the time taken to perform analysis becomes disproportionate to the difficulty of the problem.

3.6 Blast wave-structure interaction

As the blast wave moves outwards it engulfs every object that lies within its path. Objects most at risk typically include people and structures, with the risk of mortality or building damage increasing with the strength of the blast wave. In contrast to unobstructed free-air explosions, the strength of the wave in an obstructed explosion is not simply a function of the scaled distance. Structures that interact with the blast waves can profoundly alter their strength through a range of blast loading phenomena that we shall explore in the present section.

3.6.1 Reflections

The interaction between a structure and a blast wave generates a different pressure history from the idealised representation in figure 3.1. When a blast wave impinges upon a surface a reflection occurs, raising the pressure above the incident pressure.

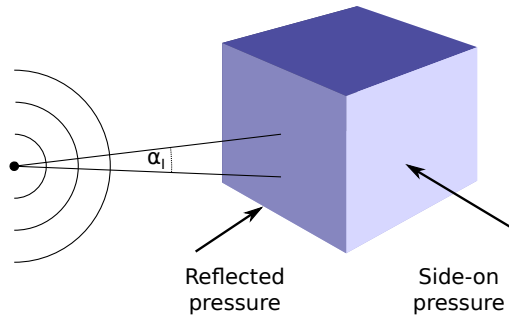


Figure 3.5: Types of wave reflection.

This is called the *reflected pressure*. In an ideal elastic case, the normal reflection of air molecules from a rigid surface should lead to a reflected pressure that is double the incident pressure. In fact, due to non-linear effects in the gas, reflected air particles become obstructed by subsequent particles. This leads to a significantly higher reflected pressure, between 2 and 8 times the incident pressure [58]. The following equation shows that it is the dynamic pressure of the gas that is responsible for the large reflected pressure p_r :

$$p_r = 2p_s + (\gamma + 1)q_s, \quad (3.10)$$

where

$$q_s = \frac{1}{2}\rho_s u_s^2 \quad (3.11)$$

is the dynamic pressure of the gas, a function of ρ_s the density and u_s the gas velocity [59].

Three types of reflection occur: the first case involves the normal reflection of the blast wave when the angle of incidence $\alpha_i = 0^\circ$. This type of reflection generates the highest reflected pressures. As the angle of incidence increases, oblique reflections — the second type of reflection — occur. Once the angle has reached the critical angle α_c a Mach reflection occurs. Eventually the reflecting surface becomes perpendicular to the front of the blast wave ($\alpha_i = 90^\circ$). At this point the reflected pressure reaches a minimum and is equal to the incident pressure. This is termed the *side-on pressure*.

Contrary to intuition, the reflected pressure does not decrease smoothly between its maximum at $\alpha_i = 0^\circ$ and minimum at $\alpha_i = 90^\circ$. A local maximum is observed in the 40° to 55° range [60]. The reason for this is the creation of a Mach stem between these angles. The coalesced wave that is created can cause the local reflected pressure to become substantially higher than for the regularly reflected case.

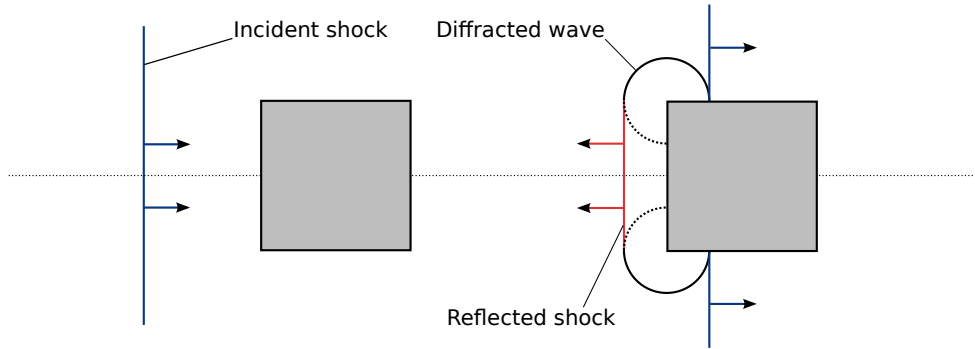


Figure 3.6: An illustration of the effects of blast wave clearing around a solid obstacle. The incident wave is reflected, forming a diffracted region and rarefaction wave.

3.6.2 Clearing

When a large-radius or planar blast wave normally impinges upon an obstruction of finite size, a reflection occurs along the normal face of the building, generating a reflected pressure. At the building sides, there is effectively no obstruction and lower incident pressures are observed. A pressure imbalance initiates a flow from the high pressure region towards the building sides. This flow is identified by a rarefaction which moves from the corners of the structure to the centre of the loaded face. Figure 3.6 illustrates this process.

The effect of clearing is a more rapid return to ambient conditions when compared to reflection from an infinitely wide normal surface. The rate of relief depends on the building geometry and is a complex problem to solve. There exist a number of semi-empirical approaches for the prediction of clearing effects. Most are based on scaled blast parameters, assuming that the building is perpendicular to the blast and that the wave is effectively planar. Methods for the calculation of these effects are outlined in [48, 61–64].

At the centre of these models lies the assumption that the cleared blast pressure decays linearly from the peak reflected pressure during the clearing time t_c . After this time, the pressure is described by the stagnation pressure

$$p_{\text{stag}} = p(t) + C_D q_s(t), \quad (3.12)$$

where C_D is the drag coefficient of the structure.

The semi-empirical assumptions used today have a number of drawbacks. The methods assume that the clearing targets are small enough that the clearing effects occur uniformly across the loaded surface. There is also a lack of agreement in the

literature on how the clearing time should be calculated [59]. Recent work to extend and improve the methodology has been performed by Ballantyne et al. [65], Rickman & Murrell [66] and Rigby [59]. The methods succeed in reasonably approximating cleared pressures for simple geometries. However, for complex urban geometries the methods fall short and computational methods should be used instead.

3.6.3 Channelling and shielding

When blast waves occur in urban areas, the presence of city streets leads to the shielding and channelling of shocks. Intuitively, one would assume that city streets have an overall effect of shielding and protecting nearby structures. However, streets can confine blast waves, channelling their energy and causing a greater degree of destruction in certain ‘hot spots’. The nature of channelling and shielding is highly complex. Research has shown that semi-empirical methods including the ConWep and AT Planner tools generally fail to predict the blast characteristics that arise from these phenomena [67].

One of the first investigations into the effect of street configuration was performed by Smith et al. [68]. In this study, a simple 1/50th scale model of a street was constructed, consisting of two parallel concrete beams. At each end, a concrete building was placed and a charge was detonated in the centre of the street. The authors recorded the pressure signal and compared to a scenario without the buildings. The confining effect of the street was shown to significantly increase the pressure on the surface of the building (by approximately a factor of four).

The authors extended this pilot study, exploring a range of different street configurations that included a crossroads, a T-junction, a 90° bend, a straight street and a cul-de-sac. A small charge was placed at the centre of each configuration and a series of pressure gauges was situated along the walls. The height of the buildings was made sufficiently large that any effects of blast wave clearing over the top of the street would be negligible. The authors performed an experimental and a numerical study of the problem, demonstrating the blast enhancing effect of certain configurations. The layouts that created the highest confinement, such as the cul-de-sac, produced the greatest increase in overpressures compared to the unconfined case.

Smith and Rose further extended the study in [69], using straight small-scale streets of width w and building height h . An experimental and numerical study using the code Air3d [70] investigated the effects of channelling and clearing by varying w and h . The authors found that for scaled street widths $w/W^{1/3} < 4.8 \text{ m/kg}^{1/3}$, the effect of reflections from buildings on the other side of the street leads to higher pressures and impulses when compared to a single infinitely high reflective surface. Above this

width, the buildings are too far apart for reflections to have a significant effect. As the building height increased, the extra confinement led to increased pressures and impulses. Buildings higher than $3.2 \text{ m/kg}^{1/3}$ showed no extra effect on the blast wave strength and could be considered infinitely high. An earlier, numerical study was also performed by Rose in his thesis [70].

Similar numerical studies were performed by Remennikov [71, 72] investigating the effects of channelling and shielding. The authors investigated the shielding effects when a small building was placed between the charge and a larger building. Their simulations showed that the primary shock reflected off the larger building, eventually striking the rear of the smaller building and generating pressures two and a half times as high as those observed during the initial loading of the front of the building. A separate channelling study was performed, producing results in agreement with the work mentioned in this section. The effect of urban geometry on the propagation of the blast wave is summarised in their conclusion that ‘channelling of the blast is shown to increase peak pressure by about 400% and peak impulse by about 500% at extended distances from the source compared with analytical results for the blast wave expanding hemispherically over a flat surface’.

In [73] and [74] Smith et al. investigated the outcome when the effects of channelling and shielding are combined, conducting experiments through arrays of small-scale concrete buildings. Experimental and numerical results were obtained for a charge located within an array of terraced and detached houses. It was found that the presence of buildings between the charge and monitoring gauge had a shielding effect, reducing the blast strength compared to a free-field explosion.

The authors then investigated the detonation of a charge in front of a randomly and regularly spaced array of buildings. The blast resultants were measured on the other side of the building array. It was discovered that, no matter the layout of the buildings, the array always resulted in a reduction of blast strength. However, this reduction was modest (in excess of 10%) and suggested that, in a complex array of buildings, the positive effects of clearing are largely offset by channelling.

3.6.4 Building porosity

In most blast studies, an assumption is made that buildings are rigid and perfectly reflective. In reality this is not the case. Buildings usually devote a significant proportion of their surface area to frangible materials such as glass. Depending on the strength of the blast, it is common for these materials to deform and even break, absorbing and deflecting some of the energy of the explosion. Methods that take into account façade failure tend to be less conservative overall.

Smith et al. developed an experimental and numerical study to understand the effects of façade failure on blast waves propagating outside a building [73]. A 1/50th scale model of a building was created with gaps in the façade, allowing for a porosity that could be varied between 24 % and 77 %. Gauges were placed on the front of the building and the impulse was shown to decay linearly with an increase in pressure, both in the numerical and experimental results. As the porosity of the façade was increased, more energy was vented from the street, leading to a corresponding drop in impulse.

Gauges mounted on the interior core of the building showed that, if the blast was to penetrate the building, serious damage could occur to the internal structure and occupants. The authors concluded that engineers should strive to develop façades that are as robust as possible to minimise the effects of building damage.

A large body of work has been achieved studying the effects of street layout on blast wave resultants. However, nearly every study has assumed rigid, perfectly reflecting buildings. It is clear that these assumptions lead to an overly conservative estimate of pressures and impulse. The question of how conservative is still relatively unknown. Having studied the literature, we propose to study this problem by introducing the concept of building porosity into some of the previous studies on channelling.

3.6.5 Blast walls

A blast wall is a barrier that separates a building from a damaging blast load. The prevalence of war and terrorism during the 20th and 21st centuries has led to much interest in improving blast wall design to maximise the protective effects of such a structure. A significant amount of experimental research has been performed since the Second World War. However, during the past 20 years, the improvements in computing power have led to a large increase in the number of numerical studies.

When a blast wave impacts a wall, the shock normal to the wall is reflected. However, the wave above the wall experiences diffraction and the wave ‘rolls over’ the wall. This means that sections of the target building lying below the top of the wall are not necessarily protected [75].

Early studies performed during the last World War and subsequent troubles in the Middle East and Northern Ireland focussed on understanding how high walls should be in order to provide a certain level of protection against a specific bomb. It was found that behind the wall, a significant reduction in blast strength occurs up to five to six wall-heights from the barrier [76]. During the same period, researchers were trying to better understand the wave phenomena that occur behind the wall

after obstruction of the wave. Beyer was able to outline the trajectory of the blast wave, showing how it reflects off the ground and forms a potentially dangerous Mach stem [77]. This influenced engineers to improve the design of blast walls, attempting to mitigate the risk from Mach reflections [78].

Several studies have been performed, looking at how the design of the wall can be altered to mitigate some of these effects. The UK Ministry of Defence sponsored research into the performance of walls featuring an overhanging canopy on the charge side. It was found that walls with a canopy inclined at 90° to the wall offered a modest improvement over plane walls [76]. Recent work by Zhou and Hao has suggested that the form of the barrier can have significant effect on its protective capacity [15]. The researchers showed that the reduction in blast load does not depend solely on the building height and the positions of the wall, charge and building. Sochet et al. extended this work, studying various barrier geometries and concluding that the ideal wall shape *is a parallelepiped with significant height and thickness* [79].

When a blast wave passes through a series of evenly spaced obstacles diffraction occurs. Waves from adjacent obstacles can interact with one another and cancel out through destructive interference. Several authors have investigated this concept with the aim of making architecturally appealing walls formed from a series of columns [80]. Niollet et al. found that by placing a series of cylindrical bars between the charge and a blast wall, fast wave attenuation was observed [81]. Chaudhuri et al. and Zong et al. investigated the effect of an array consisting of rigid columns of various geometries [82, 83]. Circular and triangular columns were found to work best.

Other more elaborate, innovative concepts for protecting buildings including curtains and terrain modelling have been proposed but lie outside of the scope of this study. See the work of Gebbeken and Döge for a review [84].

In most buildings, windows are regularly spaced in much the same way as the columns in the blast walls of the aforementioned studies. These window arrays are therefore likely to produce the same diffraction effects when impinged upon by blast waves. By varying the window width and spacing it may be possible improve wave attenuation, possibly reducing the strength of blast waves that propagate into a building. We believe this could be an interesting topic of research and are not aware of any previous work on the subject.

3.6.6 Building shape and complex geometries

The shape of buildings have a role to play in reducing blast loading. Research has indicated that certain structural shapes can significantly affect the blast load.

Gebbeken and Döge performed a study investigating these effects [85]. The authors found that in square and rectangular long-edge shapes, the peak reflected pressure is nearly constant across the edge facing the explosion. For circular structures, the strength of the reflected pressure decreases gradually from the centre of the shape. The researchers also compared convex and non-convex buildings, concluding that convex buildings are not always more effective than non-convex structures at reducing blast loads.

The effect of blast in real cityscapes has been studied by several researchers. In [86], Smith et al. presented an experimental and numerical study of the effects of a blast in a generic cityscape containing simple buildings with a non-regular shape and streets of different widths and orientations. In the 1/50th scale model, charges were detonated at six different locations and a series of gauges recorded the pressures. Interestingly, the distribution of strong loading was not intuitive. This led the authors to conclude that the use of CFD techniques offers the best approach for calculating blast loads in complex urban environments.

During the past five years there has been a significant body of work combining blast with more complex geometries that closely resemble real world objects. Urban GIS data has been used to create realistic urban models for blast simulation with the aim of producing tools for urban disaster recovery following a terrorist attack. Work by Mensinger & Trometer [87] and Ripley et al. [88] is of note. Other authors have demonstrated CFD tools capable of simulating blast scenarios that include military vehicles [89], train carriages [90], train stations [91], oil and gas installations [92] and building interiors with multiple rooms [93].

3.6.7 Comments and conclusions

In this section we have reviewed the underlying theory on the formation of blast waves and their interaction with solid obstacles. Having studied the literature, we have identified two areas where the knowledge base is lacking and could benefit from further research: The effect of building porosity on blast wave channelling and shielding is not well understood. We propose to repeat some of the previous channelling studies with a variable building porosity as a way of investigating this phenomenon.

Secondly, we would like to study whether the layout of windows in buildings can be optimised in such a way as to reduce the strength of blast waves that propagate into a building. Through the use of diffraction, we hope to propose an optimal layout that could reduce the risk to the building's internal structure and occupants.

3.7 Numerical model

In this section we describe the numerical model with which we simulate the detonation of a high explosive and the evolution of the subsequent blast waves. The conservative, differential form of the Euler Equations described in section 2.1 is used with an additional source term s :

$$\partial_t \mathbf{u} + \partial_x \mathbf{f}(\mathbf{u}) + \partial_y \mathbf{g}(\mathbf{u}) + \partial_z \mathbf{h}(\mathbf{u}) = s \quad (3.13)$$

where $\mathbf{f}(\mathbf{u})$, $\mathbf{g}(\mathbf{u})$ and $\mathbf{h}(\mathbf{u})$ are the flux vectors of the conserved variables vector \mathbf{u} . The approach employed to model the energy release from the explosion is based on the approach of Rigas and Sklavounos [94]. Energy is released into the system at a rate proportional to energetic release during the burning of the reactants. This energy is released into the system for a finite time t_{det} and assumes a constant detonation velocity u_{CJ} . The explosive is assumed to have an initial density ρ_{det} and energy density Q_{det} . The detonation wave is assumed to move outwards spherically until reaching a radius $r_{\text{det}} = t_{\text{det}} u_{\text{det}}$. The explosion model is linked the Euler equations through the source term in equation 3.13

$$s = \begin{bmatrix} 0 \\ 0 \\ \frac{Q_{\text{det}}}{V} \frac{dV}{dt} \end{bmatrix}, \quad (3.14)$$

where V is the volume of the explosive sphere ($\frac{4}{3}\pi r^3$) with time dependence

$$\frac{dV}{dt} = \begin{cases} 4\pi u_{\text{CJ}}^3 t^2, & t < t_{\text{det}} \text{ and } r < r_{\text{det}} \\ 0, & \text{otherwise.} \end{cases} \quad (3.15)$$

This ensures that the energy release is proportional to the area of the surface of the sphere where the burning occurs.

Equation 3.13 is solved using operator splitting. An Eulerian finite-volume MUSCL HANCOCK scheme with an exact or HLLC Riemann solver is used to solve for the hyperbolic side. A fourth order Runge Kutta method is then used to solve the source-term ODE. In all subsequent simulations we choose the ambient state to be $\rho = 1.225 \text{ kg/m}^3$, $v = 0 \text{ m/s}$, $p = 101.325 \text{ kPa}$.

3.8 Numerical validation

In this section we present the numerical validation of the blast framework. We demonstrate a number of tests which validate each component, including the TVD flux solver, the explosion model and the cut-cell geometry method.

Test	ρ_L	u_L	p_L	ρ_R	u_R	p_R
1	1.0	0.75	1.0	0.125	0.0	0.1
2	1.0	-2.0	0.4	1.0	2.0	0.4
3	1.0	0.0	1000.0	1.0	0.0	0.01
4	5.99924	19.5975	460.894	5.99242	-6.19633	46.0950
5	1.0	-19.59745	1000.0	1.0	-19.59745	0.01

Table 3.1: Initial data for five one-dimensional test problems from Toro [17].

3.8.1 One-dimensional shock tube problems

The first test involves a one-dimensional shock tube problem that tests for the correctness of the hyperbolic solver. We choose five one-dimensional test problems from Toro [17] and note the initial conditions in table 3.1. In each test, two ideal gases with $\gamma = 1.4$ are separated by a discontinuity at position x_0 . Each test has an exact solution and is therefore useful for verifying a hyperbolic solver. A numerical solution is computed with $M = 200$ cells in a spatial domain where $x \in [0, 1]$ with a CFL number $C_{\text{eff}} = 0.9$. An HLLC Riemann solver is used. Results for the five tests are shown in figures 3.7 to 3.11 plotted against an exact solution.

Test 1 is a modified version of the popular Sod’s problem [95]. A right shock, a right travelling contact wave and a left sonic rarefaction are produced. The test is useful for testing for the entropy satisfaction of the numerical method. Test 2 involves two outwardly moving rarefactions which form a near vacuum in the centre of the domain. This tests for the ability of the numerical method to cope with low density flows. Tests 3 and 4 are very severe tests designed to test the ability of the method to cope with strong shocks. Finally, test 5 is designed to assess how the method deals with a stationary contact discontinuity.

The results show a good representation of shocks and contact discontinuities, with minimal diffusion. Oscillations are kept to a minimum and are only observed in the vicinity of the strongest shocks. The most visible deficiency is the solution for internal energy in test 2. The energy is calculated from the pressure and density which both take very small values in the vacuum. The floating point representation of these numbers causes small numerical errors to be amplified, creating large errors that appear in the resulting internal energy. This is a well known problem which affects many other numerical methods.

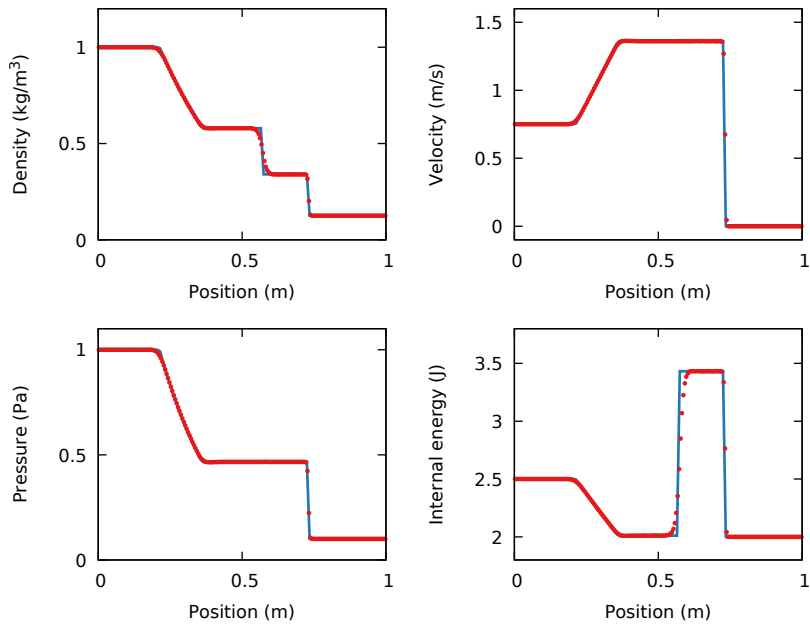


Figure 3.7: MUSCL HANCOCK applied to test 1 from Toro [17], with $x_0 = 0.3$. Numerical results are shown as red points, with exact results in blue at $t = 0.2$.

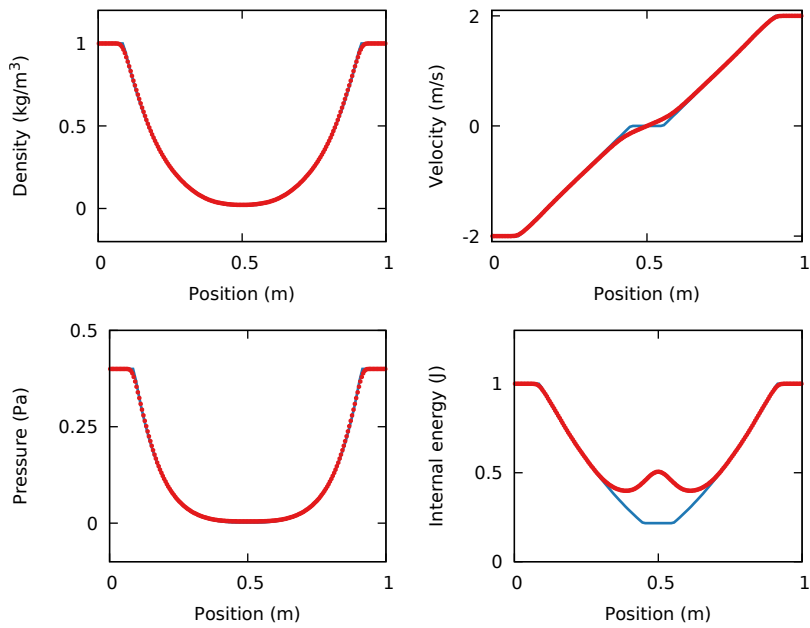


Figure 3.8: MUSCL HANCOCK applied to test 2 from Toro [17], with $x_0 = 0.5$. Numerical results are shown as red points, with exact results in blue at $t = 0.15$.

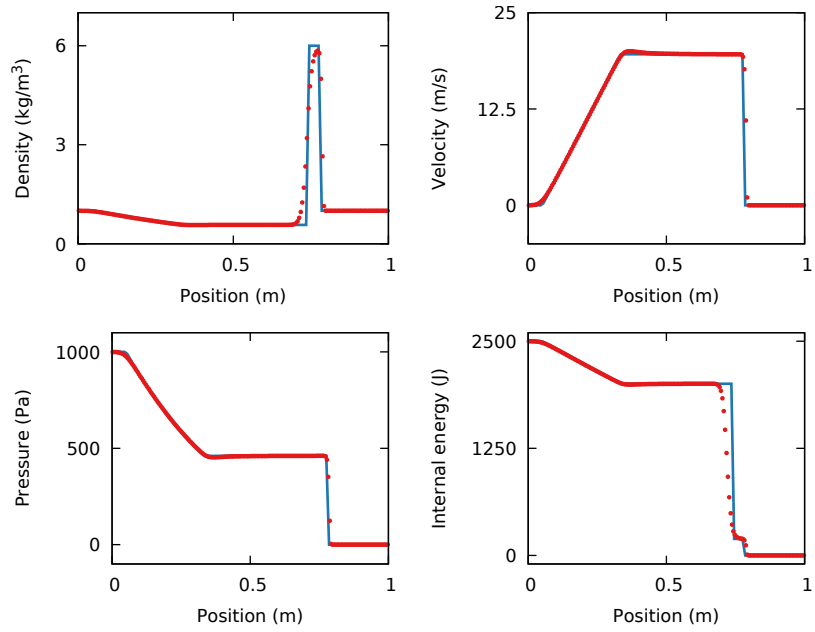


Figure 3.9: MUSCL HANCOCK applied to test 3 from Toro [17], with $x_0 = 0.5$. Numerical results are shown as red points, with exact results in blue at $t = 0.012$.

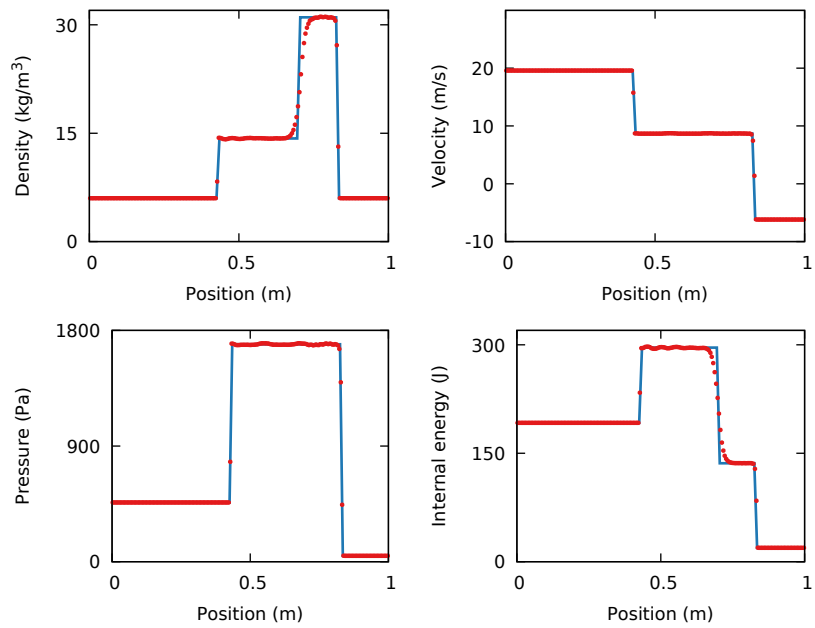


Figure 3.10: MUSCL HANCOCK applied to test 4 from Toro [17], with $x_0 = 0.4$. Numerical results are shown as red points, with exact results in blue at $t = 0.035$.

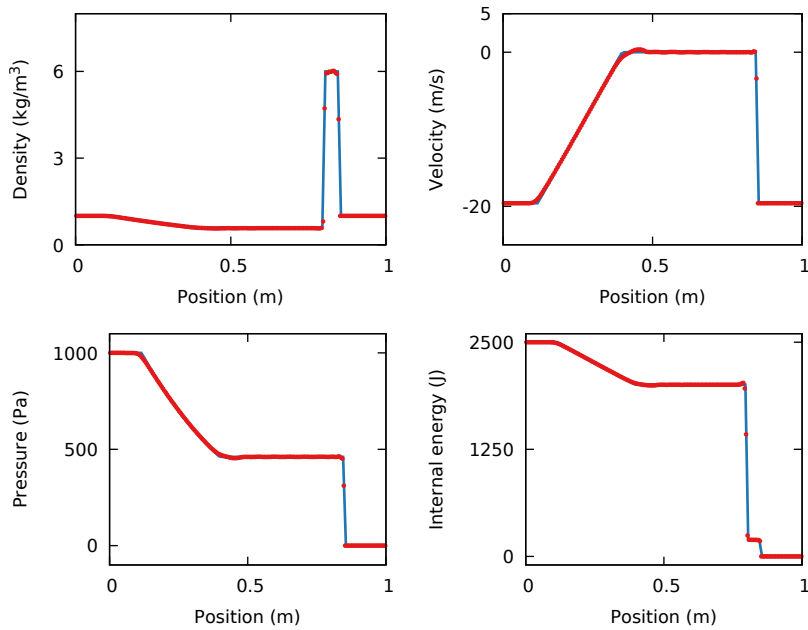


Figure 3.11: MUSCL HANCOCK applied to test 5 from Toro [17], with $x_0 = 0.8$. Numerical results are shown as red points, with exact results in blue at $t = 0.012$.

3.8.2 Shock diffraction over a sharp edge

In the real world, blast waves interact with and diffract around solid objects. We set up a simple shock diffraction test to demonstrate the code's ability to capture this process.

Shock diffraction occurs when a shock wave encounters a sudden area expansion after passing through an obstacle. The wave spreads, covering the new area and several complex flow features are created. Figure 3.12 shows the features that are created when a right moving weak shock (Mach number below 1.8) diffracts around the sharp obstacle shown in blue. A shear layer is created when the shocked flow is unable to travel around the sharp corner and a vortex is formed. This shear layer is unstable, with Kelvin-Helmholtz structures eventually forming. This has been observed both experimentally and numerically by Sun and Takayama [96].

Despite the complexity of the process, shock diffraction has been studied in great length and the correct flow features are easily recognisable [97, 98]. The diffraction experiments of Dyke have produced shadowgraph images that we use for validation purposes [99].

A 2D simulation was performed with a domain of size $3\text{ m} \times 3\text{ m}$ using 1200 cells

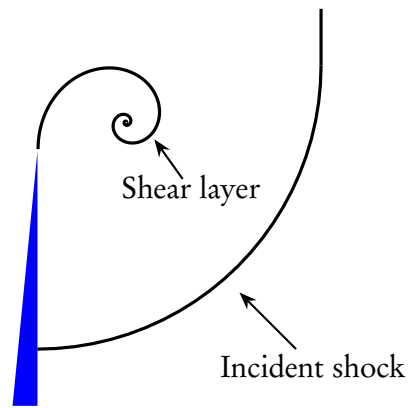


Figure 3.12: Diffraction of a weak shock around a sharp object.

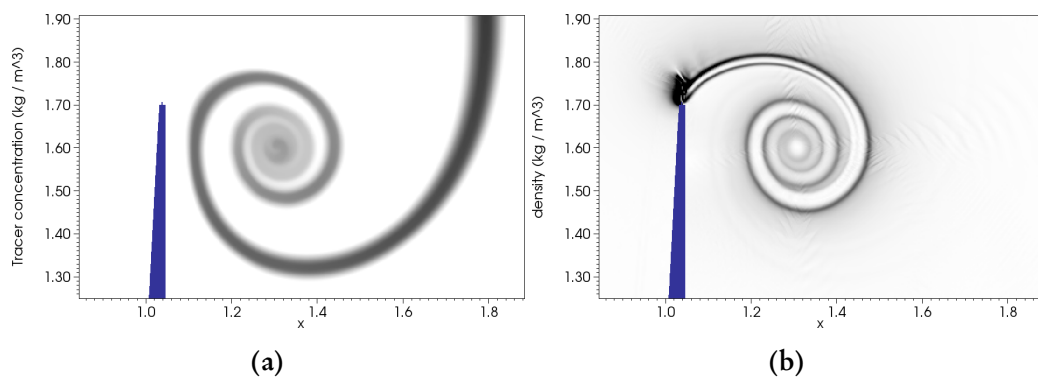


Figure 3.13: Diffraction of a shock wave over a sharp edge: A column of massless tracer is entrained by the fluid flow, causing a vortex to be formed. Tracer concentration (left) and a density schlieren (right) are shown for a MUSCL HANCOCK scheme at $t = 5$ ms.

in each direction. A right moving Mach 1.3 shock was initialised in the left half of the domain. A solid knife edge of height 1.75 m was placed in front of the shock and a 1 cm thick vertical column of massless tracer was initialised between the tip of the knife and the top of the domain. As the shock diffracts over the knife edge, the tracer, advected by the vortical flow field, should roll up and form a vortex. Figure 3.13 shows the tracer field (left) and density schlieren (right) at $t = 5$ ms, demonstrating good agreement with the experimental results published by Dyke [99].

3.8.3 Free-field blast

The previous tests demonstrated the framework's ability to capture the propagation and interaction of shocks. In blast, these shocks arise from explosions, and the next important step is to verify that these shocks have been generated correctly by the numerical source term. To test the model's suitability we simulate a free-air explosion and compare the blast wave characteristics with an empirical model.

A free-air burst from a 1 kg spherical TNT charge was simulated with the source term approach. Exploiting the symmetry of the problem, a 1D simulation was performed at a resolution of 1 mm. A series of gauges was placed at varying intervals from $0.3 \text{ m/kg}^{1/3}$ to $30 \text{ m/kg}^{1/3}$ from the charge centre. At each gauge, the maximum overpressure and wave arrival time were recorded. These are plotted against scaled distance in figure 3.14. The empirical Kingery Bulmash predictions are shown for comparison.

A good correspondence is achieved between the simulated and predicted characteristics. There is a slight divergence between the overpressures at small scaled distances. As mentioned earlier in the chapter, for distances below $1 \text{ kg/m}^{1/3}$, the agreement between the various empirical relationships begins to break down because of inconsistencies in the underlying data. Furthermore, the explosive model used in this thesis does not capture the ignition and detonation of the explosive. This means that the near-field effects associated with these processes are not captured.

3.8.4 Cityscape blast experiment

The final test involves the simulation of blast propagation within a complex cityscape geometry. The scenario is a useful validation test for the code's ability to handle non-grid aligned geometries. The scenario also provides a useful test for the complex interaction, diffraction and reflection of waves within the geometry.

The test is taken from experimental work performed by Brittle in [100] where a typical street geometry was created in 1/50th scale using concrete blocks. The layout

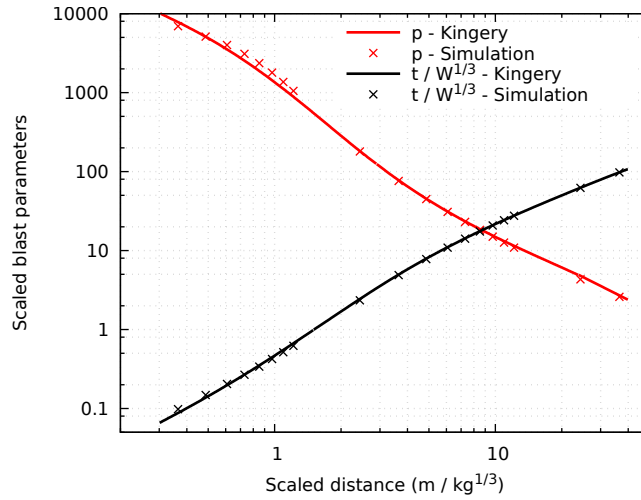


Figure 3.14: Comparison of peak pressure and arrival time. Results from the numerical simulation are shown as points and are compared with the Kingery Bulmash predictions (lines).

represents a road network that one might find in a conventional city centre, with both grid and non-grid aligned lanes that are spaced to give a road width of 15 m when scaled up. The buildings are laid out in such a way as to provide a range of different reflection angles and confinement levels. Figure 3.15 shows the street layout, with buildings shown in black.

In the experiment, six 16 g TNT charges P1 to P6 were positioned at various locations. We chose to simulate the test with charge P1 located at $(x, y, z) = (0.4789 \text{ m}, 0.3512 \text{ m}, 0.04 \text{ m})$, shown in blue in figure 3.15. At full scale, this corresponded to a 2000 kg truck bomb detonated 2 m above the ground. In the numerical simulation, the charge was assumed to be perfectly spherical and the ground completely flat and reflective. 22 pressure gauges G1 to G22 were evenly spaced across the left and right end walls. An AMR mesh was used featuring two levels of refinement, affording a maximum resolution of 2 cm. The simulation was run until a final time of $t = 8 \text{ ms}$.

Figure 3.16 shows a series of snapshots of the blast wave pressure iso-surface at times $t = 0.2 \text{ ms}$, $t = 0.4 \text{ ms}$, $t = 8 \text{ ms}$, and $t = 14 \text{ ms}$. The buildings are shown as yellow objects. Pressure histories are shown in figure 3.17 for gauges G1, G3, G11 and G21 (locations indicated in red in figure 3.15). The experiment is shown in black, with simulation results in red.

Gauge G1 has the most direct line of travel from the charge to the gauge, and the timing and amplitude of the initial blast wave is captured well. The characteristic

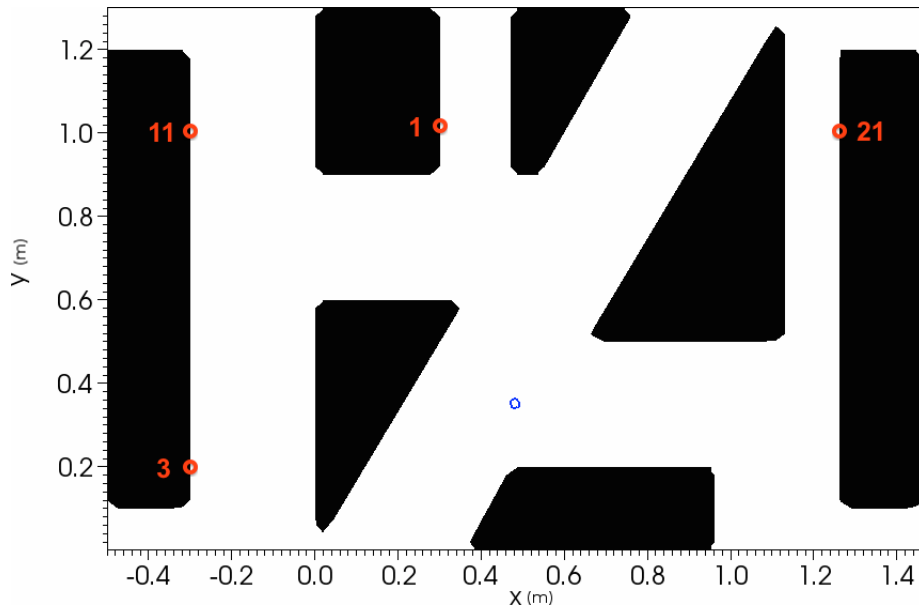


Figure 3.15: Map of the cityscape test site with buildings shown in black and the charge as a blue ring. The pressure gauge positions are indicated in red. The geometry layout was chosen to mimic a conventional street configuration with a realistic road system.

underpressure that follows the initial wave is captured too. Gauge G11 has the next shortest path from the charge but relies on wave reflections to be reached. The numerical results capture the primary peak well and generally demonstrate a good agreement with the experiment. The experimental data shows a more complex structure of wave interactions than observed in gauge G1. As time progresses, the numerical and experimental results diverge as the errors in the numerical method compound from the inability to sufficiently capture all wave interactions. These errors arise from insufficient numerical resolution around the weaker waves that arise from these interactions. This does not cause significant concern as we are most interested in the primary wave which carries most of the capacity for damage.

Gauges G3 and G21 exist along the most indirect paths from the charge. They also exhibit discrepancies in certain areas. Generally peak heights are similar to the experimental data and gauge G21 captures the general shape of the complete blast profile well. The main issue is the timing difference for the entry of the first wave, with the effect most pronounced for the shielded gauges. These differences could be explained by shortcomings in the experimental setup. The concrete blocks were not fixed to their location and were not expected to move. In fact, slight movements of the blocks near the charge were measured, suggesting that some of the incident energy

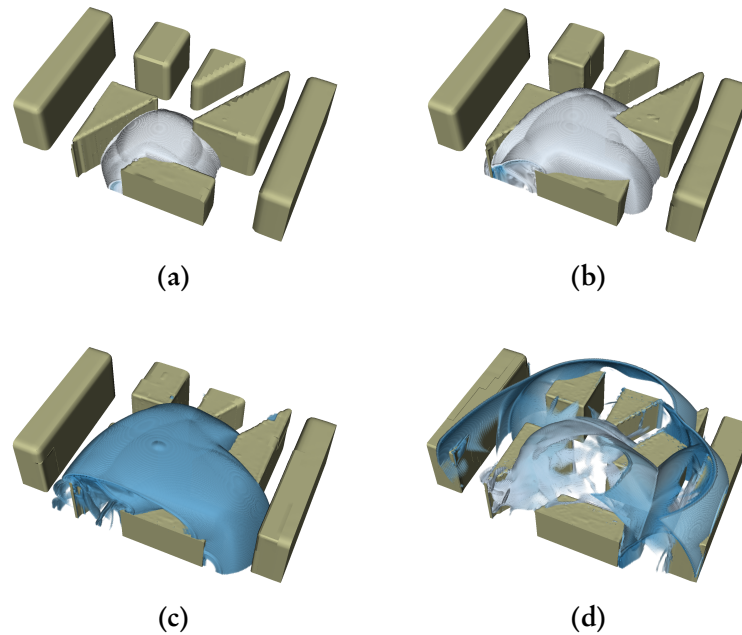


Figure 3.16: Volume plot of the pressure iso-surface for the cityscape blast experiment. Snapshots are shown for the following times: (a) $t = 0.2$ ms, (b) $t = 0.4$ ms, (c) $t = 8$ ms, (d) $t = 14$ ms.

from the blast had been absorbed by the structures. The charge was assumed to be perfectly spherical and the ground slab perfectly flat and reflective. Neither of these assertions are completely true and could account for some part of the discrepancy. The existence of pressure waves travelling through the ground was not considered, which could account for some of the extra signal on the experimental data. A further reason for the timing errors may lie with the choice of equation of state (EOS). An ideal-gas EOS is used for this simulation, which is not appropriate for the gaseous products released from the explosion. A JWL or Williamsburg EOS may be better suited to the problem, allowing one to capture the effects of shock heating and the resulting change in speed of subsequent reflected shock-waves.

Overall, the blast framework shows a good correlation with most of the pressure histories, demonstrating the code's validity for capturing blast propagation in complex 3D geometries.

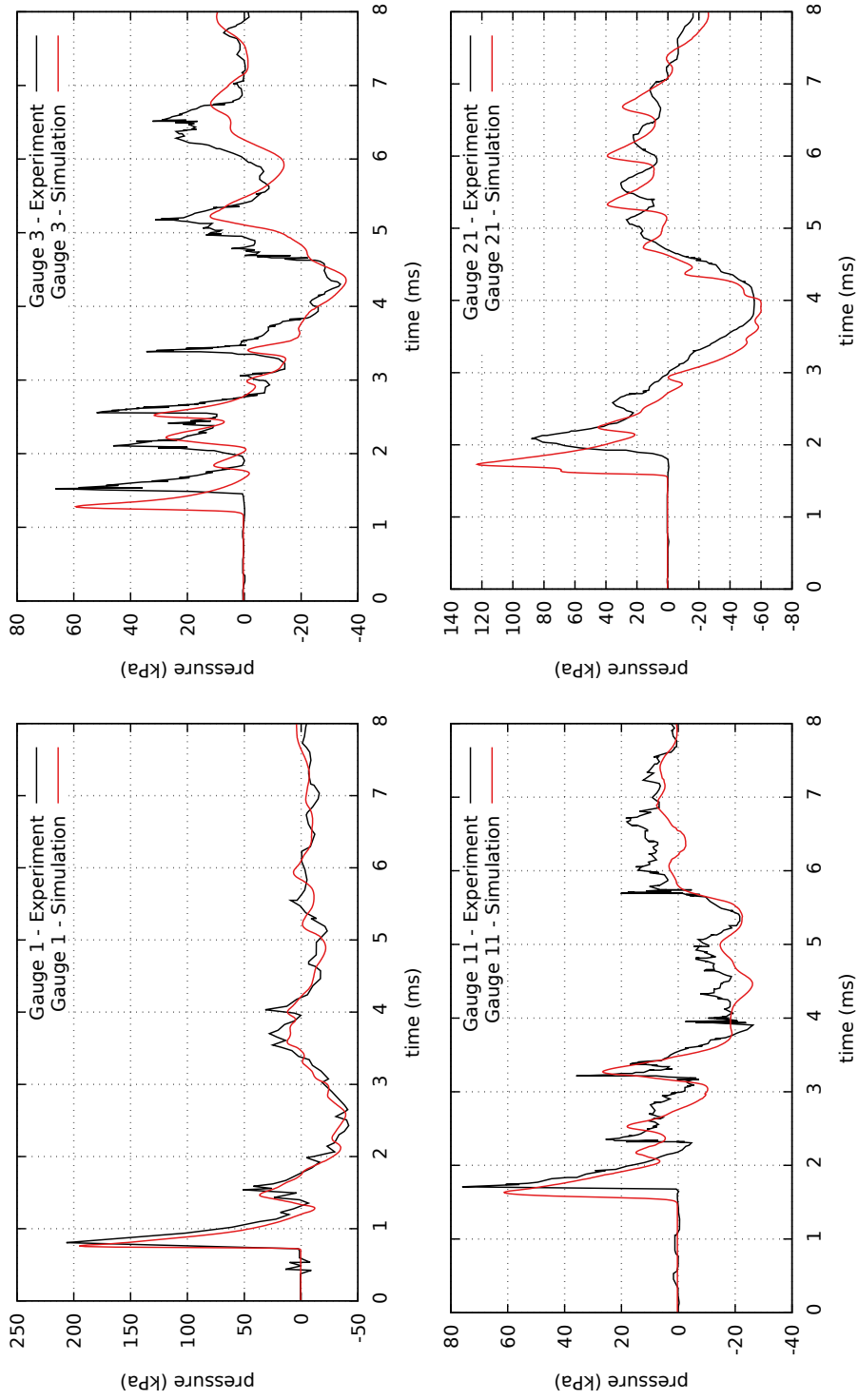


Figure 3.17: Overpressure lineout for gauges G1, G3, G11 and G21 during the first 8 ms of the cityscape blast case. Experimental data is shown in black and numerical results are shown in red.

Chapter 4

Shock capturing using adaptive mesh refinement

ADAPTIVE mesh refinement (AMR) increases the resolution of the computational mesh in regions of the solution where higher accuracy is deemed necessary. Typically these areas will contain flow features such as discontinuous shocks which require a high level of accuracy to avoid any smearing of the shock front. Other areas of the domain where the flow is continuous do not need the same resolution. Using AMR, the cell size can be increased in these areas and the local expense of the simulation reduced.

AMR is particularly useful for the simulation of blast waves arising from the detonation of high explosives. A typical free air explosion results in an outward-moving, spherical blast wave consisting of a high pressure shock followed by a gradual return to ambient pressure. In the pre-shocked regions, the flow is usually continuous and requires a lower resolution to maintain sufficient accuracy in the solution. In contrast, it is necessary to maximise the resolution across the leading shock of the blast wave to maintain the correct peak height as the blast wave travels away from the source. This will lead to a better prediction of the forces exerted on structures from the detonation of high explosives.

A critical element of AMR involves the decision over where and when to refine. The aim is to maximise refinement in areas that require it and minimise it elsewhere. At present, this is not straight forward and it is common to run an expensive 3D simulation only to find that the AMR algorithm has not refined the areas of interest sufficiently well and a new simulation needs to be performed. The aim of the work in this chapter is to improve the efficacy of the approach and make the benefits of AMR easier to obtain for the non-expert.

We begin this chapter with an introduction to AMR and a brief discussion of the current shortcomings that we hope to address. In section 4.2 we present our efforts to develop a new flagging criterion which addresses these shortcomings. We then perform a convergence study to find a mesh resolution which offers a good balance between accuracy and computational expense. Finally, in section 4.4 we conclude the chapter by presenting a series of numerical tests which compare the new flagging approach with an existing method.

4.1 Introduction

In practice, most high resolution shock capturing schemes only manage first order accuracy near discontinuities. It is necessary to increase the resolution in these areas to ensure appropriate definition of flow features. For conventional meshes this would entail an increase in resolution across the entire computational domain, even in smooth areas. This can drastically increase the expense of the simulation, especially in three dimensions where the cost is $\mathcal{O}(N^4)$ where N is the number of cells along each edge. AMR solves this problem by increasing the spatial and temporal resolution in certain regions of flow. These regions are identified using criteria based on the flow properties.

AMR can be divided into two approaches: In tree-based AMR, computational cells are organised in a tree structure. Each cell may be refined or unrefined separately from its neighbours. This method has the benefit of great flexibility and efficiency in specifying which cells to refine or unrefine. However, the major drawback is an inability to use regular grid-based solvers with tree-based AMR. Examples worth noting include the work of Khoklov [101] and Dezeuw & Powell [102].

Block-based AMR is a variant of tree-based AMR where blocks of cells can be refined rather than individual cells. Each grid in the hierarchy has an equal number of cells. New blocks are created through the bisection of the current grid into four or eight refined blocks for 2D and 3D simulations respectively. This method has the advantage of a simpler grid structure and a guaranteed workload per grid. The schemes of Keppens et al. [103], van der Holst & Keppens [104] and MacNeice et al. [105] represent good examples of this method.

The second method involves a patch-based approach to AMR. As with block-based methods, logically rectangular sub-grids can be created containing refined cells. However, patch-based methods differ by allowing individual sub-grids to overlap, rotate and take on arbitrary shapes. This approach was originally devised by Berger, Oliger and Colella [106, 107] and later extended by Quirk [108–111]. These schemes

create a refined mesh by layering successively finer patches over regions where refinement is needed. Patches exist in a hierarchy defined at runtime by specifying the number of refinement levels and the degree of refinement between each level. Patches that share the same resolution form an AMR level.

These methods are both flexible and memory efficient and, unlike tree-based methods, allow for regular grid-based solvers to be used. For these reasons we choose to use a scheme based on the work of Berger, Oliger & Colella and also from the later work of Deiterding [112]. The description that follows will focus on this method.

4.1.1 Grid hierarchy

The AMR method uses a hierarchy of embedded grids that are used to discretise the domain. The base level, level 0, covers the extent of the domain. Each patch is logically rectangular and it is possible to reference all cells using an (i, j) coordinate system.

Refinement can be applied to regions of the domain by embedding finer rectangular patches into the coarser level. The new patches then form the next AMR level: level 1. New patches are formed through the sub-division of cells on a rectangular region of refinement defined on the coarser level. This ensures that new patches remain aligned with the coarser grid. Any factor can be used for the number of subdivisions of a coarse cell, but must be the same for each coarse cell that is sub-divided. Each patch cell on the finer level can therefore be referenced using an (i, j) coordinate system. This refinement process can be repeated indefinitely, producing finer patches on an arbitrary number of levels. An example of this hierarchy is illustrated in figure 4.1.

The grid system can be defined more formally by defining a grid hierarchy G which is composed of a series of $l_{\max} + 1$ grids, where l_{\max} is the highest (finest) AMR level. We define a grid as a collection of all patches on a single AMR level. The notation G_l represents the grid at level l . At this level we denote the k^{th} patch as $G_{l,k}$. G_l can then be expressed as

$$G_l = \bigcup_{k=1}^{n_{G_l}} G_{l,k}, \quad (4.1)$$

where n_{G_l} is the number of patches on G_l . For each grid G_l we define the following coordinate system

$$\mathbf{C}_l = \{(i_l, j_l) : i_l \in \mathbb{N}, j_l \in \mathbb{N}\}. \quad (4.2)$$

Cells contained within the patch $G_{l,k}$ can be identified relative to the patch using the

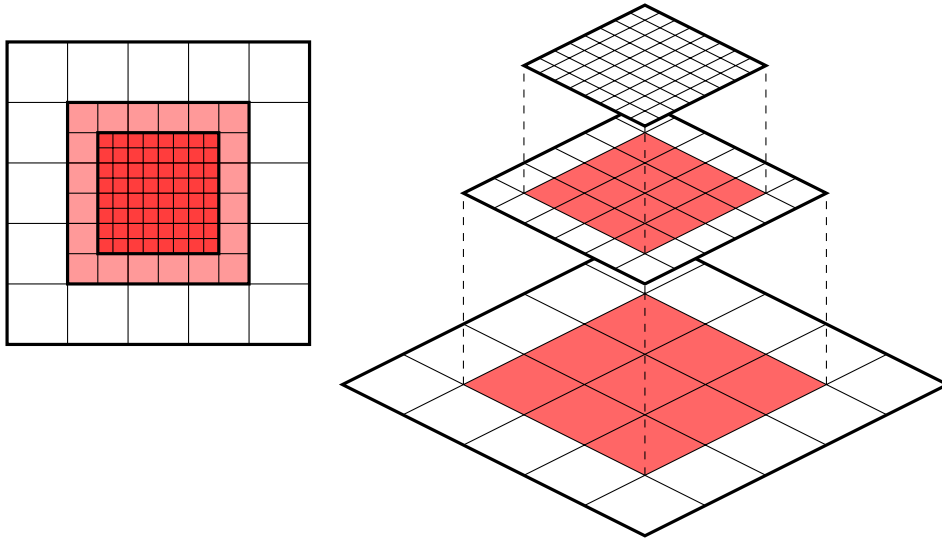


Figure 4.1: An example of the AMR hierarchy. A series of finer patches are embedded within a coarser grid.

coordinate system $\mathbf{P}_{l,k}$

$$\mathbf{P}_{l,k} = \{(i, j) : i \in \mathbb{N}, j \in \mathbb{N}, 1 \leq i \leq I_k, 1 \leq j \leq J_k\}, \quad (4.3)$$

where I_k and J_k are the number of cells along the x and y directions respectively of patch k .

The geometry of the grid G_0 is defined by the problem. Each finer grid l has its geometry defined by the level $l-1$. Since coarse cells are subdivided by a factor r , there exists a simple relationship between the coordinate systems \mathbf{C}_l and \mathbf{C}_{l-1} . A cell at (i_l, j_l) on level l is created following the sub division of cell (i_{l-1}, j_{l-1}) with coordinates

$$i_{l-1} = \frac{i_l - 1}{r_l} + 1 \quad (4.4)$$

$$j_{l-1} = \frac{j_l - 1}{r_l} + 1, \quad (4.5)$$

where r_l is the refinement factor between levels $l-1$ and l .

All patches must be nested. In other words, the region covered by a patch at level l must be wholly contained within one or more coarse patches at level $l-1$. A patch on level l may even straddle two or more patches on level $l-1$ as long as its entire area is contained within grid G_{l-1} . This requirement can be expressed as

$$G_l \subseteq G_{l-1}. \quad (4.6)$$

4.1.2 Time stepping

To ensure the stability of the time integration process, every cell must be integrated using a Courant number C_{cfl} of no greater than C_{max} , as required by the method's condition for convergence. If a cell is scaled by a factor r , the time step must also be scaled by this factor to maintain the same Courant number. The shrinking of the time step requires an additional $r - 1$ time steps to reach $t + \Delta t$.

This has a significant implication for AMR where the rate of evolution of the simulation is usually restricted by the finest cell size. As the grid is progressively refined, the number of time steps taken for each mesh cell increases. With this in mind, the overall philosophy of an AMR scheme is to consider refinement in both space *and* time. The number of time steps, over the entire hierarchy, required to progress the solution over some period of time is then minimised.

To demonstrate the advantage of temporal refinement we consider a one dimensional grid containing m cells at level 0. Each grid at level l covers p cells on the upper grid $l - 1$. The same refinement factor r is used for all grids, with a total of $m + r p l_{\text{max}}$ cells across all grids. If we were to use a uniform time step to track a feature over n cells, the computational cost W_{u} would be proportional to

$$n r^{l_{\text{max}}} (m + r p l_{\text{max}}). \quad (4.7)$$

If we instead use temporal refinement, where the time step is progressively reduced by r between grid levels, the computational effort W_{tr} becomes

$$n \left[m + p r (r + r^2 + \dots + r^{l_{\text{max}}}) \right], \quad (4.8)$$

which is equivalent to

$$n \left[m + p r^2 \left(\frac{r^{l_{\text{max}}} - 1}{r - 1} \right) \right]. \quad (4.9)$$

In the case of large m and l_{max} we can express the ratios of computational effort as

$$\left(\frac{r - 1}{r} \right) l_{\text{max}} < \frac{W_{\text{u}}}{W_{\text{tr}}} < r^{l_{\text{max}}}. \quad (4.10)$$

This shows that temporal refinement is less computationally expensive than uniform refinement provided that the complexity of the problem is high enough. Furthermore, the degree of the computational saving increases with the cell count m , refinement factor r and number of AMR levels l_{max} [108].

The temporal refinement method used for structured grid AMR is simple thanks to the hierarchical nature of the underlying grids. For a grid G_l , its time step Δt_l is related to the coarser grid G_{l-1} by

$$\Delta t_l = \frac{\Delta t_{l-1}}{r_l}, \quad (4.11)$$

where r_l is the refinement factor between grids G_{l-1} and G_l . The advancement of the solution can then be obtained through the recursive time integration of the grid levels. For example, the integration of one time step on grid G_{l-1} would necessitate the integration of r_l time steps on grid G_l . This process descends through the levels recursively until grid $G_{l_{\max}}$ is reached.

4.1.3 Patch boundaries

In order to correctly integrate the flow solution across the grid hierarchy, the connectivity between patches must be adequately defined. Each patch must contain boundary conditions that are obtained from neighbouring meshes in the hierarchy. The interface of a patch boundary can take one of three forms: *external* boundaries border the edge of the computational domain, *fine-fine* boundaries exist between patches on the same level and *fine-coarse* boundaries exist at the interface of patches on grids G_l and G_{l-1} .

One of the strengths of patch-based AMR is that conventional grid-based flux methods can be used to integrate the solution on each patch. The flux method requires no knowledge of the AMR hierarchy and can be applied to data on a patch in the same way as a non-AMR domain. The numerical fluxes at patch edges are obtained by surrounding the patch with a layer of ghost cells equal to the number required by the scheme. For a typical second order method this requires two cells along the patch boundary. An example of patch boundaries and the use of ghost cells is shown in figure 4.2.

Before the integration, the ghost cells are initialised with data obtained from the relevant boundary from patches that overlap or underlie the ghost region. The initialisation process is limited to three types of procedure, depending on whether a *fine-fine*, *fine-coarse* or *external* boundary is used. It is possible that some regions may experience multiple overlaps. In this case, *fine-fine* boundaries are preferred to ensure that accuracy is preserved. This method ensures that all overlapping cells on the same grid are identical.

Interfaces defined as external boundaries are treated in the same way as external boundaries without AMR. No knowledge of the grid connectivity is required and a standard boundary condition (reflective, transmissive etc.) can be applied.

Fine-fine boundaries

Fine-fine boundaries exist at the overlap of patches on the same level. Figure 4.3 shows an overlap between patches $G_{l,1}$ (top) and $G_{l,2}$ (bottom) on the same level.

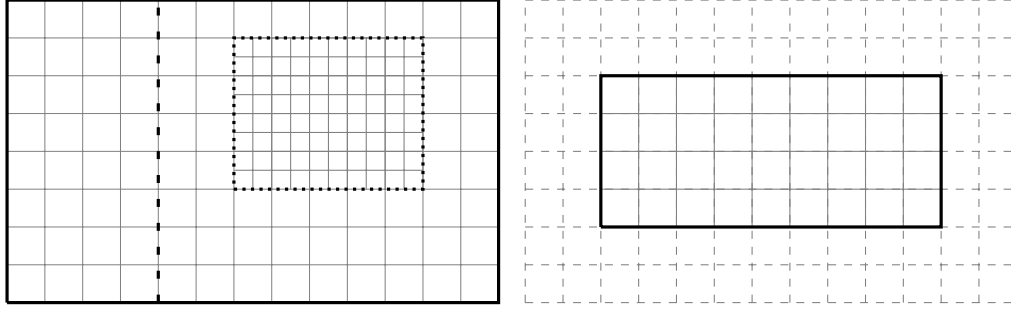


Figure 4.2: (a) The three types of patch boundaries: *external* (solid), *fine-fine* (dashed) and *fine-coarse* (dotted). (b) Ghost cells surrounding a patch.

Because these patches are on the same grid, this boundary is classed as *fine-fine*. For each ghost cell in $G_{l,2}$ there exists a direct connection to a regular cell in $G_{l,1}$. States are simply copied across as indicated by the arrows in figure 4.3.

Fine-coarse boundaries

Figure 4.4 shows an example of a *fine-coarse* boundary. Patch $G_{l,1}$ is completely covered by $G_{l-1,1}$ on the coarser grid and a refinement factor $r = 2$ is used, meaning that the ghost cell band of $G_{l,1}$ occupies a single cell width of $G_{l-1,1}$.

We consider the implications of time-stepping on the propagation of states between the two patches. For a single time step on the coarse patch $G_{l-1,1}$ with time step Δt_{l-1} there will be two time steps on the finer patch $G_{l,1}$ with time step $\Delta t_l = \frac{\Delta t_{l-1}}{2}$. At the beginning of each fine time step, the ghost cells in $G_{l,1}$ must be initialised using data from $G_{l-1,1}$. This presents a complication as data is only available on the coarse level at times t and $t + \Delta t_{l-1}$. To overcome this problem, states are linearly interpolated in time to find the intermediate state at $t = t + \Delta t_l$

$$u_{l-1,1}^{t+\Delta t_l} = \frac{u_{l-1,1}^t + u_{l-1,1}^{t+\Delta t_{l-1}}}{2}. \quad (4.12)$$

Unlike *fine-fine* boundaries, *fine-coarse* cells are of different sizes and their cell centres will not necessarily overlap in space. Once the temporal interpolation has been performed on the coarse patch, the states are then spatially interpolated across to the finer patch, as shown in figure 4.5.

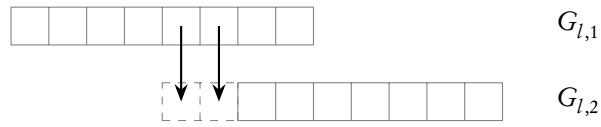


Figure 4.3: An example of a *fine-fine* patch boundary.

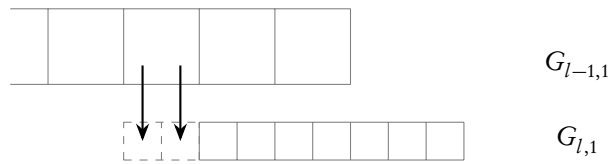


Figure 4.4: An example of a *fine-coarse* patch boundary.

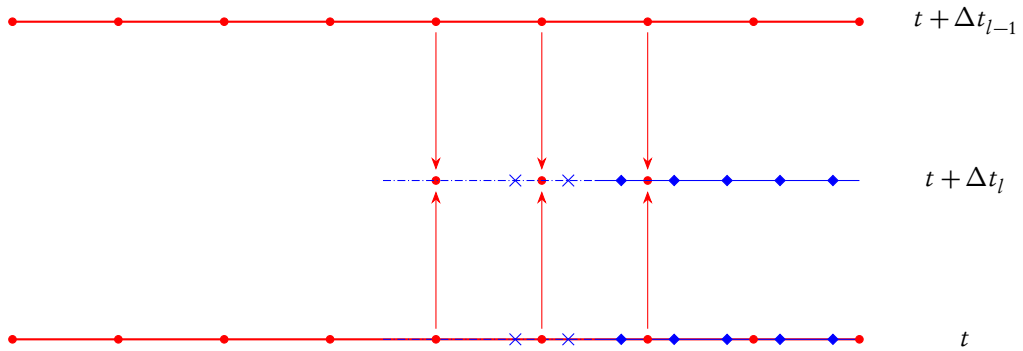


Figure 4.5: The *fine-coarse* data interpolation process. Coarse nodes are shown as red circles, with fine nodes as blue diamonds. Cells in the ghost region are indicated by crosses. Linear interpolation in time is performed across a *fine-coarse* boundary.

4.1.4 Grid adaption

Consider an example of a shock propagating through clear air. Suppose a coarse grid is used to cover the domain, with a fine grid across the shock front. If no effort is made to adapt the grids then the shock will eventually leave the vicinity of the fine grid and smearing will occur. The AMR method overcomes this challenge through the use of an adaption process that allows for grids to move with the features of interest. This process is divided into three stages: (i) flagging, (ii) clustering and (iii) transfer of the solution. We use the term ‘re-grid’ to describe when adaption occurs during the simulation. The term ‘re-grid frequency’ describes the number of time steps that form the interval between each re-grid operation.

Flagging

The flagging process involves the identification of flow regions that require extra refinement. A flagging algorithm typically involves the application of specific criteria to cells in order to deduce whether they require flagging for refinement. A range of rules exist, generally falling under the definition of heuristic or error-based methods.

Richardson extrapolation is a notable example in the field of error-based methods. This method compares the solution on the current grid after two steps with the solution on another grid which is twice as coarse after a single time step. Cells which exhibit an error greater than a tolerance will be flagged for refinement. The method outlined by Berger and Colella in [107] and later improved by Bell et al. in [113] is commonly used, with similar techniques being employed in a range of different contexts [103, 114]. A review of truncation error methods can be found in [115]. The downside of these methods is their relatively high computational cost. However, they are fairly easy to implement and are independent of the underlying PDE being solved.

Heuristic methods use a function based on physical quantities to determine whether a cell requires refinement. They are less rigorous than error-based methods but have the ability to identify specific flow features that other methods may miss. A commonly used function is based on the relative difference of a quantity u across a cell of width Δx :

$$\left(\frac{u(x + \Delta x, t) - u(x, t)}{u(x + \Delta x, t) + u(x, t)} \right)^2 > \epsilon \quad (4.13)$$

where the tolerance ϵ is an empirically chosen figure that is problem-dependant. If ϵ is chosen incorrectly either too much or too little refinement will occur, to the detriment of the computational expense or accuracy of the solution. For the simulation of blast waves we use pressure to ensure that the front of the blast wave is

captured. Additionally, density can be used in order to locate contact discontinuities using the following test [111]:

$$\frac{|\rho_r - \rho_l|}{\rho_r + \rho_l} > \frac{|p_r - p_l|}{p_r + p_l} \quad \text{and} \quad |p_r - p_l| > \text{roundoff}. \quad (4.14)$$

Other more complex criteria have been developed. These include a measure of vorticity [116] and functions involving higher-order derivatives of the solution [117]. Other authors have implemented combinations of local truncation error and heuristic methods [118, 119].

Clustering

The second stage of the AMR process involves the creation of new patches from a cluster of flagged cells. For tree and block-based AMR, this process is trivial as the size and shape of refined levels is pre-defined. In patch-based AMR, a clustering algorithm is used to devise an array of patches that will completely cover the flagged cells in a way that minimises the overall computational cost of the simulation. This process is illustrated in figure 4.6.

An early approach was laid out by Berger [120]. In this algorithm, flagged cells are surrounded by a rectangular patch which includes a buffer zone of flagged cells in each direction. The buffer zone ensures that the refined solution does not propagate outside the patch before the next re-grid operation. Since the CFL condition guarantees that a wave will travel no farther than one cell per time step one typically sets the number of buffer cells to the re-grid frequency. Each rectangle is then bisected until the ratio of flagged to non-flagged cells reaches the desired level of efficiency. This method generally produces acceptable grids but has the tendency to produce overlapping grids with sub-optimal efficiencies due to the simple bisection operation.

Berger and Rigoutsos [121] improved on this method, developing an algorithm that could overcome these problems. In their work, the authors adopted ideas related to edge detection that originated from psychophysical and neurophysiological experiments. Instead of a bisection, the algorithm is able to split patches along edges where transitions from flagged to unflagged regions occur. The scheme improves the performance of AMR by increasing the overall patch efficiency.

The method has since been extended to 3D [113] and subsequent work has been done to improve performance by placing restrictions on the shape and size of patches [122–124]. Friedel et al. proposed a further improvement by assigning workload costs to candidate patches [125]. Patches are chosen in such a way that they minimise the computational expense of the simulation. Advancements in the parallel performance of the scheme have also been achieved by a range of authors [126–132].

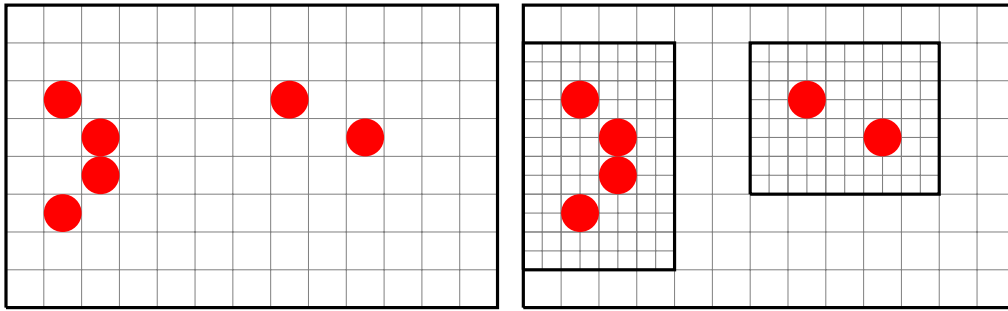


Figure 4.6: An example of the AMR clustering process. Cells requiring refinement are flagged (red). The clustering algorithm then generates new patches covering the flags and their buffer region.

Transfer of solution

New AMR grids that are created require initialisation with the field solution. A popular method involves the interpolation of the known solution from the coarse grid to the new fine grid [111]. Linear or quadratic interpolation can be used, including the use of splines to reconstruct data on the coarse grid. The benefit of these methods is their ability to preserve monotonicity and ensure conservation.

In situations where new grids overlap existing grids, the solution in the overlap region can be copied across without the need for interpolation. One of the great benefits of AMR algorithms of the type developed by Quirk [111] is that flow discontinuities always lie in these regions, meaning that the adaption process does not introduce errors near discontinuities.

4.1.5 Shortcomings

In section 4.1.4 we touched upon the dependency of refinement on the flagging tolerance. If set too high over-refinement occurs, increasing the expense of the simulation; too low and refinement is lost around important features, reducing the accuracy of the solution. For blast-related problems, the optimum tolerance can be difficult to calculate. Our current solution is to use a relative difference criterion. As the blast wave propagates away from the source, the height of the overpressure peak decreases and the relative difference reduces. Eventually, in most cases, the relative difference across the primary wave will no longer exceed the tolerance and refinement will cease. Often one will run an expensive 3D blast simulation only to find that refinement around the blast wave has been lost several hours in. This can be extremely disruptive.

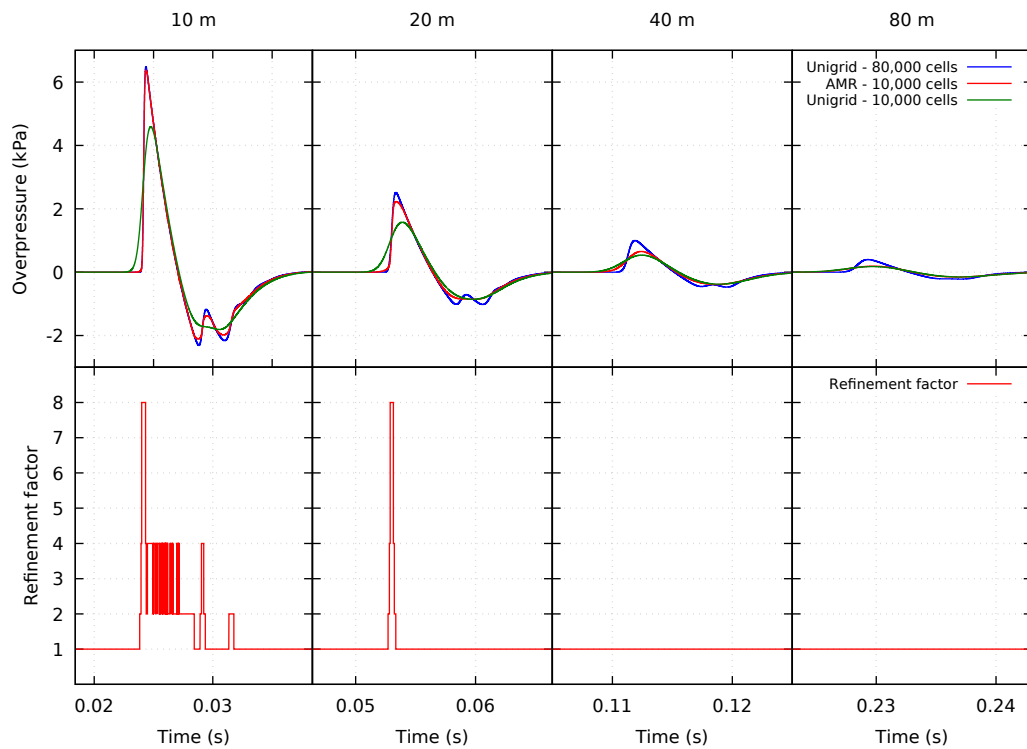


Figure 4.7: A graph of overpressure and AMR refinement factor for a blast wave measured using gauges at 10, 20, 40 and 80 m from the source.

This problem is illustrated in figure 4.7. The figure shows the overpressure profile of a blast wave as recorded by four separate gauges at 10, 20, 40 and 80 m from the source. On the top row, the blue and green lines represent a high and low resolution non-AMR (uniform grid) simulation respectively (8×10^4 vs. 1×10^4 cells). The red line shows a simulation using AMR with a base cell count of 1×10^4 on the coarsest grid and maximum effective cell count of 8×10^4 on the finest grid. The bottom row of graphs indicates the total refinement factor for the AMR simulation, with 1 being no refinement and 8 maximum refinement.

At 10 m the relative difference across much of the blast wave exceeds the flagging tolerance and refinement occurs. However, once the wave reaches 20 m from the source the overall difference has reduced and only the shock front is refined. By 40 m no refinement is occurring and the grid resolution around the blast wave is no longer sufficient. The lack of resolution around the wave results in diffusion of the primary shock and a reduction in the peak height. The AMR solution eventually resembles the low resolution simulation.

At large standoff distances, the shock pressure profile of a blast wave can be very similar to the rarefaction. Difference or gradient-based approaches struggle to distinguish between these features, leading to unnecessary over-refinement behind the shock. This example demonstrates the need for an ability to apply refinement only to compressive shocks while avoiding rarefactions and small ripples.

In certain situations, the problems described above can be partially mitigated through the careful choice of AMR parameters, something that a person with good knowledge of the numerics of CFD and AMR might be able to do. In practice, many commercial users of CFD codes do not possess this ability. With this in mind, we look to make AMR more effective and easier to use for the non-expert by devising a new flagging criterion which

- is easier to tune and is able to track important flow features for longer distances than existing methods,
- provides a selective way of identifying the features of the blast wave worth refining.

4.2 Flagging

In this section we outline a new approach to AMR flagging that addresses the inability of current methods to direct and maintain flagging around the important features of the blast wave. We discuss some possible approaches and conclude by outlining a new method: a time dependant relative difference and a modified second-derivative error norm for compressive shocks.

4.2.1 Relative difference

A commonly used flagging criterion is the relative difference of a quantity u across the blast wave:

$$\left(\frac{\Delta u}{u}\right)^2 > \text{tolerance}, \quad (4.15)$$

where pressure and density are typically used for the quantity u .

The advantage of this criterion is its simplicity. However, if not chosen carefully, the fixed tolerance can lead to a premature loss of refinement once the blast wave has decayed sufficiently. To rectify this problem we investigate the idea of a new, time-dependant tolerance that can adapt to the diminishing strength of the blast wave as time progresses.

Figure 4.8 shows a profile of a typical blast wave. Pressure is shown left, with the relative difference across the solution on the right. The primary shock and the two trailing shocks are represented by narrow peaks, with the rarefactions as wider, flatter features.

By tuning the tolerance it is possible to pick out the features of interest. In the present example, a tolerance of 1×10^{-5} would refine the leading shock. Reducing the tolerance to 1×10^{-6} would extend refinement to the secondary shock and so on. The lower the tolerance, the more features are refined.

These tolerances remain valid for a limited duration. As time progresses the strength of the blast wave reduces along with the value of the flagging criterion across each of the features. Figure 4.9 shows this process for the blast wave shown in figure 4.8. In this figure the relative difference is measured across the primary shock as the wave travels outward up to a distance of 100 m. The points are fitted to provide an indication of how the flagging tolerance should scale with distance for a typical blast wave.

The curve fit indicates that the flagging criterion across the zone of interest varies by approximately a factor of 1×10^5 across a distance of 100 m from the charge location. This represents a significant variation across a relatively modest distance and illustrates the difficulties attaining adequate refinement up to a particular standoff. This problem is not solved by simply reducing the tolerance. This could lead to over refinement during the early stage of the simulation when the signal is strong.

Using the data in figure 4.9 we introduce a new flagging criterion which uses the relative difference as a function of time, adapting the tolerance as the strength of the blast wave diminishes. The test performed in section 4.1.5 was repeated with the new criterion. Three simulations were performed: a high-resolution benchmark case (8×10^4 cells, no AMR); a low resolution case (1×10^4 cells, no AMR) and an AMR simulation with a base cell count of 1×10^4 cells, reaching an effective cell count of 8×10^4 cells at full refinement.

Figure 4.10 shows the results at four different gauge positions. The pressure solution (top) and refinement factor (bottom) are shown for each gauge. The time-dependant flagging criterion manages to maintain a high degree of refinement around the primary shock even at 80 m from source. We contrast this with the test involving a static tolerance (figure 4.7) where refinement was lost by the time the wave had reached the 40 m gauge. The peak height of the primary wave is improved and is close to the benchmark solution, remaining well-defined up to 80 m.

Despite this improvement, the AMR peak could still be higher. The 10 m gauge in figure 4.10 shows us that the flagging module is not applying a sufficient degree of refinement to the leading shock. The AMR patch is too narrow and does not extend

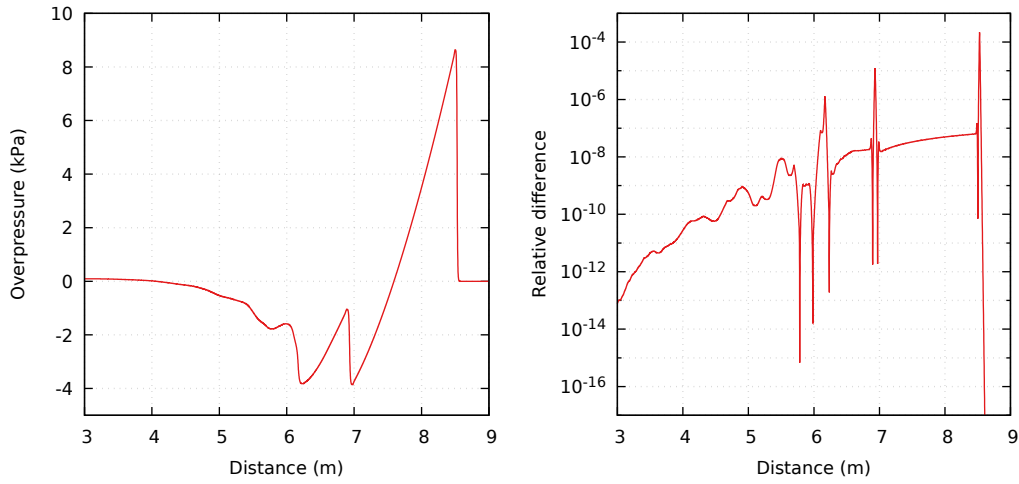


Figure 4.8: Overpressure and relative difference as a function of distance from the charge. The left graph shows a typical blast wave profile, with the variation of the difference flagging variable shown to the right.

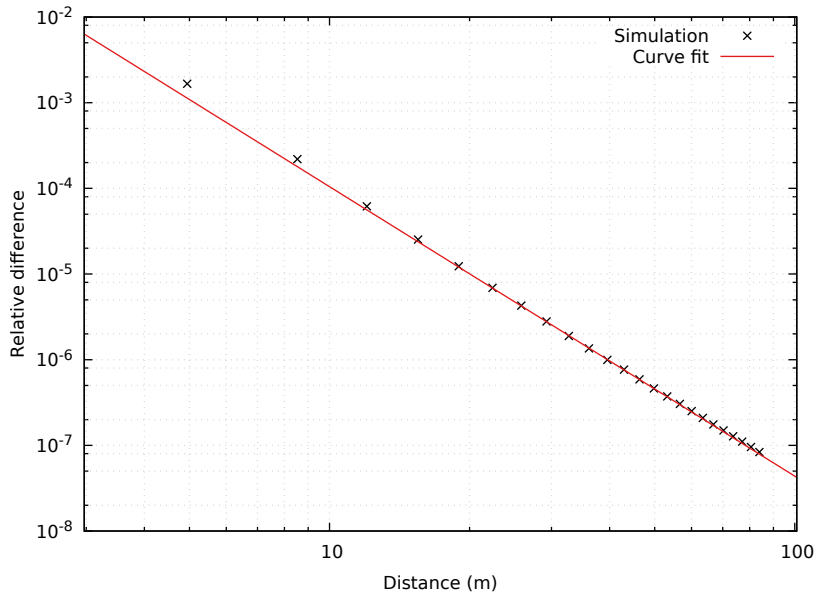


Figure 4.9: Relative difference at the primary shock as a function of distance for a range of distances from the charge (points). The points are fitted with a function to yield a continuous relationship.

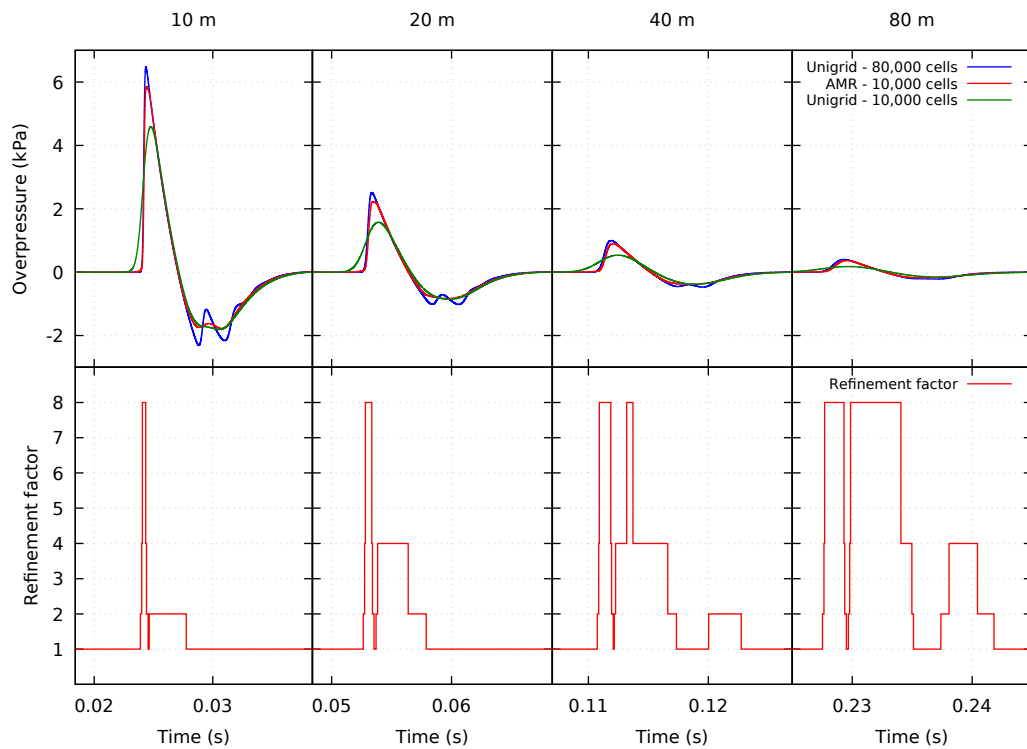


Figure 4.10: A graph of overpressure and AMR refinement factor for a blast wave measured using gauges at 10, 20, 40 and 80 m from the source. The tolerance is set to flag on the leading shock.

far enough across the peak.

The solution can be improved further by tuning the tolerance. Figure 4.11 shows the effects of relaxing the tolerance, resulting in increased AMR coverage around the secondary shock. A significant improvement in the AMR peak heights is observed and the solution is nearly indistinguishable from the high resolution uniform grid case. Overall, the AMR method manages to preserve the solution well with a fraction of the cells of the uniform grid method.

By varying the flagging tolerance as a function of the simulation time, we have shown that refinement can be maintained around the blast wave at long standoffs, avoiding over-refinement during the early stage of the simulation.

Despite these encouraging results, we found it difficult to extend the method to more complex multi-dimensional problems. The relative difference of the pressure across the blast wave is not only a function of time. The strength of the wave depends on the numerical method, grid resolution, charge mass and charge composition

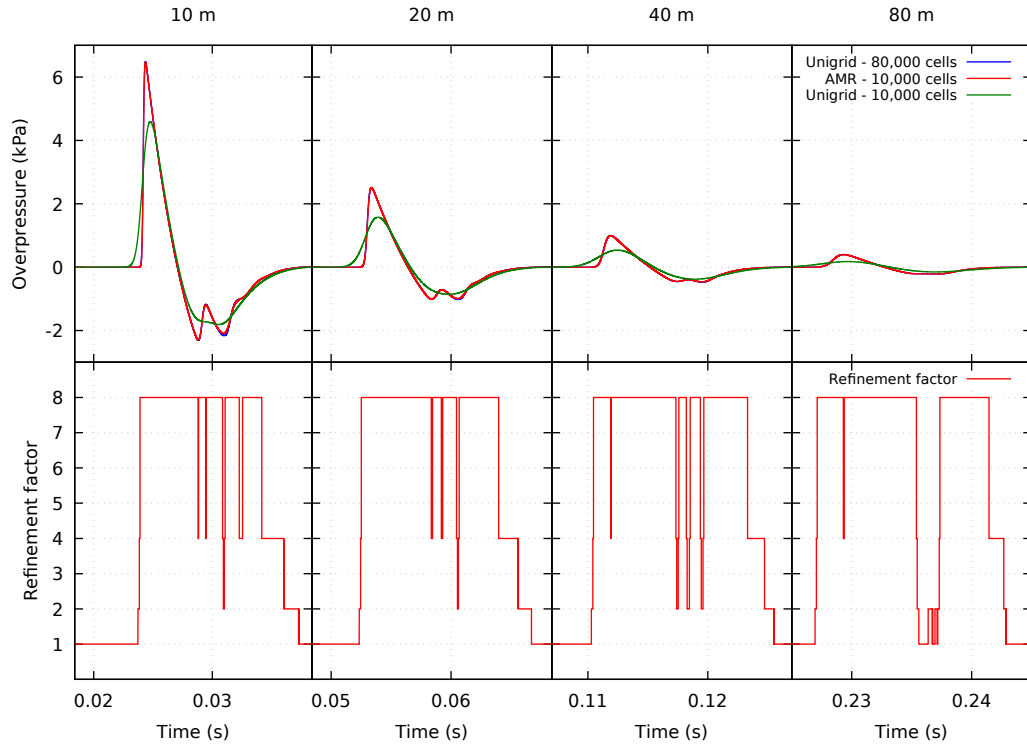


Figure 4.11: A graph of overpressure and AMR refinement factor for a blast wave measured using gauges at 10, 20, 40 and 80 m from the source. The tolerance is relaxed, allowing for a greater degree of refinement around the blast wave.

among other things. Finding a relationship between all of these factors proved extremely challenging and an alternative criterion was sought.

4.2.2 A modified second-derivative error norm for compressive shocks (ENCS)

In this section we present a new flagging criterion that overcomes several shortcomings of the methods discussed in the preceding section. The method uses a combination of a divergence masking criterion and a second-derivative error norm. The outcome is a dimensionless error norm that is applied only in regions of compressive flow (e.g. shocks).

For each cell, the following refinement indicator is calculated:

$$\zeta = \begin{cases} 1 & \text{if } E > E_{\text{ref}}, \text{ and } \nabla \cdot \mathbf{v} < v_{\text{ref}}, \\ 0 & \text{otherwise,} \end{cases} \quad (4.16)$$

where we flag the cell for refinement if $\zeta = 1$.

The term $\nabla \cdot \boldsymbol{v} < v_{\text{ref}}$ is a divergence check that ensures flagging only occurs in regions where the divergence of the velocity field is below the tolerance v_{ref} . This avoids unnecessary refinement in areas of expansion such as rarefactions. In regions exhibiting suitable compression an error norm E is calculated. Refinement will occur if the value of E exceeds the tolerance E_{ref} .

For the calculation of an error norm we adopt the method of Löhner outlined in [117] and later used in [133–135]. Löhner’s error estimator is a modified second derivative which is normalised by the average of the gradient across one cell:

$$E = \sqrt{\frac{\sum_{pq} \left(\frac{\partial^2 u}{\partial x_p \partial x_q} \right)^2}{\sum_{pq} \left[\left(\left| \frac{\partial u}{\partial x_p} \right|_{i_q + \frac{1}{2}} + \left| \frac{\partial u}{\partial x_p} \right|_{i_q - \frac{1}{2}} \right) \frac{1}{\Delta x_q} + \epsilon \left| \frac{\partial^2}{\partial x_p \partial x_q} \right| |u| \right]^2}} \quad (4.17)$$

where the sum is carried out over the coordinate directions. The variable u is any suitable simulation variable. In our case we use pressure. The last term in the denominator acts as a noise filter and prevents refinement in regions containing small ripples. The constant ϵ controls this function and is somewhat application specific.

The error norm has several useful properties:

- The method is entirely local, avoiding any global computation.
- Unlike difference flagging, the error norm is dimensionless and bounded such that $0 \leq E < 1$. This means that preset tolerances can be employed.
- The error norm ignores small ripples, preventing unnecessary refinement in such regions.

The use of the error norm with a divergence check brings one further benefit: refinement is prevented in zones of expansion such as rarefactions. These features typically trail a blast wave and may have steep gradients that cause refinement when using a gradient or difference criterion. However, refinement in these areas is not usually necessary as it does not significantly effect the peak pressure of the blast wave.

The Löhner error norm calculation is more expensive than a gradient or difference criterion computation. However, the divergence calculation is of equivalent expense to a gradient calculation and is calculated first. This means that the more expensive Löhner error calculation is only performed in areas of compressive flow.

The new flagging method is referred to as ENCS (Error Norm for Compressive Shocks) and is outlined in algorithm 2. The function begins by looping through the cells on each AMR level. The divergence and Löhner error norm are calculated for each cell. The cell will be flagged for refinement if the error norm is above its

Algorithm 2 Main steps of the ENCS flagging method

```
for all AMR levels do
  for all cells on AMR level  $n$  do
     $F \leftarrow \text{false}$  ▷ Set refinement flag to false
    if  $\nabla \cdot \mathbf{v} < v_{\text{ref}}$  then ▷ Check whether flow is compressive
      if  $E > E_{\text{ref}}$  AND  $|\mathbf{u}| > 1 \times 10^{-6}$  then
         $F \leftarrow \text{true}$  ▷ Flag cell for refinement
      end if
    end if
  end for
end for
```

tolerance, the divergence is below its tolerance and the magnitude of the flagged quantity u is large enough.

4.3 Solution convergence

High explosives, including TNT, produce a detonation front that moves at several thousand metres per second inside the charge. A strong shock wave develops once the detonation front reaches the air and rapidly decreases in strength as it propagates outward. High spatial and temporal accuracy is required to capture these phenomena, corresponding to a cell size of approximately 1 mm for 1 kg of TNT. These conditions can be relaxed in the far-field, where a minimum cell size of several centimetres might be acceptable [136].

It is important for the blast-code user to choose to the right resolution for a given charge size and standoff. A resolution that is too coarse will lead to underestimation of overpressures. And a resolution that is too fine will negatively impact the performance of the simulation. In this section we study the effect of resolution on the accuracy of the solution and suggest a cell size that offers an acceptable balance between computational expense and solution accuracy for near- to far-field explosions.

4.3.1 One dimensional setup

We begin by by setting up a spherical 1D free-field explosion of TNT, performing three simulations at cell sizes Δr of 0.5 cm, 1 cm and 2 cm. A second order MUSCL HANCOCK scheme is used with a CFL number of 0.9. We enforce a cell size of $\Delta r/3$

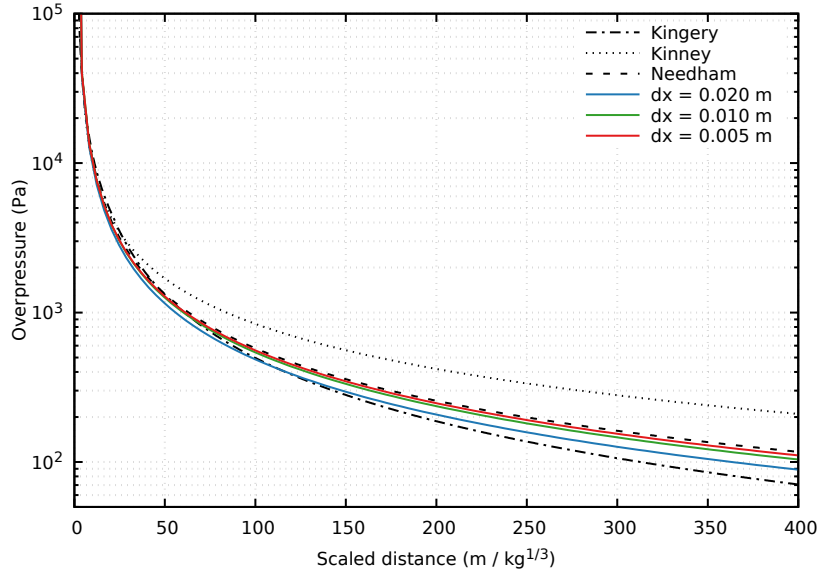


Figure 4.12: Peak overpressure vs. scaled distance for a 1D TNT free air burst. 0.5 cm (red), 1 cm (green) and 2 cm (blue) cell sizes are used. Scaled fits are shown in black.

during the first 1 ms of the simulation to ensure adequate resolution during the early phase of the detonation. An ideal gas equation of state is used along with the TNT material parameters in table 4.1.

Figure 4.12 shows the peak overpressure with respect to range for the three resolutions. Also presented are three TNT equivalent scaling curves from Kinney [137], Kingery [6] and Needham [50]. The MUSCL scheme shows good convergence in the near-field for all resolutions. As the scaled distance increases, some divergence in the results is observed and good convergence is observed for cell sizes of 1 cm and below. We also observe that the numerical results are in very good agreement with Needham’s fit.

Figure 4.13 shows the effect of cell size on the computational expense of the simulation, the peak overpressure and arrival time of the blast wave at a gauge

ρ_{TNT} (kg m^{-3})	E_{TNT} (J kg^{-1})	u_{CJ} (m s^{-1})
1650	4520×10^3	6851

Table 4.1: Density, specific energy and CJ velocity parameters used for TNT.

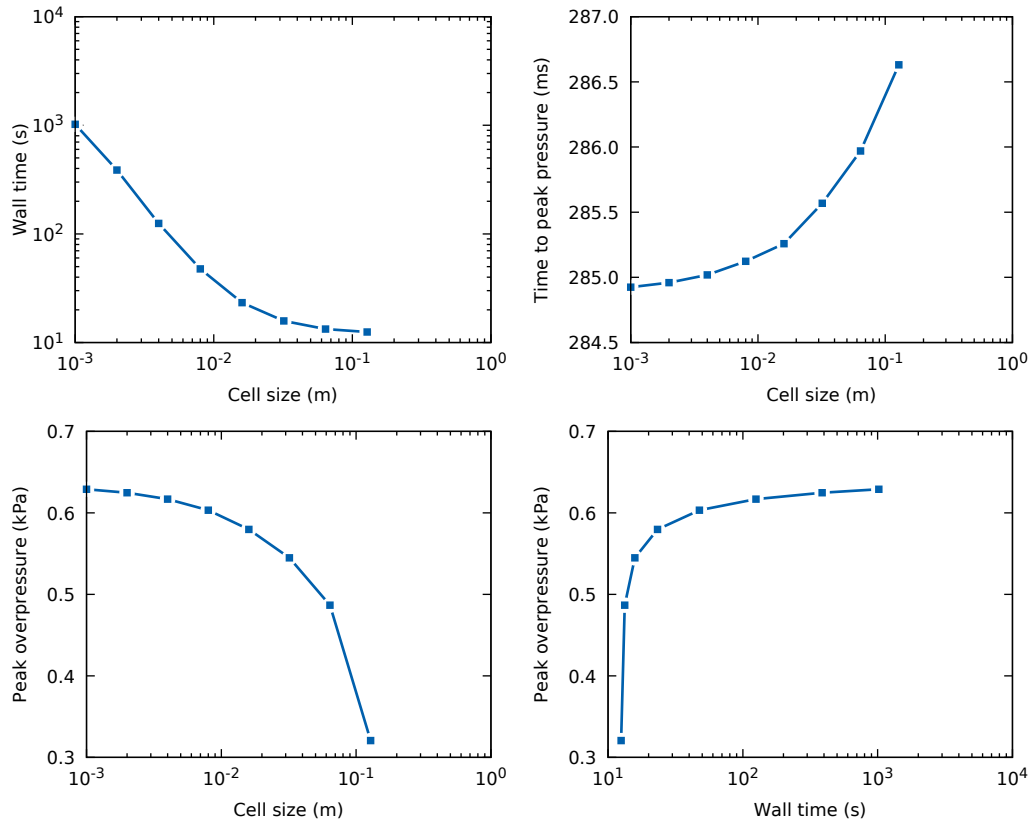


Figure 4.13: Four charts showing CPU time, peak overpressure and peak overpressure time as a function of cell size. The fourth chart shows peak overpressure as a function of the overall cost of the simulation.

located 100 m from the source. Unsurprisingly we find the overpressure and arrival times to be well converged at 1 cm. We also observe that any improvement in accuracy above this resolution leads to a disproportionate increase in computational expense, outweighing the marginal gains in accuracy.

Considering the balance between accuracy and computational expense, we choose 1 cm as an optimum cell size for the 1 kg charge. Using Hopkinson scaling we can represent this distance independently of the charge mass, resulting in a converged resolution of $\Delta r = 1 \text{ cm}/\text{kg}^{1/3}$ for any TNT equivalent explosive. As an example, a charge of mass 100 kg would correspond to a cell size of $\Delta r = 4.6 \text{ cm}$.

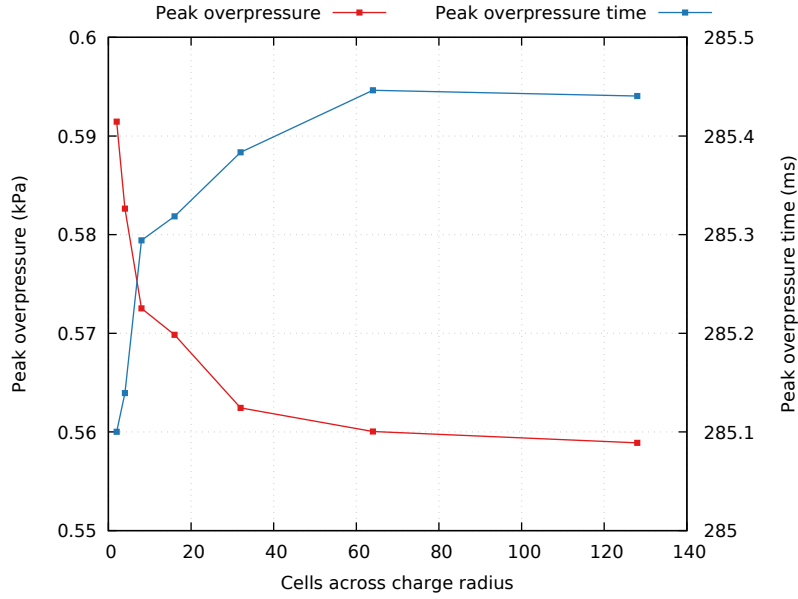


Figure 4.14: Chart showing the relationship between the number of cells across the charge radius, peak pressure (blue) and peak pressure time (red).

4.3.2 Radial resolution across the charge

During the early phase of the explosion the detonation front travels through the charge, eventually reaching the gas and forming a blast wave. This transient process requires a very fine resolution, significantly higher than the stage when the shock reaches the far-field. To maximise computational efficiency we use a different resolution for each process, maintaining a fixed, high resolution AMR mesh around the charge during the formation of the blast wave while using a coarser mesh for the rest of the domain.

As a test, we repeat the 1D 1 kg TNT free-field simulation with a cell size Δr of 2.5 cm. We add a fixed AMR mesh around the charge for the first 1 ms of the simulation. The resolution of this mesh is varied, providing between 4 and 128 cells across the charge radius. A gauge is placed 100 m from the source and the overpressure and arrival time of the blast wave is recorded.

Figure 4.14 shows how the peak overpressure and arrival time vary with the number of cells across the charge. The solution is well converged when 50 cells are placed across the charge radius, corresponding to a resolution Δr of $1 \times 10^{-3} \text{ m/kg}^{1/3}$. This agrees with previous work suggesting a minimum of 50 cells [138].

In practice, this cell size could be difficult to achieve without adversely affecting

performance. We recommend relaxing this figure, aiming for a minimum of 5 cells across the charge radius. This resolution Δr of $1 \times 10^{-2} \text{ m/kg}^{1/3}$ corresponds to a modest error of 5 %.

4.4 Numerical results

In the current section we present numerical results for a series of tests which demonstrate the benefits of ENCS. We begin by investigating whether the new flagging method exceeds the minimum acceptable refinement of the solution. This is equivalent to stating that the AMR solution must match a uniform grid solution at the resolution of the finest AMR level. Having shown this, we will show that ENCS minimises the area flagged for refinement without compromising the quality of the solution.

4.4.1 One dimensional study

In the mesh sensitivity study of section 4.3 we demonstrated that a cell size of $1 \text{ cm/kg}^{1/3}$ was necessary to obtain a well converged solution. We perform the same 1D spherical TNT free-air burst simulation, using AMR instead of a uniform grid. We use six levels of AMR, each with a refinement factor of three. This corresponds to a total factor of 243 between the coarsest and finest meshes, allowing a maximum resolution of 1 cm with a base resolution of 2.43 m.

The top row of figure 4.15 shows this AMR solution at a distance of 50, 200 and 350 m from the charge (shown blue). Surprisingly, the AMR simulation produces the best solution, with some smoothing observed in the uniform grid results (shown red). This discrepancy was found to arise from numerical diffusion associated with a smaller time step in the uniform grid simulation.

During the detonation, the cells within the charge undergo a process of heating as energy from the reaction is deposited within this zone. The blast wave forms and eventually departs, leaving a hot region in which the sound speed is large with respect to the rest of the domain. Since the time step is inversely proportional to the sound speed, this zone acts as a bottleneck, minimising the global time step, thereby increasing the level of numerical diffusion. The hot zone will eventually cool through the process of thermal diffusion, but at a time-scale that is much longer than the lifetime of the blast wave.

The AMR simulation does not experience this problem because refinement around the charge location is lost once the blast wave has departed. The numerical diffusion from the coarse mesh rapidly reduces the temperature and the limit placed upon the

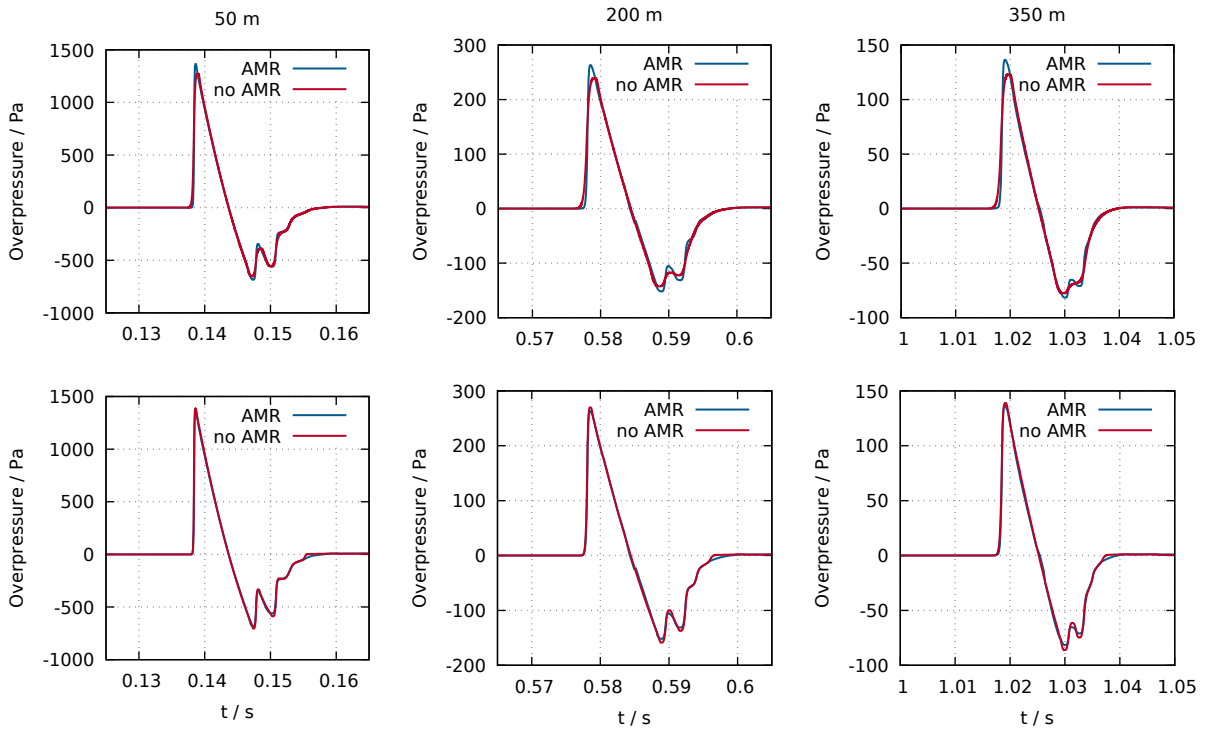


Figure 4.15: 1D spherical air burst simulations for 1 kg of TNT at 50, 200 and 350 m with AMR (blue) and without AMR (red). The bottom row shows the effect of coarsening the mesh around the charge location during the simulation.

time step. This is an unintended benefit of AMR since we are not interested in the solution within the charge zone once the blast wave has passed.

The bottom row of figure 4.15 shows the effect when a 5 m region around the charge location is coarsened (red curve). A very good agreement is now observed with the AMR results, indicating that ENCS is capable of reproducing a uniform grid solution. Only a slight smoothing occurs for later reflections as the signal will have travelled through coarse cells.

Figure 4.16 shows the results of the convergence study of section 4.3 with an extra curve (shown orange) for the AMR simulation. A very good agreement with the uniform grid is observed up to a scaled distance of $400 \text{ m/kg}^{1/3}$.

The distribution of AMR coverage throughout the simulation is illustrated in figure 4.17. The figure shows spatial profiles of the solution at 50, 300 and 1000 ms. The refinement level is shown below, varying between 0 (no refinement) and 5 (full refinement). In each profile, the areas of maximum refinement are limited to the

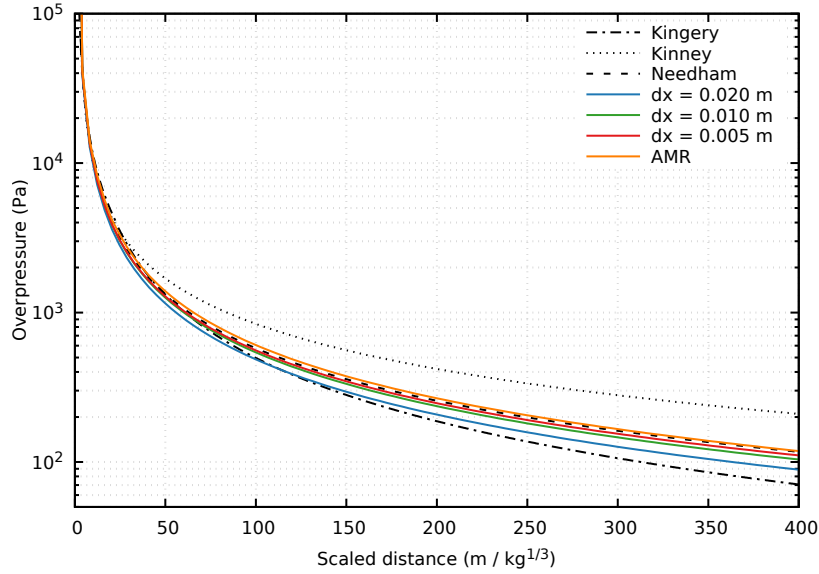


Figure 4.16: Peak overpressure vs. scaled distance for a 1D TNT free air burst. Uniform grid simulations at 0.5 cm (red), 1 cm (green) and 2 cm (blue) cell sizes are shown with a 1 cm AMR simulation (orange). Scaled fits are shown in black.

primary and reflected shocks, with no unnecessary coverage across the rarefaction.

These results stand in contrast to previous AMR studies in which refinement is maintained across the entirety of the blast wave, from initial shock through to the subsequent reflections (see [136] as an example). We have shown that this is not strictly necessary, and that flagging can be minimised without harming the solution.

4.4.2 Two dimensional study

The 1D study showed that it is possible to accurately calculate the solution for 1 kg of TNT using a fraction of the number of cells of a uniform grid simulation. We demonstrated that it was possible to further minimise the flagged region by limiting refinement to regions of compressive flow. Having shown this ‘tighter’ approach to flagging, we turn our attention to the tunability of the method.

In our introduction we stated the following as one of our aims: the ability to maintain precise refinement of flow features across longer distances than is currently possible with existing methods. This ability is particularly important for simulations over large scaled distances. Here the flagging tolerance is set to be sensitive, ensuring that weak flow features at large scaled distances are still refined. This can have unin-

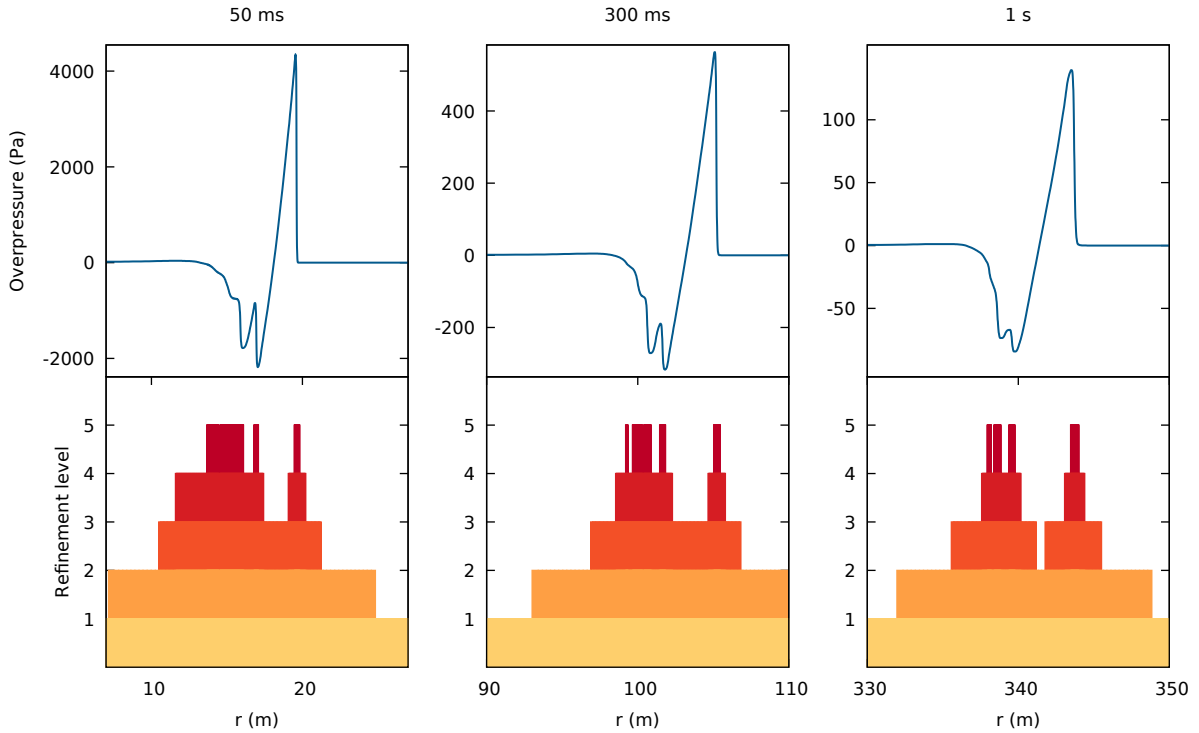


Figure 4.17: An illustration of the refinement coverage in 1D for 1 kg of TNT in the free-field. A pressure spatial profile is shown (top row) with the refinement level (bottom row) for 50, 300 and 1000 ms.

tended consequences during the early phase of the simulation where the relatively strong signal leads to over-refinement.

Extension of ENCS to higher dimensions is straight forward. We perform the 1D spherical problem studied in the previous section in 2D axisymmetry. The same cell size and AMR parameters are used. The 1 kg TNT explosive is situated at the origin and reflective boundary conditions are applied to the x and y axes. The simulation is run to $t = 600$ ms, allowing the blast wave to reach a distance of 200 m from the charge.

The simulation was first performed with the present-day approach: difference flagging, using pressure as the flagging variable. The tolerance was chosen to maintain refinement of the primary wave and the first two reflected shocks up to a chosen distance. The top row of figure 4.18 shows the early- and late-stage refinement at 20 m and 200 m respectively when the flagging tolerance is tuned to maintain feature refinement up to 200 m. The colour of the shading refers to the depth of the AMR level,

with darker patches indicating greater refinement. At the late-stage, the refinement is fairly well distributed. However, the increase in sensitivity has led to some unwanted refinement of the rarefaction behind the primary shock. During the early-stage, this sensitivity has caused significant over refinement.

The flagging tolerance was then relaxed to improve the quality of refinement during the early-stage of the simulation. The figures in the middle row show much improved refinement at 20 m. But this comes at the cost of a complete loss of refinement at 200 m.

The simulation was repeated using ENCS, flagging on pressure. A single tolerance was chosen, in contrast to the previous simulation that used difference flagging and had to be optimised first for the near-field and secondly for the far-field. The bottom row of figure 4.18 shows the results. In both early- and late-stages, an excellent distribution of refinement is maintained across the features of interest. The late-stage ENCS solution compares favourably with difference flagging optimised for the far-field. Because of the compressibility check, the sensitivity of ENCS has been increased without any risk of the rarefaction being flagged for refinement (as is occurring with the difference method tuned for the late-stage).

In this study we have shown that the ENCS flagging method offers significantly improved feature tracking over longer distances when compared to existing methods. The scheme has demonstrated an ability to restrict refinement to compressive shocks without adversely affecting the solution. In addition to this, ENCS is less sensitive to tuning, making it easier for the code user to find the right tolerance. As with any empirical scheme, some problem-specific choice of tolerance is still necessary and we shall deal with this issue later in the chapter. For large-scale blast applications where long distance feature tracking is necessary (e.g. cityscapes), we believe that this method represents a significant improvement over present-day solutions.

4.4.3 The Health and Safety Laboratory test case

We choose a 3D experimental test case to bring together all aspects of the improved approach to AMR flagging. We replicate the study published by the Fire and Explosion Group at the Health and Safety Laboratory (HSL) in Buxton, UK [139]. In this publication the authors performed several experiments that involved the hemispheric, surface explosion of PE4 high explosive in a clear and obstructed environment.

A total of six tests were performed. For each test, the domain on the left side of the charge was left unobstructed. On the right side, a series of concrete blocks were placed in varying configurations. Pressure gauges were located throughout the test area, and recorded the pressure time history following the explosion, capturing the

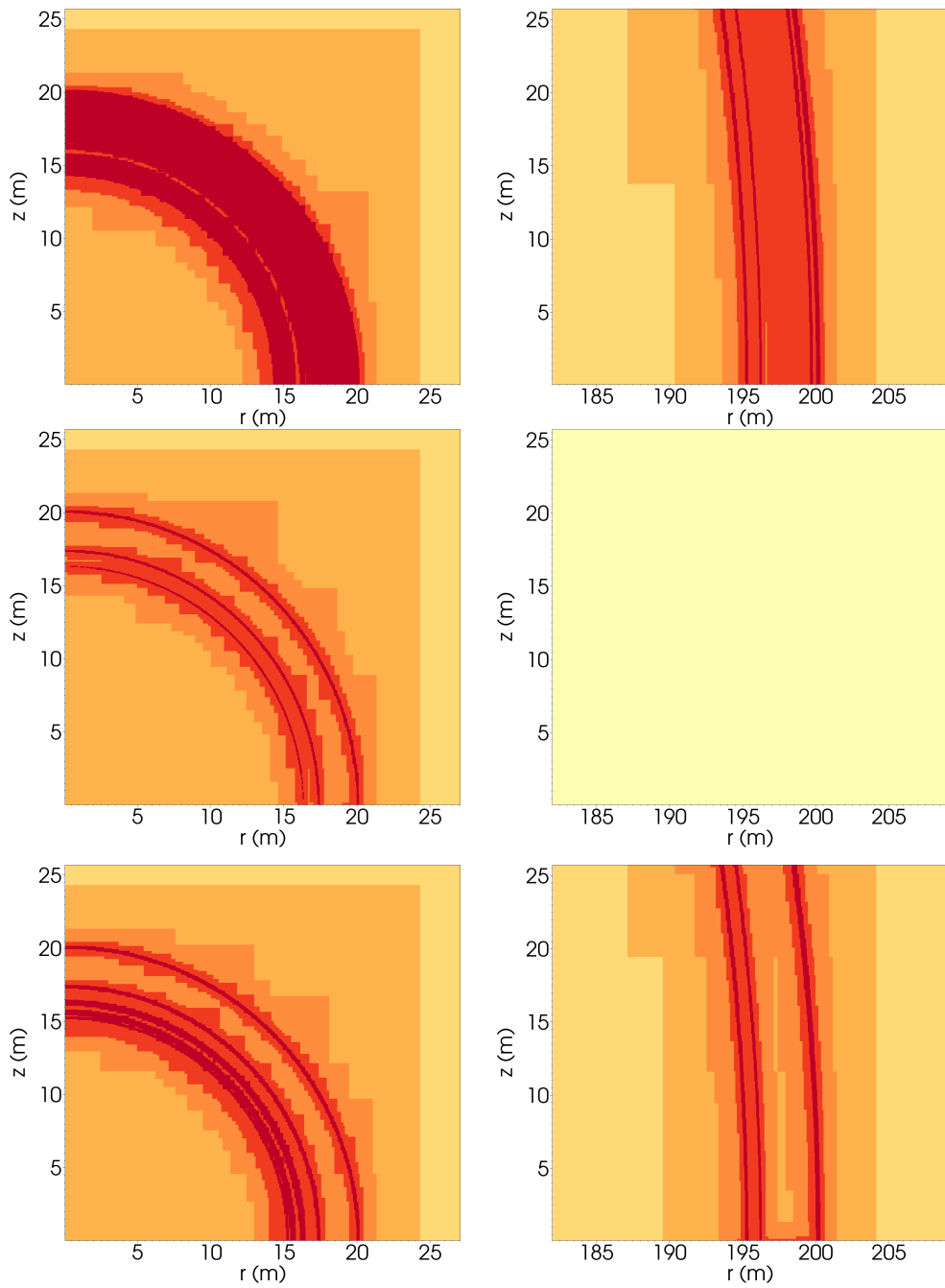


Figure 4.18: Refinement coverage in 2D axisymmetry for 1 kg of TNT in the free-field at early- and late-stages (left and right columns respectively). ENCS is shown (bottom row) with difference flagging tuned for late- and early-stages (top and middle rows respectively).

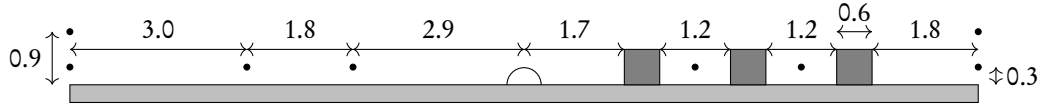


Figure 4.19: Experimental setup for the HSL test 1. A 320 g hemisphere of PE4 is placed in the centre and a series of pressure gauges are arranged along the slab. Three concrete blocks are placed to the right of the charge, with the left side remaining clear. All units are in metres.

results for an obstructed and unobstructed blast. We replicate these tests because they represent a realistic scenario and permit the validation of the numerical method.

We choose test 1. In this test a 320 g charge of PE4 was formed into a hemisphere and placed on a steel plate fixed to a concrete slab. A series of gauges was arranged on this slab at distances shown in figure 4.19. A detonator inserted into the top of the charge was used to initiate the detonation. The experiment is equivalent to a spherical free-air detonation of approximately double the hemispherical charge mass. This is due to the reflection from the concrete slab.

Two 3D simulations were performed: the first covering the left half of the setup shown in figure 4.19 and the second covering the right half. The two runs represent a clear and an obstructed scenario respectively. In the obstructed test, three solid rectangular slabs were placed in the domain, representing the concrete blocks in the experiment. In both tests the charge was initialised at the domain boundary and a symmetry boundary condition was used. The CJ parameters used are shown in table 4.2. ENCS flagging is used with a single layer of AMR of refinement factor 4. This provides a maximum resolution of 2.5 cm.

Figure 4.20 shows the pressure history from gauges 4 and 6 from the clear and obstructed tests respectively. These gauges are the closest to the charge, located a distance of 2.9 m from the source of the explosion. In both tests, the height and timing of the primary peaks are captured well. The secondary wave in the clear test is slightly behind the experiment. This is attributed to a lack of resolution around this relatively weak shock. Figure 4.21 shows the pressure and refinement for both tests at $t = 15$ ms. The clear test shows a good distribution of refinement,

ρ_{PE4} (kg m^{-3})	E_{PE4} (J kg^{-1})	U_{CJ} (m s^{-1})
1560	5876×10^3	8500

Table 4.2: Density, specific energy and CJ velocity parameters used for PE4.

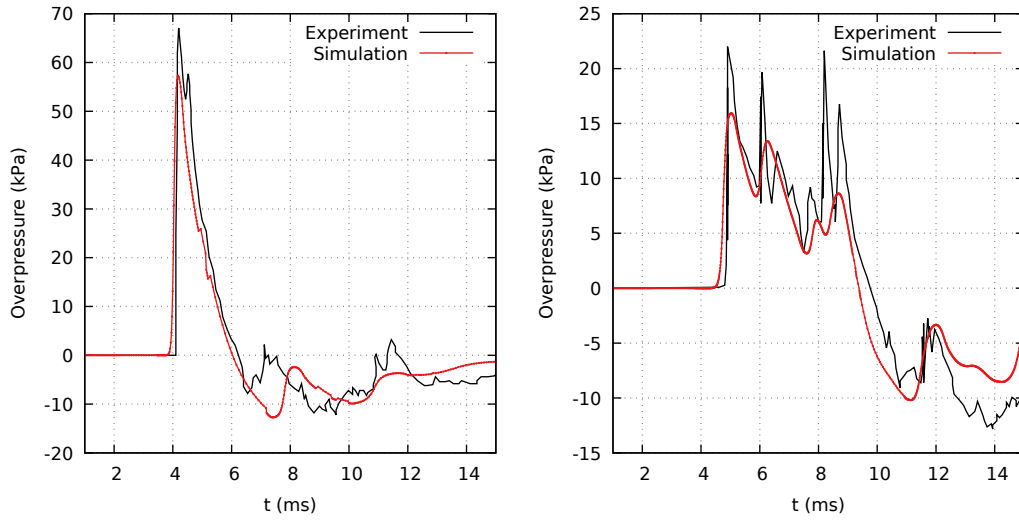


Figure 4.20: Results from the HSL detonation of 320 g of PE4. The results from pressure gauge 4 for the clear test is shown on the left. Gauge 6 from the obstructed test is shown on the right.

capturing the primary wave and the first two reflected shocks. No unnecessary refinement is observed between the waves. When the obstruction is added, the solution becomes more chaotic, with reflections coming from the concrete blocks. Overall AMR coverage has increased but is still modest.

4.4.4 Parameter study

The values of the flagging tolerance E_{ref} and noise filter coefficient ϵ are somewhat model dependant and a range of values have been quoted in the literature [133–135]. A parameter study was performed in order to find the values for E_{ref} and ϵ that best suited the current application. E_{ref} must be low enough to maintain refinement at long distances from the explosion. Similarly, ϵ has to be large enough to prevent refinement of unnecessary ripples without causing unrefinement at long distances where the peak overpressure of the blast wave is small.

The properties of blast waves arising from different masses of the same explosive are equivalent when expressed as a function of scaled distance. The Hopkinson-Cranz scaling law [53] expresses the scaled distance Z as a function of the distance R scaled by the cube root of the charge mass W :

$$Z = \frac{R}{W^{\frac{1}{3}}}, \quad (4.18)$$

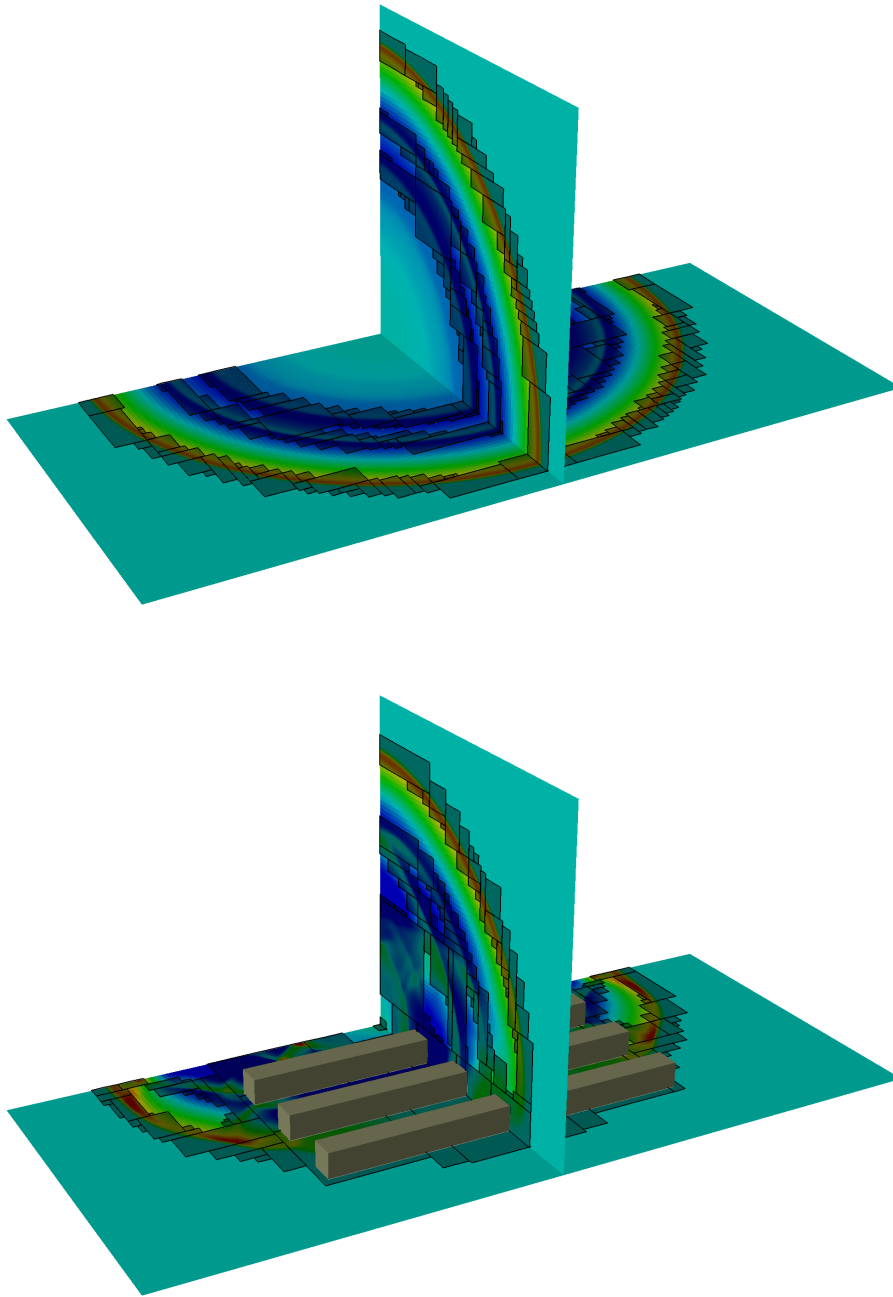


Figure 4.21: Results from the HSL detonation of 320 g of PE4. Pressure and areas of refinement are shown for the clear and obstructed test at $t = 15$ ms.

allowing the properties of large-scale explosions to be predicted from small-scale tests. Using this scaling law, we aim to obtain a maximum acceptable scaled distance at which refinement around the leading shock of the blast wave is guaranteed (given a chosen flagging tolerance).

A parameter study involving a 1 kg surface explosion of PE4 was performed in axial symmetry using a domain of size $[0 \text{ m}, 100 \text{ m}] \times [0 \text{ m}, 100 \text{ m}]$ at a resolution of 2.5 cm. The simulation was performed for all combinations of values for E_{ref} and ϵ shown in table 4.3.

Parameter	
E_{ref}	$1 \times 10^{-3}, 1 \times 10^{-2}, 1 \times 10^{-1}, 2 \times 10^{-1}, 4 \times 10^{-1}$
ϵ	$1 \times 10^{-4}, 5 \times 10^{-4}, 1 \times 10^{-3}, 5 \times 10^{-3}, 1 \times 10^{-2}, 5 \times 10^{-2}, 1 \times 10^{-1}, 5 \times 10^{-1}, 1$

Table 4.3: Values of E_{ref} and ϵ used in the parameter study.

A total of 44 tests were performed. Each test was ranked based on the peak pressure of the blast wave and degree of refinement at a number of points in time. The optimum parameters should lead to a maximisation of the height of the blast wave whilst minimising the degree of refinement. Results indicating too great or too little refinement would be dismissed.

The study indicated that choosing $0.01 < E_{\text{ref}} < 0.1$ and $\epsilon = 0.01$ resulted in a well-balanced degree of refinement. Figure 4.22 shows the blast wave at an early and late point in time for $E_{\text{ref}} = 0.1$ (top row) and $E_{\text{ref}} = 0.01$ (bottom row) with $\epsilon = 0.01$. At the early time (figure left) we can see tight refinement around the primary and secondary shocks, with the tertiary shock captured when $E_{\text{ref}} = 0.01$. In both cases no refinement occurs within the rarefaction. The blast wave reaches approximately 46 m (figure right) before the method loses identification of the primary wave. This increases in excess of 100 m when the tolerance is reduced to 0.01.

Considering this in terms of scaled distance leads us to conclude that the flagging method is capable of capturing the primary shock up to a maximum scaled distance of $45 \text{ m/kg}^{1/3} < Z < 100 \text{ m/kg}^{1/3}$ when E_{ref} is set within the range $[0.01, 0.1]$. Typical blast scenarios involve a charge mass somewhere between 0.25 kg and 2000 kg. This would correspond to a range of approximately $[30 \text{ m}, 60 \text{ m}]$ and $[580 \text{ m}, 1250 \text{ m}]$ respectively.

The test performed in sections 4.1.5 and 4.2.1 was then repeated using the ENCS flagging method. The blast wave arising from a spherical explosion of 0.32 g of PE4 in 1D spherical symmetry was measured using a series of pressure gauges. The results in figure 4.23 show the pressure trace (top) along with the degree of refinement (bottom). Three simulations were performed: the first using AMR (red) with a base

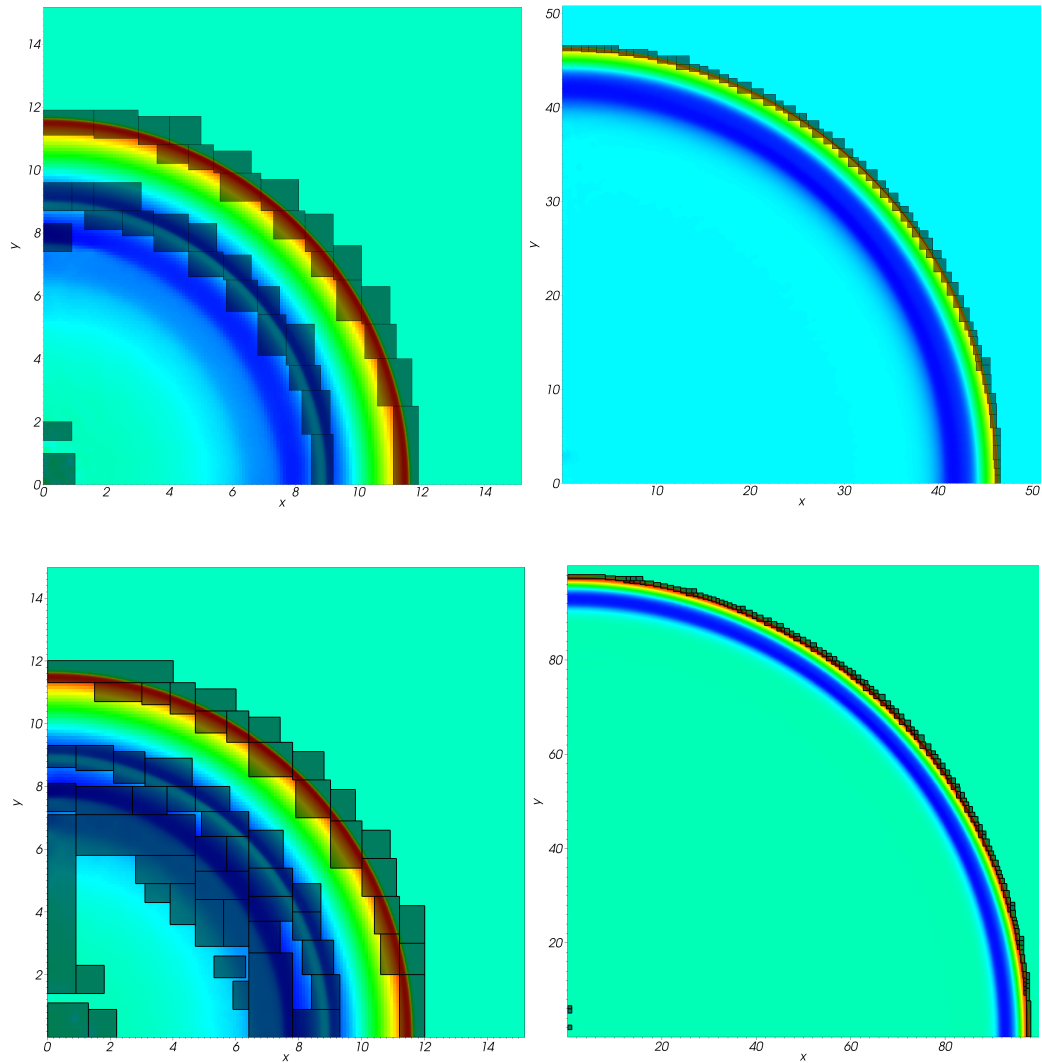


Figure 4.22: A pseudocolour of pressure, illustrating the blast wave emanating from a 1 kg PE4 surface explosion for two different simulations. A snapshot of the blast wave at a short and a long distance are shown on the left and right respectively. Regions of refinement are shaded grey. The flagging tolerance E_{ref} is set to 0.1 (top row) and 0.01 (bottom row)

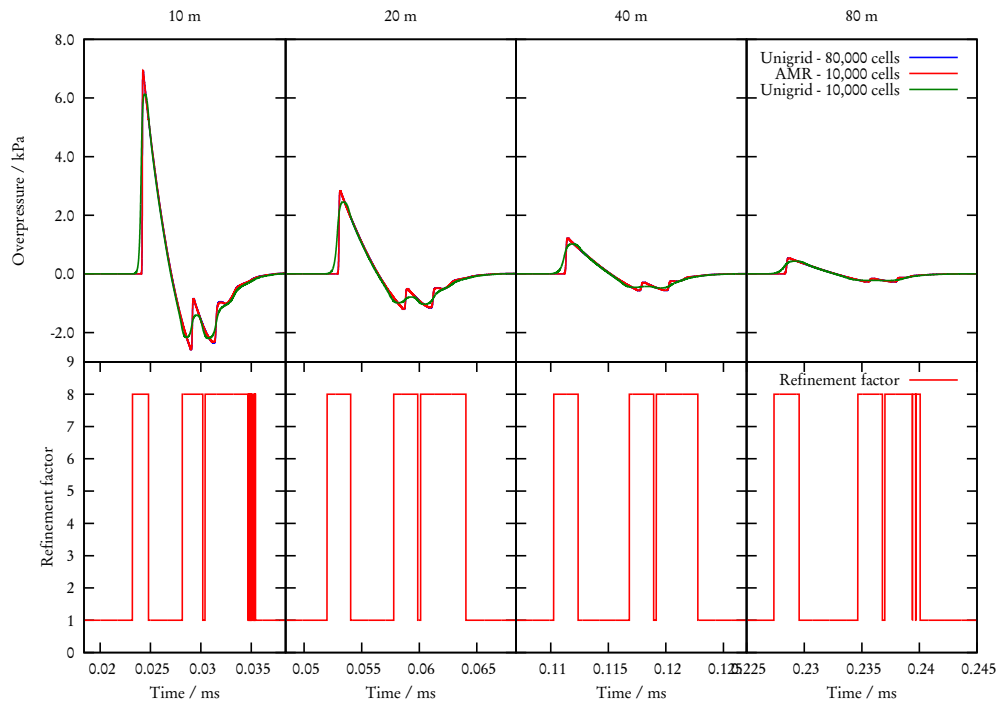


Figure 4.23: A graph of overpressure and AMR refinement factor for a spherical free air explosion. The pressure is measured using gauges at 10, 20, 40 and 80 m from the source.

resolution of 1×10^4 cells and highest effective resolution of 8×10^4 cells. This was followed by two uniform grid simulations at 1×10^4 (green) and 8×10^4 cells (blue). An enlarged profile is shown for each gauge in figure 4.24.

The method performs extremely well at replicating the primary, secondary and tertiary blast waves. Refinement is used precisely, targeting the three shocks and avoiding unnecessary refinement of the rarefaction. The AMR profile is nearly indistinguishable from the high resolution uniform grid simulation. This test indicates that the divergence mask does not negatively impact the peak height by preventing refinement of the rarefaction.

4.5 Conclusion

In this chapter, we have made several improvements to our AMR approach, with the overall aim of making it more reliable and easier to use for the non-expert. We began by identifying the main problems associated with AMR: the inability of most

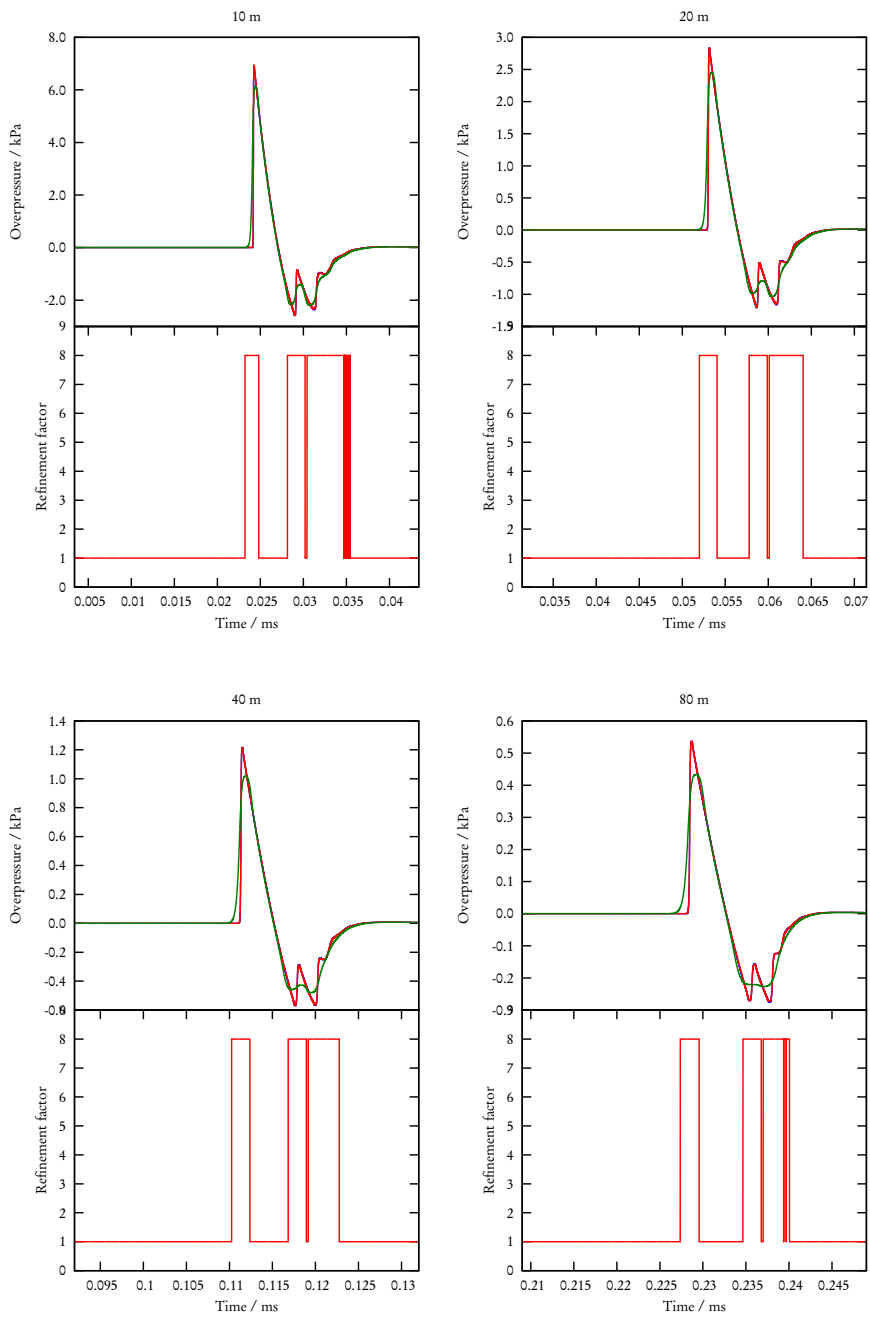


Figure 4.24: A graph of overpressure and AMR refinement factor for a spherical free air explosion. The pressure is measured using gauges at 10, 20, 40 and 80 m from the source. The AMR solution is shown in red with a high and low resolution uniform grid solution shown in blue and green respectively.

methods to flag only the relevant flow features and the challenging task of tuning AMR parameters to ensure adequate refinement for the particular application.

A time dependency was introduced to the existing difference flagging criterion. With this approach, one dimensional shock tracking was achieved across longer distances. However, extending the method to higher dimensions proved unsuccessful. Instead, a new second-derivative error norm criterion for compressive shocks was proposed (ENCS). The approach has a number of benefits over existing methods. The tolerance is bounded between 0 and 1 and is easier to tune. The method also avoids unnecessary refinement of rarefactions thanks to a divergence check.

A convergence study was performed to ascertain an acceptable cell size for a blast simulation using a MUSCL HANCOCK scheme. Computational expense was also taken into account. A cell size of $\Delta r = 1 \text{ cm/kg}^{1/3}$ was found to provide well converged solutions without excessive cost. A further study was performed to investigate the effect of cell size across the charge radius. Good convergence was found when 50 cells were maintained across this width. It was shown that the condition could be relaxed to just 5 cells (equivalent to $\Delta r = 1 \text{ cm/kg}^{1/3}$) without significantly affecting the solution.

Using the recommended resolution, a series of numerical blast tests were performed with and without AMR. ENCS was able to avoid refinement of rarefactions, limiting flagging to shocks without any negative impact on the solution. The study was extended to 2D axisymmetry and the new method was compared with a difference flagging criterion for long distance blast propagation. ENCS was shown to be easier to tune and exhibited significantly improved feature tracking over longer distances when compared with the existing method. The scheme was applied to a 3D validation test case involving the detonation of high explosive in a clear and a partially obstructed domain. Finally, a parameter study was performed in which the flagging tolerance E_{ref} and noise filter coefficient ϵ were varied and a recommended range of values was suggested.

Chapter 5

Blast damage in urban cityscapes

IN chapter 3 we considered several ways in which urban geometry affects the propagation of blast waves and the subsequent loading that these structures are subjected to. In this chapter we consider the inverse situation, namely the effect that blast waves have on objects that lie within their path. The prediction of blast wave propagation in urban areas is a critical element in the estimation of terrorism risk. Yet this knowledge is of little use unless it is used to predict some form of damage.

Immediately following a terrorist attack there is often some kind of damage to property. In 1993 the IRA detonated a large truck bomb on Bishopsgate, a major road in London's financial district. Extensive damage occurred to the local area, with numerous buildings requiring demolition as a result of the blast damage. Total insured losses were estimated at \$907 million [140]. At the time this was considered to be the world's most expensive terror attack. But this figure is dwarfed by estimates from the 2001 World Trade Center (WTC) attacks, which resulted in \$22.7 billion in property damage around the WTC complex and an insured loss to property of approximately \$19 billion [141].

The second type of damage was economic in form. The near destruction of a significant area of New York City's business district caused longer-term economic repercussions. Business relocation, a slump in property values and a reduction in tourism had a significant impact on the local economy. It is estimated that the New York City Finance Department collected \$200 million less in taxes than the previous fiscal year [140].

The third major form of damage is human. While no monetary value can be assigned to a human life, its value is obvious. The attacks of 2001 led to the deaths of nearly three thousand people, with over six thousand injured [142]. These attacks

left a deep imprint in society, astonishing the world with the scale and ambition of modern-day terrorism.

As anyone who reads the news will be aware, the threat to the world from global terrorism shows no signs of abating. The protection of major cities such as New York, London and Paris is extremely important to government officials. Part of this protection involves understanding the consequences of potential attacks so that a reasonable estimate of risk can be calculated and mitigated through government terrorism preparedness schemes.

It is not only governments that have an interest in modelling the consequences of terrorism. Insurers and re-insurers that provide terrorism-based insurance perform consequence analysis to quantify the effects of specific attacks. These figures feed into a larger risk model, which governs the price of insurance premiums and capital held by these companies.

Having methods that can accurately model the outcome of an attack would be extremely useful for government and the insurance industry. It is known that terrorists prepare attacks based on expected consequences, choosing a scenario where the expected damage is maximised. More accurate information would allow governments to deploy resources accordingly. Correspondingly, insurers could better predict the financial implications of an attack which could lead to a reduction in premiums and capital held as simple, conservative models are retired in favour of more accurate methods.

Our aim in this chapter is to provide an argument for the use of CFD methods for the prediction of insured loss given an urban terrorist attack. We plan to achieve this through a comparative study of empirical and CFD-based loss models. The study will provide a quantification of the improvements to loss calculation that can be achieved through CFD-based modelling. We will focus on the insurance market, performing a review of an insurer's approach to terrorism risk before performing a comparative study of several loss modelling approaches. The argument for the use of methods that capture geometrical effects will be supported by a separate study demonstrating the importance of charge location on the outcome of the explosion.

In section 5.1 we present the theory on how structures and people interact with blast waves, reviewing the approaches for predicting blast-induced damage. In section 5.2 we look at how the insurance industry models terrorism risk, with a focus on deterministic loss models. In sections 5.3 and 5.4 we conduct a validation and a numerical study to demonstrate the effect of simple urban geometry on the distribution of damage following an explosion. In section 5.5 we study the effect of charge placement on blast wave resultants to justify the use of CFD methods that take urban geometry into account. We then apply three deterministic loss models to

a hypothetical urban bombing and perform a comparative study of predictions of financial loss. The findings are presented in section 5.7.

5.1 Structural response to blast loading

Objects that lie within the path of an explosion will eventually be engulfed by the blast wave and experience forces on their surfaces. The size and construction of these objects can vary considerably: from large solid buildings to small relatively ‘soft’ objects such as humans or animals. The size, shape and material properties of objects plays a significant role in their reaction to blast loads and subsequent damage.

In this section we will outline the relevant theory on how structures and people respond to blast loading. The topic is very broad and covers a wide range of subject areas. Rather than attempt to cover the whole field, we will outline the areas of knowledge concerned with the response of buildings, glazing and humans to blast loads.

Blast forces result in the elastic deformation of the object up to a yield point where irreversible plastic deformation occurs. Eventually, under enough force, the material will fracture, causing permanent damage to the structure. The properties of building materials vary greatly: materials such as steel and aluminium have relatively high ductility and have high levels of tensile strain up to the point of fracture. On the other hand, iron and concrete are brittle and demonstrate a relatively small amount of strain prior to rupture.

5.1.1 Elastic deformation of structures

The elastic deformation of a structure under blast loading can be described using a simplified single degree of freedom (SDOF) model where the object is described as a single structure of mass M that is loaded with a time dependant force $F(t)$. The object is allowed to move under a single degree of freedom, resisting the force with resistance kx , where x is the degree of displacement and k the material stiffness. In reality, buildings are composed of a number of different objects which can move independently of one another under blast loading. However, despite floors being able to move differently to others, they have little effect on the overall movement of the structure [49].

Modelling the load pulse on the positive phase of the blast wave, we represent $F(t)$ by the equation

$$F(t) = F \left(1 - \frac{t}{t_d} \right) \quad (5.1)$$

where t_d is the positive phase duration of the blast wave that delivers an impulse of $I = \frac{1}{2}Ft_d$ to the structure. The corresponding equation of motion for this system is

$$M\frac{d^2x}{dt^2} + kx = F\left(1 - \frac{t}{t_d}\right). \quad (5.2)$$

The solution for x when $0 < t < t_d$ can be written in the following form:

$$x(t) = \frac{F}{k}(1 - \cos(\omega t)) + \frac{F}{kt_d}\left(\frac{\sin(\omega t)}{\omega} - t\right), \quad (5.3)$$

where $\omega = \sqrt{k/M}$ is the system's natural frequency of oscillation. Under loading, the structure will eventually reach a point of maximum deflection x_m when the velocity is zero. By differentiating equation 5.3 and setting dx/dt to zero we find that

$$0 = \omega \sin(\omega t_m) + \frac{1}{t_d} \cos(\omega t_m) - \frac{1}{t_d}, \quad (5.4)$$

where t_m is the time at which $x = x_m$. The equation can be solved to give a solution for t_m in the form

$$t_m = f(\omega t_d). \quad (5.5)$$

This can be used to find a solution for the maximum displacement in terms of the structure's natural period T and the duration of the positive phase t_d :

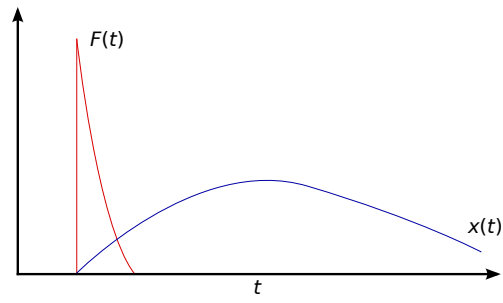
$$\frac{x_m}{F/k} = \psi\left(\frac{t_d}{T}\right). \quad (5.6)$$

This suggests that the natural period T of the structure and its relation to the positive phase duration t_d play an important role in the deformation of the structure. In fact, three distinct loading regimes can be identified which depend on the ratio t_d/T .

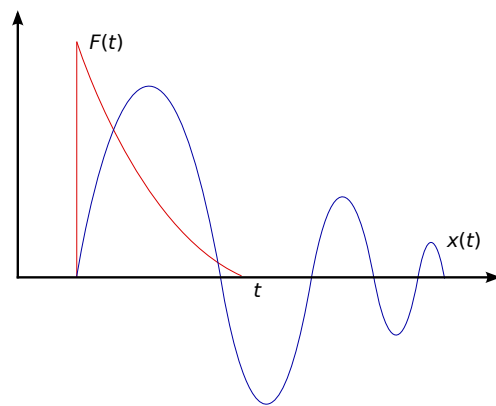
If the duration of loading is very long compared to the natural period, the structure will reach maximum deformation long before the end of the positive phase. The maximum displacement is dependent on the peak force from the blast wave F which is related to the overpressure. We call this *quasi-static* loading and it occurs when $t_d/T < 0.1$. Nuclear blasts, earthquakes and large quantities of high explosives typically produce this type of loading.

As t_d reduces and approaches T , the structure reaches maximum deformation in a similar time to the duration of the blast wave. This state is termed *dynamic* loading and the deformation of the structure depends equally on the maximum force F and the impulse I delivered by the wave ($0.1 < t_d/T < 10$).

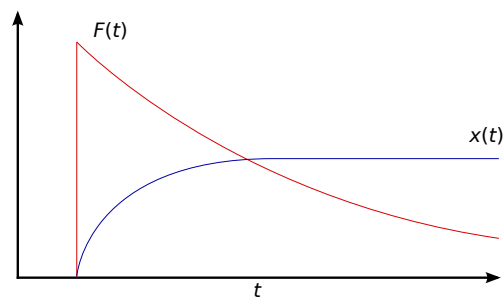
Finally, for short duration blast waves ($t_d/T > 10$), t_d is much smaller than T and the load on the structure is usually over before any significant movement occurs. In this case, the deformation is a function of the impulse I delivered to



(a)



(b)



(c)

Figure 5.1: The three different types of structural blast loading: (a) impulsive, (b) dynamic and (c) quasi-static. The displacement $x(t)$ of the object is shown when a force $F(t)$ is applied.

the structure. This is termed *impulsive* loading. Figure 5.1 shows the blast force $F(t)$ and corresponding deformation $x(t)$ for these three loading regimes.

When modelling building damage it is useful to be aware of the type of loading that the building sustains. It is possible to derive a reasonable estimation of this regime by considering the building's natural period and the duration of the positive phase of the blast wave. Studies have been performed to estimate the natural period of building structures, relating T to the building dimensions. In practice, very rough correlations have been found, but are enough to indicate the type of loading that the structure might sustain. One of these correlations suggests that, for a modern building

$$T = 0.09 \frac{H}{\sqrt{B}}, \quad (5.7)$$

where H and B are the height and breadth of the structure respectively [49]. Assuming typical cubic building dimensions of $H = B = 50$ m, we calculate a period of approximately 0.6 seconds. A typical blast wave from a high explosive source might have a positive phase duration of 40 milliseconds. Calculating the loading ratio, we find that

$$\frac{t_d}{T} = 0.07, \quad (5.8)$$

which places us firmly in the impulsive loading regime. In fact, the majority of structures in urban areas have a period that is far greater than the duration of the positive phase of the blast wave. These structures barely move before the blast wave has passed and can be considered as rigid throughout the loading. This means that structural response can be calculated without taking into account the interaction between the blast wave and the deforming structure.

5.1.2 Pressure-impulse diagrams

For a particular structure, the damage or deformation can be visualised using a pressure-impulse (PI) diagram. On this chart it is possible to plot a curve indicating the combinations of pressure and impulse that produce the same amount of damage. This is termed an iso-damage curve. The PI diagram in figure 5.2 shows a sketch of an iso-damage curve for an SDOF elastic structure that is loaded with an ideal blast wave. The three loading regimes are also shown.

PI curves are unique to the type of structure and the degree of damage. Using the right curve for the building construction type, it is possible to establish a relationship between pressure-impulse readings and expected damage levels. PI curves are widely available for popular materials. As an example, the US Department of Defense publishes a range of curves for various structures including vehicles and

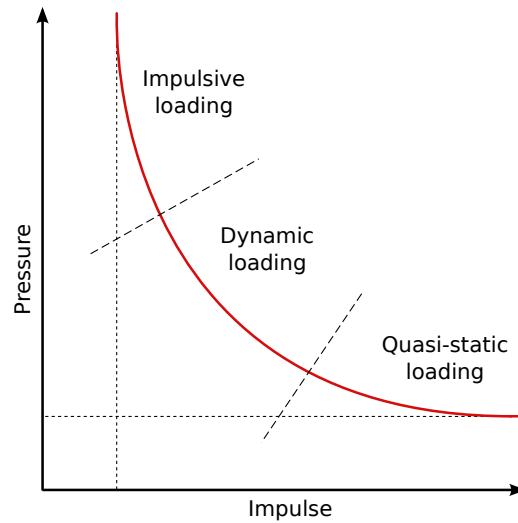


Figure 5.2: A typical pressure-impulse diagram.

buildings constructed from metal, brick, concrete and wood [143]. Each curve represents a damage level from an explosion that varies between 0.1 % and 100 %. The damage curves indicate the degree of repair or replacement required in the building. Therefore, a level of 100 % corresponds to complete financial loss of the building, not necessarily its complete collapse.

Once in possession of the range of curves and pressure-impulse measurements from the surface of the structure, a reasonable estimate of damage can be obtained. For impulsive loading, PI curves represent a popular method of damage prediction because of their relative simplicity and the lack of a need to model any structural response to the blast wave. A simpler alternative is the use of an overpressure-only method, ignoring the effects of impulse. This approach is simpler and less accurate because it does not take into account the response of the building. However, what the method lacks in accuracy it gains in simplicity and affords the user a way to predict damage without the need for PI curves.

Table 5.1 shows the relationship between peak side on overpressure p_{so} and various types of structural damage. At the lowest end of the scale, minor structural damage is sustained. Roof tiles may be damaged, plaster cracked and some windows shattered. As the blast increases in strength, panels of sheet metal can buckle and masonry walls may fail. At large enough overpressures, the explosion can result in the destruction of reinforced concrete structures and the complete demolition of buildings.

Damage	p_{so} (kPa)
Windows shatter, minor damage to some buildings	5.5
Panels of sheet metal buckled	10
Failure of concrete walls	16.3
Serious damage to steel framed buildings	40
Severe damage to reinforced concrete structures	50
Most buildings destroyed	75

Table 5.1: Overpressures for various types of blast damage [49, 144].

5.1.3 Effects of explosive blast on buildings

The structural system of buildings can be divided into three sections: the primary structural frame of the building is the strongest component. It consists of the main gravity and lateral load bearing system which may consist of girders, columns, beams and walls. The columns and girders found at the base of the building tend to be the strongest as they must bear the cumulative forces of gravity and wind from the floors above. Since most blast loads usually originate from the ground, it is the lower primary structure that usually experiences the highest blast forces.

Explosive devices can inflict serious damage to this primary structure, leaving it vulnerable to progressive collapse if insufficient structural redundancy exists and the load cannot be redistributed amongst the surviving columns. An example of this is the 1995 Oklahoma bombing, where a vehicle-borne improvised explosive device (VBIED) was detonated outside the Alfred P. Murrah Federal Building in Oklahoma City. A 40 foot lateral transfer girder was destroyed causing the failure of adjacent columns and the collapse of most of the front of the building [142]. In the aftermath of the attack, lessons were learnt. Aside from strengthening the primary structure, the effects of blast damage can be mitigated by introducing redundancy into the frame, so that if one column fails, the load can be redistributed amongst the surviving columns.

The secondary structure consists of local floor beams and slabs, the strength of which does not depend on the size of the building. The greatest vulnerability of this system is from uplift infill pressures that occur when the blast wave travels through the building, forcing floors upwards. This effect can be mitigated by the third building component: the external façade. A strengthened façade can prevent the ingress of blast into the building, protecting it from the full extent of infill pressures.

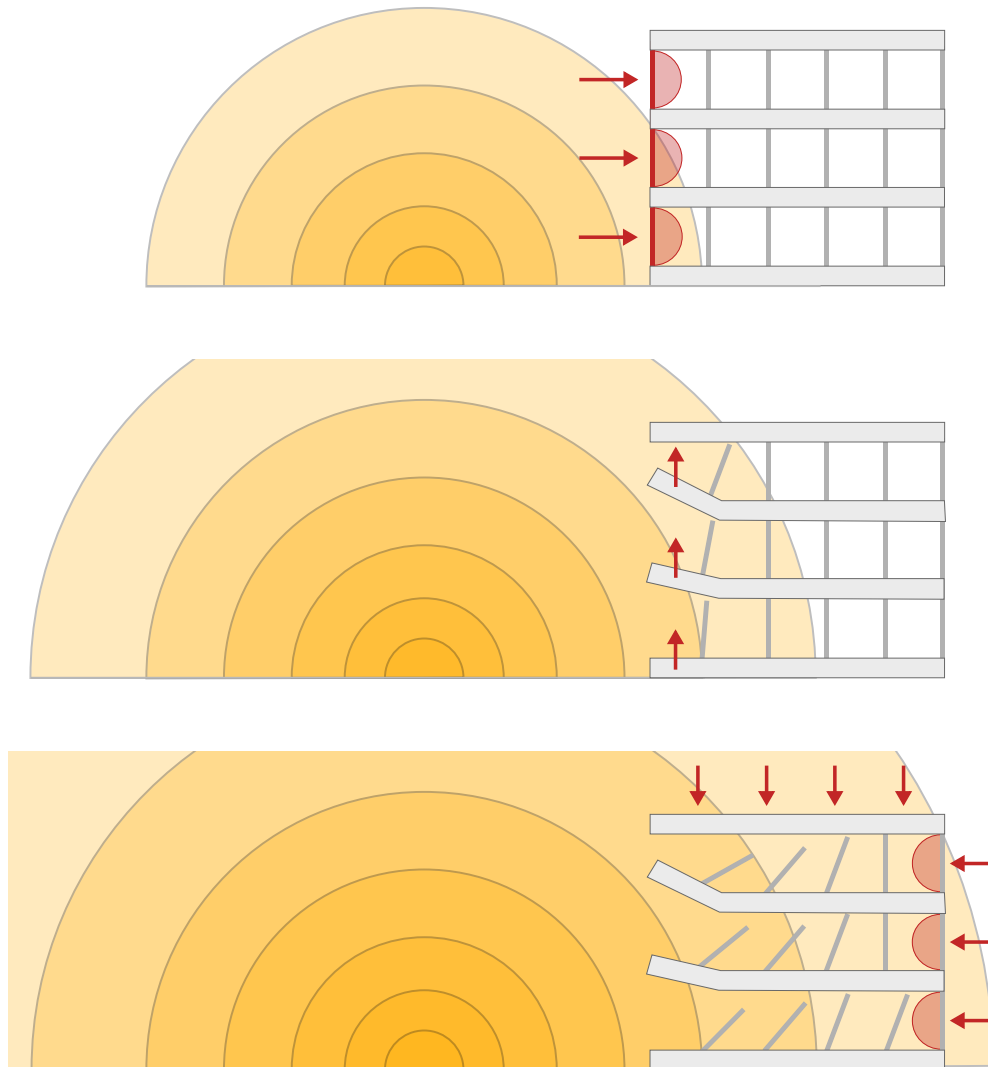


Figure 5.3: The sequence of building damage following an explosion. 1) The blast wave breaks through the façade, damaging windows and walls. 2) The wave enters the building and infill pressures force floors upwards. 3) The structure is surrounded by the blast wave. Downward and side pressures are experienced by the roof and walls [142].

Failure mode	p_{so} (kPa)	
	1 t TNT	10 t TNT
5 % broken	1.1	0.7
10 % broken	2.5	1.7
90 % broken	6.3	4.2

Table 5.2: Window blast damage overpressures for two charge sizes, demonstrating the effect of positive phase duration on the damage characteristics of TNT [146].

Figure 5.3 shows a graphical representation of this series of events. As the blast wave makes contact with the building it penetrates the façade. Once inside the building, the wave is channelled through each floor. The infill pressures force the floors upwards and may result in the destruction of columns. Eventually the blast wave engulfs the entire building and a downward force is applied through the roof. The building sides also experience lateral forces.

5.1.4 Effects of explosive blast on glazing

A common feature in many historic urban terrorist attacks has been the relative lack of serious structural damage to buildings. In the Bishopsgate bombing of 1993, only the nearby church of St Agnes was damaged beyond repair. In the 1996 IRA Docklands bombing, only the building next to the bomb had to be demolished. In both of these cases it was the extensive glazing damage to nearby buildings' façades that caused the greatest disruption to business and life [145]. Once a façade has failed, even superficial damage to the working environment is enough to prevent a firm from being able to do business.

Glass is a brittle material which is liable to fail suddenly and produce sharp fragments. This represents a hazard to anyone in the vicinity of a window that is loaded by a blast wave. When a window does fail, the occupants of the building are not only exposed to the hazards of the blast wave but also to any sharp fragments of glass generated by the destruction of the windows. It is important for the glazing engineer to design glazing that not only withstands the blast wave, but also fails in a safe way if breaching does occur.

The manufacturing process of glass can greatly affect its properties and most glass used today falls into three distinct types [146]. The most basic form of this material is *annealed* glass. In this state, the glass contains a random series of microscopic flaws

that run across the surface of the pane. If enough stress is applied, the pane will shatter along these lines. Large, sharp, jagged fragments are produced. This poses a serious hazard to building occupants located next to a blast loaded pane that shatters.

The properties of glass can be improved by reheating and then cooling annealed glass. This changes the distribution of stress within the material and increases its strength. A further benefit of this process is the failure property of the pane. Once shattered, the glass breaks up into many small, blunt-edged pieces that present less of a hazard to building occupants. This form of glass is termed *toughened* glass.

Laminated glass is a composite material that is formed from successive layers of glass and a polyvinyl butyral (PVB) interlayer. PVB is a highly ductile plastic that also has significant tensile strength. After sufficient strain, the glass will eventually crack. The laminated layer is able to hold it in place, forming a second layer of defence which is able to absorb energy from the blast wave by deforming significantly under stress. Laminated glass is particularly well suited to the protection of façades from blast loading because of its ability to absorb blast energy and prevent the projection into the air of hazardous shards of glass. This ability to prevent blast wave ingress into a building can protect lives and save the firm significant sums of money by avoiding business interruption.

The relationship between the type of explosion and the performance of the glass can be highly non-linear. The resistance displacement function for glass is also complicated. A time history analysis using SDOF theory to predict the damage sustained from a particular load pulse is usually the recommended approach. An explanation of this methodology can be found in the UK Glazing Hazard Guide [147] and the US Army Corps of Engineers UFC 3-340-02 report [60].

Table 5.2 shows various failure modes for window panes for a 1 t and a 10 t TNT charge. Different failure rates are observed for the two charges when compared at the same scaled distance. This is a good example of why it is important to take into account overpressure and impulse when considering glazing damage. The positive phase duration of the 10 t charge is larger than the 1 t charge. This results in a different loading duration and greater damage for the same overpressure. A rough estimation of damage can be obtained with just an overpressure measurement. But the inclusion of impulse improves the accuracy.

5.1.5 Effects of explosive blast on the human body

Blast-induced injuries may occur for several reasons. Primary injuries result from the direct exposure to the pressure variations of the blast wave. Because of the small surface area of humans, the blast wave diffracts and clears very quickly, rapidly engulfing

Effect	Likelihood	p_{so} (kPa)
Eardrum rupture	Threshold	34
	50 %	103
Lung damage	Threshold	207
	50 %	552
Lethality	Threshold	689
	50 %	896
	Near 100 %	1379

Table 5.3: Overpressures for primary blast injuries [142].

the target and submitting it to severe compression. This sudden compression can cause pressure waves to pass through the internal organs, producing damage at the intersections between different tissues [148]. Primary injuries can vary in severity, from eardrum rupture and lung damage through to haemorrhage and oedema.

Table 5.3 shows the relationship between incident overpressure and a range of primary injuries. These effects occur at relatively high pressures compared to the damage inflicted on buildings. Humans have a smaller surface area, which allows the blast wave to clear faster and relieve the pressure. Furthermore, the material properties of the human body allow for greater deformation prior to fracture. In addition to the pressure table, an iso-damage approach for lung damage can be used. Pressure-impulse diagrams have been developed by Baker et al. [48]. Similar diagrams for ear damage are also available, although damage levels are usually calculated using an overpressure approach [146].

Secondary injuries are caused by the impact of the human body with debris scattered by the blast wave. For building occupants, debris is most often associated with parts of the failed façade, structural elements and furnishings. Typical injuries sustained are lacerations, blunt injuries and eye penetration [149]. Tertiary injuries occur when the individual is thrown into the air by the strength of the blast wind, often striking the ground or other hard objects. This can lead to bone fracture and various head injuries. Criteria for the prediction of secondary injuries has been compiled by Ahlers [150] and summarised by Baker [151]. For tertiary injuries, the work of Baker [152] is recommended.

It is important to note that secondary and tertiary injuries can be just as likely as primary injuries. Lacerations from flying glass fragments have been common in

blast incidents. In the Oklahoma City bombing, airborne glass and window-blinds were attributed to 40 percent of those injured [142]. The failure of windows is a key risk in structural blast loading because of its likelihood of occurrence and the consequences for property loss, business interruption and human casualties. The ability to accurately predict window failure is therefore very useful when calculating the overall effects of an urban terrorist attack.

5.2 Catastrophe modelling in the insurance industry

The terrorist attacks of September 2001 caused an unprecedented loss of life, property and income. The magnitude of the financial cost of the attacks dwarfed anything previously seen in US history [153]. Billions of dollars were due in insurance payouts for the loss of property, business interruption and for the compensation of those injured or killed in the attacks. In the immediate aftermath, it was clear that the insurance industry had greatly misunderstood the risk from terrorism. Insurers soon realised that this risk was too poorly understood to be managed and began to stop covering terrorism losses [154].

In the months that followed the attacks, the insurance industry began to realise that the risk of losses from terrorism was no longer so low that the threat could be covered under most standard insurance policies. The events of 9/11 had demonstrated that terrorism could cause catastrophic losses across multiple lines of businesses without warning.

Eventually, the insurance industry was able to respond to this new threat by offering products that yielded a better understanding of the possible losses in specific regions or from attacks on insured properties. At the heart of this new approach was the use of catastrophe modelling, a method that was already being applied to study the threat from natural disasters such as hurricanes, floods and earthquakes. This type of modelling allowed the insurance industry to predict the likelihood that terrorist attacks might occur, their potential consequences and the distribution of risk in time and in space [154].

Today, over a decade on from the events of 9/11, terrorism continues to be a major global issue. The threat to the West from Al-Qaeda has largely been replaced by the Islamic State (ISIS) terrorist organisation. Since the rapid expansion of ISIS, the frequency of attacks has increased, with a focus on causing mass-casualties [155]. As the nature and distribution of these attacks evolve, the insurance industry continues to improve and update its capability to predict the probability and consequences of these events.

In this section we shall explain the nature and implications of terrorism risk, focussing on the types of loss that a typical business insures against. We will explain how insurers model this risk before describing how loss in the event of an attack is modelled in the market today.

5.2.1 Insuring against loss

All companies face the risk that their business may be adversely affected by events that lie out of their control. This can range from theft or damage of company property to employee litigation. Each of these risks carries with it a negative financial implication and it is in the company's interest to remove this future risk. Insurers offer products to mitigate the financial implications of a possible future event. In return for a series of payments (premiums), the insurer agrees to take on a share of the liability from a particular risk. In the event of terrorism, companies face three major forms of financial damage that require insuring against: human loss, property loss and business interruption.

Human losses are classed as the financial liability for fatalities or those who incur temporary or permanent disabilities as a result of a terrorist attack. These losses can arise from the litigation of victims and their families with the aim of recovering economic (loss of work) and non-economic (emotional distress) damages. These damages can amount to a significant sum. For example, the 9/11 Victims Compensation Fund, which was set up in the aftermath of the World Trade Center attacks provided approximately 7 billion dollars in compensation to the families of 9/11 victims [156].

Property damage is the dollar value of all physical assets partially or completely destroyed as a result of an attack. This includes damage to the insured building and can extend from minor damage to the façade all the way to full collapse. Fixtures, fittings and other contents inside the building are also covered. This form of damage can be extended to the building infrastructure in the form of gas, electricity and telecommunication lines that may be ruptured during an attack.

In order to determine an estimate of the physical loss, the insurer may take a bottom-up approach, obtaining a figure for total building loss (TBL) for a group of buildings using the following formula:

$$TBL = \sum_i RC_i SM_i DR_i \quad (5.9)$$

where RC_i is the replacement cost per square metre, SM_i is the floor area and DR_i is the damage ratio of building i [141].

The replacement cost of the building is the dollar value to completely rebuild the structure given complete destruction. For example, replacement costs for the WTC complex in 2001 dollars were estimated to be \$450–\$500 per square foot and can vary depending on the cost of rebuilding in the affected area. The damage ratio represents the ratio of loss to replacement cost. Complete or partial collapse of a building represents a 100 % damage ratio, while moderate damage would be roughly 20 % [141].

This method was applied to the 2001 World Trade Centre attacks by Grossi [141]. The WTC complex was completely destroyed and incurred a damage ratio of 100 %. Much of the surrounding buildings incurred major or moderate damage, with significant damage to tenant's contents and city infrastructure in the surrounding area. Overall, property damage was estimated at \$9.95 billion.

Business interruption (BI) represents the financial losses to a company from the inability to do business as a result a terrorist incident. BI can affect even those far from the incident site and arises from physical damage to the building; infrastructure outage (power, telecommunications); civil authority (an exclusion zone placed around the disaster zone); contingent BI (loss from damage to a business supplier).

In the WTC attacks, not only was the World Trade Centre completely destroyed, but many of the surrounding buildings had their windows smashed or were placed inside an exclusion zone and evacuated. The quantity of dust blown throughout the area also hampered businesses from resuming operations. Such was the devastation, an estimated \$9.8 billion was paid out for business interruption losses in the wake of the attacks, equivalent in scale to the loss of property.

The previous figure emphasises the importance of insuring against business interruption. Only the windows of a building need shatter for the company to be unable to do business. This means that insured losses can extend far from the site of the attack, even when property damage is minimal.

5.2.2 Understanding terrorism risk

There is no single definition of terrorism risk. However, there is a general agreement in risk literature that defines risk as a function of three metrics: *threat*, *vulnerability* and *consequence* [157].

A threat is represented by a person or organisation that has a capability to perform an attack. The threat is the probability that a specific target is attacked at a specific time. Vulnerability is the probability that damages will occur given a specific attack at a specific time for a particular target. Consequence is the expected magnitude of damage sustained given a successful terrorist attack.



Figure 5.4: A Venn diagram representation of risk [158].

Terrorism risk represents the expected consequences of attacks by factoring in the probability that an attack will occur (threat), the chance that it will be successful (vulnerability) and the magnitude of the damages sustained (consequence). Mathematically, risk can be thought of as

$$\begin{aligned}
 \text{Risk} &= \text{Pr}(\text{attack occurs}) \times \\
 &\quad \text{Pr}(\text{attack results in damage} \mid \text{attack occurs}) \times \\
 &\quad \text{E}(\text{damage} \mid \text{attack occurs and results in damage}) \quad (5.10) \\
 &= \text{Threat} \times \text{Vulnerability} \times \text{Consequence}.
 \end{aligned}$$

Figure 5.4 illustrates this concept in the form of a Venn diagram. In the centre, risk lies at the intersection of threat, vulnerability and consequence.

This approach brings with it the advantage that risk can be managed by individually targeting each area. Intelligence services and the police can focus their approach to risk management on the *threat* by targeting those who are likely to commit such offences. Governments and engineers can focus on *vulnerability* by improving the blast resilience of structures and other targets. Finally, first responders can maximise the effectiveness of disaster response by having tools capable of simulating the *consequences* of a given attack. This information can lead to better preparedness in the event that such an attack happens.

5.2.3 Modelling terrorism risk

Large corporations with a high risk of losing global assets from terrorism will arrange for insurance cover as part of their insurance policy via an insurance broker. The

broker will arrange for primary cover through the insurance market. At this level, if the risks are complex, the broker or insurer may be using internal models to help price the policy. As a result of providing cover to many clients, the insurer may build up an aggregation of terrorism risk which puts their business under threat in the event of a major event. To mitigate this, the insurer will arrange for reinsurance which will compensate them in the event of a major event with large losses.

At the reinsurance level, the scale of losses is very high and reinsurers and brokers require detailed risk modelling for the pricing of premiums and the holding of capital reserves. To achieve this, reinsurers typically outsource the task of risk modelling to external catastrophe modelling companies. However, some of the major reinsurers have in-house modelling capabilities. In the market today, there are six main agencies delivering models to the market: the three catastrophe modelling companies RMS, AIR and EQECAT (now CoreLogic); and the reinsurance brokers Aon Benfield, Guy Carpenter and Willis.

The models used by these companies have continually evolved with the changing face of terrorism since their inception in 2002. At their heart are three main techniques used to model risk: *probabilistic modelling*, *exposure concentration analysis* and *deterministic modelling*.

Probabilistic modelling

Probabilistic modelling allows the insurer to predict the likelihood and severity of a range of different types of attacks, ranging from conventional bombs and aeroplane crashes to chemical and nuclear attacks. Compared to natural disasters, terrorist attacks occur relatively infrequently and evolve rapidly. This makes it difficult to look at historical patterns of terrorism to devise future estimates of attacks.

Instead, risk modelling agencies use the subjective judgements from a range of experts from law enforcement, defence and government agencies. The Delphi method, an approach developed by the RAND corporation during the Cold War, uses a questionnaire where the anonymised responses are recirculated between respondents. These experts are allowed to change their mind in light of previous responses, before eventually agreeing on a prediction. The likelihood of attack modes, target types and target locations are then agreed upon.

Probabilistic modelling enables insurers to estimate the probability of loss for a wide range of potential attacks, including those events that have not previously been considered. However, this approach is extremely subjective and despite expert opinion, reliable estimates of terrorism are very difficult to predict.

Exposure concentration analysis

Exposure concentration analysis identifies and measures the concentration of exposure around potential terrorist targets. Potential targets are usually taken from a landmark database or a high value location in an insurer's portfolio. A ring analysis is then performed, where a series of concentric circles are drawn around the target, representing gradually diminishing damage ratios. The aggregated exposure in and around various distances from the targets is then calculated. This gives the insurer a simple visual representation of where their main exposures accumulate.

This type of analysis is simple to perform and requires neither computational power nor a panel of experts. However, because the method does not take into account the effect of the geometry on the blast wave, the predictions are very approximate. Nor does the method predict any form of damage ratio, resulting in the calculation of total exposure rather than predicted loss.

Deterministic modelling

Deterministic modelling represents a compromise between the uncertainties of probabilistic models and the inaccuracies of exposure concentration analysis. By performing a 'what-if' analysis, a specific yet hypothetical scenario can be analysed with a higher degree of certainty. Typically an insurer would first perform an exposure analysis to determine where their highest concentration of exposure lies. This exposure could be very large, necessitating a more detailed analysis of the risks to avoid over or underestimating the loss potential. Once the location of the target is chosen, the insurer runs a series of studies using a range of common weapon types. Each study indicates the estimated financial loss arising from that particular event.

The techniques used to estimate these losses are more complex than an exposure concentration analysis. The complexity varies greatly, ranging from simple analytic models to expensive 3D CFD simulations. The most commonly used method is a concentric circle analysis in which an attack hazard footprint is used. The footprint specifies a damage level as a function of the location from the centre of the attack site. The size of the footprint can vary depending on the size of the weapon, varying from a hundred square metres for a small bomb to several hundred square kilometres for a nuclear attack [154].

Figure 5.5 illustrates the use of the concentric ring model for a hypothetical urban explosion scenario. The shaded circles represent different damage levels which decrease with increasing distance from the bomb location. The blue dots represent the locations of the insurer's properties. Each property is assigned a damage ratio accordant with the zone in which it lies. A measure of total building loss (TBL) can

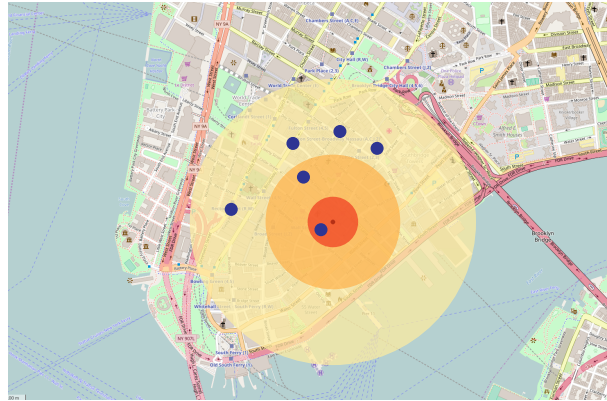


Figure 5.5: An example of a concentric ring analysis for a hypothetical attack in New York City. Each of the blue dots represents an insured location [159].

then be calculated for the portfolio.

Concentric circle analysis is computationally inexpensive, enabling insurers to test large permutations of different attack types. However, the approach is extremely inaccurate in urban areas because the effects of multiple building geometries are not taken into account. In fact, because of the effect of buildings, we expect a greater severity of damage to the buildings in the immediate vicinity of the blast and a lower severity of damage to the buildings further away. This leads to an overestimation of loss far from the blast and an underestimation of loss near the blast.

The vertical effects of the blast are also ignored. It is well known that the strength of the blast wave diminishes with increasing height. For a tall building, this could result in significant damage to the lower floors while the upper part remains intact. A circular model would ignore this.

Improvements have been made to concentric circle models to take the surrounding urban density into account. The catastrophe modelling company AIR has developed a radial damage function that can change shape depending on an ‘urbanicity’ factor that varies from an open area to a dense urban canyon [160]. As the building density of the location increases, the damage levels of the circles are altered to skew damage towards the blast epicentre. This leads to an improvement in the prediction of damage but neglects the complex wave interactions in streets that are key to accurately modelling damage. Additionally, these methods are only valid on the ground and, in contrast with CFD, they cannot predict damage to higher floors of the buildings.

The most accurate and complex deterministic modelling approach is the use of computational fluid dynamics (CFD) simulations. In this approach, the physical equations governing blast wave propagation are solved numerically in a 3D representation of the cityscape. This approach is significantly more expensive than the use of concentric circles, but offers a much greater degree of accuracy as the interaction between the blast wave and the urban environment is implicitly captured.

As we have mentioned in the preceding chapters, the propagation of blast waves in urban areas can create highly localised effects because of channelling and reflections from individual buildings. An insurer's portfolio is also highly localised. Therefore, to adequately model the damage from an urban explosion it is necessary to take into account the complex propagation of the blast wave, something that concentric circle analysis simply cannot do, no matter how well urbanicity is taken into account.

Today in the risk modelling market, concentric circle analysis remains the predominant form of deterministic analysis due to its simplicity and speed. However, there is a growing awareness in the industry of the shortcomings of these methods and some companies (notably RMS and Aon Benfield) are adopting CFD techniques. However, uptake is slow and many firms are still using simple inaccurate models [16].

Relatively little published research exists in the field of deterministic CFD loss models for the insurance industry. In their paper, Stoltz et al. presented a deterministic CFD approach to modelling property loss resulting from a bombing in an American city. The authors performed a simulation of an urban explosion in San Antonio, Texas and measured the overpressures on the faces of the city buildings. A loss model was used which mapped the overpressures to property damage and the resulting financial loss. The authors presented an integrated methodology for mapping the physics of the blast to an estimate of financial loss.

The authors demonstrated a viable approach to loss estimation. However, there was no discussion of the accuracy of CFD with respect to other models. We propose to study this to understand how estimates of human loss, property loss and business interruption vary between simple concentric and CFD modelling approaches. If the improvement in accuracy is significant, it could motivate those in the industry who are reticent of CFD techniques to adopt such methods.

5.3 Blast wave clearing

When a blast wave impinges upon a solid structure, reflected pressures are produced on the surface. Because of the finite size of the structure, a rarefaction or clearing wave forms that propagates inwards from the edges and relieves the pressure from

the front face. This phenomena is termed *blast wave clearing* and is the simplest and most common type of wave-structure interaction observed in urban areas. During clearing, the interaction of the blast wave with the structure can lead to a large variation in pressure and impulse around the object. Because of this, it serves as a useful investigation into how urban geometry influences the distribution of blast resultants and the resulting damage.

In this section we will perform a study of a simple blast clearing experiment. We will validate the code against this type of wave interaction and analyse how the placement of a solid structure affects the distribution of blast resultants within its vicinity. We repeat the experimental study of Rose and Smith [70], in which the authors performed a series of 1/10 scale blast wave clearing experiments, supplementing the results with a numerical study using the code Air3d. The code is a computational fluid dynamics package that uses a variant of the Advection Upstream Splitting Method (AUSM) with the MUSCL HANCOCK method, solving the Euler equations in 1D, 2D and 3D [70]. Air3d also has the ability to model mesh-aligned geometries.

The experimental setup is shown in figure 5.6. A 23.7 g Demex 100 charge was located a height of 0.1 m above an 8 mm steel plate. A Pendine block was situated 1.5 m from the explosive and mounted with four pressure gauges as shown in the figure. Gauges G1 and G2 were mounted on the front face of the block and recorded the reflected pressures. Gauge G4 was positioned a small distance from the block at the same radial distance from the charge as G1 so as to record the incident pressure. Gauge G3 was mounted on the rear of the block. Smith and Rose assumed a TNT equivalence of 1.15 for Demex 100. This corresponds to a charge mass of 27.26 g of TNT.

The approach taken in the numerical study was to exploit the symmetry of the problem in order to maximise computational efficiency. The first stage of the simulation involved a one-dimensional spherical analysis up to a distance of 0.1 m when the wave made contact with the steel plate. The charge radius was 16.0 mm and necessitated a resolution of approximately 0.3 mm if 50 cells were to be maintained across the charge radius. Due to the small domain length, this posed no significant computational expense so a resolution $\Delta r = 0.2$ mm was chosen instead.

The next stage of the analysis involved a two-dimensional axisymmetric study. A domain measuring $x = 1.5$ m by $y = 1.5$ m was used, allowing the problem to be evolved up to the time when the blast wave reaches the block. In chapter 4, we recommended a resolution of $1 \text{ cm/kg}^{1/3}$ once the blast wave has fully developed. For the Demex 100 charge, this corresponded to a cell size of 3 mm. Due to the lack of computational expense we chose a cell size of 2 mm, comfortably within this figure.

The axisymmetric solution was run until a time of 2.3 ms and mapped into a

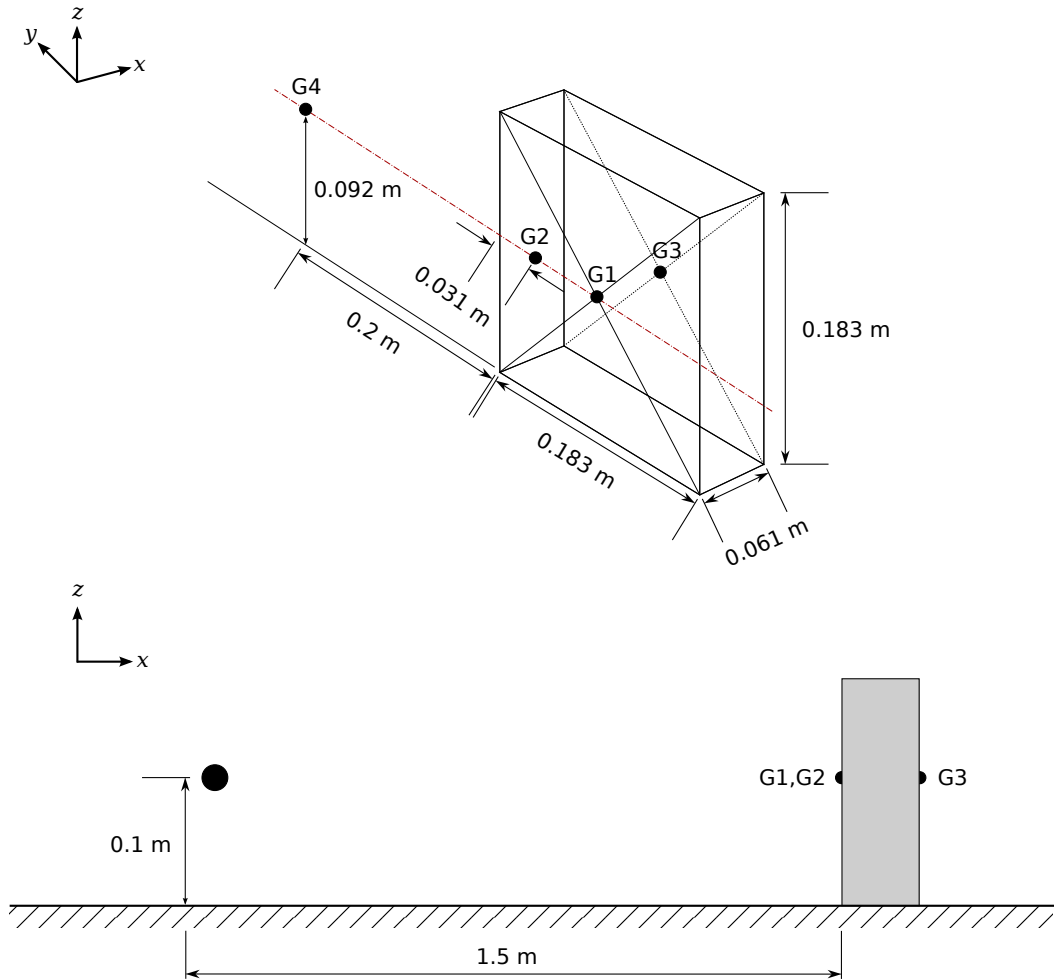


Figure 5.6: Details of the test structure for the blast wave clearing scenario, showing the locations of the four gauges (top). A schematic of the experimental configuration showing the Demex 100 charge, the test structure and the gauges is shown below.

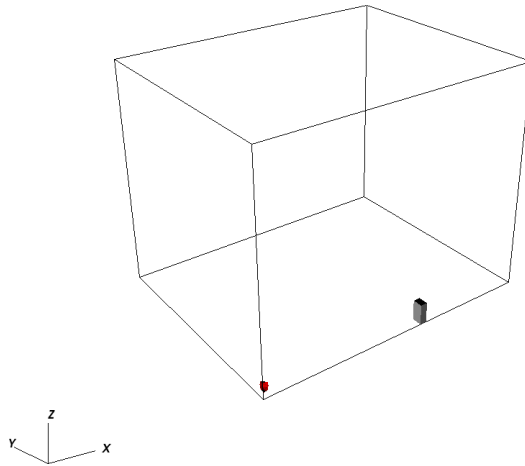


Figure 5.7: The three dimensional domain for the blast wave clearing scenario, in which a solid block (shown grey) is impinged upon by a blast wave from a TNT charge (shown red). The computational domain shows the experimental setup in quarter space.

three-dimensional quarter model of the problem. Figure 5.7 shows the full extent of the domain, in which the charge and half of the Pendine block are visible. The domain was 2.52 m along the x axis. The transverse lengths were chosen to be 2 m to ensure that interactions with the boundaries could not affect the solution at the gauges. Reflective boundaries were imposed at the planes of symmetry and ground at $x = 0$, $y = 0$ and $z = 0$. Transmissive conditions were imposed at the remaining boundaries.

The recommended resolution of 3 mm was impractical for the 3D simulation. Instead, a mesh sensitivity study was performed with three cell sizes: 10 mm, 20 mm and 40 mm. The peak overpressure at gauge G1 was recorded and is presented for each of the resolutions in figure 5.8. The experimental results are also shown for comparison. Reasonable convergence is observed for the primary peak, and the solution recorded with the 10 mm cell size is acceptably close to the experiment. This resolution was found to offer a reasonable balance between accuracy and cost and was used for the following study.

5.3.1 Results

A pressure schlieren is shown in figure 5.9 at $t = 3.05$ ms along the line of symmetry at $y = 0$. The diffracted wave is shown clearing the block. The reflected wave can be seen moving in the opposite direction. Also visible is the weaker secondary shock which has not yet made contact with the block. In the $y = 0$ slice of the same figure

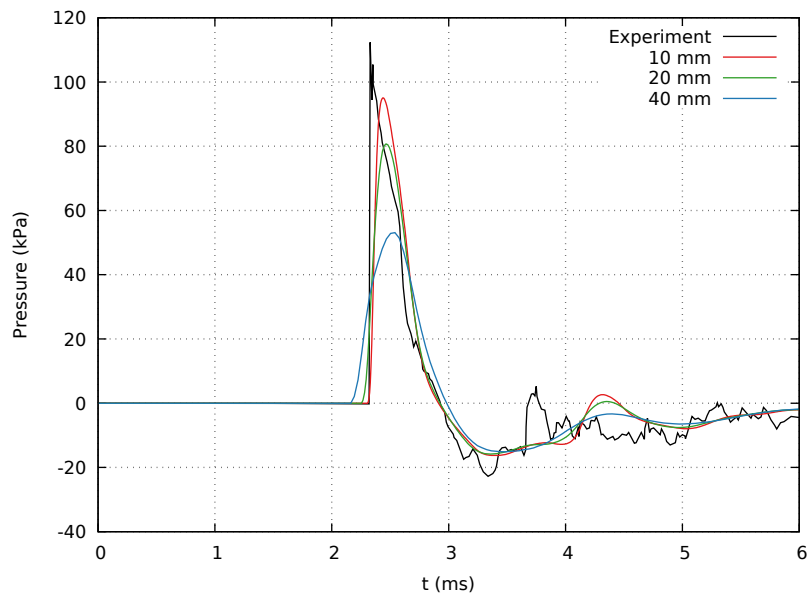


Figure 5.8: Comparison of overpressure for 3D cell sizes of 10, 20 and 40 mm for the CFD simulation (gauge G1).

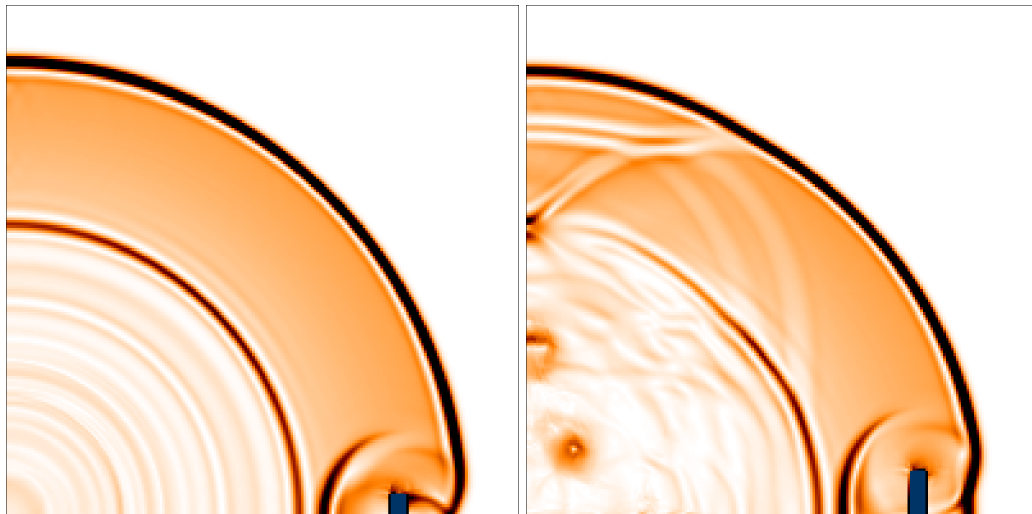


Figure 5.9: Pressure schlieren for the blast wave clearing scenario in which a solid block is impacted by a blast wave from a TNT equivalent charge. The reflected and diffracted waves are observed in the slices taken on the ground at $z = 0$ (left) and at $y = 0$ (right) ($t = 3.05$ ms).

we identify a slight bulge at the top of the primary blast wave which is composed of the primary and ground reflected waves since the charge was detonated above the ground. Also observable in the bottom left hand quarter are a series of weak pressure fluctuations that have occurred as a result of wave interactions between the ground reflected and incident shocks. The left image of figure 5.9 shows further weak fluctuations in the form of concentric circles. These are numerical artefacts from the process of mapping the axisymmetric solution into the 3D domain.

The left column of figure 5.10 shows the overpressure histories at gauges G1, G3 and G4 throughout the experiment. The experimental data is shown along the simulation and the Air3d analysis. The first, strong peak corresponds to the primary wave which is followed in each reading by the weaker secondary wave visible in figure 5.9.

For the first shock wave there is generally very good agreement with the experiment and results from Air3d. Timings and peak heights are closely matched. Neither the simulation nor the Air3d results capture the secondary peak well. At the front gauges G1 and G4, the height of the peak is captured correctly but the timing is incorrect. The secondary peak at the rear gauge G3 is not captured at all by the simulations. This is a very weak shock relative to the primary wave. It needs a proportionally higher resolution to be resolved correctly and a cell size of 10 mm is insufficient. We do not consider this a problem as we are only concerned with the primary shock which makes by far the greatest contribution to the structural damage. Overall, the accuracy of the simulation is good and the results demonstrate the ability of the code to capture this type of blast-structure interaction.

The simulation was repeated in an identical manner but without the Pendine block. The blast wave was allowed to propagate unimpeded and the resulting overpressure was measured at each of the gauge locations and was termed the *free-field* pressure. The pressure histories are presented alongside the results from the clearing study in the right column of figure 5.10. The two datasets demonstrate the effect that the block has on the blast wave resultants.

At the front gauge G1 we see that the effect of the block is to raise significantly the pressure on the front face. The small surface area of the block means that clearing rapidly relieves the pressure, which quickly drops below the free-field result. Overall, peak pressure is increased by approximately 120%. Despite the shorter positive phase duration, impulse is increased by about 60%. At the rear gauge G3, the main difference between the free-field and clearing histories is the timing of the waves. In the clearing scenario, the signal is delayed by the time taken for the diffracted wave to pass around the structure and reach the gauge. In our case, this delay is approximately 0.3 ms. The clearing peak pressure is only 15% lower than the free-field

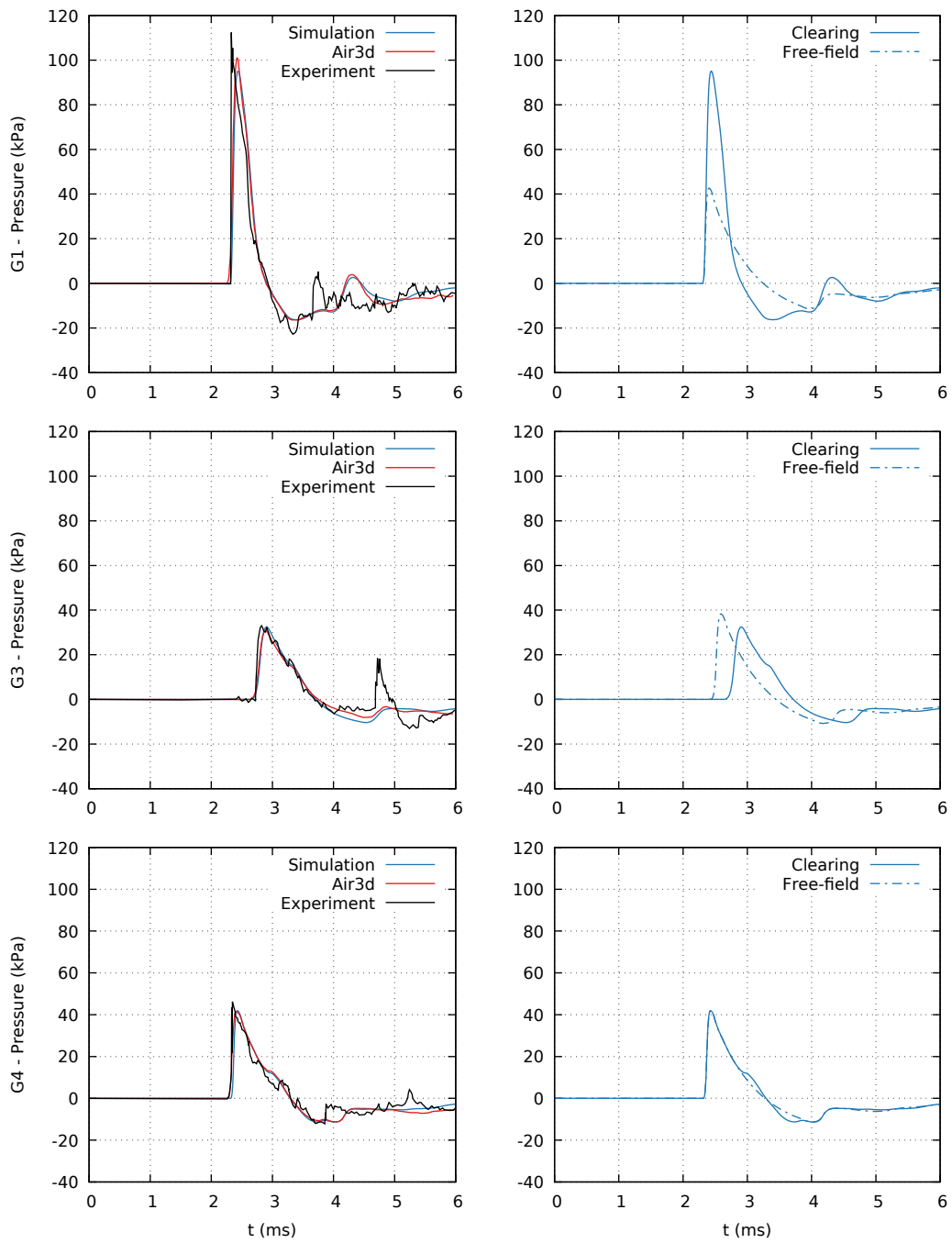


Figure 5.10: Pressure histories at gauges G1, G3 and G4 mounted on the solid block which is impacted by a blast wave from a TNT source. Results are shown for the numerical simulation, experiment and Air3d analysis (left column). Obstructed and free-field pressures are also shown for the numerical simulation (right column).

pressure. The difference in impulse amounts to less than 1%. This suggests that, while the block has a large effect of increasing the strength of blast resultants on the front face, it provides minimal shielding protection to anything located behind the structure. This is because of the small surface area of the block which allows the blast wave to rapidly diffract around the object. Gauge G₄, which was placed a small distance away from the block, but at the same radial distance from the charge as G₁, indicates little difference between the clearing and free-field pressures. The clearing wave shows a small secondary wave that appears during the expansion phase of the primary wave. This is a reflection that occurs when the primary wave makes contact with the block.

An estimate of glazing damage can be obtained by using a pressure-impulse curve for annealed glass from the US Department of Defense report [143]. The report provides a series of pressure-impulse iso-damage curves for a range of different glazing types. For each glazing type, a number of iso-damage curves are presented, each representing the percentage probability of glass breakage for a given combination of pressure and impulse. The blast resultants indicate that, at the front face of the block, we expect a 50% probability of glazing damage. On the rear face, the effect of shielding results in a probability of approximately 20%. This is a significant difference and demonstrates how the interaction of the blast wave with an object can produce a highly variable distribution of damage.

5.3.2 Comments and conclusions

In this section, we performed a numerical validation study of a simple blast wave clearing experiment. The purpose of the analysis was to validate the code against a common type of urban wave-structure interaction and to study how simple urban geometry can influence the distribution of blast damage compared to the free-field. We measured the overpressure at three gauge points located around a solid cuboid structure. The simulation solution closely matched the experiment and demonstrated the code's ability to capture this kind of phenomenon.

Measurements of blast resultants around the block showed that the effect of the block structure was to increase the peak pressure and impulse at the front face by 120% and 60% respectively. At the rear, the small surface area of the block was found to have little effect on the resulting wave. Using US Department of Defense iso-damage curves, we showed that the probability of glazing breakage on the structure was found to be 2.5 times higher at the front face compared to the back. This demonstrates how the interaction of a blast wave with a simple urban structure can significantly alter the distribution of blast resultants compared to the free-field. The

distribution is no longer related solely to the distance from the charge and can only be predicted accurately by solving the underlying equations governing the physics of the problem. Having validated the code and demonstrated the effect of urban geometry at a simple level, we continue by considering a more realistic scenario involving multiple buildings.

5.4 Clearing and channelling in city streets

In most cases, real urban explosions involve the interaction of the blast wave with multiple buildings rather than the single, isolated obstacle used in the previous study. The streets that form cities not only protect structures in their locality through shielding, they also confine and channel blast waves. In this study we extend the realism of the problem by considering the effects of channelling in addition to clearing. The results of the numerical study provide an understanding of how urban geometry can influence the distribution of blast resultants.

Figure 5.11 shows the setup for the study. The existing 3D computational domain is expanded to measure 3.08 m along the x axis and 3 m in the transverse directions. The same 27.26 g TNT equivalent charge is used, detonating from the same height above ground. The Pendine block is extruded along the y axis and duplicated to form four evenly spaced rows which extend along the extent of the domain. These represent four rows of terraced buildings forming three confined streets. If the charge were scaled up to a 2 t lorry bomb, this would correspond to a row of two-storey buildings of approximately 8 m height separated by a road measuring 5 m wide. Within the centre of each street is located a line of gauges at a height of $z = 0.092$ m and spaced at 10 mm intervals. The line extends from the edge of the domain (and line of symmetry) at $y = 0$ to $y = 1.5$ m.

The standoff between the charge and the first row is unchanged. The same spherical and axisymmetric analyses were performed and mapped into the three dimensional simulation. The same boundary conditions are also used, maintaining the quarter space approach. Figure 5.12 shows the full extent of the domain, in which the charge and four terraces are visible.

Since the domain was expanded, a new mesh sensitivity study was undertaken. A simulation without the geometry was performed and the overpressure at the furthest gauge line from the charge (GL3) was recorded at $y = 0$. The results are shown for three cell sizes in figure 5.13: 10 mm, 20 mm and 40 mm. No experimental data exists at this point. The overpressure predicted by the Kingery Bulmash equation is shown instead. Good convergence is observed and the solution at 10 mm is within 10 % of

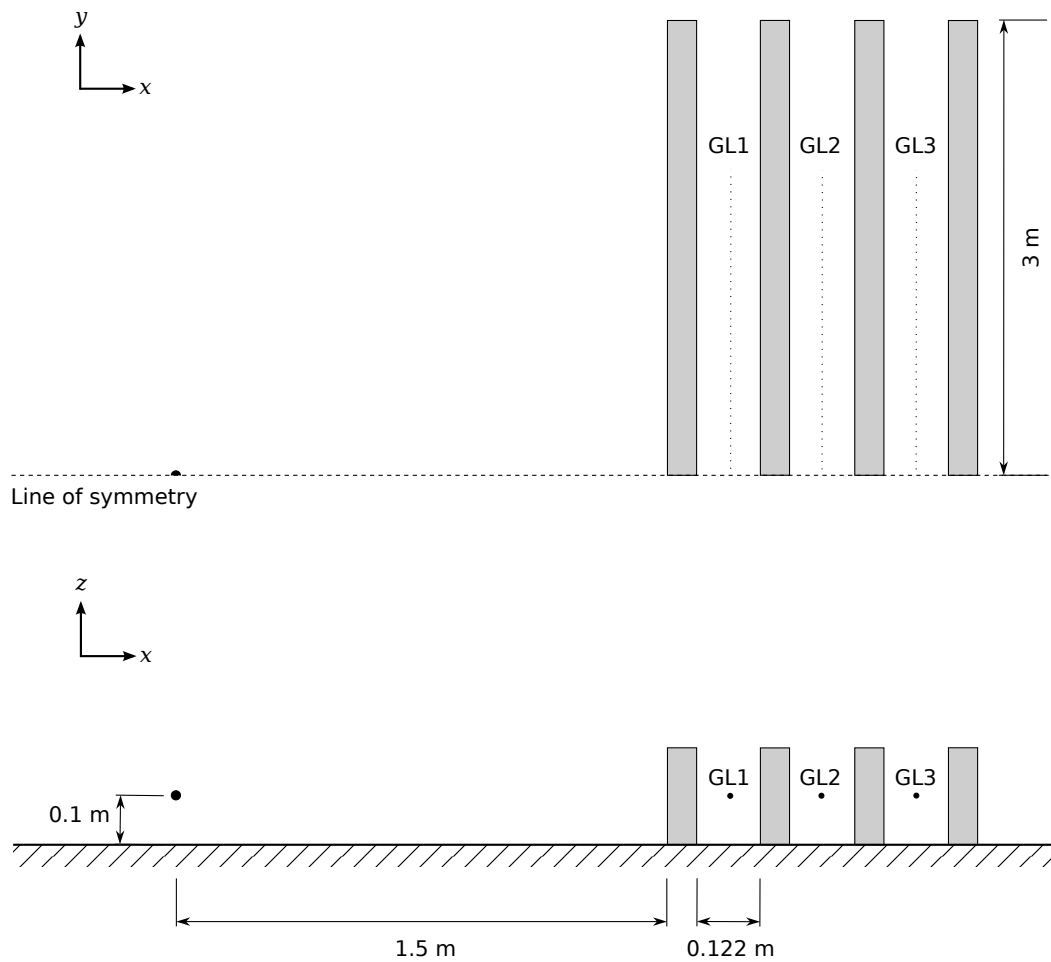


Figure 5.11: Two views of the test structures showing the locations of the charge and three gauge lines GL1, GL2 and GL3 for a scenario in which a simplified urban layout of straight streets is impacted by a blast wave from a TNT source. The test structure from the previous study is extruded and duplicated to form three streets.

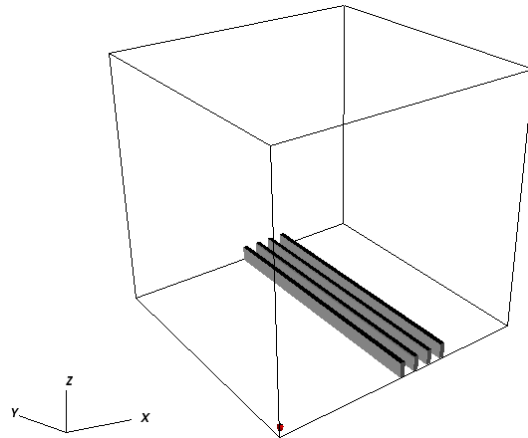


Figure 5.12: The three dimensional domain for the city street scenario, in which buildings forming a simple street configuration (shown grey) are impacted by a blast wave from a TNT source (shown red). The computational domain shows the experimental setup in quarter space.

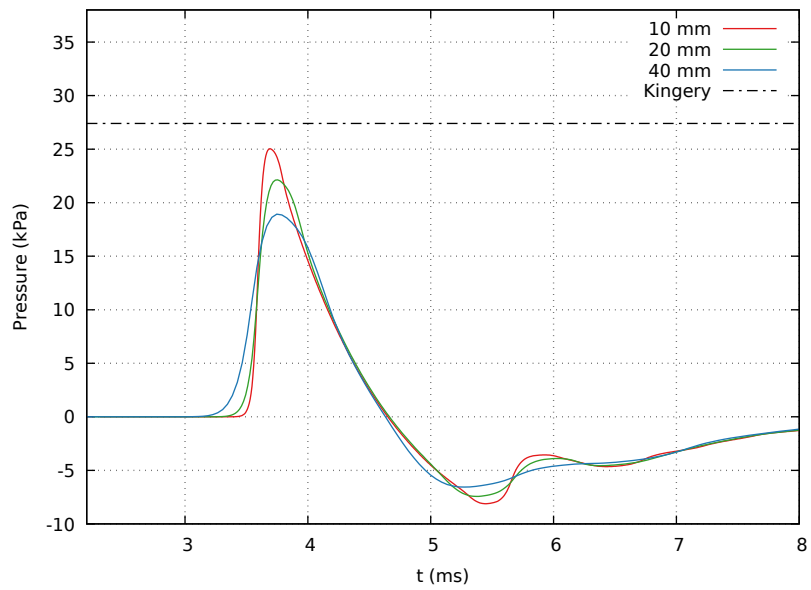


Figure 5.13: Comparison of overpressure histories at the furthest gauge line (GL_3) at $y = 0$ for 3D cell sizes of 10, 20 and 40 mm for the CFD simulation. The analytic prediction from the Kingery Bulmash scaling curves is shown dashed.

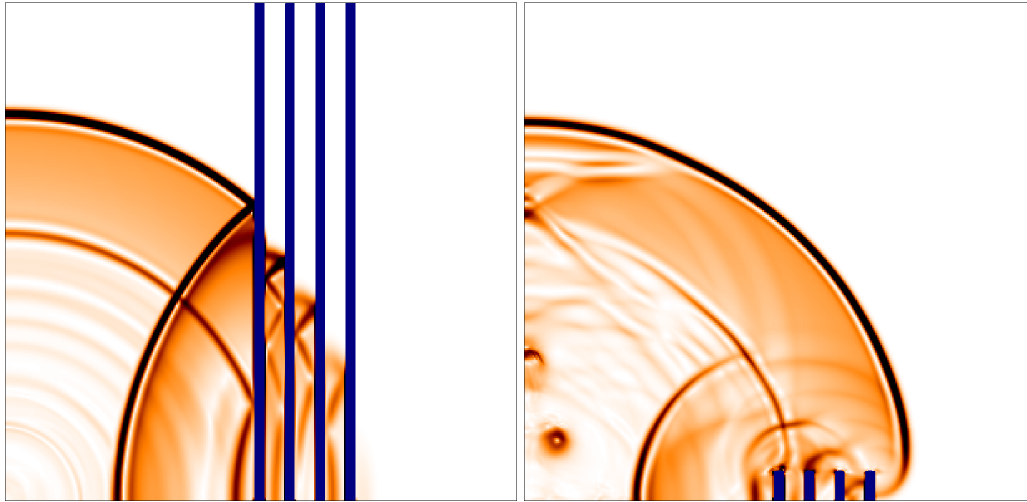


Figure 5.14: Pressure schlieren showing the wave channelling along the streets on the ground at $z = 0$ (left). A slice at $y = 0$ is also displayed (right) showing the primary, diffracted and reflected waves at $t = 4.5$ ms.

the analytic prediction, indicating that the cell size is sufficient.

5.4.1 Results

Figure 5.14 shows a pressure schlieren at the ground level and along the axis of symmetry. The effect of the streets is to produce a more complex network of waves when compared with the previous study. The right side of figure 5.14 shows four separate reflected waves produced from the interaction of the primary wave with the four rows. A diffracted wave is also observed propagating downwards from the row furthest from the charge.

The situation at the ground shows the reflection of the primary and secondary waves from the first row. A complex network of reflections is observed moving along the streets. These channelled waves are formed from the reflection of the diffracted wave off the buildings that line the street. Successive reflections occur and are confined within the street by the tall buildings, maintaining their strength and forcing them to propagate along the street. Because of this effect, the channelled waves remain stronger over distance than the unconfined waves. The only significant reduction in strength comes from vertical clearing over the top of the buildings.

To better understand the influence on the geometry on the nature of the blast wave, we define the following amplification factors AF_p and AF_f for pressure and

impulse respectively:

$$AF_P = \frac{P_c}{P_f}, \quad AF_I = \frac{I_c}{I_f}. \quad (5.11)$$

The *clearing* pressure or impulse recorded at each gauge (P_c or I_c respectively) was divided by the equivalent quantity from a simulation in which the geometry was removed and the solution resembled a *free-field* explosion (P_f or I_f). The amplification factors make it easier to understand the effect that the geometry has on the blast wave: an amplification factor of 1 indicates that the geometry has had no effect on the blast resultant. A factor below 1 indicates that the geometry has had the effect of weakening the blast resultant below the free-field strength.

This amplification factor is plotted along each of the three gauge lines in the study and is shown in figure 5.15 for peak overpressure (top) and impulse (bottom) as a function of scaled distance Z , where $Z = 0$ represents the gauge line at the axis of symmetry $y = 0$. In the discussion that follows we refer to this point as the centre of the gauge line. Because of the axis of symmetry, the gauge line is reflected across the plane at $y = 0$.

At the centre of the gauge line, the pressure amplification is below 1, indicating that the effect of the buildings has been to reduce the peak pressure observed in the streets through the shielding of the blast wave. For streets further away from the blast, the effect is more profound and the reduction in peak pressure approaches 40%. As one moves along each street, the pressure amplification factor increases. By $Z = 5$, this factor has exceeded 1 for the front street, implying that the peak pressure exceeds the free-field. This finding would be surprising if the only effects occurring were shielding and clearing.

The same factor for impulse shows a similar trend, except that the amplification factor is greater than 1 in all cases. At its lowest value in the third street, the geometry is shown to increase the recorded impulse by over 30%. This compares to a reduction in peak pressure of almost 40%. These findings can be explained by studying the pressure histories at the gauges. Figure 5.16 shows these histories from two gauges within the closest street to the charge (street 1) at either ends of the gauge line. Both charts show the signal from the clearing and free-field simulations, with the top and bottom charts representing gauges at $Z = 0$ and $Z = 5$ respectively.

The centreline gauge at $Z = 0$ shows the formation of a coalesced wave created from the multiple reflections that occur as the diffracted wave makes contact with the street structure. The diffracted wave is observed as the first peak and is weaker than the successive reflected waves and significantly weaker than the free-field wave. This coalesced wave is channelled along the street. Because of the confinement, its strength diminishes more slowly than the free-field wave. Eventually, at the end of

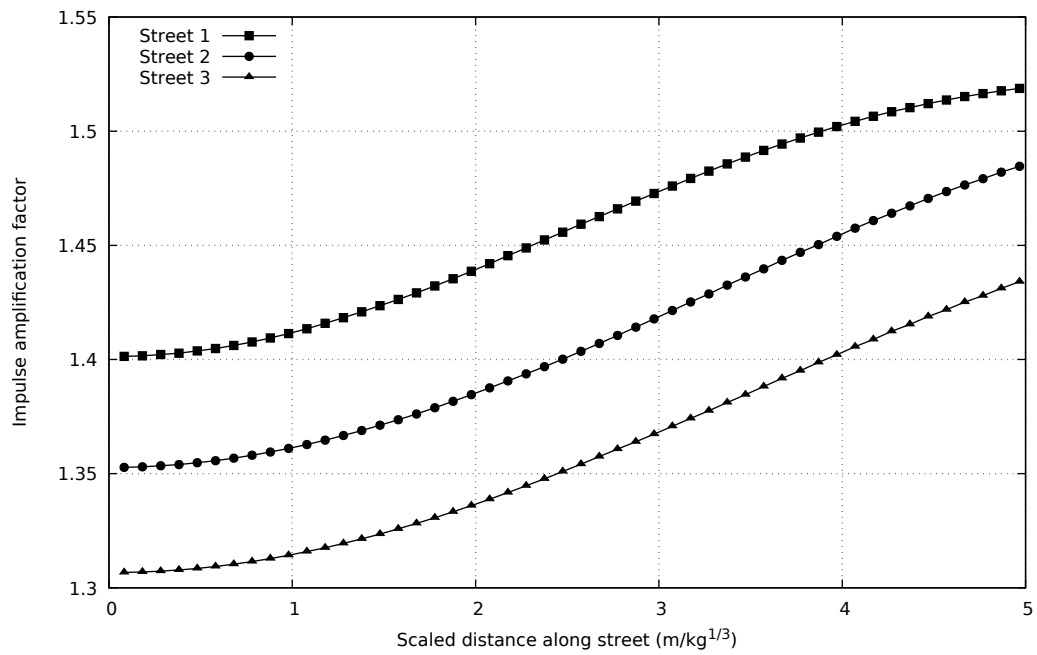
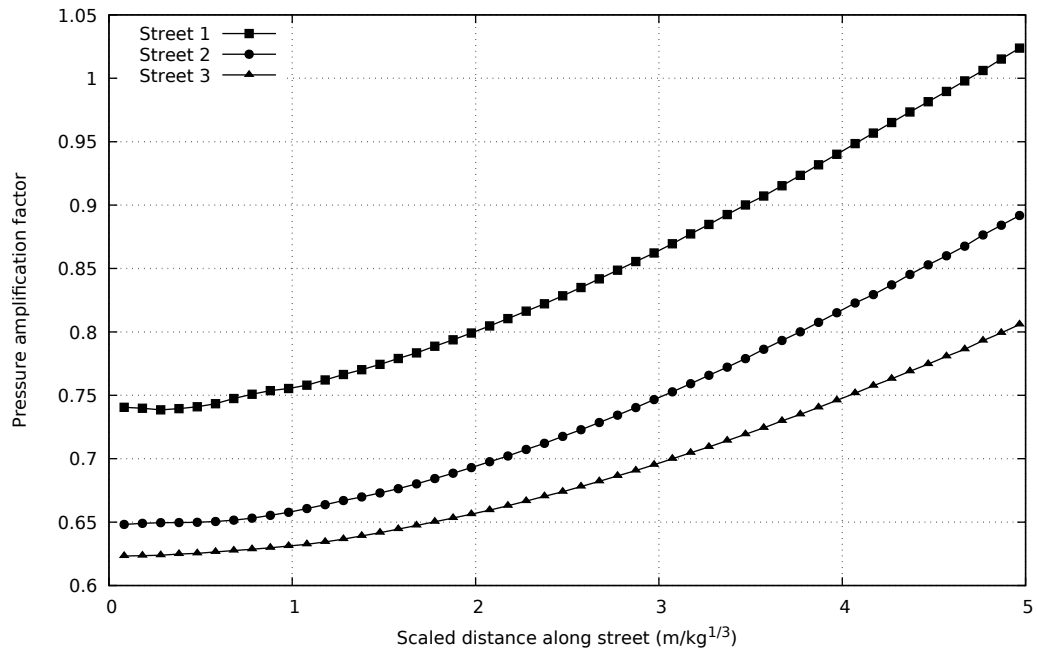


Figure 5.15: Pressure and impulse amplification factor measured along each of the three streets for the city street scenario.

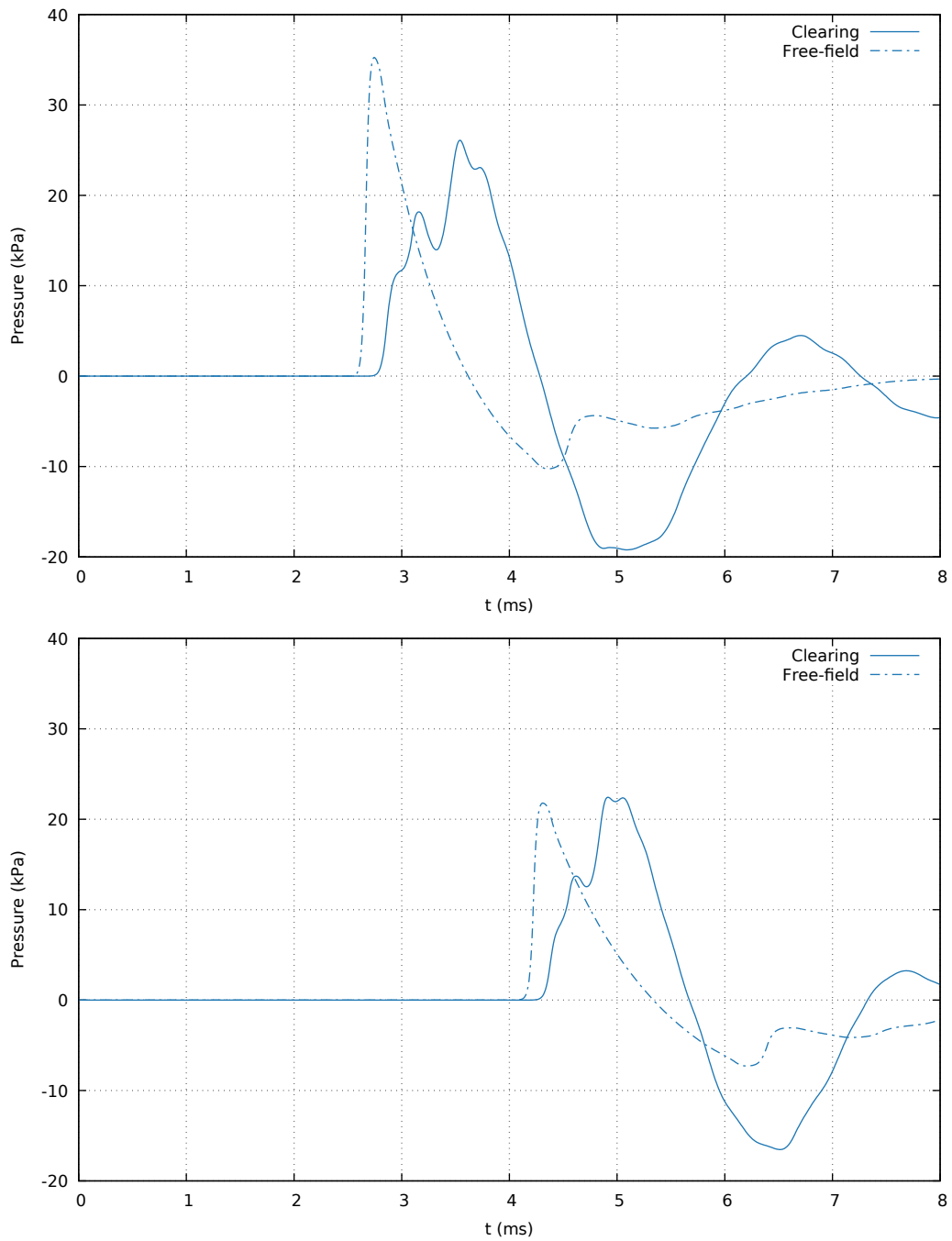


Figure 5.16: Pressure histories from two gauges in street 1 for the *clearing* and *free-field* simulations. The top gauge is located along the charge centreline at $Z = 0$. The bottom gauge is located at the end of the array at $Z = 5$.

the gauge row at $Z = 5$, the pressure of the channelled wave exceeds the free-field wave. This explains the observed trend of the pressure amplification factor. The impulse amplification factor can also be explained by noting that the clearing wave is formed from a series of coalesced reflections, leading to a prolonging of the positive phase and a corresponding increase in impulse compared to the free-field.

The significance of these results is that the proportional change in the strength of blast resultants from the inclusion of a geometry bears little relation to the distance from the charge. We have shown that it is the region of the street further away from the blast where the geometry has led to the greatest proportional increase in the strength of blast resultants. At the centreline, the result is mixed, with a reduction in pressure and an increase in impulse. These results occur because of the combined effects of channelling and shielding which have opposing effects on the blast wave.

5.4.2 Comments and conclusions

In this section we extended the previous numerical study to investigate the type of blast-structure interaction that occurs in simplified city streets. The purpose of the analysis was to extend the complexity of the previous study to understand how typical urban geometries influence the distribution of blast resultants. Measurements of pressure and impulse within the streets showed that the counteracting effects of channelling and shielding led to proportional changes in the strength of the blast wave that were unrelated to the distance from the source. These findings are non-intuitive and are unobtainable with simpler empirical methods.

Having demonstrated the significance of these effects, we propose to increase the realism of the problem one step further to account for actual city streets. In the section that follows we will perform a similar study using urban geometry derived from a LIDAR dataset of a city. Our aim is to demonstrate that these effects remain significant in real-world streets and that CFD methods have the ability to capture them.

5.5 The effect of charge placement on blast wave resultants

We have demonstrated that simplified urban geometry has a significant effect on the propagation of the blast wave and the damage that ensues. In this section, we extend the study to account for realistic urban geometry in order to strengthen our argument. We also hypothesise that, because of the effect of urban layout on blast propagation, movement of the source of the explosion can result in a significant change to the distribution of blast resultants. We test this hypothesis through a

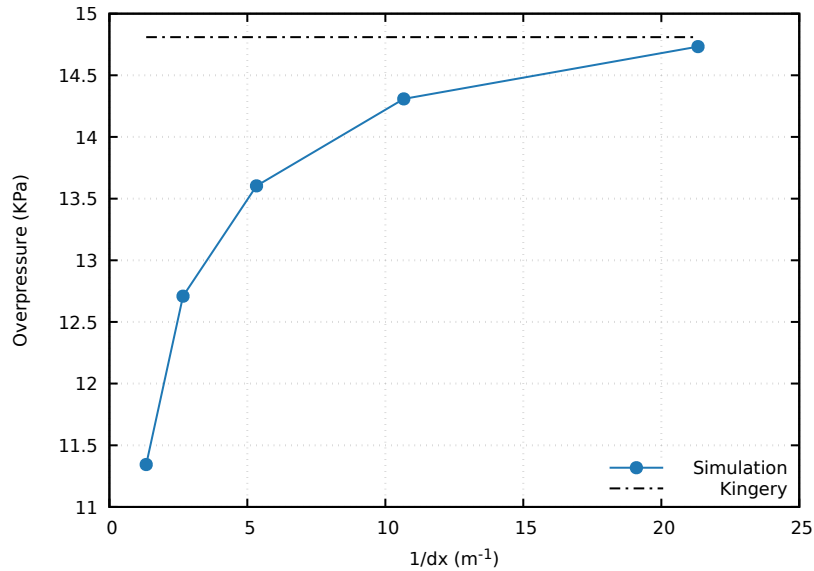


Figure 5.17: Peak overpressure against the reciprocal of cell size for 1000 kg of TNT in the free field.

numerical study of a hypothetical bombing in a city, in which we vary the charge location and record the differences in the strength of the blast wave in the vicinity of the explosion. We compare the results with an empirical model which does not take the geometry into account. The findings of the study form part of our argument for whether CFD methods are better suited to urban blast simulation than empirical methods.

As a first test, we consider a hemispheric, surface explosion of 1000 kg of TNT in the free field. A series of 2D axisymmetric simulations are performed in order to fix the cell size for the study. We wish to obtain the largest possible cell size that provides an acceptably converged pressure 100 m from the source. A range of cell sizes between 75 cm and 4.7 cm were considered.

Figure 5.17 shows the peak overpressure 100 m from the source with respect to the reciprocal of the cell size. The figure also presents the prediction from the Kingery & Bulmash model. The pressure is observed to converge towards a value slightly greater than the Kingery fit. We expect this because the Kingery model is based on surface burst experiments which implicitly capture the capacity of the ground to absorb some of the blast energy, reducing the peak pressure slightly. The CFD simulation, on the other hand, models the ground as perfectly reflecting.

The cell size of 37.5 cm produces an acceptably converged peak pressure that is

within 15 % of the Kingery prediction. In three dimensions, this corresponds to a domain containing approximately 265 million cells and approaches the limit of what is practicable with today's hardware. This cell size offers an acceptable balance of accuracy and computational cost and will be used in the subsequent study.

5.5.1 Urban park scenario

A hypothetical scenario was chosen involving the detonation of a truck bomb in a busy region of a city. A realistic urban layout was used in order to capture the effects of real world buildings on blast resultants. A 400×350 metre zone was chosen on the North West border of an urban park. This region is highlighted within the red box at the top of figure 5.18. The domain is shown in more detail in the bottom left sub-figure. Building outlines and heights were obtained from the Landmap Project shapefile dataset [40].

Two charge locations are considered: The first *unobstructed* case involves a 1000 kg charge placed on the road between the park and the bordering buildings. This charge represents a typical size used in similar attacks by the IRA. A second charge is located 50 m North of the first, on a road running parallel to the park. In this location, the source is surrounded either side by two blocks of flats. We call this the *obstructed* location. The two positions are shown in the bottom left of figure 5.18.

For each charge location, an empirical and a CFD method are used to predict the distribution of blast resultants in the park following the detonation of each charge. The predictions of both models are compared with one another to understand how an empirical method which does not capture geometrical effects compares with a CFD approach. By moving the charge only a small distance, we aim to demonstrate the effect of charge placement on blast resultants.

The empirical model used is based on the Kingery & Bulmash scaled blast parameters described in section 3.3 [6]. The CFD approach is described and validated in section 3.8. A 3D computational domain measuring $x = 400$ m across the park, $y = 350$ m by $z = 100$ m high was used. Three gauge lines (GL1, GL2 and GL3) were placed in the park at 50 metre intervals from the location of the unobstructed charge and are shown in figure 5.18.

5.5.2 Pressure contours

Figure 5.19 shows a two-dimensional contour plot of peak pressure for the two charge locations at $z = 2$ m, with colour ranging from light (lowest pressures) to dark (highest pressures). The top row shows the predicted distribution of peak pressures

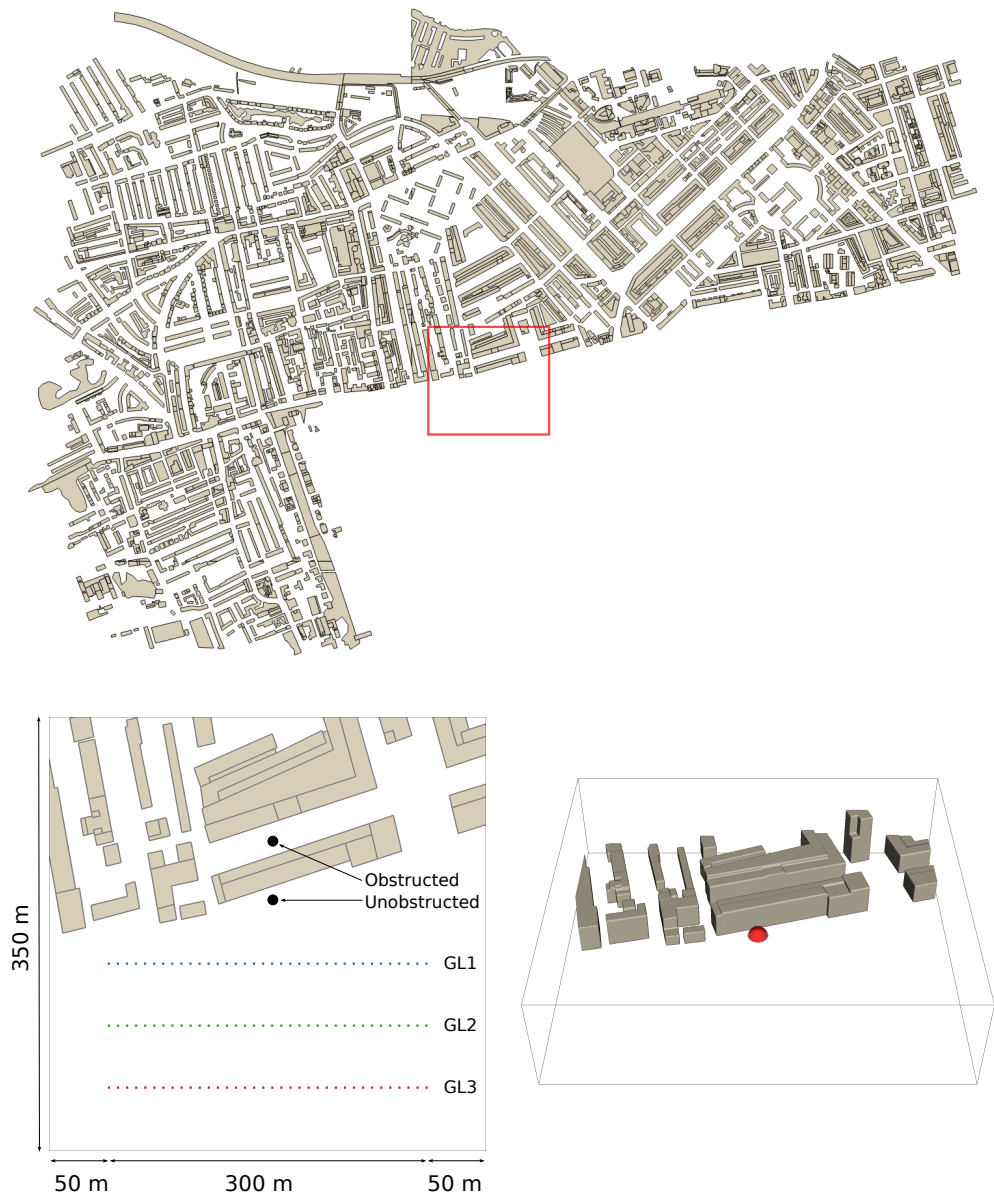


Figure 5.18: From top, moving clockwise: 1) a shapefile containing building outlines for the region bordering the urban park. The computational domain is highlighted in red. 2) A 3D representation of the computational domain with a contour showing the front of the blast wave for the unobstructed location at $t = 5$ ms. 3) A 2D representation of the domain showing the charge and gauge lines.

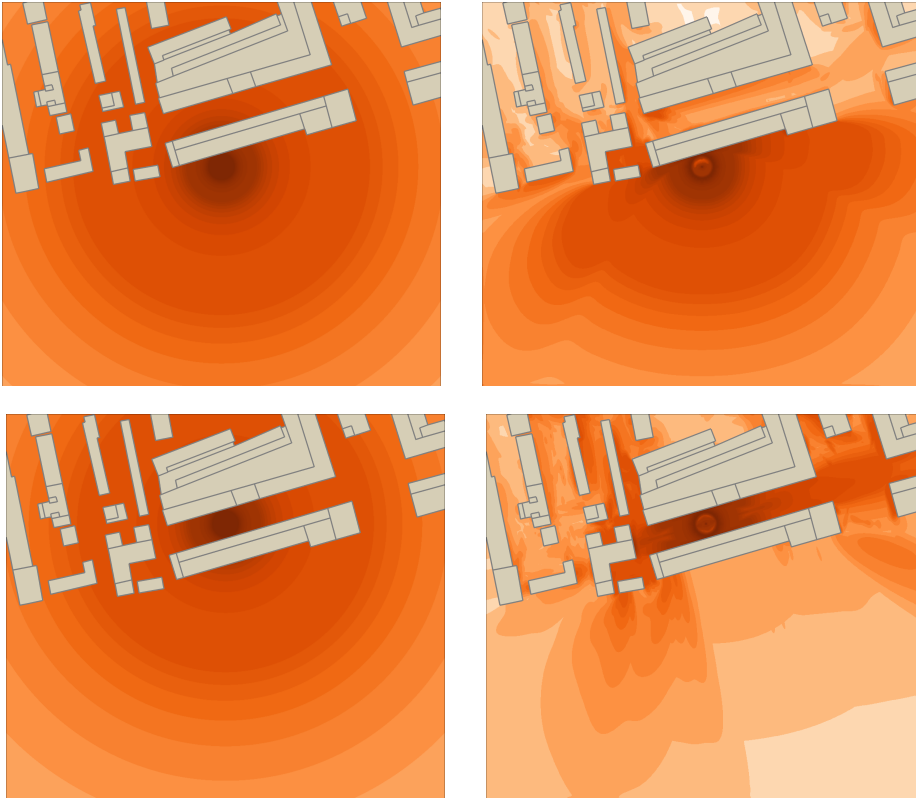


Figure 5.19: Overpressure contours at $z = 2\text{m}$ for the urban park bombing scenario. The empirical model is shown (left) with the simulation results from the CFD model (right). The unobstructed charge location is shown on the top row, indicating good agreement between the two methods for pressures within the park. When the charge is moved 50 m North to the obstructed location (bottom row), the predicted damage distributions diverge significantly.

from the empirical and CFD models for the unobstructed charge. In the region of the park, the empirical method appears to perform well at predicting pressure, closely matching the CFD model despite ignoring the effects of the geometry.

When the charge is displaced to the neighbouring street, a very different distribution is observed. The tall blocks of flats have a channelling effect on the blast wave. The majority of the blast wave energy is directed along the street and enters the park via the narrow streets on the West side of the domain. The effect of the building separating the park and source is to shield the blast wave, reducing the strength of blast resultants in the park.

In this case, the urban geometry has had a significant effect on the propagation of the blast wave. This is most evident when comparing the empirical and CFD predictions. The empirical method has not captured the localised effects of the blast and provides a poor prediction in this case.

5.5.3 Gauge analysis

The blast resultants recorded at the three gauge rows are presented in figures 5.20 and 5.21. The gauge arrays are coloured blue, green and red, in order of proximity to the charge. Figure 5.20 shows the peak pressure recorded across the array for the empirical (dashed lines) and CFD (solid lines) models. The unobstructed scenario is shown on top and the obstructed scenario shown below. The distance between the broken and solid lines represents the discrepancy between the two models' predictions.

When the charge is located next to the park a good agreement is observed. Both models predict a similarly shaped relationship between charge location and peak overpressure. The gauge closest to the charge records a pressure of 38.4 kPa for the CFD model and 43.2 kPa for the empirical model. A disparity of approximately 10% is observed for most of the gauges in the domain and is attributed partly to the influence of the cell size on the CFD simulation.

To quantify the difference between the two models, we define the following pressure amplification factor

$$AF_p = \frac{P_{\text{emp}}}{P_{\text{CFD}}}, \quad (5.12)$$

which is the ratio of the empirical and CFD pressure predictions. An amplification factor of 1 indicates an exact agreement between the two methods. An amplification factor of above 1 indicates an over-prediction by the empirical method relative to the CFD model.

The top chart in figure 5.21 shows the amplification factor for the unobstructed

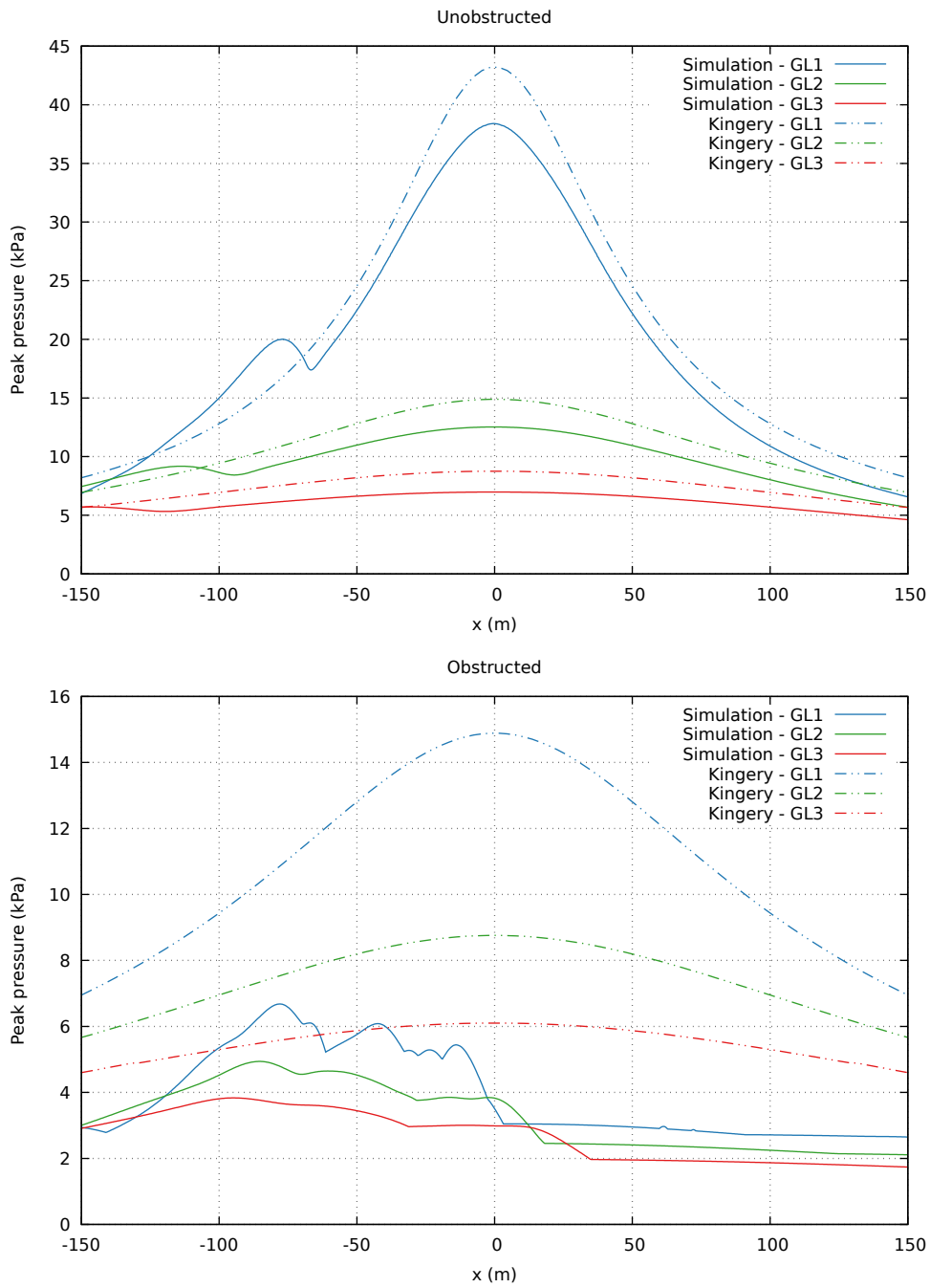


Figure 5.20: Recorded peak pressures at gauge lines GL1 to GL3 for the urban park scenario. Dashed lines indicate the predictions of the Kingery & Bulmash empirical model. Solid lines indicate the predictions of the CFD simulation. Separate graphs are presented for the two charge locations (note the difference in scale). The charge is located at $x = 0$ m.

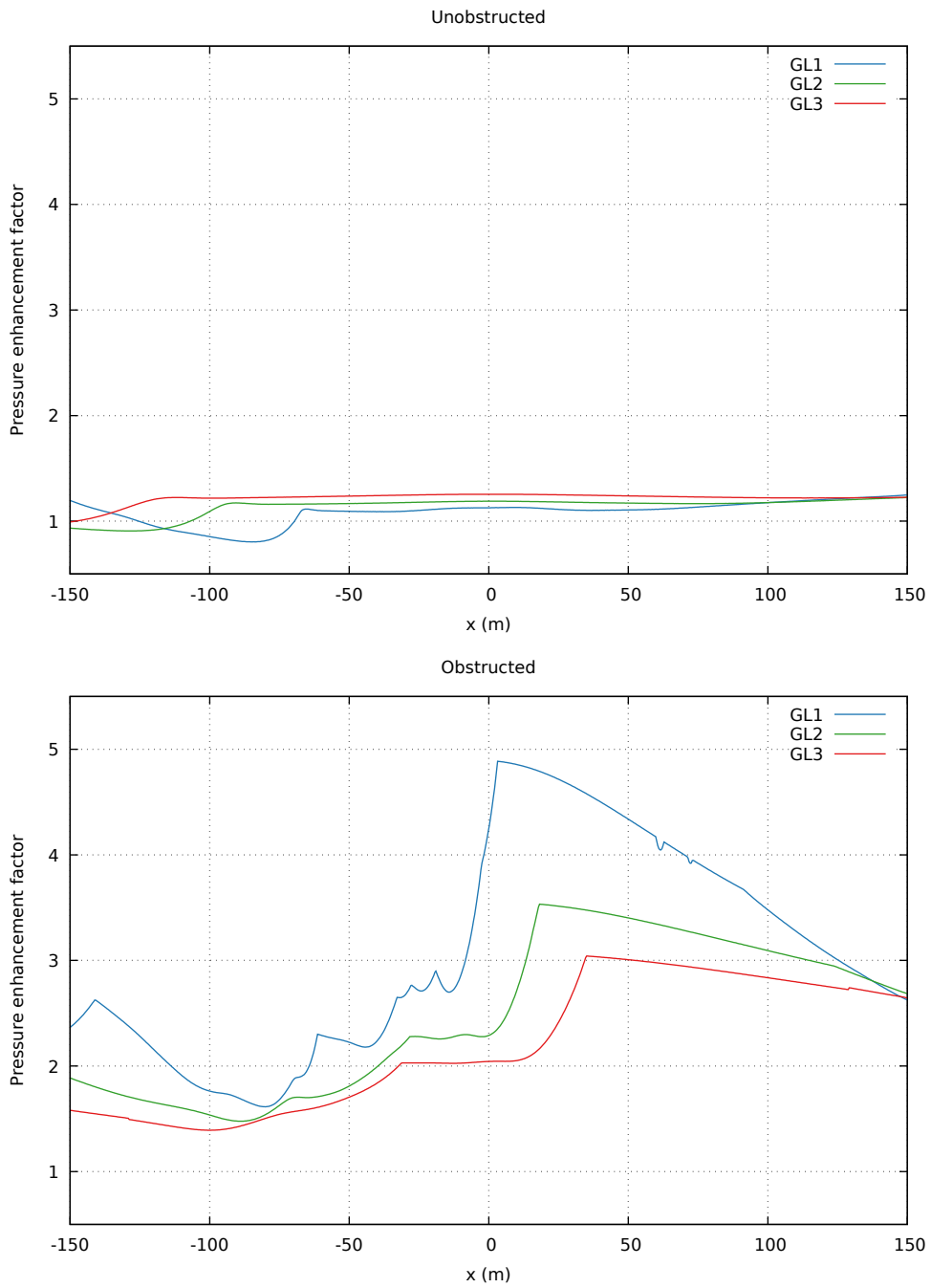


Figure 5.21: The pressure predictions from the two models in figure 5.20 were combined to create a pressure amplification factor. This is shown for gauge lines GL1 to GL3 for the two charge locations. The factor measures the extent to which the empirical model over- or underestimates the pressure relative to the CFD method.

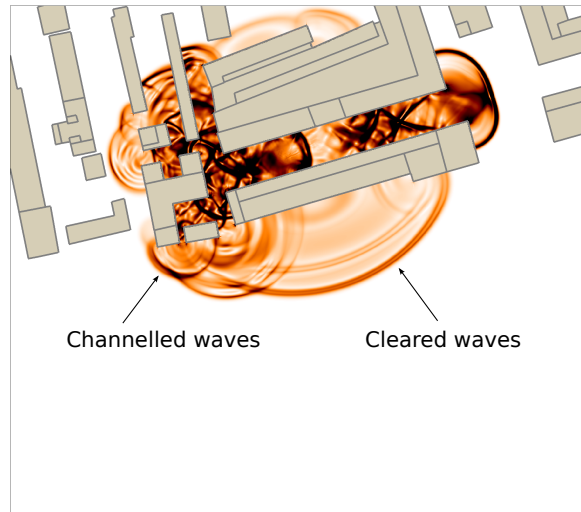


Figure 5.22: A pressure schlieren at $z = 2\text{ m}$, $t = 300\text{ ms}$ showing the wave structure following the obstructed explosion inside a confined street bordering an urban park.

case. Overall, the factor does not exceed 1.25, indicating that the empirical method achieves a reasonable prediction of pressure within the park, despite not taking the urban geometry into account. When the charge is moved into the adjoining street, a significant change in the predicted pressure is observed. The shielding effect of the building and the fact that the charge is 50 m further away results in a significant reduction in predicted pressures by the CFD model. The pressure amplification factor exceeds 4.8 in some regions of the domain, suggesting a significant over-prediction of pressure by the empirical method.

The pressure distribution along the gauge lines no longer has the bell shape associated with the Kingery curves. Instead, the bottom chart in figure 5.20 shows two distinct regions consisting of higher and lower pressures found in the left and right halves of the domain respectively. This can be explained by studying the distribution of waves in figure 5.22 and noting the types of wave-structure interaction that occur. The left half gauge readings are dominated by horizontally channelled waves that emanate from the two narrow streets in the left half of the domain. The right half of the gauge line is dominated by waves that vertically clear the large block of flats before diffracting to ground.

The contribution from these waves to the pressures recorded in figures 5.20 and 5.21 can be explained by studying the gauge pressure histories. The top chart of figure 5.23 shows a pressure time series for a pair of gauges located on gauge line GL1 at $x = \pm 10\text{ m}$. Both gauges are equidistant from the charge at $x = 0\text{ m}$. The gauge to

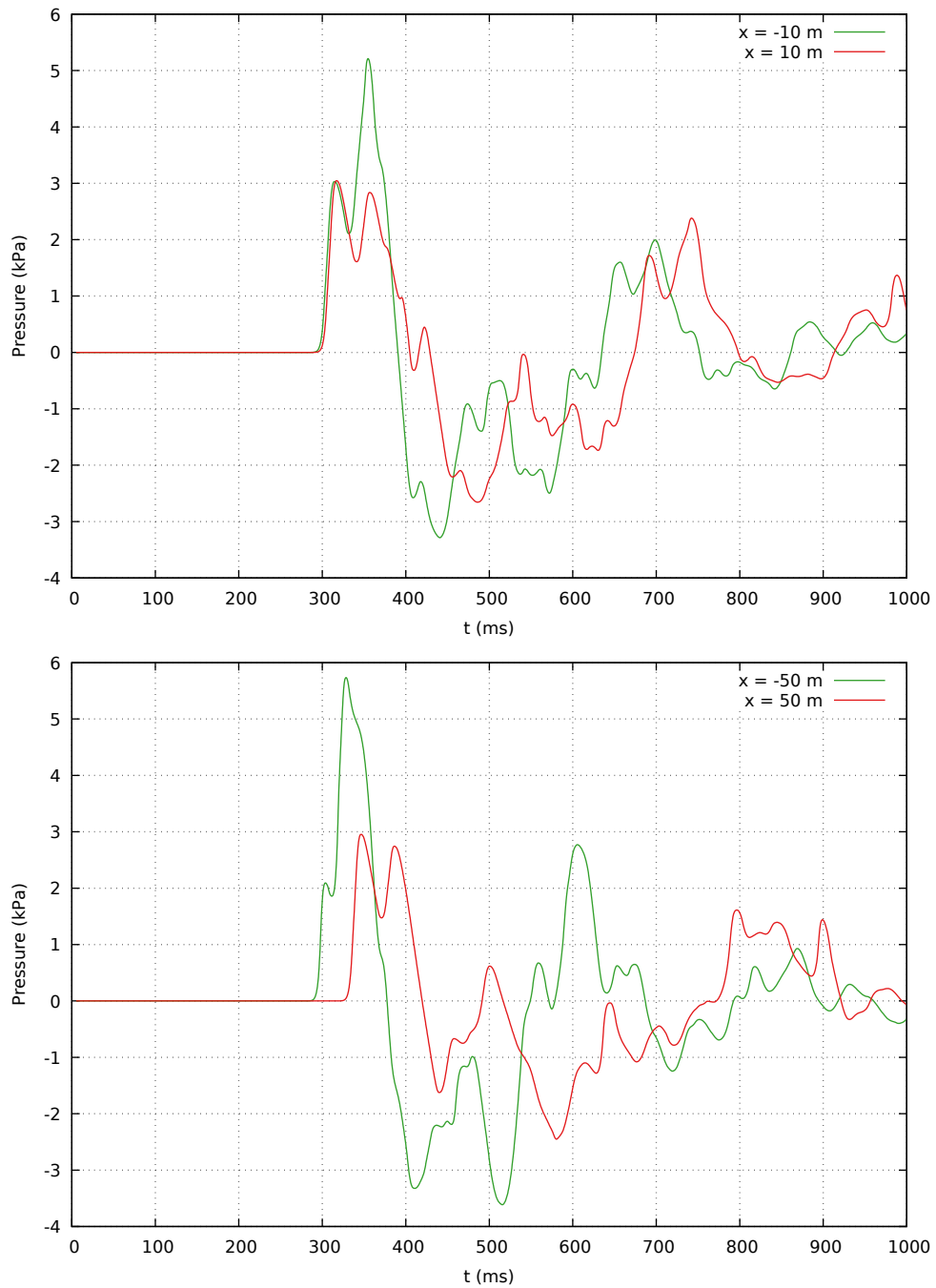


Figure 5.23: CFD prediction of pressure histories following the obstructed explosion. Two pairs of gauges are chosen along gauge line GL1. Each pair is equidistant from the charge located at $x = 0$ m. The first pair is located at $x = \pm 10$ m (shown top). The second pair is located slightly further away at $x = \pm 50$ m (shown bottom).

the right of the centreline shows the arrival at $t = 300\text{ms}$ of two coalesced waves that have vertically cleared the large apartment building. The second wave originates from a reflection in the confined street that trails the primary blast wave.

The gauge to the left of the centreline ($x = -10\text{m}$) shows the two cleared waves coalesced with a third wave. This is the wave that originates from the horizontal channelling of the blast wave along the street and into the park. The channelling effect of the confined street maintains the strength of the wave in contrast to the cleared wave which weakens faster by virtue of experiencing less confinement. The channelled wave dominates the pressure history of the left gauge and is the reason for the higher maximum pressures observed in the left half of the domain.

As one moves away from the charge, the difference in blast resultants either side of the domain increases. The bottom chart of figure 5.23 shows the pressure histories for a pair of gauges on gauge line GL1 at $x = \pm 50\text{m}$. Both gauges are located the same distance from the charge but experience significant differences in pressure histories due to their respective proximities to the channelled and cleared waves. The left hand gauge near the source of the channelled wave experiences a peak pressure of 5.7 kPa and an impulse of 255.8 kPams. The gauge on the opposite side of the centreline that is dominated by the cleared wave records a peak pressure of 3.0 kPa and an impulse of 166.0 kPams. This represents a change in blast resultants by 52 % and 65 % for pressure and impulse respectively. Because of the equidistance of the gauges, the empirical model predicts the same overpressure of 12.73 kPa for both gauges. Not only is the variability in pressure not captured, it is also overestimated by a factor between 2.2 and 4.2.

Using a pressure-impulse curve from the US Department of Defense (DOD) report [143] it is possible to predict the level of glazing damage sustained by a hypothetical structure located at either of these two gauge positions. At the left gauge we predict 70 % of glazing to break. If a building was located next to the right gauge, the glazing damage would reduce to 30 %. The empirical model is significantly more conservative, predicting 90 % glazing failure at both locations.

Not only does the empirical model significantly over-predict damage for the obstructed blast, it also fails to capture the highly localised nature of the damage. Any structure unlucky enough to be located near the source of the channelled wave could expect to incur more than twice the damage experienced by a building on the right side of the domain. This has been shown to be true even when both locations are equidistant from the source.

5.5.4 Comments and conclusions

In this study we investigated the hypothesis that charge location has a significant effect on blast resultants in an urban cityscape. We investigated this through a hypothetical urban blast scenario, in which an explosive charge was placed in two locations which were closely positioned but geometrically distinct. A CFD and an empirical model were used to predict the distribution of blast resultants in the park following the explosion. We make the following conclusions following the study:

- The unobstructed scenario produced a fairly even distribution of blast resultants within the park. The empirical method provided a reasonable estimation of pressure and the general shape of the distribution within the park corresponded well with the CFD method. Analysis of gauges concluded that the empirical method overestimated pressure by a factor of up to 1.25 when compared to the CFD model. We consider this a reasonable prediction given the simplicity of the approach.
- The obstructed scenario produced a highly variable, highly local distribution of blast resultants in the park. Visual analysis of the peak pressure field within the park yielded significant differences between the two models, with the empirical method unable to capture the effects of the geometry. Analysis of two gauges equidistant from the charge but in different regions of the park revealed glazing damage ratios that varied from 30 % to 70 %, more than doubling the degree of damage. The empirical method predicted no difference in damage between these points, assigning a damage ratio of 90 %.
- In addition to the inability to capture the locality of damage, the empirical method was found to be extremely conservative. Gauge analysis of the obstructed case concluded that pressure was overestimated by a factor between 1.5 and 4.8 compared to the CFD method.

This study has shown that realistic urban geometry does have a significant effect on the propagation of the blast wave, leading to highly localised regions of damage. By moving the charge a small distance, we have observed a significant change in the pattern of damage. This demonstrates the need for predictive methods to suitably capture the effects of urban geometry, justifying the use of CFD over empirical methods in these circumstances.

5.6 A CFD-based approach to deterministic risk modelling

In this section we present a new CFD model for predicting terrorism risk in urban environments. We present the model alongside an existing, simpler circular and hemispherical method that will be used in the comparison study in the next section.

5.6.1 PRA circular terrorism loss model

The Bank of England Prudential Regulation Authority (PRA) is the UK insurance industry regulator. As part of efforts to strengthen the resilience of the industry against large losses, the regulator mandates that insurers perform catastrophe stress tests. Firms are expected to model the financial implications on their portfolios from a range of different catastrophe scenarios and submit gross estimates of loss. The events range from natural disasters to economic and cyber crises and are meant to cover the full range of loss events that insurers can face.

The terrorism event involves the detonation of a two tonne TNT truck bomb in the City of London at 3pm UK time. In conjunction with the catastrophe modelling firm RMS, the PRA has developed a circular model for predicting property damage, fatalities and disabilities in the region of the blast [161]. Property and persons that lie within a particular zone are assigned a loss ratio. For property this refers to the extent of the damage, varying from 0% (no damage) to 100% (complete destruction). For human losses, this refers to the proportion of people in the zone who incur disabilities or fatalities. Table 5.4 shows these losses for each concentric zone.

Distance (m)	Property damage	Disabilities	Fatalities
0 - 100	60 %	15 %	10 %
100 - 200	20 %	5 %	1 %
200 - 400	5 %	1 %	0 %

Table 5.4: Insured loss ratios for the PRA terrorism scenario [161].

5.6.2 Towards a CFD-based approach

The above approach expresses loss as a function of distance from the explosion. We know that in urban areas this is a gross oversimplification because the effects of urban layout are not taken into account. We present an alternative approach that uses CFD to simulate the propagation of the blast wave through the streets. By capturing the

p_{so} (kPa)	p_r (kPa)	Property damage	Disabilities	Fatalities
> 20.58	> 44.66	60 %	15 %	10 %
20.58 - 8.10	44.66 - 16.73	20 %	5 %	1 %
8.10 - 3.29	16.73 - 6.67	5 %	1 %	0 %

Table 5.5: Insured loss assumptions for the CFD terrorism model.

complex wave effects and the build-up of pressure on buildings we aim to arrive at a more accurate prediction of loss.

The central component of the approach is a 3D solver for the Euler equations with an ideal gas explosion model that we presented and validated in chapter 3. Urban geometry of London is obtained from the Joint Information Systems Committee (JISC) funded Landmap service which offers LIDAR-derived Digital Surface Models (DSM) for cities in England and Scotland [40]. The geometry is imported into the code and the location and size of the explosive source is chosen.

An overpressure-based method is used to calculate loss ratios by measuring the maximum overpressure recorded on a building façade. This is a general approach to measuring damage as the construction type of the building is not taken into account, neither is the impulse experienced during the loading. For the present study, a full pressure-impulse analysis is not necessary as we are more interested in the difference between the simple and CFD model rather than their objective accuracy.

For ease of comparison between the two methods, we adopt the PRA loss categories shown in table 5.4. These losses represent the damage from a 2 t unobstructed hemispherical, TNT surface explosion and can be expressed either as a function of overpressure or distance. Using the Kingery & Bulmash equations, we can calculate the ranges of incident and reflected overpressures for each of the three loss zones of the concentric model (0 - 100 m, 100 - 200 m and 200 - 400 m. These overpressures are presented in table 5.5.

The model records pressures in three locations: in the street, on building exteriors and inside buildings (using an approximate method). The mapping table 5.5 is used to translate these pressures into property and human losses. In streets, the mapping is performed using incident pressures. Because of reflection effects, reflected pressures are used for building exteriors. It is also possible to perform a more granular damage analysis of individual floors by using the pressures recorded at each storey.

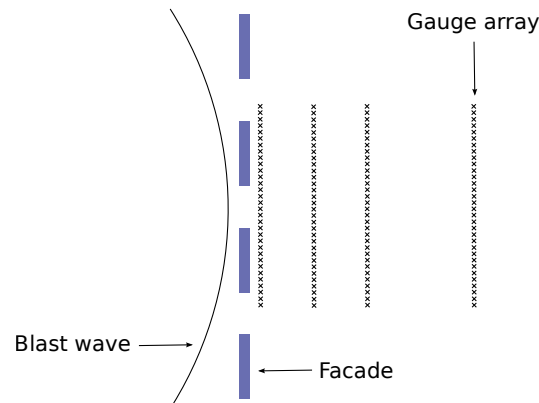


Figure 5.24: Diagram of the simulation setup for the measurement of a façade attenuation factor.

5.6.3 Pressure prediction inside buildings

The model represents buildings as rigid, perfectly reflecting objects. In reality, building façades exhibit some degree of permeability when windows fail and the blast wave is allowed to enter the building. The presence of this wave inside the building represents a hazard to occupants due to the primary and secondary effects of the pressure field. This motivates the development of a method for predicting blast wave resultants inside a building that has been breached.

At the core of this approach is the understanding that a semi-porous façade that is impinged upon by a blast wave will reflect a fraction of its energy. The wave that is admitted will be weaker than an unobstructed wave. The overpressure of the resulting wave will have been reduced by a factor that is dependent on the geometry of the façade and the nature of the incident wave. Knowledge of this attenuation factor and the state of the wave just before it hits the building should be enough to form a reasonable prediction for the overpressure after breaching the façade.

A three-dimensional numerical study was performed to calculate a façade attenuation factor for a typical building. In keeping with the rest of the model, we limit our study to overpressure rather than impulse. Figure 5.24 shows a sketch of the simulation configuration. A spherical blast wave is set up so that it normally strikes a rigid, porous façade. A series of gauges are placed in lines behind the façade at a distance of 1, 5, 10 and 20 metres from the wall. Maximum overpressures are recorded at each gauge location. We denote these as *shielded* overpressures p_{shielded} .

The façade is then removed and the simulation is rerun in the same fashion and

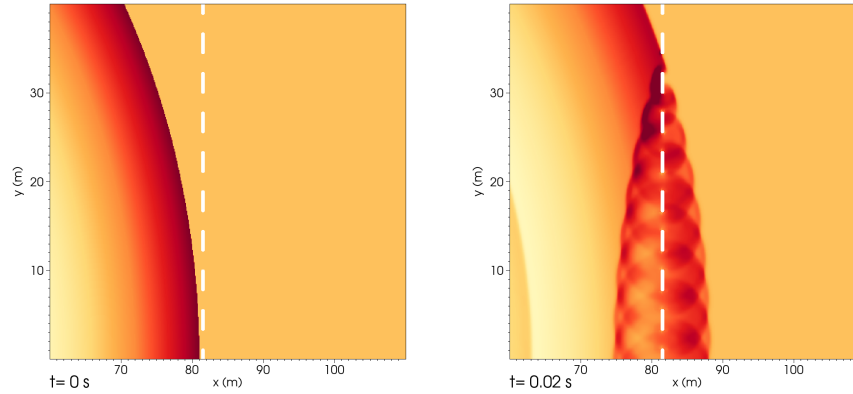


Figure 5.25: A blast wave with an incident pressure of 20 kPa impinges upon a 45 % porosity façade, experiencing a reduction in peak overpressure.

unshielded overpressures $p_{\text{unshielded}}$ are recorded. A façade attenuation factor β is calculated at each gauge using the relation

$$\beta = \frac{p_{\text{shielded}}}{p_{\text{unshielded}}}. \quad (5.13)$$

The façade porosity was fixed at 45 %, a common porosity for today’s office buildings. The incident overpressure of the blast wave was varied between 5 kPa and 80 kPa to reflect the range of possible loading pressures.

Despite the large range of incident pressures, it was found that the reduction in overpressure of the shielded wave was modest and did not change significantly (10 % to 20 % compared to the unshielded wave). The mean of the range was chosen, resulting in an attenuation factor $\beta = 0.85$. Further work could be done to derive a relationship between β and the overpressure of the incident wave. However, we do not think this worthwhile as the approximation of perfectly reflective buildings in the simulation already introduces significant inaccuracies into the solution. Anything other than a rough method to extrapolate these pressures into buildings is unlikely to yield any improvement to the predictive capabilities of the model.

We now describe how the model uses the attenuation factor β to predict internal overpressures. Firstly, the maximum reflected overpressure experienced by the building façade is recorded. This reflected pressure is then converted to an incident pressure by solving the reflection equation initially derived by Rankine and Hugoniot

$$p_r = 2p_s \frac{7p_0 + 4p_s}{7p_0 + p_s} \quad (5.14)$$

for the incident overpressure p_s , where p_0 is the ambient pressure and p_r is the reflected overpressure [146]. This provides an estimation of the blast wave pressure just before it makes contact with the building. The façade attenuation factor is applied to the incident pressure to derive a prediction of the shielded incident pressure of the wave just after it has passed through the façade:

$$\bar{p}_s = \beta p_s. \quad (5.15)$$

It is important to note that the post-façade pressure \bar{p}_s is only valid up to a short distance into the building as the prediction ignores any decay of blast resultants as the wave propagates outward. The model is therefore suitable for the prediction of blast pressures experienced by building occupants located in the immediate vicinity of the failed façade.

5.6.4 Quantifying property loss and business interruption

A dollar value estimate for the property loss for a single building can be obtained from the product of the replacement cost per square metre (RC), the total floor area (SM) and the damage ratio of the building (DR):

$$BL = RC \times SM \times DR. \quad (5.16)$$

The damage ratio is obtained by mapping the largest recorded overpressure on the building surface to a loss using table 5.5. Loss can be calculated on a floor by floor basis or by assuming a single damage ratio for the building. The total floor area can be obtained from building models or by using a simple estimate of storey height in conjunction with the building height. In our case, we make the assumption that a typical height of a London office storey is 4 m. The replacement cost is usually calculated by a professional building surveyor. For the purposes of our study, we assume a fixed cost of 2000 pounds per square metre [162].

The total building loss (TBL) is obtained by summing the individual building losses over the disaster zone. This represents the total cost to rebuild or repair the affected buildings and should be equivalent to the insured property loss when clean-up and infrastructure repair costs are ignored.

Business interruption (BI) loss is calculated by measuring the loss of earnings experienced by a company in the aftermath of a disaster. The figure is unique to each company and depends on historic financial projections to calculate a shortfall. This information is unavailable in the present model. Rather than calculate a dollar value of business interruption, we state whether a building has or has not suffered any BI. A shattered window is enough to interrupt a business's operations. We

therefore express business interruption as the proportion of total insured floor space that experiences some form of damage.

5.6.5 Quantifying human loss

Human loss is obtained from the product of the human density inside the building (HD), the total floor area (SM) and the damage ratio for fatalities or disabilities (DR):

$$HL = HD \times SM \times DR. \quad (5.17)$$

Since the vast majority of people will be inside a building at the time of the explosion, we calculate human loss by considering the properties of the blast wave inside the building and neglecting the streets. The damage ratio DR is obtained by mapping the maximum interior pressure inside the building \bar{p}_s to a loss for disabilities or fatalities using table 5.5. The density of people inside the building (HD) is assumed to be 0.09 people per square metre, the average for office space in London [163]. The total human loss (THL) is then obtained by summing the loss figures for all buildings in the disaster zone.

5.7 A comparative study of a circular, hemispherical and CFD consequence model

In this section we compare a simple ‘rule-of-thumb’ approach with a CFD model for estimating insured loss from a terrorist attack. CFD methods offer the insurer greater accuracy due to their ability to take into account the complexity of the urban environment. However, these models are computationally expensive and are seeing limited use in the industry today [16]. The purpose of this study is to demonstrate the magnitude of improvement in accuracy between simple and CFD methods to understand whether it makes economic sense to move towards higher accuracy modelling. The study will apply a series of simple and CFD models to a hypothetical terrorism scenario. Estimates of property loss, business interruption and human loss will be presented and compared.

5.7.1 Terrorism event on Lime Street, London

The terror event is taken from the Bank of England PRA General Insurance Stress Test 2015 [161]. At 3pm UK time, a 2 t TNT equivalent bomb is detonated in a medium size box van next to the Lloyd’s building in the City of London. The polar coordinates



Figure 5.26: Plan of the disaster zone for the Lime Street terror scenario with the charge location marked in the centre.

of the bomb location are assumed to be latitude $51.513558^{\circ}\text{N}$, longitude 0.081547°W . The test is chosen because it represents a realistic scenario for a UK terror attack. The location of the blast is the busy heart of London's financial centre and contains many locations of high symbolic and monetary value. An attack here would likely cause significant business interruption, property and human loss.

A 600 metre by 600 metre zone was chosen for the study, giving a total building floor area of 2.4 million square metres when multiple storeys are considered. The domain is shown in figure 5.26 with the charge marked in the centre as a black dot. The domain dimensions represent the largest area that can be modelled by the 3D CFD model before computation becomes prohibitively expensive. Urban data for the region is acquired from the Landmap LIDAR dataset [40].

5.7.2 Property loss and business interruption

Figure 5.27 shows a graphical representation of property loss for the circular concentric ring model at a height of 2 m, 40 m and 80 m above the ground. The left column shows the damage footprint overlaid onto the streets at each height. The buildings are coloured according to the zones in which they lie and are presented in the right column. The mapping between colours and loss ratios is shown in table 5.6, along with an estimate of business interruption for each damage zone, represented as the proportion of total floor space incurring some form of damage. A prediction of property value loss is also shown for each model.

The circular model predicts that all buildings in the domain experience some

level of damage, with 100 % of floor space experiencing business interruption. As the altitude increases, the damage footprint remains the same because the height above blast is not taken into account. At 80 m, the few buildings still tall enough to exist at this altitude receive the same degree of damage as those at street level. This is a limitation of the method which leads to an overestimation of loss, especially for tall buildings that may only sustain damage to their lower floors.

A modification was made to the model to account for a hemispherical, rather than circular, loss distribution. Figure 5.28 shows the effect of this change. At a higher altitude the damage footprint becomes noticeably smaller and a minor reduction in building damage is observed. Overall, the change is minimal and 100 % of the total floor area still experiences some form of business interruption. Both models predict similar figures for overall property loss: 453.0 and 440.2 million pounds for the circular and hemispherical models respectively.

Figure 5.29 shows the loss results for the CFD model. The damage footprint in the streets is noticeably different to the simple models due to wave interactions with the geometry. Channelling effects widen the most severe damage category along the central East-West road. Conversely, shielding effects from nearby buildings reduce the size of this region in some areas. Overall, the proportion of floor area within this category has not changed significantly between the three models.

The floor area contained within the 5 % and 20 % damage categories has reduced significantly. The shielding effects from the buildings in the vicinity of the blast causes the wave strength to decay rapidly. Beyond 100 m from the source, the reduction in strength of blast overpressure results in little damage. Use of the CFD model has led to a reduction in predicted total business interruption by 68 %. The CFD method estimates total building loss as 198.1 million pounds. This is a decrease of approximately 55 % from the predictions of the empirical models.

In 1993 the IRA detonated a similar truck bomb on Bishopsgate, not far from




Damage ratio	Colour	Business interruption (%)			Property loss (GBP millions)		
		Circular	Hemi.	CFD	Circular	Hemi.	CFD
5 %		53	55	17	75.1	77.3	23.0
20 %		36	35	7	200.0	194.4	40.0
60 %		11	10	8	178.2	168.5	135.1
		100	100	32	453.0	440.2	198.1

Table 5.6: Business interruption and property loss estimates for the three loss models.

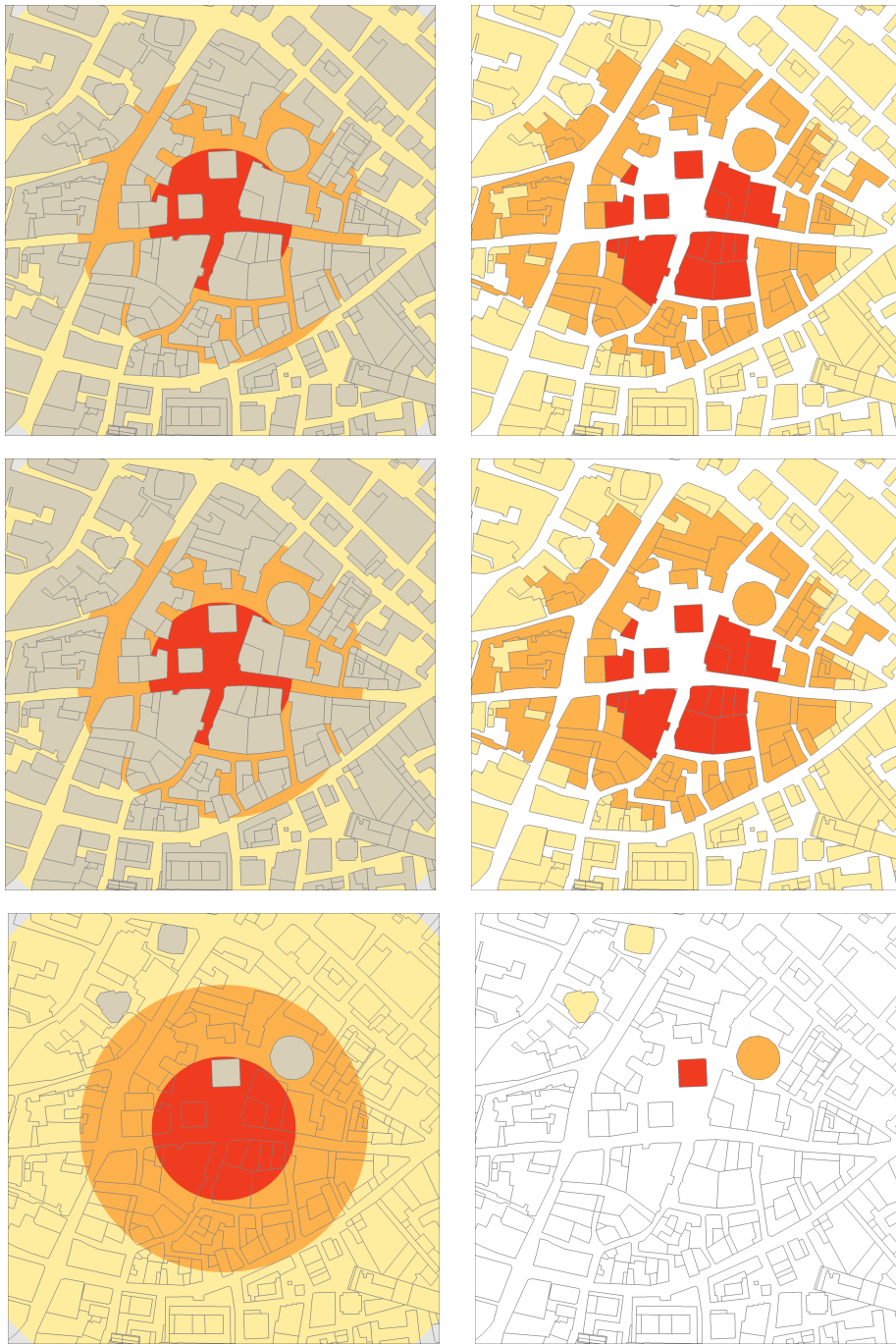


Figure 5.27: Predicted property loss following a hypothetical bombing on Lime Street in the City of London. An existing circular loss model is used to predict street (left) and building (right) property loss categories at a height of 2 m (top), 40 m (middle) and 80 m (bottom). Darker colours indicate greater loss.

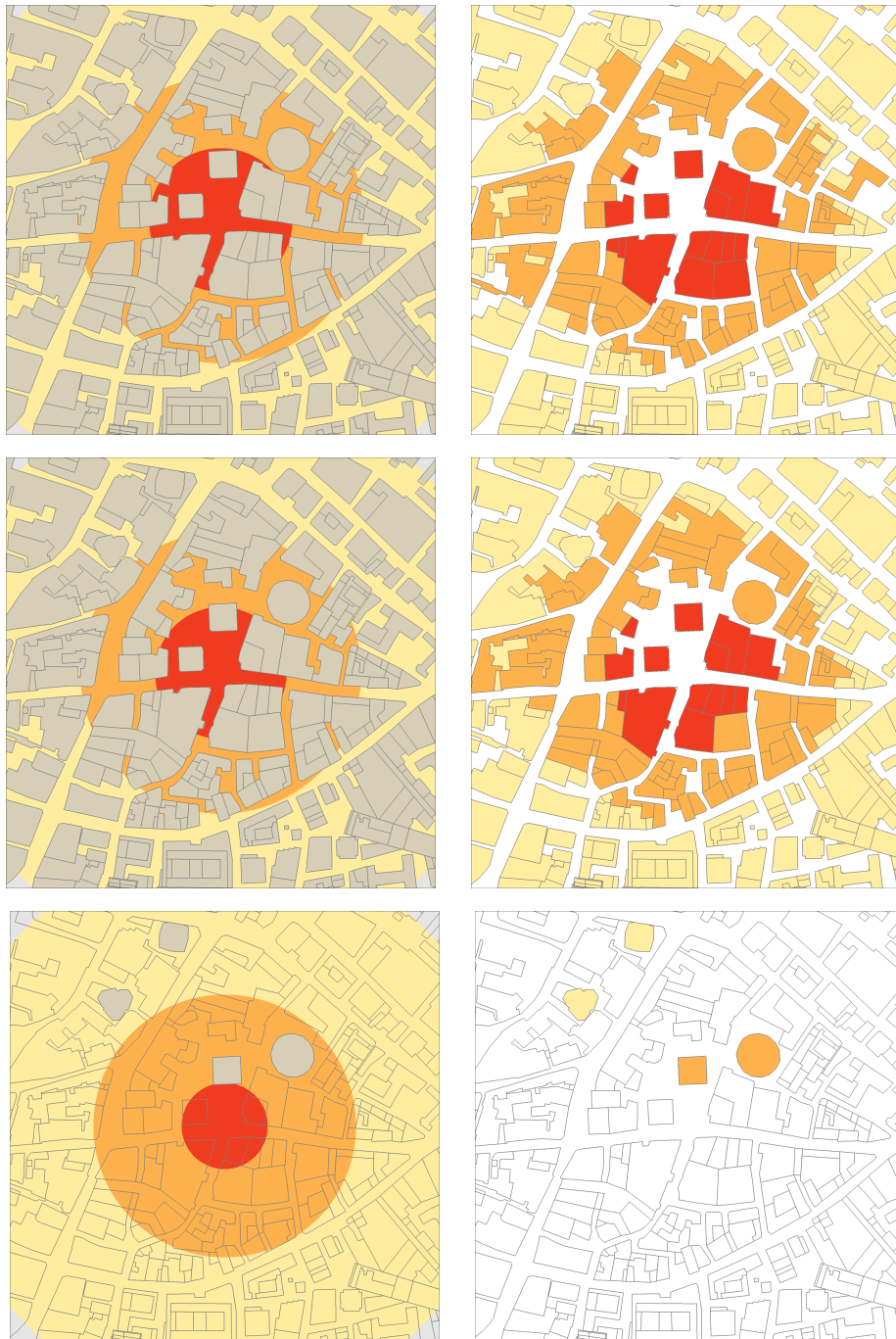


Figure 5.28: Predicted property loss following a hypothetical bombing on Lime Street in the City of London. An existing hemispherical loss model is used to predict street (left) and building (right) property loss categories at a height of 2 m (top), 40 m (middle) and 80 m (bottom). Darker colours indicate greater loss.

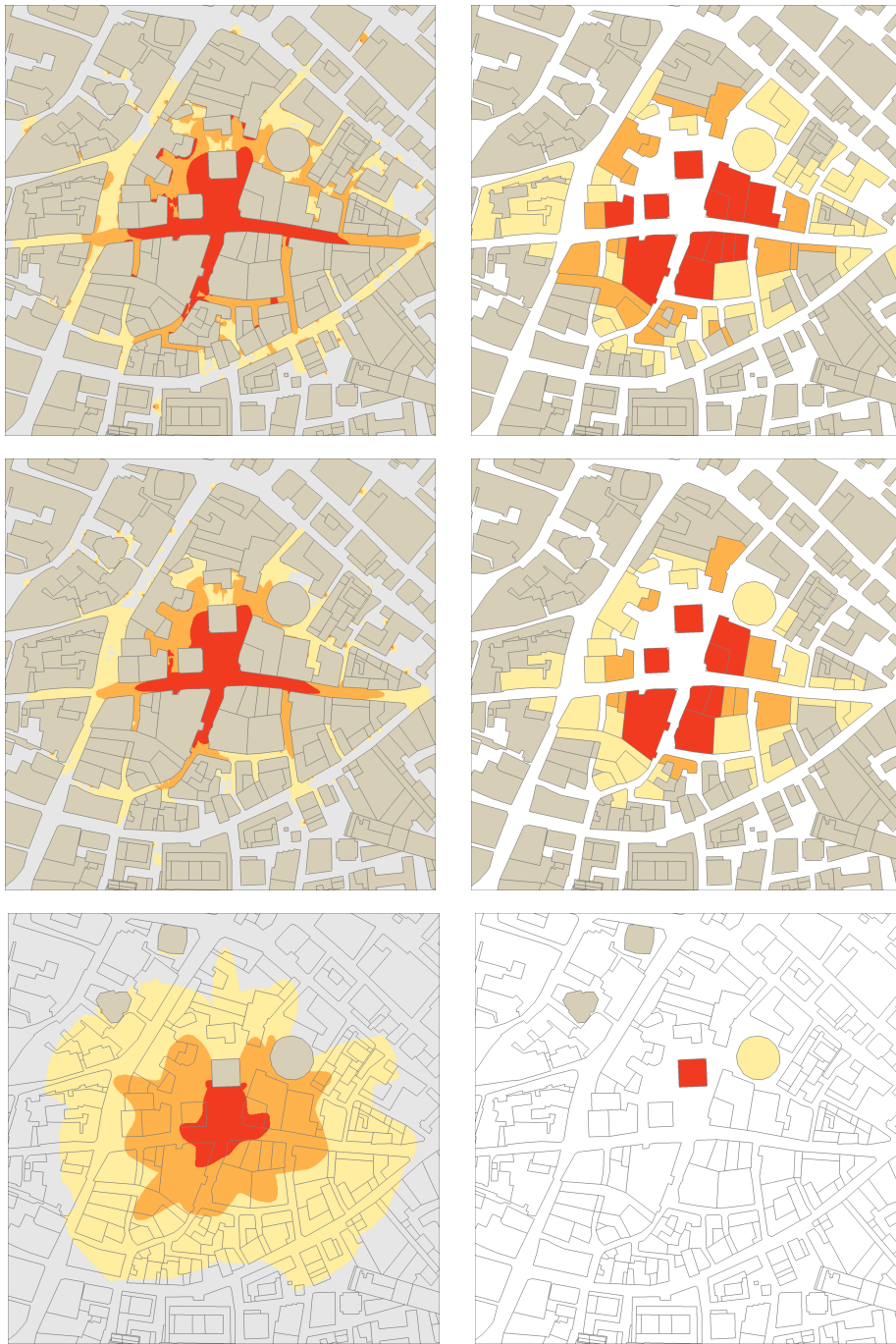


Figure 5.29: Predicted property loss following a hypothetical bombing on Lime Street in the City of London. A new CFD loss model is used to predict street (left) and building (right) property loss categories at a height of 2 m (top), 40 m (middle) and 80 m (bottom). Darker colours indicate greater loss.

Lime Street. The bombing caused 350 million pounds of property damage [164], somewhat larger than predicted by the CFD model. A possible explanation is the fact that the models considered here do not include the additional costs of infrastructure repair and the replacement of fixtures and fittings. Regardless of these differences, it is clear to see that the CFD model leads to a significant reduction in property and business interruption loss estimates.

5.7.3 Human loss

Figures 5.30 to 5.32 show the distribution of human loss for the circular, hemispherical and CFD models respectively. The loss categories are coloured according to the key in table 5.7.

The damage footprints are similar in shape to the outlines in the property loss estimates. A minor change in the size of the footprint is observed when comparing the hemispherical and circular models. Due to the effects discussed earlier, the footprint changes dramatically when a CFD model is used. The circular and hemispherical models predict a significant number of disabilities (4849 and 4699 respectively) and fatalities (1756 and 1673 respectively).

In the 1996 Oklahoma City bombing, a 2300 kg TNT equivalent bomb was detonated in downtown Oklahoma City next to the Alfred P. Murrah Federal Building [142]. The size of the charge and the location in which the bomb was detonated make it similar in nature to the Lime Street scenario. The Oklahoma bombing caused a total of 674 disabilities and 168 fatalities [165]. This magnitude of loss is a factor of ten smaller than that predicted by the concentric models, indicating a significant over-prediction of loss. This is attributed partly to the fact that the models' damage footprints do not consider the urban geometry. Damage is also applied uniformly throughout each floor, meaning that occupants in the building core experience the




Disabilities	Fatalities	Colour	Disabilities			Fatalities		
			Circular	Hemi.	CFD	Circular	Hemi.	CFD
1 %	0 %		668	684	176	0	0	0
5 %	1 %		2209	2151	583	442	430	117
15 %	10 %		1972	1864	1088	1314	1242	726
			4849	4699	1848	1756	1673	842

Table 5.7: Human loss estimates for the three loss models.



Figure 5.30: Predicted human loss following a hypothetical bombing on Lime Street in the City of London. An existing circular loss model is used to predict casualties in streets (left) and buildings (right) at a height of 2 m (top), 40 m (middle) and 80 m (bottom). Darker colours indicate greater loss.

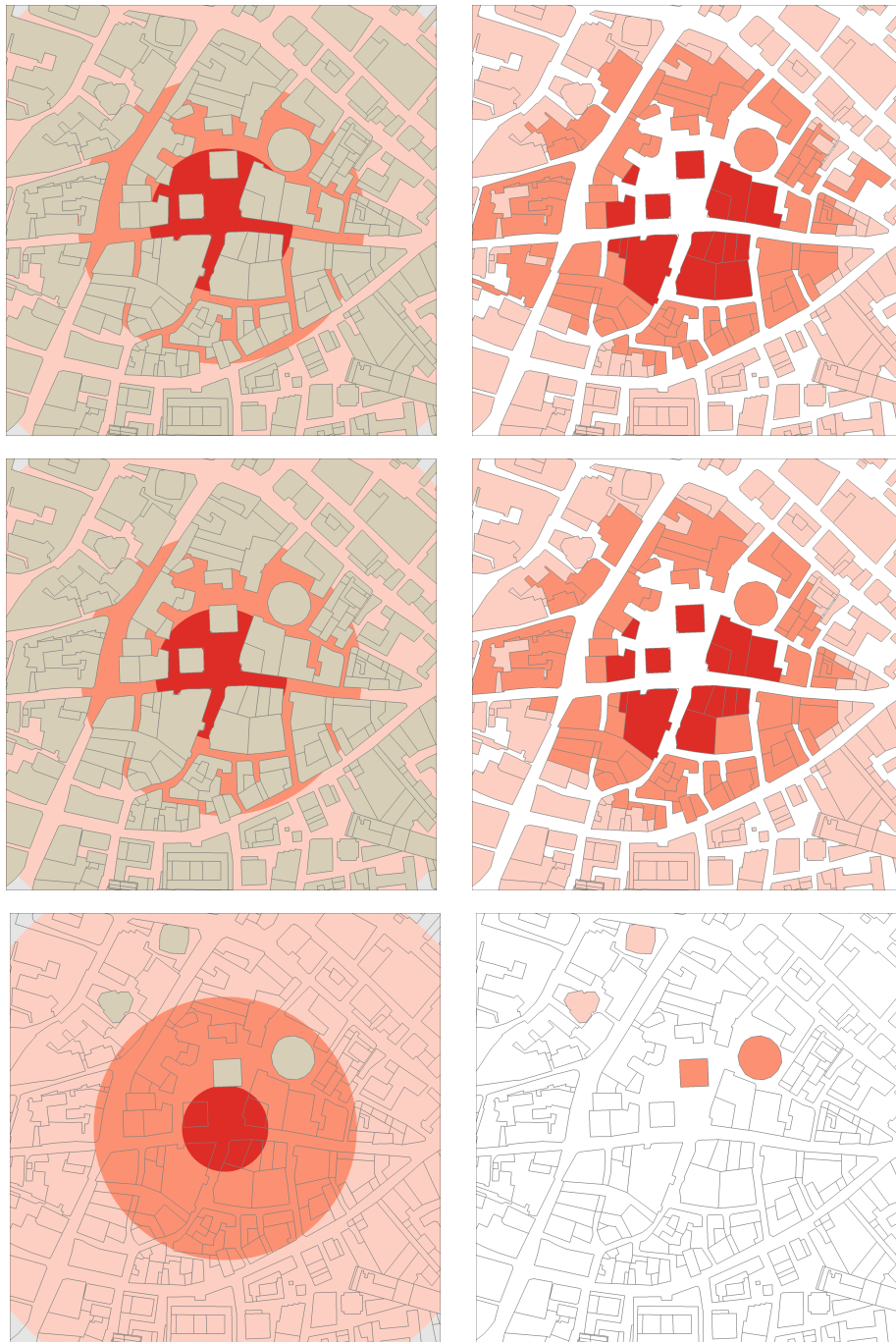


Figure 5.31: Predicted human loss following a hypothetical bombing on Lime Street in the City of London. An existing hemispherical loss model is used to predict casualties in streets (left) and buildings (right) at a height of 2 m (top), 40 m (middle) and 80 m (bottom). Darker colours indicate greater loss.

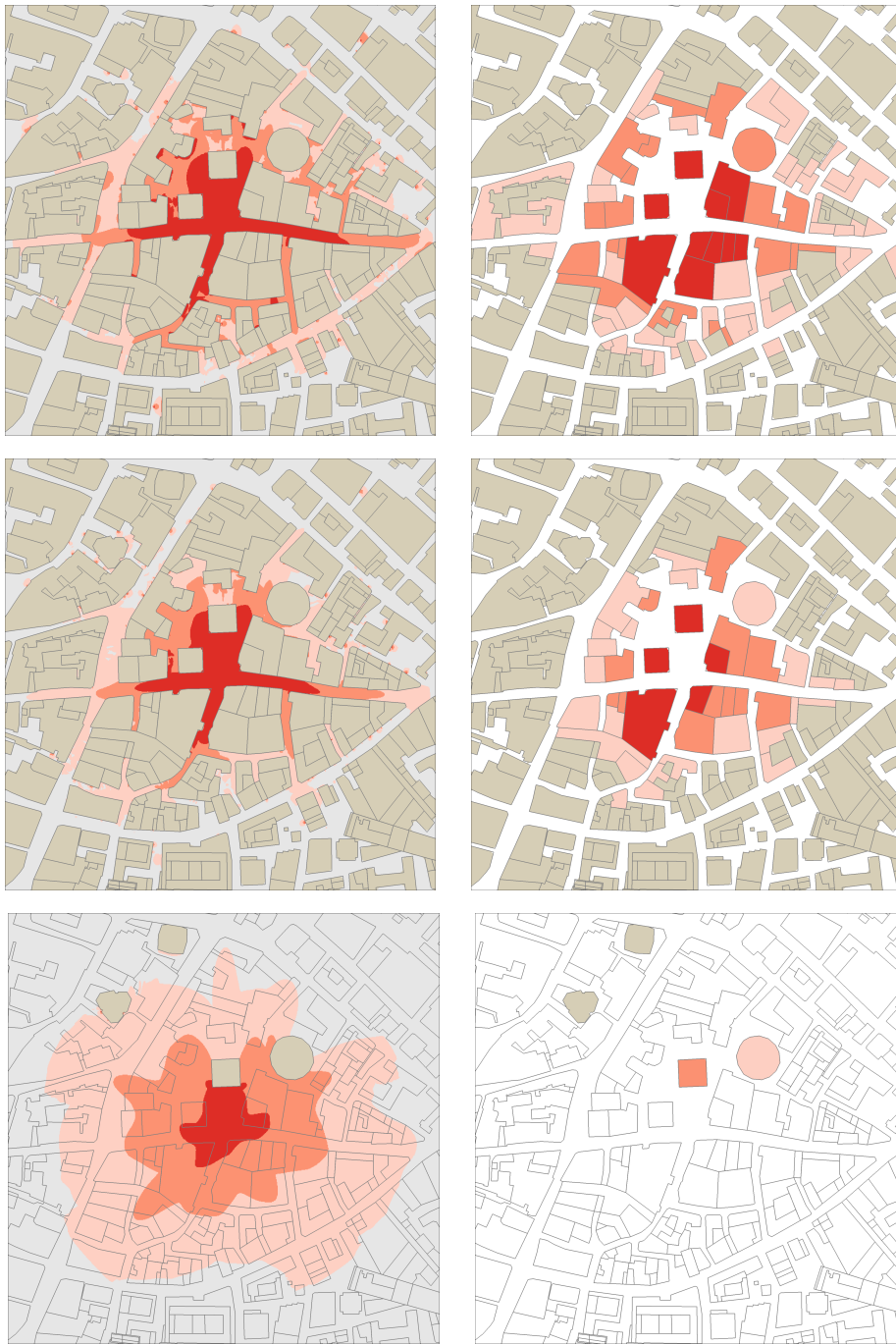


Figure 5.32: Predicted human loss following a hypothetical bombing on Lime Street in the City of London. A new CFD loss model is used to predict casualties in streets (left) and buildings (right) at a height of 2 m (top), 40 m (middle) and 80 m (bottom). Darker colours indicate greater loss.

same degree of loss as those near the exterior of the building.

When the effects of urban geometry are considered, the loss estimates decrease. The CFD model predicts a total of 1848 disabilities and 842 fatalities, a reduction of approximately 60 % and 50 % respectively compared to the concentric methods. These estimates seem more realistic but are still likely to be an overestimate because of the assumption that the damage is applied uniformly across the entire floor.

In reality, the risk to those located further than a few metres from regions of blast ingress is probably minimal while the primary structure of the building remains intact. Assuming that blast ingress occurs only through the façade and occupants are evenly distributed inside the building, we might estimate that only 20 % of the building occupants experience some degree of loss. If we apply this correction to the CFD model loss figures, we predict a total of 370 disabilities and 168 deaths. This is significantly closer to the Oklahoma loss figure and represents a more realistic estimate of human loss. This produces a 90 % reduction of predicted casualties when compared to concentric loss models.

In summary, we have demonstrated that by adopting a CFD approach to deterministic risk modelling, a significant reduction in human loss estimates can be obtained. For the hypothetical scenario considered in this section, overall casualties have been reduced by 60 % to 90 %.

5.8 Conclusion

In this chapter we have demonstrated that urban geometry has a profound impact on the distribution of damage following an urban blast. We have justified the use of CFD for urban blast damage prediction, quantifying the significant improvements in accuracy afforded by CFD when compared to empirical methods which do not take urban geometry into account.

We began by validating the code against a simple case of urban blast-structure interaction. The code was found to closely match experiment and produced a highly variable distribution of damage around the structure. In the study that followed, we increased the complexity of the study to account for simplified city streets. In this case, the combined effects of channelling and shielding produced a complex, non-intuitive distribution of blast resultants along the streets. The study demonstrated the significance of these effects and the importance of capturing them using a CFD approach.

We extended the study to test for these effects in realistic urban cityscapes by investigating the effect of charge placement on blast resultants. The damage associated

with an explosion in a London park was simulated using an empirical and CFD model. By displacing the charge a small distance, a disproportionate change in the distribution of blast resultants within the park was observed. Damage ratios were found to double when moving between two locations equidistant from the charge.

In the study that followed, three consequence models were applied to a hypothetical terrorism scenario and estimates of business interruption, property and human loss were produced by each model. Two concentric models which did not capture the effects of the city geometry on the blast wave were compared to a CFD-based approach. By capturing the effects of urban geometry, a number of important conclusions were found:

- Property loss: We observed a minimum 55 % reduction in loss estimates compared to the empirical methods. This is equivalent to a difference of over 240 million pounds.
- Business interruption: The proportion of insured property experiencing some form of business interruption dropped by nearly 70 %.
- Human loss: A reduction of total casualties by approximately 60 % occurred. When a correction was applied to account for the shielding of those in the core of the building, the reduction increased to over 90 %.

These findings suggest that simple concentric models significantly over-predict insured loss for terrorist bombings in urban areas. In the hypothetical situation considered in this chapter, this prediction is likely to be measured in the hundreds of millions of pounds. This overestimation of loss could result in higher premiums and capital requirements for the insurer, increasing the overall cost to the insurer and reducing their competitiveness.

In conclusion, despite the extra computational and monetary expense associated with CFD loss models, the reduction in premiums associated with their higher accuracy makes a strong economic argument for their widespread adoption by the industry.

It is worth identifying some of the deficiencies of the CFD model that could be improved by further work. The current model assumes that all buildings are rigid and perfectly reflective. It is obvious that this is not always true in the real world. Almost all buildings have windows that are liable to fail and absorb some of the energy of the blast wave. In chapter 6 we will study this phenomenon, with the aim of understanding the implication it has for the propagation of the blast wave in confined streets.

Chapter 6

The effect of urban geometry on blast resultants

A typical urban setting consists of a network of roads, buildings and other structures. When impinged upon by a blast wave, these geometries are capable of producing a wide range of complex wave phenomena including reflections, clearing, channelling and diffraction. These wave interactions can greatly affect the strength of the blast resultants compared to the free-field. For buildings and their occupants, this can have significant repercussions, increasing the risk to human life and the structural integrity of the buildings.

In chapter 5 we studied the effect of urban layout on the distribution of damage following an explosion. We concluded that this effect can be significant, highly complex and its modelling is best suited to computational rather than empirical methods. It was noted that, while there have been many investigations into the effects of channelling and shielding of blast waves, there has been little consideration of the effects of building porosity. Additionally, we are unaware of any studies on the diffraction effects of window layout for mitigating the effects of blast inside buildings. In this chapter we explore these effects, replicating and extending previous work by incorporating a building porosity.

We begin the chapter by validating the code for building porosity studies by replicating the investigation of Smith et al. [73]. We then perform a study of the effects of street width on blast propagation, extending the work of Rose [70] by introducing a variable building porosity. Finally, we devise a new investigation into the effects of window layout for minimising blast resultants inside a building that is externally loaded.

6.1 Validation

In chapter 3 we validated the code for simulating blast wave propagation in complex cityscape geometries. In this section we validate the method for urban geometries with porous façades.

The experiments performed by Smith et al. [73] provide a means for validation. In their study, the authors experimentally and numerically investigated the effects of façade failure by detonating a TNT charge in the proximity of a building with a variable façade porosity. The numerical study was performed using the code Air3d [166].

The experiments were conducted at 1/50th scale with an 11.13 g SX2 explosive wrapped around an L2A1 detonator, equivalent to a 13 g spherical TNT charge. The explosive was detonated on a polystyrene block at a height of 25 mm above the ground. At full scale, this is equivalent to a 1625 kg truck bomb 1.25 m above ground. A study of typical road widths suggested a full street width of 15 m (0.3 m at the experimental scale). The charge was placed in the centre of the street.

A scale model of a building consisting of ten storeys with a full-scale floor height of 5 m was placed at the side of the street. At the experimental scale, the models measured 1300 mm long and 1045 mm high and were formed from a number of 210 × 100 × 65 mm bricks. 5 mm thick steel plates were used as floors at lower levels, with plywood flooring higher up. By adjusting the layout of the bricks, the authors were able to vary the porosity of the building, achieving five configurations: 0 %, 24 %, 48 %, 62 % and 77 % porosity, claiming that this covered the observed range of porosities for most buildings.

Figure 6.1 shows the brick layout for each of the four porous configurations. In the experiment, twelve pressure transducers were used for each configuration (numbered in the figure). The authors explicitly documented the positions of the charge, gauges and bricks for the 24 % model (shown in sub-figure (a)). For the remaining three configurations some educated guesswork had to be done. The predicted brick layouts are shown in sub-figures (b)–(c). In the study, experimental results were only presented for gauge 7. We therefore ignored the other gauges in our validation study.

We set up our simulation to exploit the symmetry of the experiment. First, a one dimensional, spherically symmetric analysis was performed from the charge centre to a radius of 25 mm (until the blast wave reaches the ground) using a resolution of 0.05 mm. A two-dimensional analysis was then performed to a radius of 150 mm, when the wave reaches the building façade. A resolution of 1 mm was used. Finally, a three-dimensional study was performed in quarter-space, with the charge positioned

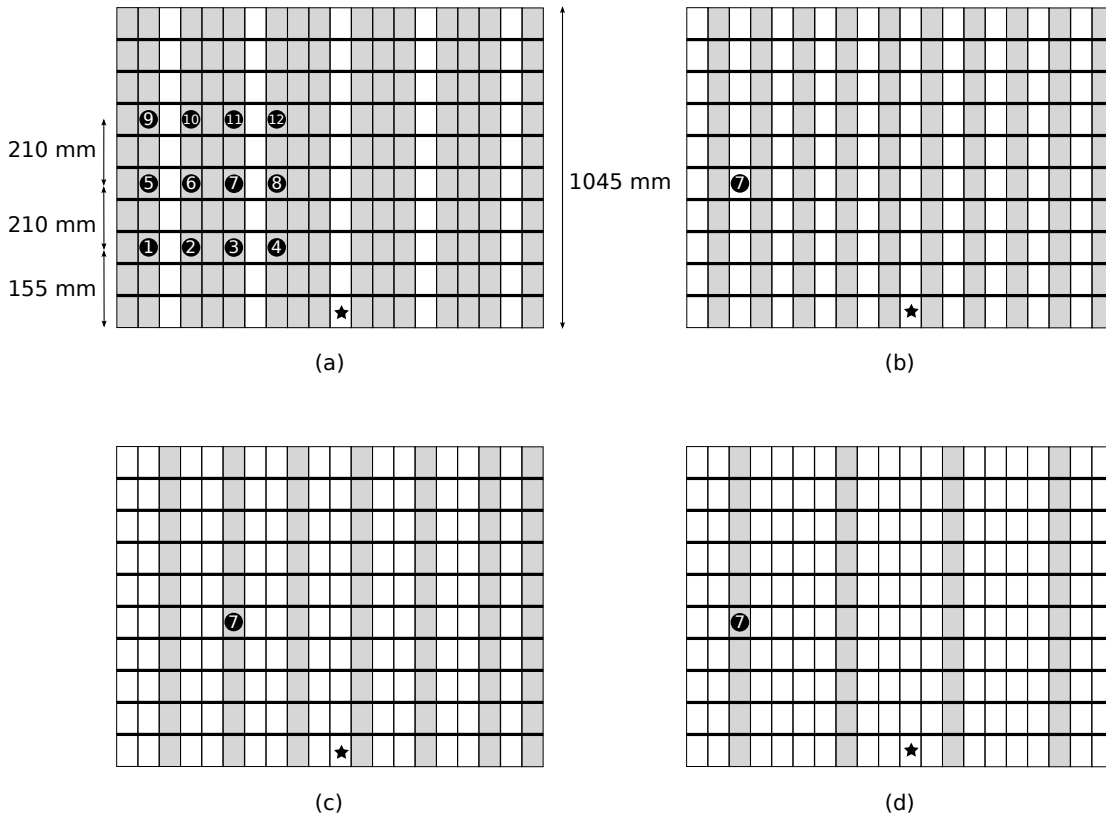


Figure 6.1: Porous building construction for the four different porosities: (a) 24 %, (b) 48 %, (c) 62 % and (d) 77 %. Bricks are shown in grey, with holes in white. Gauge locations are shown as numbered circles. The star indicates the charge location.

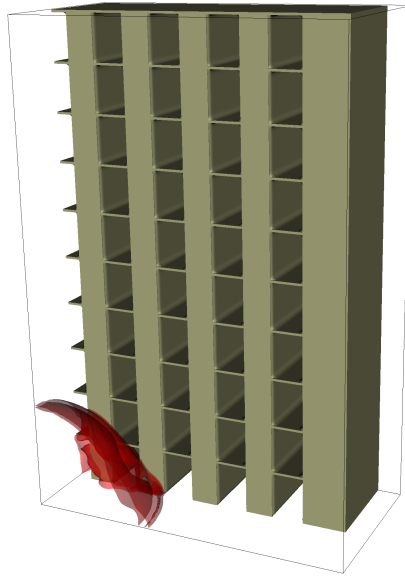


Figure 6.2: A contour of the pressure iso-surface (shown red) at $t = 0.1$ ms for the 48 % porosity configuration. The building façade is shown as a brown solid, indicating the numerical setup in quarter-space.

at the domain origin. Square cells of width 5 mm were used. The simulation was run up to a final time of 250 ms.

Figure 6.2 shows a representation of the domain shortly after the detonation, with a contour of the pressure iso-surface. The building structure was created using the code's internal geometry tool. Simple shapes can be defined from within the simulation settings file and various operations including unions (logical OR), intersections (logical AND), rotations and translations can be applied to these objects. In our case, a solid cuboid forming the outline of the building was created. To generate the windows, the geometry was intersected with a regular array of cuboid 'holes'.

6.1.1 Results

Figure 6.3 shows a comparison of pressure history at gauge location 7 for each of the four porosity configurations. Our simulation results are shown in blue and compared with the experiment and Air3d. It is worth noting that the relative distance between the gauge and charge centre was constant for the 24 %, 48 % and 62 % porosities. It had to be slightly further away for the 77 % geometry due to the brick configuration.

The experimental results show a secondary wave, reflected from the other side of

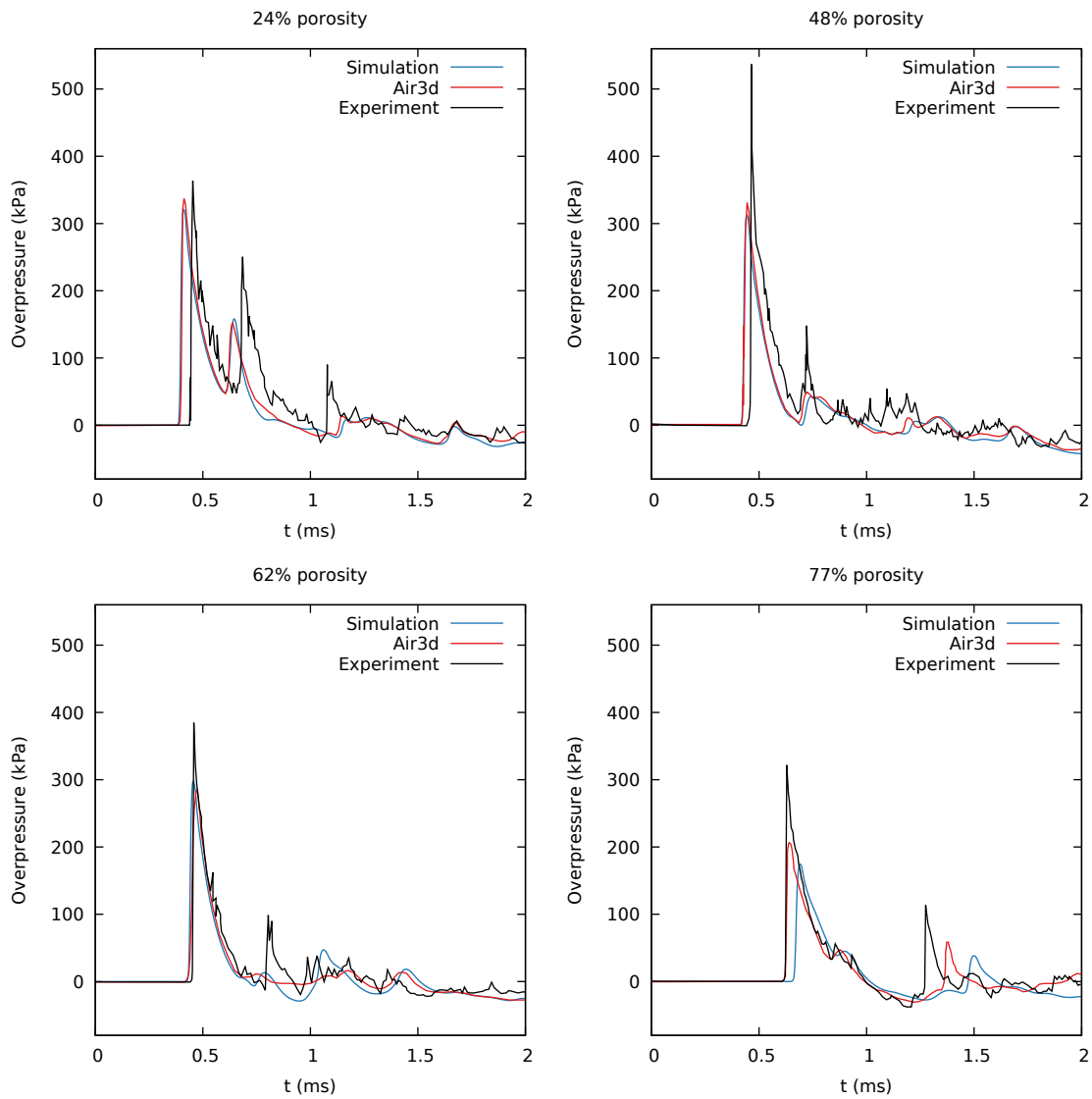


Figure 6.3: Pressure histories at gauge location 7 for 24 %, 48 %, 62 % and 77 % porosity.

the street that weakens and arrives later as the porosity is increased. The weakening occurs due to the increase in the area of openings in the building façade. This acts by venting the pressure from the street and weakening the overall wave. For the 24 % and 48 % configuration, the reflected wave is clearly visible in our simulation, with its strength and arrival time agreeing fairly well with experiment.

For the latter two porosities, the experimental setup was ambiguous. While the code has succeeded in capturing the strength of the reflected waves, the timings are slightly incorrect, suggesting a small setup mismatch with the experiment. Agreement with the author's Air3d code is generally excellent throughout. In general, peak heights appear to have been underestimated. This was also noted by the authors, having postulated that the original estimate of TNT equivalence may have been slightly in error.

In summary, we agree with the authors' conclusions that façade porosity has a significant impact on the strength of reflected waves. We have demonstrated a good agreement with the original experimental and numerical study, capturing the effects of porosity. Having demonstrated that the code is capable of simulating porosity, we shall continue by presenting a more detailed numerical study on the subject.

6.2 The effect of street width on blast propagation

In this section we perform the numerical study of Rose [70], investigating the effect of street width on the strength of the blast wave. We first repeat the study before extending it by including effects of porosity.

In his analysis, Rose devised a systematic way of studying how the effects of street width and building height affect the blast wave resultants when a charge is detonated in the middle of the street. Figure 6.4 shows two views of a street of width w and length l bounded either side by two buildings of height b and depth d . A hemispherical charge is located at the centre of the configuration. The inherent symmetry in the scenario means that the problem can be viewed in quarter space, reducing the computational expense.

Rose performed two separate studies: the first fixing the building height b to be effectively infinite and varying the street width w . In the second study, the author introduced a variable building height, studying how this parameter affected the blast wave resultants. We choose to implement the first study given the limited time available.

Four different street widths are used: $w = 8, 16, 24$ and 32 m. The building height b was chosen to be equal to the height of the computational domain, providing an

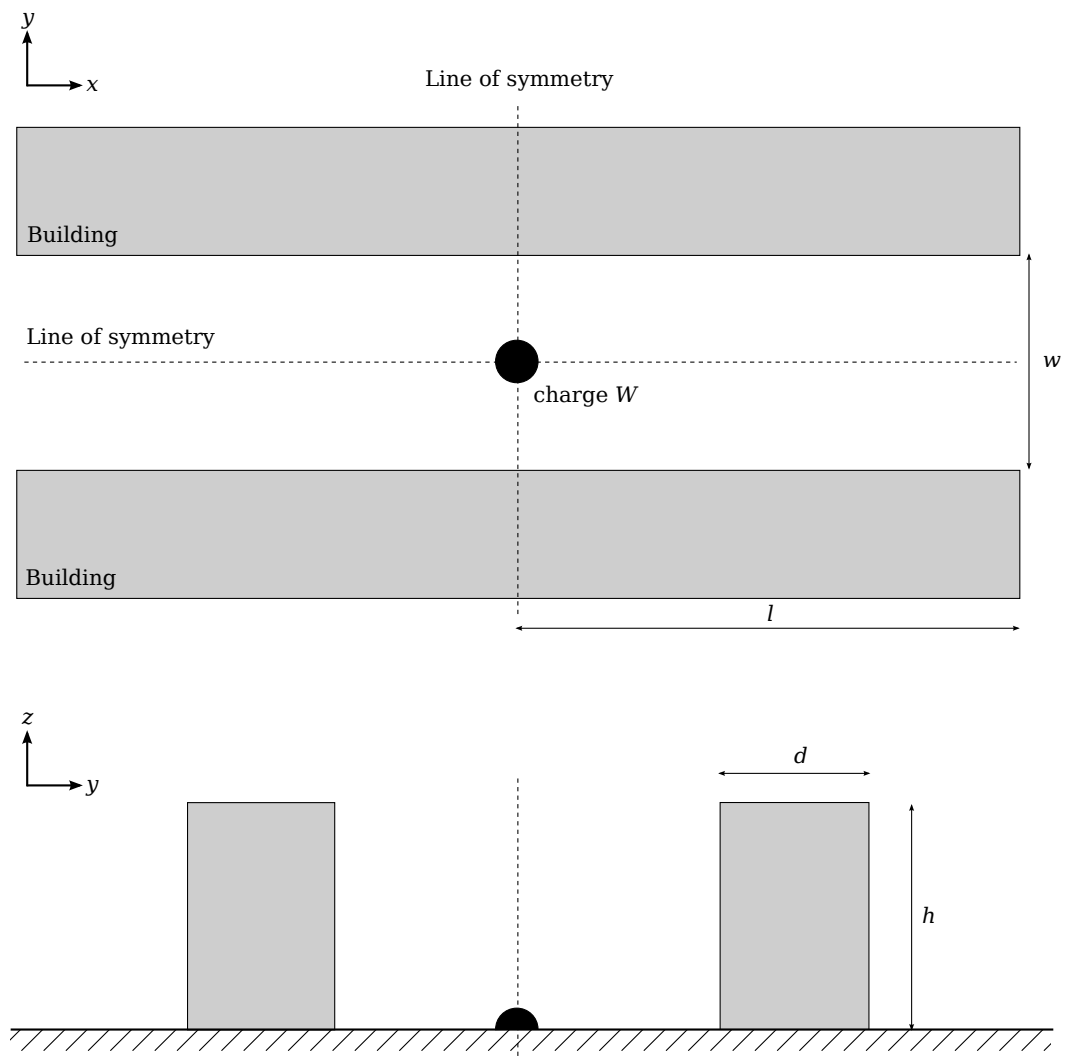


Figure 6.4: An illustration of the experimental setup for the street width simulation showing the building layout and symmetry.

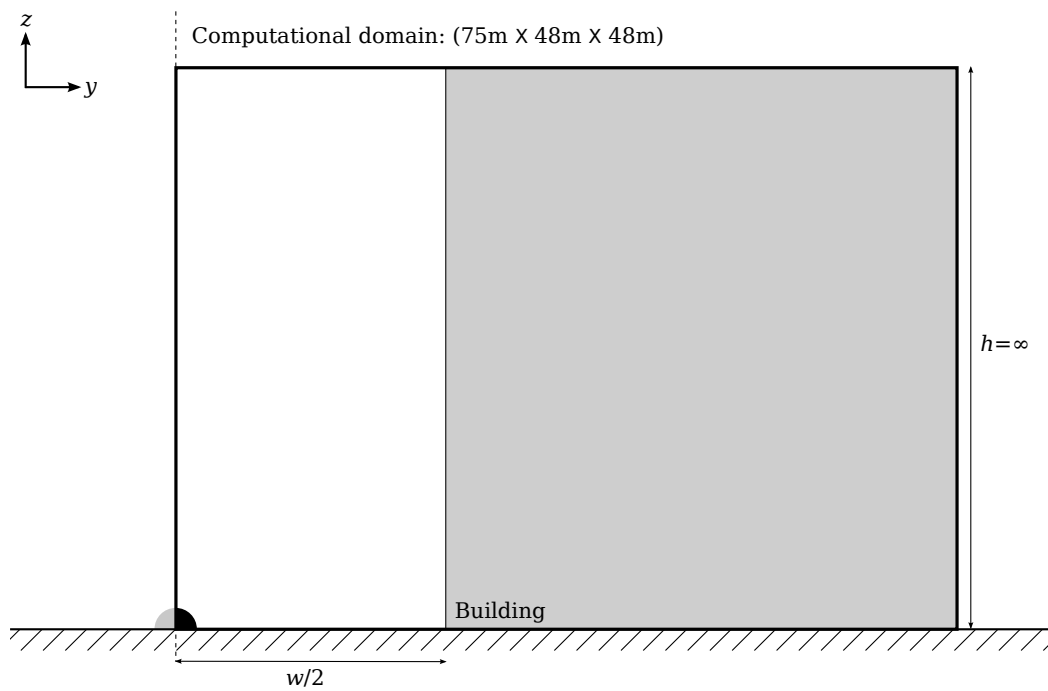


Figure 6.5: An illustration of the computational domain.

effective building height of infinity to remove any effects of clearing. The depth d of the building was also modelled as infinite by extending the building to the domain boundary. Figure 6.5 shows the computational domain measuring $(75\text{ m} \times 48\text{ m} \times 48\text{ m})$.

For each of the four analyses above, a further study was performed in half-space, in effect with only a single building. The pressures recorded were labelled *true reflected* pressures and were used as a comparison with the *street reflected* pressures from the quarter-space study. The idea being that the true reflected scenario represents the limiting case where the road with w is effectively infinite and the effects of channelling are not felt.

A series of pressure transducers were placed on the surface of the building along the length of the street. The gauges were placed at intervals of 5 m from $x = 0\text{ m}$ to $x = 50\text{ m}$ at a height of $z = 2\text{ m}$. The building was allowed to extend across the entire domain, providing an effectively infinite length l . This reduced the number of problem parameters and ensured that the effects of clearing were negated from the study.

The charge was modelled as a 1000 kg hemisphere of TNT located at the origin of the domain. By locating the charge on the ground, one dimensional symmetry could be obtained up to the building face. For each street width w , a one dimensional simulation with a resolution of 2 mm was run to a distance of $w/2$. In Rose's original study, computational restrictions limited him to a three dimensional resolution of 0.5 m which the author admitted was inadequate to sufficiently resolve the resulting peak pressures. In repeating this study, we improve on this, using a cell size of 0.125 m which is close enough to the optimum resolution of $1\text{ cm}/\text{kg}^{1/3}$ to yield a well converged solution.

It is worth mentioning that this initial study has previously been performed by Rose in his thesis. We will present our results in the same format as the author in order to verify our findings against his. Having satisfied ourselves that our conclusions agree, we will extend the study by introducing a building porosity.

6.2.1 Results

The effect of the street is to confine the blast wave, increasing the strength above the unconfined true reflected case. Therefore, the true reflected impulse serves as a lower bound for the street reflected cases as reflections from the other side of the street will not occur. Figure 6.6 shows the total impulse recorded at each gauge along the width of the building for both reflection types. Measurement is performed at street level ($z = 2\text{ m}$).

It is immediately obvious that the difference between these two curves varies

significantly with the width of the road. For the narrowest roads, the street reflected impulses are significantly higher than the true reflected impulses across the entire building length. As the road is widened and confinement is reduced, these effects are only experienced by the gauges further along the building. The widest street shows the most extreme example of this. The low confinement causes only the furthest 3–4 gauges to show any significant increase in impulse.

Whalen [167] proposed a method for quantifying the effect of confinement by defining an impulse amplification factor:

$$\text{Impulse amplification factor} = \frac{\text{Street reflected impulse}}{\text{True reflected impulse}}, \quad (6.1)$$

allowing him to measure the degree to which the confinement from the street leads to an increase in the impulse.

Figure 6.7 shows the results from figure 6.6 expressed in terms of this factor. For all street configurations, the amplification of the impulse increases with the distance from the charge. As confinement is reduced, the effect becomes less pronounced. For the widest road of width 32 m, the most severe increase in the street reflected impulse is approximately 50%. This contrasts with an increase of approximately 200% for the narrowest street.

Figures 6.6 and 6.7 clearly show that confinement has an amplifying effect on the impulse. Yet they do not explain how or why this effect occurs. To gain a better understanding we need to study the pressure histories from the gauges. Figures 6.8 and 6.9 show the histories for the 25 m and 50 m gauges from the 8 m and 32 m street widths respectively. The figures show that the main contribution to the variation in impulse is from the reflection of waves from the opposing building. In the narrowest streets, the reflections return with little delay and combine with the primary wave to form a single strong wave. As successive reflections combine, the wave strengthens relative to the unconfined case. In wider streets, the reflections take longer to return. The build-up in strength of the wave occurs further from the source and impulse amplification is only observed in the more distant gauges. Figure 6.9 shows these reflections: at 50 m from the source we observe a primary wave followed by two successive waves.

Another important factor that affects the impulse is the timing of the reflections. If a reflection were to occur during the expansion of the preceding wave, the overall contribution to the impulse may not amount to much. This can be seen at the 25 m gauge in figure 6.9, where the secondary wave arrives before the end of the primary wave.

In his thesis, the author concluded that, for narrow streets where the scaled width $w/W^{1/3} \leq 2 \text{ m/kg}^{1/3}$, reflections combine to form a single strengthened wave

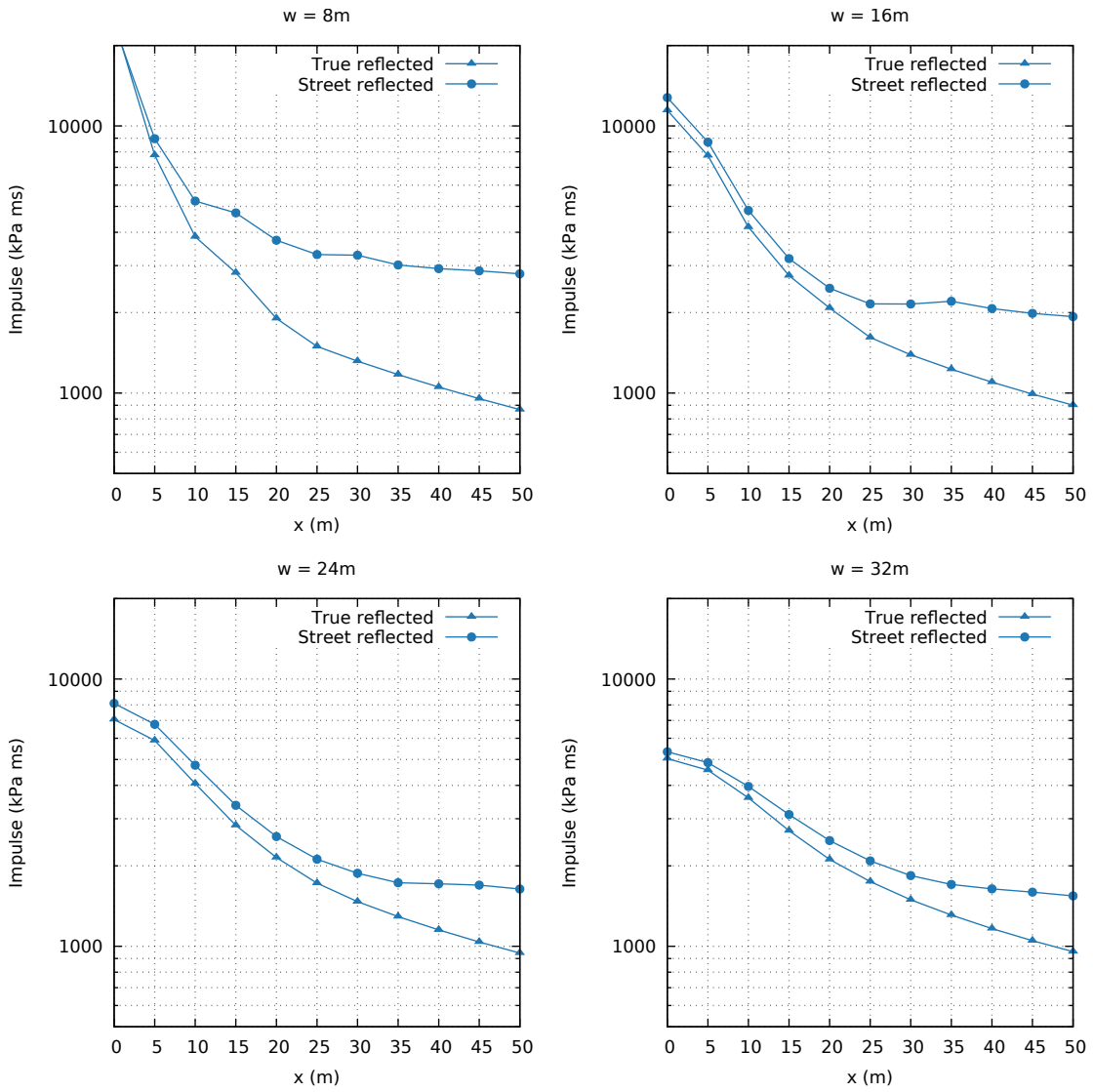


Figure 6.6: True reflected and street reflected impulse at street width $w = 8, 16, 24, 32$ m.

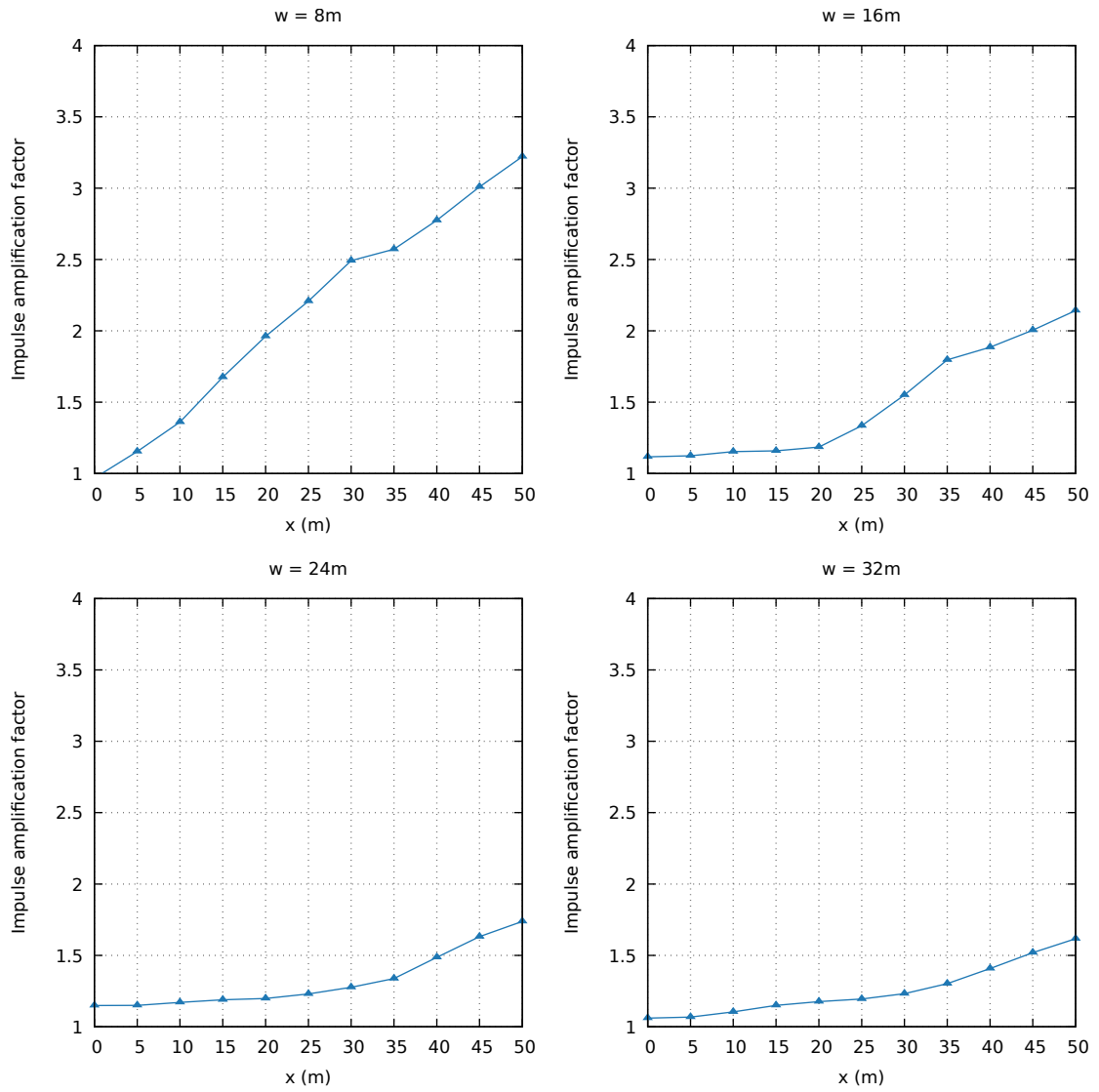


Figure 6.7: Impulse amplification factor at $z = 2\text{m}$.

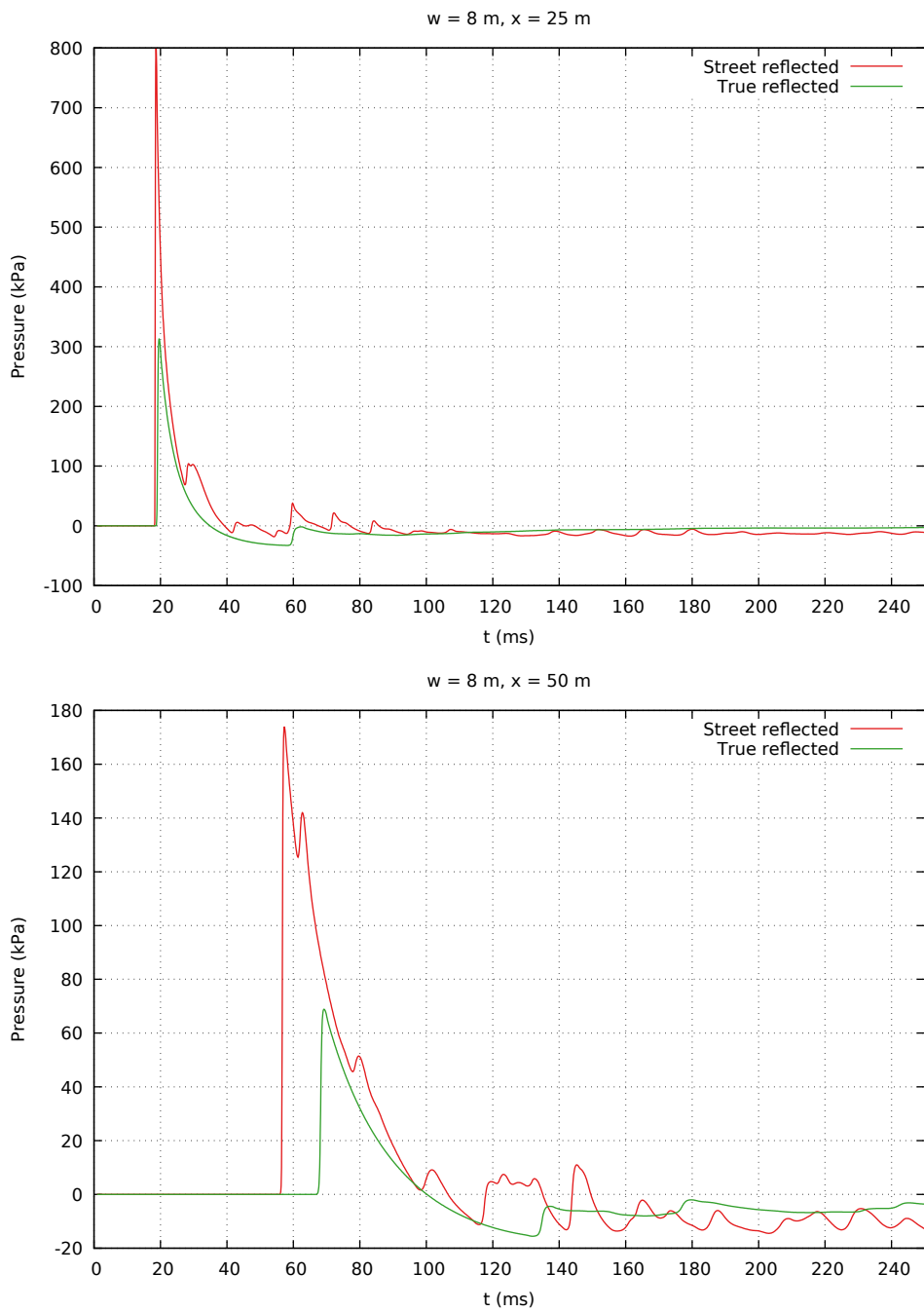


Figure 6.8: Gauge pressure history at $z = 2\text{ m}$ for the 8 m street width.

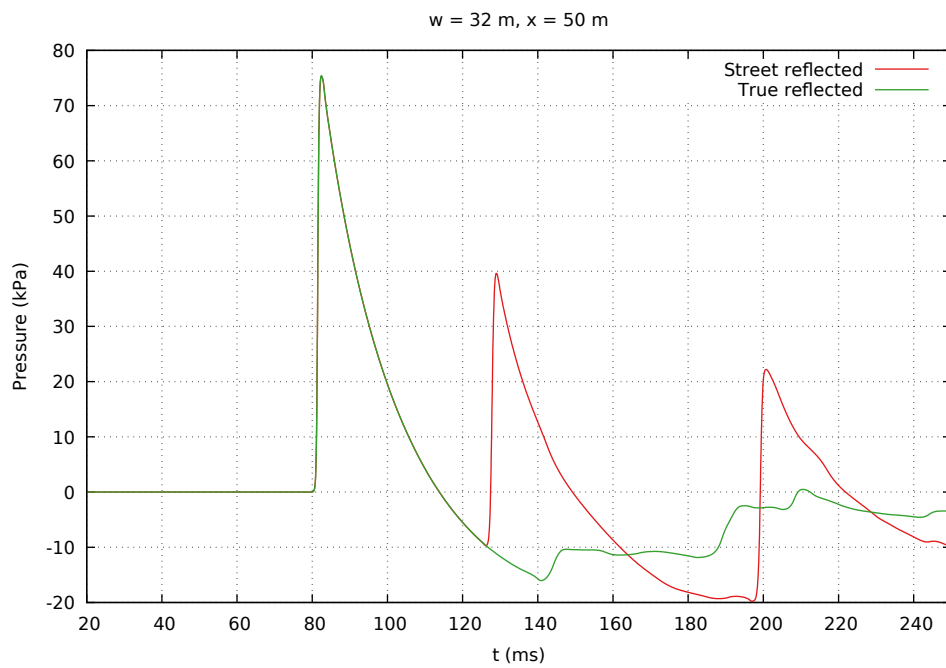
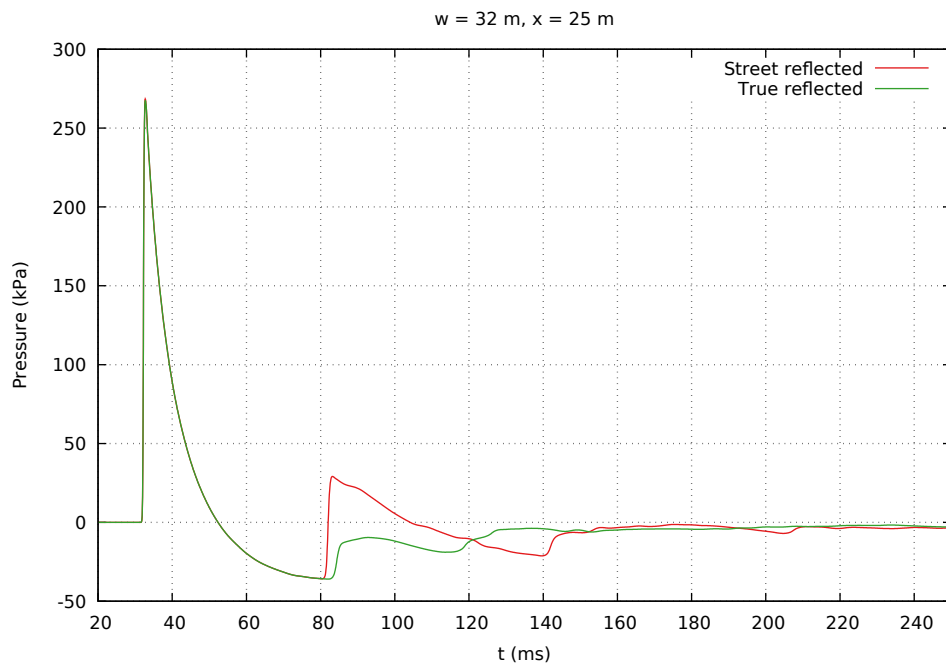


Figure 6.9: Gauge pressure history at $z = 2 \text{ m}$ for the 32 m street width.

which amplifies the impulse along the entire gauge array. For scaled widths where $w/W^{1/3} > 3.2 \text{ m/kg}^{1/3}$, the effects of confinement have little effect on the recorded impulse. Only at distances greater than $5 \text{ m/kg}^{1/3}$ along the street do reflections have any impact. The author also noted that buildings in the real world have a finite height, allowing for clearing effects to reduce the confinement even further. He concluded that it would be reasonable to expect no confinement effects when $w/W^{1/3} > 3.2 \text{ m/kg}^{1/3}$.

Our findings broadly agree with these conclusions. The only significant difference that we have observed is an increase in the predicted pressures and impulses as a result of the improved resolution used in the present study. Most figures exhibit an increase somewhere between 10 % and 50 %.

6.3 The effect of building porosity on blast propagation

Having demonstrated the confinement effects of city streets, we extend Rose's study incorporating the effects of building porosity. In the real world, buildings are not rigid, perfectly reflecting objects. When impinged upon by a blast wave it is common for windows to break and for the building to absorb some of the blast strength as the wave enters the building. How this affects the overall confinement effects of city streets is still largely unknown.

In their study, Smith et al. defined a building façade porosity as the percentage of the façade surface area that is devoted to windows. They conducted a study to determine typical building porosities local to their place of work, including notable international buildings that had been the subject of terrorist attacks [73]. The authors concluded that typical façade porosities varied between 20 % and 75 % for most modern buildings.

We repeat the study of section 6.2, using the same parameters before but with the addition of the following façade porosities: 0 %, 20 %, 45 % and 70 %. These cover most of the range of characteristics exhibited by buildings today.

An array of windows and floors was integrated into the building geometry of section 6.2. At each floor, 15 windows were placed across the length of the building. Each window had a height of 3.5 m and a floor thickness of 0.5 m, forming a storey height of 4 m. The overall porosity of the façade could be varied by controlling the width of each window. The quantity and position of these windows was held constant. The resulting 12 storey building is shown in figure 6.10. The rest of the numerical setup, including the charge mass and location, was identical to the previous study.

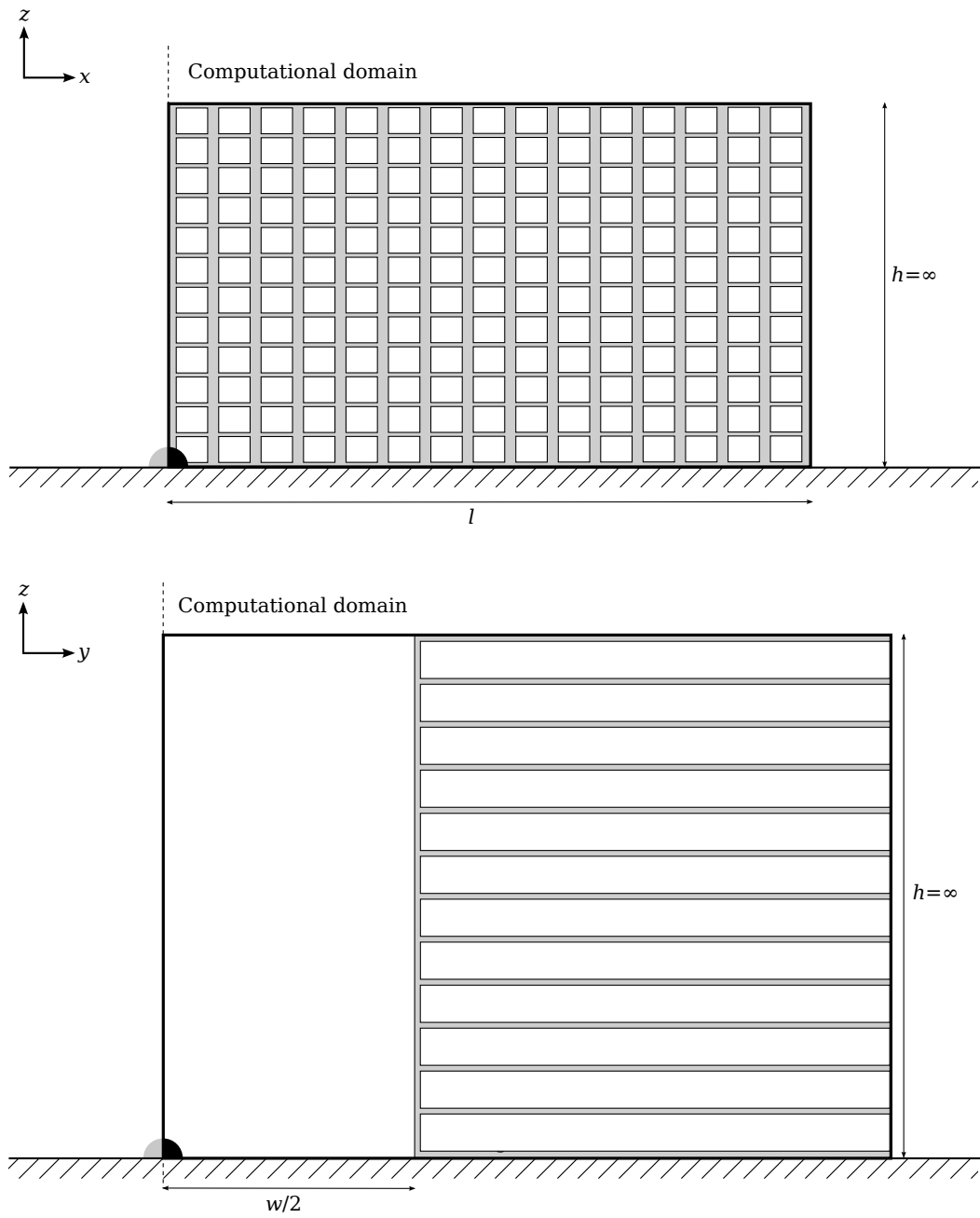


Figure 6.10: An illustration of the experimental setup for the street width simulation showing the building layout with a porous façade.

6.3.1 Results

Figure 6.11 shows the impulse amplification factor for four different façade porosities, ranging from non-porous to a porosity of 70 %. In the original study, the 8 m street showed the greatest impulse amplification due to the high level of confinement. This is still true for the porous façades. However, as the porosity increases, the amplification effect is weakened considerably. At 50 m from the source, the amplification drops from 3.2 at 0 % to 1.3 at 70 %. In other words, the porosity has reduced the effect of impulse increase provided by the confinement from 220 % to 30 %.

This effect is also observed in the widest road, although greatly reduced in strength as the confinement provided by the street is already minimal. Impulse amplification at the furthest gauge drops from 1.6 to 1.1 as the porosity increases. This means that the impulse at this point is only 10 % higher than the unconfined blast and the confinement effects of street width are almost negligible. The 8 m and 32 m street widths represent the two extreme situations of high and low confinement. The intermediate street widths show a gradual transition between these states.

Figures 6.12 and 6.13 show the 50 m pressure histories for the 8 m and 32 m streets with 45 % façade porosity. We compare these with the non-porous pressure histories in figures 6.8 and 6.9. Wave coalescence is still observed at both gauges in the 8 m street. However, the strength of the street reflected and true reflected waves is significantly diminished. In the true reflected simulation, the blast wave is allowed to partially clear through the façade, relieving much of the strength of the primary wave. In the street reflected case, the reflected wave has been diminished by ingress through the opposite building before returning. The impulse is still amplified, but the effect is less pronounced when compared with the 0 % porosity façade.

The non-porous study found that impulse amplification only occurred at the end of the 32 m street as successive wave reflections arrived. In figure 6.13 we can just make out the reflected wave at the 25 m gauge for the porous façade. However, its overall impulse is diminished. The 50 m gauge also shows a single, weak reflection rather than the two observed in the non-porous study. For the wide street, the lower degree of confinement combined with the porous façade results in minimal impulse amplification.

To summarise the findings, the impulse amplification factors were averaged along the length of the building and plotted against street width in figure 6.14 for each of the façade porosities. The red shaded box corresponds to the zone in which the amplification factor exceeds 1.3. This is generally accepted to be the region in which confinement has a significant effect on the impulse. For opaque façades, streets with a width below 30 m fall into this category. However, when we account for a typical

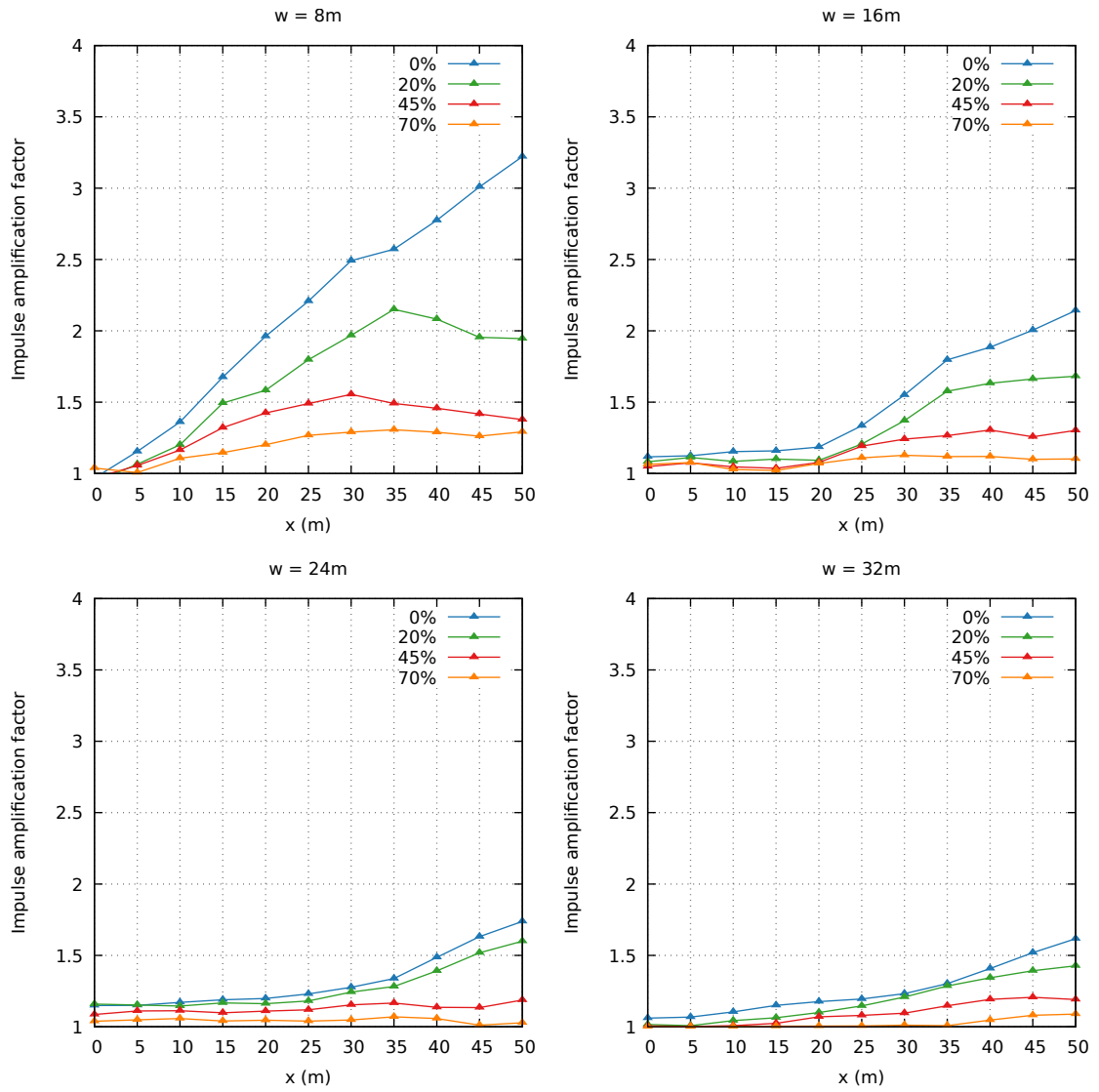


Figure 6.11: Impulse amplification factor at $z = 2m$ for a range of façade porosities.

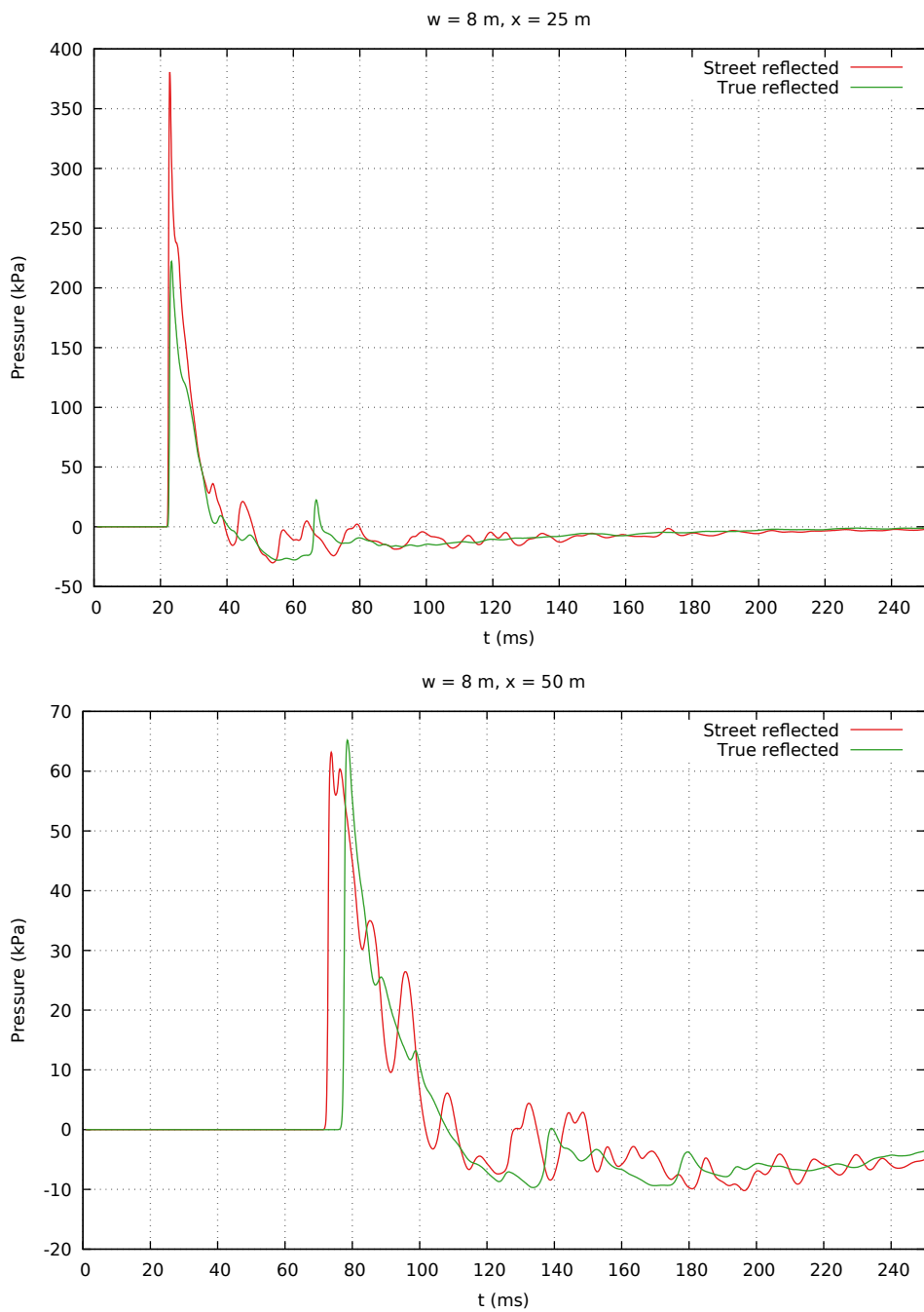


Figure 6.12: Gauge pressure history at $z = 2\text{ m}$ for the 8 m street width for the 45% porosity façade.

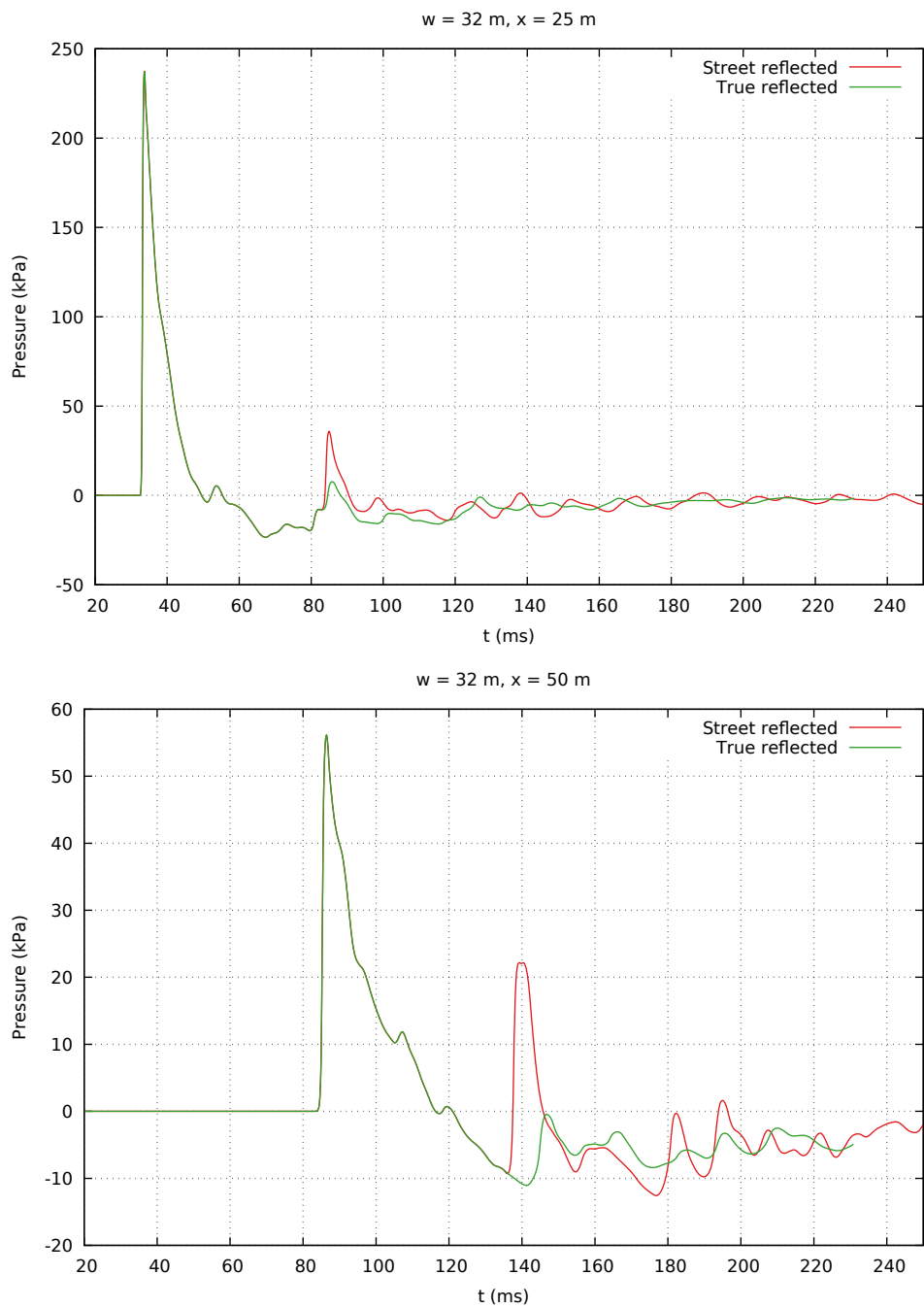


Figure 6.13: Gauge pressure history at $z = 2\text{ m}$ for the 32 m street width for the 45% porosity façade.

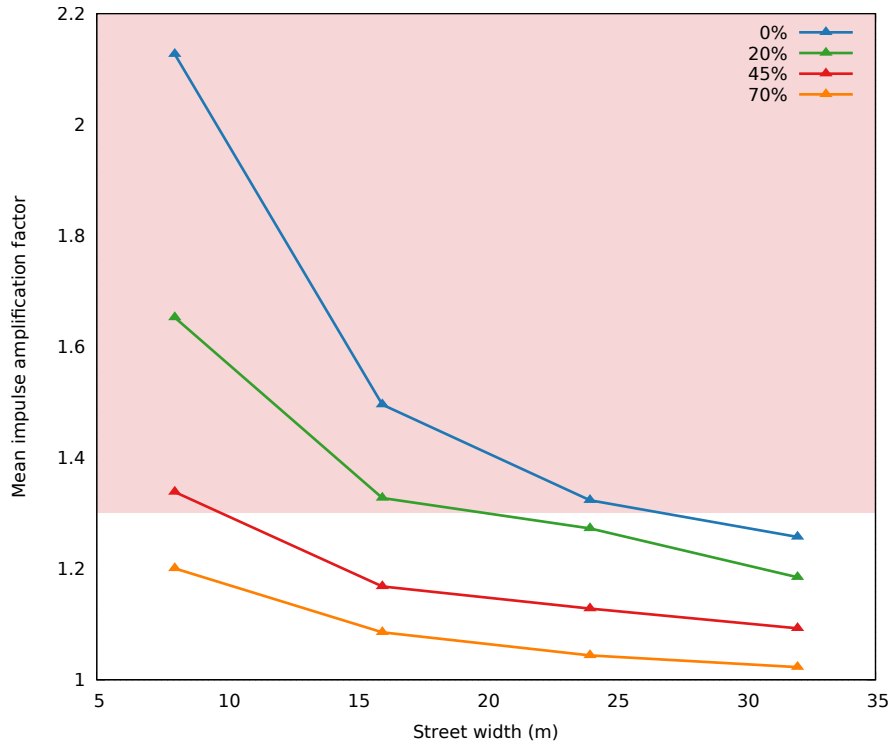


Figure 6.14: Mean impulse amplification factor vs. street width for a range of façade porosities.

45 % porosity façade, this figure changes substantially and significant confinement effects are only demonstrated for streets narrower than 8 m.

6.3.2 Comments and conclusions

In this study we considered the confinement effects of a range of scaled street widths from $w/W^{1/3} = 0.8 \text{ m/kg}^{1/3}$ to $3.2 \text{ m/kg}^{1/3}$. The scaled distance along the street varied from $0 \text{ m/kg}^{1/3}$ to $5 \text{ m/kg}^{1/3}$. The porosity of the buildings was varied between 0 % and 70 %.

In his study of non-porous buildings, Rose made the following conclusions:

- In narrow streets, reflections do not separate from the primary wave. Reflections coalesce and form a single, strengthened wave. This occurs for street widths $w/W^{1/3} \leq 2 \text{ m/kg}^{1/3}$.
- Wide streets with a scaled width $w/W^{1/3} > 3.2 \text{ m/kg}^{1/3}$ produce very little confinement.

Our extension of the original study has shown that Rose's first conclusion remains true for porous façades. Wave coalescence still occurs in narrow porous streets, although the strength of the coalesced wave reduces with increasing porosity.

Rose's second conclusion does not remain true when a façade porosity is introduced. The author states that the cut-off, above which a street fails to provide any significant confinement is at a scaled width of $3.2 \text{ m/kg}^{1/3}$. If we assume that the average building porosity is roughly 45 %, then equivalent confinement is produced by a porous street of width $0.8 \text{ m/kg}^{1/3}$. This suggests that the author's figure of $3.2 \text{ m/kg}^{1/3}$ is somewhat conservative when real buildings are considered. For the case of a 1000 kg charge, the effects of confinement are minimal when the street is wider than 8 m (in contrast to 32 m for non-porous façades). This has clear implications for the modelling of urban explosions, given that the width of most streets is close to 8 m.

In summary, the investigation has shown that the effect of façade porosity on the confinement of street blasts is significant and comparable to the effects of street width. Having better understood these phenomena, we recommend that façade porosity be taken into account when the urban cityscape features streets that lead to large discrepancies between the original study and the porosity model for a typical 45 % porosity façade. This is the case for streets of width $w/W^{1/3} < 3.2 \text{ m/kg}^{1/3}$. For wide streets, the effect of confinement is already minimal and any extra reduction in confinement from porous façades can probably be ignored.

It should be noted that a number of caveats exist:

- In our analysis, the windows were modelled as holes without any glass. In reality, a window will absorb some of the energy of the blast wave before shattering, reducing further the strength of the blast wave. This effect has been shown to exist, but studies have shown that its effect is minor compared to the overall effect of the porous façade [73].
- As Rose also notes, the maximum scaled distance down the street considered was $5 \text{ m/kg}^{1/3}$. In reality, blast wave resultants can still be hazardous to structures up to a distance of $30 \text{ m/kg}^{1/3}$. Given the computational and time resources available, it was not practical to investigate such distances.
- No consideration of building height was given. In reality, the clearing effects from the top of buildings will further reduce the confinement.
- In the real world, explosions do not normally occur in the centre of the street from an unobstructed hemispherical source. Recent terrorist attacks have seen confined explosives contained within vehicles or other structures such as bins.

Near-field confinement has been shown to significantly impact the propagation of the blast wave. However, the number of possible configurations makes including these effects impracticable.

A number of interesting extensions exist. One could study the effect of confinement at longer distances down the street (up to $30 \text{ m/kg}^{1/3}$). The inclusion of finite building heights would also be a useful addition to the knowledge base.

6.4 The effect of window layout on blast propagation

In the previous section, we showed that façade porosity has a significant negative effect on the level of blast confinement in an urban area. As the porosity of the façade increases, the strength of the blast wave in the street reduces as blast ingress occurs through the building exterior. This is beneficial for any structure or person unlucky enough to be located in the street. However, this poses a hazard for the occupants and the internal structure of the building being loaded.

As the porosity of the façade increases, the risk to the inhabitants from external blasts increases proportionately. The safest option would be to remove all windows, replacing the façade with a solid section of concrete or steel. Those inside would feel extremely safe but would no doubt be unhappy with the lack of daylight. The question then remains: how can we maximise the protective effects of the building exterior while maximising the amount of area devoted to windows?

Scientists have studied the effect of light interference for hundreds of years. Interactions between light waves can lead to a strengthening or weakening of the wave amplitude. The effect can lead to the complete cancelling out of the signal when two waves of equal wavelength and amplitude are displaced until their phases are exactly opposite. This phenomenon has also been shown to occur with acoustic waves, including blast waves.

A number of small-scale numerical and experimental studies have investigated the effects of wave attenuation on shock waves passing through solid obstacles. Rogg et al. [168], Shi and Yamamura [169], Seeraj & Skews [170], Chaudhuri et al. [82] and Berger et al. [171] all performed relevant studies. In their work the authors varied the nature of the obstruction by controlling the obstacle size, shape and spacing. The effect of the obstacles on the strength of the resulting wave was recorded, with some studies reporting an attenuation of more than 80 % for peak pressure and 30 % for impulse [171].

The above studies all used small-scale shock-tube induced waves which are of a rectangular shape, rising nearly instantaneously and maintaining a maximum

pressure for several seconds. This is very different to the triangular shape of the blast wave. Recent studies have focussed on studying the effect of wave interactions in blast walls. The investigations used experimental and numerical techniques to produce a blast wave from an explosive source. Notable studies have been performed by Niollet et al. [81] and Zong et al. [83].

In their study, Zong et al. investigated the concept of a fence-type blast wall, composed of shaped columns arranged in a regular array that was placed before the solid blast wall. This fence would attenuate some of the blast energy before it impacted the solid wall. The researchers performed a parameter study, varying the shape of the columns and the column spacing with the aim of maximising the attenuation as the waves passed between the columns. Their results indicated that column spacing has a significant effect on the wave propagation through the fence wall. Through optimal spacing and column shape, the researchers were able to achieve a reduction of blast loads by 70%.

Most office buildings have a regular layout of windows that forms a repeating semi-porous structure, much like the obstacles employed in the above studies. In this section we investigate whether, for a façade with a fixed porosity, the window layout can be optimised to maximise blast wave attenuation through wave diffraction. If this could be achieved, the protective effects of the façade could be maximised without any reduction of light entering the building.

We present a numerical investigation in which we use the same simulation setup from the previous street width study in section 6.3. A 1000 kg TNT charge is detonated in a confined street that is bordered either side by two porous office blocks of infinite height. We keep the street width and façade porosity constant. A narrow street of 8 m is chosen to maximise the confinement of the blast wave. A 40% façade porosity is used, representing a typical office block.

We add a 25 m wide structural core to the centre of the building. The core is located 10 m from the windows. A series of gauges at 0.5 m intervals is placed along the core on floors 1, 3, 5 and 7 (we denote floor 1 as the ground floor). These gauges will be used to measure the strength of the blast wave after it has penetrated the façade and impacted the core. A diagram of the building geometry in quarter space is shown in figure 6.15.

In this investigation, the number of windows per storey n is varied between four configurations: 5, 10, 20 and 30. As n changes, the façade porosity is fixed. The windows are spaced evenly along the building, with a height of 3.5 m and a variable width in order to maintain the porosity. While the blast wave has the same area to penetrate, the spacing between the windows changes.

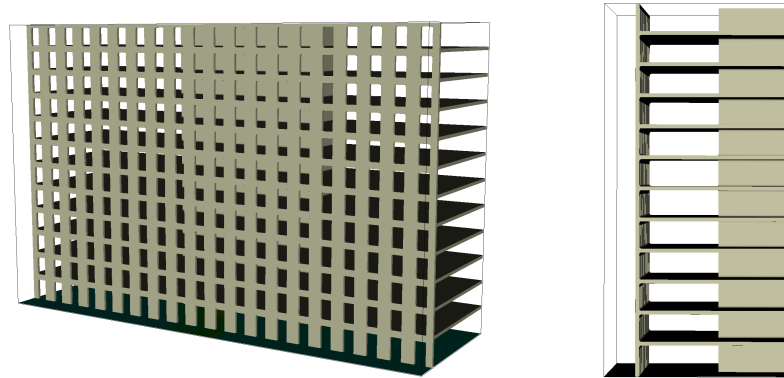


Figure 6.15: Front and side views of the computational domain featuring a twelve story office block with a fixed 40 % façade porosity and a structural core.

6.4.1 Results

Figure 6.16 shows the impulse experienced by the building core on floors 1, 3, 5 and 7 for each of the four window configurations (the core extends from $x = 25$ m to $x = 50$ m). A general trend is observed, indicating that as the number of windows increases (equivalent to the spacing between the windows decreasing) the total impulse decreases. The trend is greatest when comparing the 5 and 10 window configurations. No significant decrease in impulse is observed for $n > 20$. At the higher floors, the overall impulse reduces due to the greater distance from the charge. However, the same variation of the impulse with n occurs.

At each floor level, the following impulse amplification factor was calculated for a window number n :

$$AF_n = \frac{I_n}{I_{n=5}}, \quad (6.2)$$

where I_n is the impulse for the n window configuration averaged across the gauges on the building core. Figure 6.17 shows the relationship between this factor and n for each floor. By reducing the spacing between the windows, a significant reduction in the impulse has occurred. In the most extreme case the reduction is greater than 25 %.

The figures suggest an interesting effect, but do not explain its origins. To gain a better understanding we study the pressure history on the surface of the building core. Figure 6.18 shows the pressure recorded from a fifth floor gauge mounted on the core at $x = 30$ m. The size and shape of the primary peak is broadly the same for all window quantities n , suggesting that the window spacing does not have a significant effect on the strength of the primary blast wave.

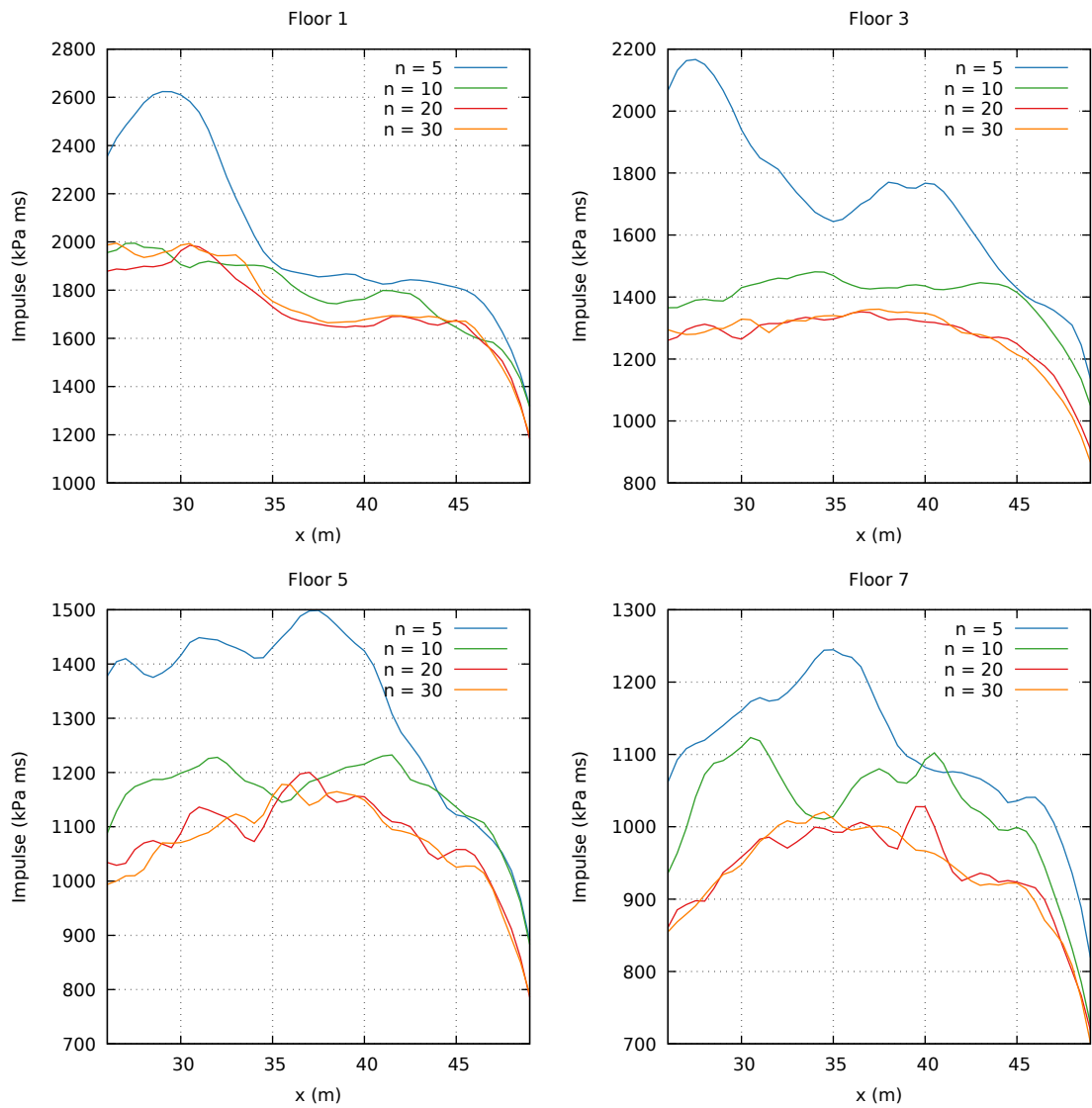


Figure 6.16: Interior impulse for a 40% porosity façade with n windows.

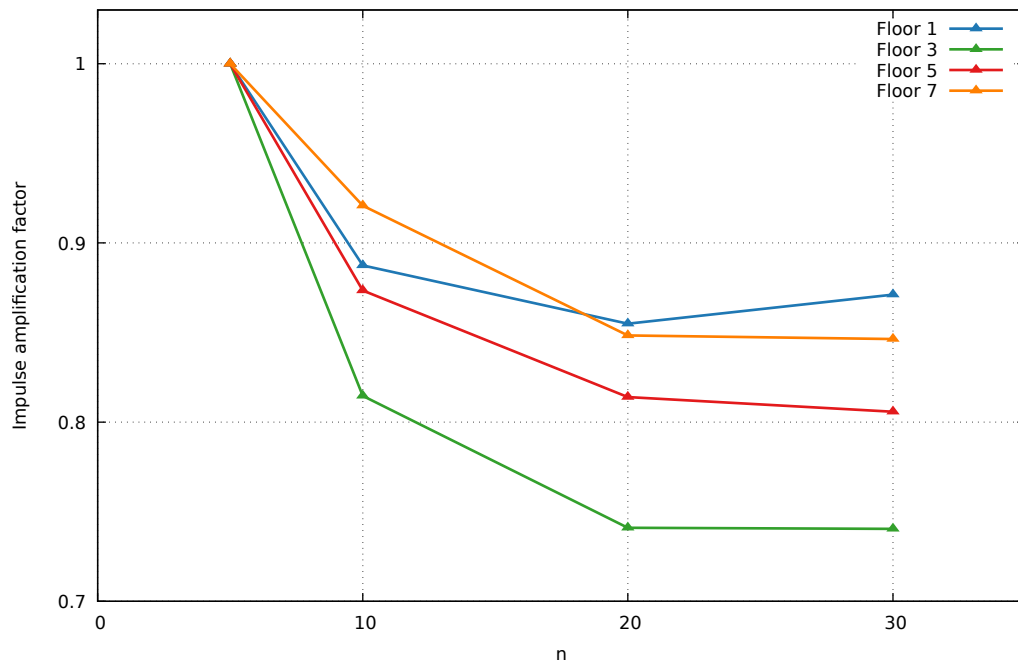


Figure 6.17: Variation of average impulse amplification factor with number of windows n .

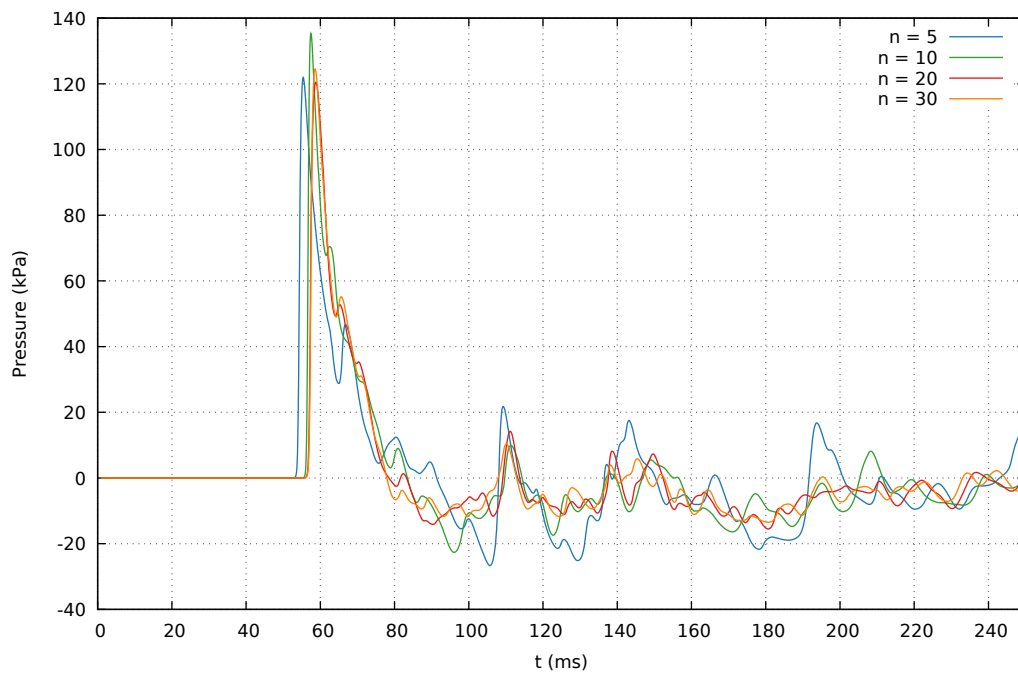


Figure 6.18: Pressure history on the surface of the building core at $x = 30$ m, floor 5.

For the $n = 5$ configuration, figure 6.18 shows a number of weaker secondary waves that trail the primary wave. Each peak on the graph represents a wave that has travelled through one of the windows. Using the Huygen's principle, we can describe each window as a spherical blast wave source. As the primary blast wave travels along the exterior of the building, the wave penetrates each window in succession. Diffraction occurs and a nearly spherical wave is created on the interior side of the window.

This process is illustrated in figures 6.19 and 6.20 where a numerical pressure schlieren is shown for each configuration. For $n = 5$, we observe 3 distinct waves inside the building. The first strikes the gauge without having interacted with the other waves. The waves that follow interact with one another which reduces their strength. As the number of windows increases, more waves are produced and the number of interactions increases, further reducing the strength of these waves. We can see from the pressure history in figure 6.18 that for $n > 20$, the number of windows is sufficiently high to provide considerable damping of the secondary waves. This leads to the reduction in impulse observed at the building core.

We can express this result more generally in terms of windows per metre, where the following figures were considered: 0.07 m^{-1} ($n = 5$), 0.13 m^{-1} ($n = 10$), 0.27 m^{-1} ($n = 20$) and 0.40 m^{-1} ($n = 30$). For window densities above 0.27 m^{-1} we observe a high degree of impulse reduction.

6.4.2 Comments and conclusions

In this study we considered the effect of window layout on blast wave resultants that penetrated a building following an external explosion of a 1000 kg TNT charge. Street width and façade porosity were fixed at 8 m and 40 % respectively. The window density was varied between 0.07 m^{-1} ($n = 5$) and 0.40 m^{-1} ($n = 30$) and the impulse along the central building core was recorded by a series of gauges across different floors. There are a number of important results:

- The effect of window density does not significantly affect the strength of the primary wave. However, there is a large impact on the secondary waves. As the window density is increased, more wave interactions occur behind the primary wave. This dampens the secondary waves, reducing the overall impulse.
- The effect of window-induced damping has been shown to be most effective for window densities of 0.27 m^{-1} . Above this, no significant improvement in impulse reduction is observed.

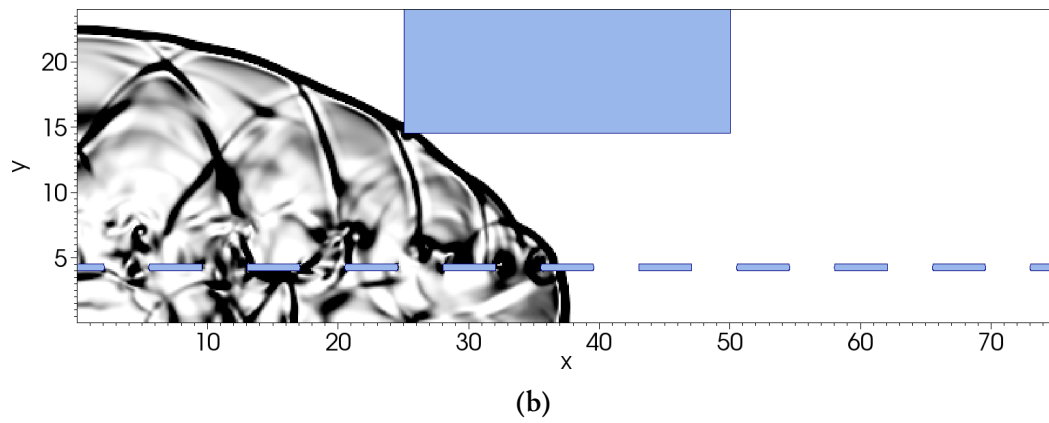
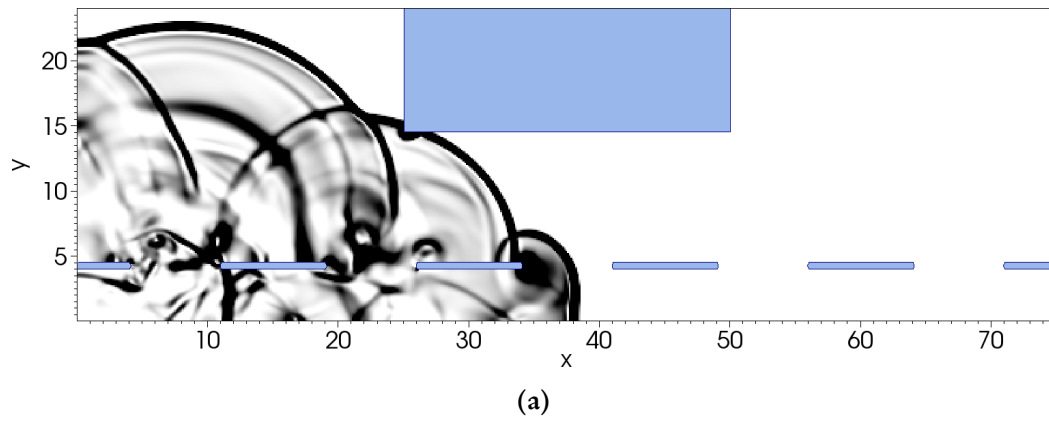


Figure 6.19: Numerical schlieren for (a) $n = 5$ and (b) $n = 10$ on floor 5 at $t = 50$ ms.

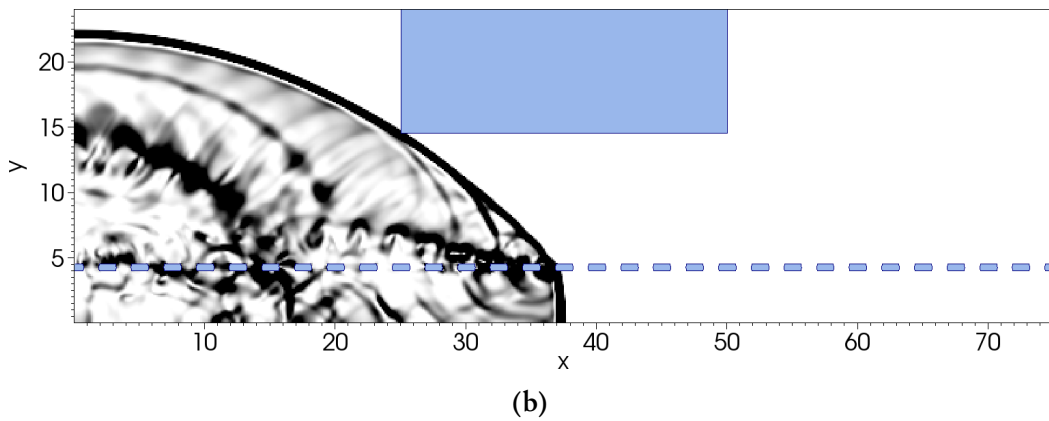
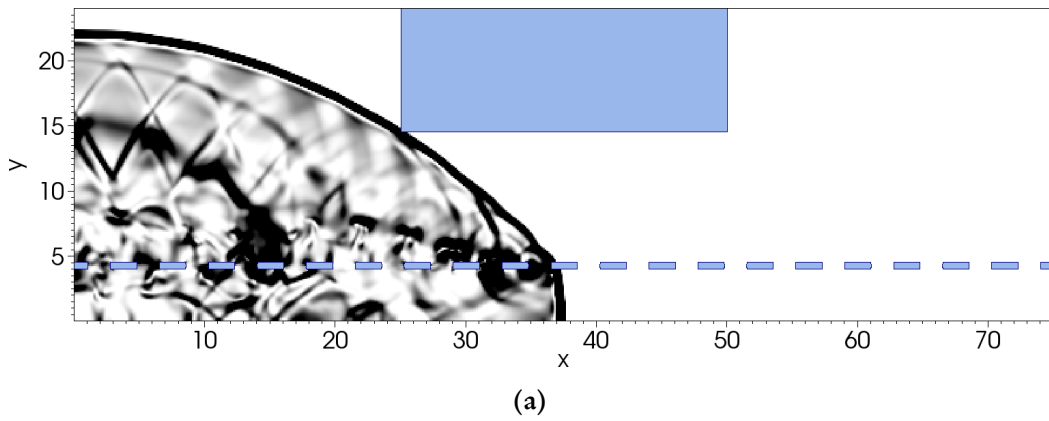


Figure 6.20: Numerical schlieren for (a) $n = 20$ and (b) $n = 30$ on floor 5 at $t = 50$ ms.

The effect of charge size and building porosity on these findings is not immediately obvious. A repeat of the study for façades of different porosities would be an interesting extension. In their work, Zong et al. trialled a range of shaped obstructions, finding that circular and triangular columns with a vertex facing the explosion offered the best protection against an explosion [83]. By altering the shape of the window frames, a future study might investigate whether such improvements could be found.

6.5 Conclusion

In this chapter we studied the effect that urban geometry has on the propagation of blast waves through city streets. Having validated the code for an experimental porosity experiment, we repeated the study of Rose, investigating the effect of street width on blast wave resultants. The original author was unable to perform the study at a sufficiently high resolution. By running the study at a converged resolution, we found that the strength of the blast wave resultants in the street had originally been underpredicted. However, Rose's conclusion that no significant confinement effects exist for scaled, non-porous street widths $w/W^{1/3} > 3.2 \text{ m/kg}^{1/3}$ was found to remain correct.

The study was extended by introducing a tuneable façade porosity that varied between 0 % and 70 %. It was found that façade porosity has just as much effect on confinement as the width of the street. For a common façade porosity of 45 %, a drastic reduction in confinement occurred. No significant confinement effects were found to exist for scaled street widths $w/W^{1/3} > 0.8 \text{ m/kg}^{1/3}$. This finding suggests that previous research has significantly overestimated the effects of confinement from streets because building porosity has not been considered.

In the following study, the simulation was repeated with a fixed façade porosity of 40 % and a street width of 8 m. By varying the window density, it was found that the strength of the blast resultants recorded inside the building could be reduced by more than 25 % through the cancellation of secondary waves by destructive interactions. This effect was most pronounced for window densities of 0.27 m^{-1} .

We recommend that façade porosity be taken into account when performing threat assessments in urban areas where the scaled street width $w/W^{1/3}$ is less than $3.2 \text{ m/kg}^{1/3}$. This will allow engineers to provide damage estimates that are more accurate and less conservative. We also recommend that the design of new buildings takes window density into account. Through judicious placement of windows, it is possible for architects to maximise the protective effect of façades without sacrificing

the amount of light entering the building.

We have shown that façade porosity is an important effect which should be taken into account for most cityscapes. The prediction of this phenomenon can only be achieved by solving the equations of fluid flow around the geometry. This brings us to another key benefit of CFD methods: their ability to implicitly capture façade porosity.

For future work we recommend the development of a new building porosity model to improve the prediction of façade porosity effects. This could be achieved by defining a new form of material interface at the building boundary. By developing a modified Riemann solver, an interface could be created which permits a fraction of the blast energy to propagate into the building, reflecting the rest. This would not only bring the benefit of improving the accuracy of street pressures, but also the ability to model the propagation of blast waves and subsequent losses within buildings. We would also recommend extending the window layout study over a range of façade porosities and street widths to deduce whether the earlier findings remain correct.

Chapter 7

Conclusions and further work

IN this thesis we have explored the benefits of a CFD-based approach to urban blast simulation. By carrying out comparative studies, and quantifying improvements in accuracy compared with empirical methods, we have demonstrated the clear advantage of embracing these methodologies. We have also demonstrated the importance of capturing the effects of façade porosity, which is only possible with CFD. Through the use of cut-cell meshing and improvements to the AMR process, we dismantled some of the barriers impeding the uptake of these methods. In the paragraphs that follow, we summarise the main conclusions of the thesis.

Shock capturing using adaptive mesh refinement

We have made a range of improvements to our AMR approach, with the overall aim of making the method more robust and easier to use for the non-expert. This study was motivated by a desire to address some of the main shortcomings of AMR: the inefficiencies of existing methods arising from an inability to restrict refinement to the necessary flow regions, and the difficulty for the user to tune the AMR parameters to maintain appropriate refinement for the duration of the simulation.

We began by studying the sensitivity of the solution to the mesh resolution and the number of cells across the radius of the charge. A recommended cell size of $1 \text{ cm/kg}^{1/3}$ was proposed along with a cell count of 50 cells across the charge radius. It was found that this figure could be relaxed to just 5 cells without negatively affecting the solution.

We introduced a new flagging criterion which was based on a second-derivative error norm and a divergence check for compressive shocks (ENCs). The approach has two major advantages over current methods: The divergence check ensures that

the method is applied only to compressive shocks, avoiding unnecessary refinement of rarefactions. Secondly, the combination of this check with an error norm allows the method to track shocks over longer distances than is currently possible with difference flagging.

A series of 1D, 2D and 3D numerical tests were performed using ENCS and the results were compared with uniform grid and difference flagging calculations. The results showed no negative impact on the solution from the new scheme's limitation of refinement to shocks. The new approach also displayed superior feature tracking over longer distances than existing methods, indicating that the method is less sensitive to changes in the tolerance. The implication of these results for the user is the following: because the method minimises unnecessary refinement, the overall cost of the simulation is reduced. In addition to this, the robust feature tracking and lower sensitivity to tuning makes it easier to choose a flagging tolerance which maintains refinement for the duration of the simulation and avoids simulations having to be rerun because of insufficient refinement at later stages.

A key hurdle in the adoption of CFD methods for blast simulation has been their computational expense and the fact that they are seen to be difficult to use. The improvements to our AMR approach have made the benefits of AMR easier to achieve for the non-expert. The cut-cell approach, upon which the code is built, removes the mesh generation bottleneck and makes the process of working with complex geometries simpler than with many equivalent codes today.

Blast damage in urban cityscapes

We studied the effects that blast waves have on urban structures in their path. We began the chapter with a validation study involving a simple case of blast-structure interaction. We extended the study to account for a simplified city street configuration. In both studies it was found that the combined effects of channelling and clearing produced a complex, non-intuitive distribution of blast resultants around the geometry, something that would not be possible to predict without a CFD method.

We extended the study a step further to account for realistic urban geometry, investigating the effect of charge placement on the outcome of a full-scale urban blast. A scenario involving an explosion next to an urban park was considered, and blast resultants were predicted using a CFD and an empirical method. When the charge was displaced a small distance, a disproportionate change in the distribution of blast resultants in the park was observed because of the effect of urban layout. The study concluded that the distribution of damage is highly sensitive to the location of the

explosive. In contrast to the CFD method, the empirical approach failed to capture this sensitivity because of its inability to account for urban geometry.

The work was followed by a comparative study of a CFD and two empirical approaches for predicting losses from a hypothetical terror scenario. A van containing high explosive was detonated in the City of London. Two empirical models and a CFD model were used to predict dollar value human loss, property loss and business interruption. A simple method for the determination of interior damage by means of a façade attenuation factor was also presented. Because the CFD model accounted for the effects of the urban geometry, the blast wave was found to propagate differently to the predictions of the empirical models which had assumed a much greater distribution of damage.

The use of the CFD method led to a reduction in property loss estimates by at least 55 %, business interruption by nearly 70 % and total human loss by approximately 60 %. When a correction was applied to the CFD human loss model accounting for greater protection inside the centre of buildings, the reduction increased to over 90 %. The reductions in risk are significant, corresponding to hundreds of millions of pounds for the scenario considered.

The findings of the study suggest that, while empirical approaches may be simpler to use than CFD methods, they significantly overestimate loss in urban situations. This is because of their inability to capture the effects of the urban geometry. We did not attempt to predict the savings that CFD methods might afford the industry through less conservative loss estimates. However, the significant differences in loss estimates between the models presents a strong argument for the widespread adoption of CFD.

The effect of urban geometry on blast resultants

In this chapter we studied the effect that urban geometry has on the propagation of blast waves. We began by replicating the numerical study of Rose [70] in which the author studied the confinement effects of different sized streets on blast wave resultants. Rose encountered technical limitations that meant the study could not achieve a high enough resolution for a sufficiently converged result. We repeated the analysis with the correct cell size and found that the extra resolution led to an increase in the predicted peak pressures and impulses, compared to the original study. Rose's main conclusion that confinement effects are significant for scaled street widths $w/W^{1/3} < 3.2\text{m/kg}^{1/3}$ was found to be correct.

The study was extended by introducing a scalable façade porosity into the build-

ings. The porosity of the façade was found to offset the confinement effects of the narrow street. The magnitude of this effect was shown to be significant and was equivalent in scale to the effects of street confinement on the propagation of the blast wave. For a common façade porosity, the predictions of Rose were revised and no significant confinement effects were observed for scaled street widths $w/W^{1/3} > 0.8\text{m/kg}^{1/3}$.

A further study was performed in which a fixed porosity was assigned to the façade and the number of windows was varied. By optimising window layout, the strength of blast resultants inside the building was reduced by up to 25%. This suggests that it is possible to arrange windows in such a way as to maximise the protective effects of the façade without reducing the amount of light that enters the building.

The findings of this chapter suggest that façade porosity is an important feature of urban geometry because of the significant effect it has on blast propagation. Empirical methods are unable to take this phenomenon into account, and strengthen the argument for the adoption of CFD for urban blast.

7.1 Further work

In this thesis we demonstrated the profound effect that building porosity has on the evolution of blast resultants in urban cityscapes. We recommend the integration of an improved building porosity model into the method. A new, semi-porous boundary condition could be defined at the building façade. By incorporating a tunable parameter, the interface could admit a fraction of the incident blast energy into the building while reflecting the rest. This would lead to significantly improved estimates of damage inside the building, and a better prediction of blast propagation within the streets.

Further work could be done to make AMR easier to use. During simulation setup, the user must choose the number of AMR levels and the refinement factors between each level. This process could be automated if a better understanding was reached of how to optimise AMR performance. By specifying the charge size and location, the code would then generate an AMR hierarchy that minimises overall computational cost, while maintaining the recommended resolution around the charge and shock.

Bibliography

- [1] Oklahoma City Police Department, “Alfred P. Murrah Building Bombing - After Action Report,” tech. rep.
- [2] E. Zinner and M. Williams, *When A Community Weeps: Case Studies In Group Survivorship*. Routledge, 2013.
- [3] “Vulnerability Assessment of Federal Facilities,” tech. rep., United States Department of Justice, 1995.
- [4] “Statistical Information on Terrorism in 2015,” tech. rep., U.S. Department of State, 2016.
- [5] A. Gray, “A year of global terrorism, captured in one map,” tech. rep., World Economic Forum, 2016.
- [6] M. M. Swisdak, “Simplified Kingery Airblast Calculations,” tech. rep., Naval Surface Warfare Center, MD, USA, 1994.
- [7] J. Britt, D. Ranta, and C. Joachim, *BlastX code, version 4.2, user’s manual*. 2001.
- [8] P. Wager, *Shock User’s Manual Version 1.0*. 2005.
- [9] D. Hyde, “ConWep - Application of TM 5-855-1. Fundamentals of Protective Design for Conventional Weapons,” tech. rep., Structural Mechanics Division, Structures Laboratory, USACE, Vicksburg, MS, USA, 1992.
- [10] A. Remennikov, “A Review of Methods for Predicting Bomb Blast Effects on Buildings,” *Journal of Battlefield Technology*, vol. 6, no. 3, pp. 5–10, 2003.
- [11] J. von Neumann and R. D. Richtmyer, “A method for the numerical calculation of hydrodynamic shocks,” *Journal of Applied Physics*, vol. 21, no. 3, pp. 232–237, 1950.

- [12] P. D. Lax, “Weak solutions of nonlinear hyperbolic equations and their numerical computation,” *Communications on Pure and Applied Mathematics*, vol. 7, no. 1, pp. 159–193, 1954.
- [13] H. Brode, “Numerical solutions of spherical blast waves,” *Journal of Applied Physics*, vol. 26, no. 6, pp. 766–775, 1955.
- [14] H. Brode, “Blast Wave from a Spherical Charge,” *Physics of Fluids*, vol. 2, no. 2, pp. 217–229, 1959.
- [15] H. Hao, Y. Hao, J. Li, and W. Chen, “Review of the current practices in blast-resistant analysis and design of concrete structures,” *Advances in Structural Engineering*, vol. 19, no. 8, pp. 1–31, 2016.
- [16] N. Wood, *Catastrophe modelling in the insurance industry - Market research report*. DaVinci Ventures, 2015.
- [17] E. F. Toro, *Riemann solvers and numerical methods for fluid dynamics*. Springer, 3rd ed., 2009.
- [18] B. V. Leer, “Towards the ultimate conservative difference scheme III. Upstream-centered finite-difference schemes for ideal compressible flow,” *Journal of Computational Physics*, vol. 23, no. 3, pp. 263–275, 1977.
- [19] B. V. Leer, “Towards the ultimate conservative difference scheme. IV. A new approach to numerical convection,” *Journal of Computational Physics*, vol. 23, no. 3, pp. 276–299, 1977.
- [20] B. V. Leer, “Towards the ultimate conservative difference scheme. V. A second-order sequel to Godunov’s method,” *Journal of Computational Physics*, vol. 32, no. 1, pp. 101–136, 1979.
- [21] B. V. Leer, “On the relation between the upwind-differencing schemes of Godunov, Engquist-Osher and Roe,” *SIAM Journal on Scientific and Statistical Computing*, vol. 5, no. 1, pp. 1–20, 1984.
- [22] J. J. Quirk, “An alternative to unstructured grids for computing gas dynamic flows around arbitrarily complex two-dimensional bodies,” *Computers & fluids*, vol. 23, no. 1, pp. 125–142, 1994.
- [23] J. Zhou and D. Causon, “Numerical solutions of the shallow water equations with discontinuous bed topography,” *International Journal for Numerical Methods in Fluids*, vol. 38, no. 8, pp. 769–788, 2002.

- [24] K. Nordin-Bates, “Grid Generation and Adaptation - Lecture Notes,” 2010.
- [25] E. Atta and J. Vadyak, “A grid overlapping scheme for flowfield computations about multicomponent configurations,” *AIAA journal*, vol. 21, no. 9, pp. 1271–1277, 1983.
- [26] J. Benek, J. Steger, F. Dougherty, and P. Buning, “Chimera. A Grid-Embedding Technique.,” tech. rep., Air Force Systems Command, U.S Air Force, 1986.
- [27] G. Chesshire and W. Henshaw, “Composite overlapping meshes for the solution of partial differential equations,” *Journal of Computational Physics*, vol. 90, no. 1, pp. 1–64, 1990.
- [28] J. Thompson, B. Soni, and N. Weatherill, *Handbook of Grid Generation*. CRC Press, 1999.
- [29] G. Chesshire and W. D. Henshaw, “A Scheme for Conservative Interpolation on Overlapping Grids,” *SIAM Journal on Scientific Computing*, vol. 15, no. 4, pp. 819–845, 1994.
- [30] E. Pärt-Enander and B. Sjögreen, “Conservative and non-conservative interpolation between overlapping grids for finite volume solutions of hyperbolic problems,” *Computers & fluids*, vol. 23, no. 3, pp. 551–574, 1994.
- [31] L. Wang and D. Caughey, “A multiblock/multigrid Euler method to simulate 2D and 3D compressible flow,” in *31st Aerospace Sciences Meeting*, p. 332, 1993.
- [32] W. Henshaw and D. Schwendeman, “Moving overlapping grids with adaptive mesh refinement for high-speed reactive and non-reactive flow,” *Journal of Computational Physics*, vol. 216, no. 2, pp. 744–779, 2006.
- [33] R. P. Fedkiw, T. Aslam, B. Merriman, and S. Osher, “A Non-oscillatory Eulerian Approach to Interfaces in Multimaterial Flows (the Ghost Fluid Method),” *Journal of Computational Physics*, vol. 152, no. 2, pp. 457–492, 1999.
- [34] R. P. Fedkiw, T. Aslam, and S. Xu, “The Ghost Fluid Method for Deflagration and Detonation Discontinuities,” *Journal of Computational Physics*, vol. 154, no. 2, pp. 393–427, 1999.
- [35] S. Millmore, *Interfaces in Numerical Relativistic hydrodynamics*. PhD thesis, University of Southampton, 2010.

- [36] R. Klein, K. R. Bates, and N. Nikiforakis, “Well-balanced compressible cut-cell simulation of atmospheric flow,” *Philosophical transactions. Series A, Mathematical, physical, and engineering sciences*, vol. 367, no. 1907, pp. 4559–75, 2009.
- [37] H. Yamazaki and T. Satomura, “Vertically combined shaved cell method in a z-coordinate nonhydrostatic atmospheric model,” *Atmospheric Science Letters*, vol. 9, no. 4, pp. 171–175, 2008.
- [38] D. Clarke, H. Hassan, and M. Salas, “Euler calculations for multielement airfoils using Cartesian grids,” *AIAA journal*, vol. 24, no. 3, pp. 353–358, 1986.
- [39] S. Mauch, “A Fast Algorithm for Computing the Closest Point and Distance Transform,” tech. rep., California Institute of Technology, 2000.
- [40] “Landmap Project.” <http://catalogue.ceda.ac.uk/uuid/7f128ocf215da6f8001eae5c2f019fe8>. Last accessed March 2017.
- [41] O. Tange, “GNU Parallel - The Command-Line Power Tool,” 2011.
- [42] G. Taylor, “The Formation of a Blast Wave by a Very Intense Explosion. II. The Atomic Explosion of 1945,” *Proceedings of the Royal Society A: Mathematical, Physical and Engineering Sciences*, vol. 201, no. 1065, pp. 175–186, 1950.
- [43] L. Sedov, *Similarity and dimensional methods in mechanics*. CRC Press, 1993.
- [44] J. von Neumann, *Collected Works*. Oxford: Pergamon, 1961.
- [45] M. P. Friedman, “A simplified analysis of spherical and cylindrical blast waves,” *Journal of Fluid Mechanics*, vol. 11, no. 1, p. 1, 1961.
- [46] F. Friedlander, “The Diffraction of Sound Pulses. I. Diffraction by a Semi-Infinite Plane,” *Proceedings of the Royal Society of London. Series A, Mathematical and Physical Sciences*, vol. 186, no. 1006, 1946.
- [47] E. L. Guzas and C. J. Earls, “Air blast load generation for simulating structural response,” *Steel and Composite Structures*, vol. 10, no. 5, pp. 429–455, 2010.
- [48] W. Baker, *Explosion hazards and evaluation*. Elsevier, 2012.
- [49] G. Kinney and K. Graham, *Explosive shocks in air*. Springer, 2013.

- [50] C. Needham, *Blast Wave Propagation*. Springer, 2010.
- [51] C. Kingery and G. Bulmash, “Airblast parameters from spherical air burst and hemispherical surface burst. ARBRL-TR-02555,” tech. rep., US Army Armament Research and Development Center, 1984.
- [52] J. Henrych and R. Major, *The dynamics of explosion and its use*. Elsevier, 1979.
- [53] M. Held, “Blast Waves in Free Air,” *Propellants, Explosives, Pyrotechnics*, vol. 8, no. 1, pp. 1–7, 1983.
- [54] Z. Bajic, J. Bogdanov, and R. Jeremic, “Blast effects evaluation using TNT equivalent,” *Scientific Technical Review*, vol. 59, no. 3-4, pp. 50–53, 2009.
- [55] J. Shin, *Air-Blast Effects on Civil Structures*. PhD thesis, State University of New York at Buffalo, 2014.
- [56] J. Britt and M. Lunsden, *Internal Blast and Thermal Environment from Internal and External Explosions: A User’s Guide for the BLASTX Code, Version 3.0*. 1994.
- [57] J. Tancreto and W. J. Zehrt, “Design for internal quasi-static pressures from partially confined explosions,” in *Proceedings of the 28th Department of Defense Explosive Safety (DDESB) Seminar*, (Orlando, FL, USA), 1998.
- [58] V. Karlos and G. Solomon, “Calculation of Blast Loads for Application to Structural Components,” tech. rep., European Commission Joint Research Centre, 2013.
- [59] S. Rigby, *Blast Wave Clearing Effects on Finite-Sized Targets Subjected to Explosive Loads*. PhD thesis, University of Sheffield, 2014.
- [60] “UFC 3-340-02 Structures to Resist the Effects of Accidental Explosions,” tech. rep., U.S. Army Corps of Engineers, Naval Facilities Engineering Command, Air Force Civil Engineer Support Agency, 2008.
- [61] W. Baker, *Explosions in air*. University of Texas press, 1973.
- [62] “Design of structures to resist the effects of accidental explosions. Technical Manual TM 5-1300,” tech. rep., US Department of the Army, 1991.
- [63] T. Rose, “An approach to the problem of blast wave clearing on finite structures using empirical procedures based on numerical simulations,” in *16th International Symposium on Military Aspects of Blast and Shock*, 2000.

- [64] P. Smith and J. Hetherington, *Blast and ballistic loading of structures*. Digital Press, 1994.
- [65] G. Ballantyne, A. Whittaker, G. Dargush, and A. Aref, "Air-blast effects on structural shapes of finite width," *Journal of Structural Engineering*, vol. 136, no. 2, pp. 152–159, 2010.
- [66] D. D. Rickman and D. W. Murrell, "Development of an Improved Methodology for Predicting Airblast Pressure Relief on a Directly Loaded Wall," *Journal of Pressure Vessel Technology*, vol. 129, no. 1, p. 195, 2007.
- [67] P. Smith and T. Rose, "Blast wave propagation in city streets - an overview," *Progress in Structural Engineering and Materials*, vol. 8, no. 1, pp. 16–28, 2006.
- [68] P. Smith, G. Whalen, L. Feng, and T. Rose, "Blast loading on buildings from explosions in City Streets," *Proceedings of the Institution of Civil Engineers: Structures and Buildings*, vol. 146, no. 1, pp. 47–55, 2001.
- [69] T. Rose and P. Smith, "Influence of the principal geometrical parameters of straight city streets on positive and negative phase blast wave impulses," *International Journal of Impact Engineering*, vol. 27, no. 4, pp. 359–376, 2002.
- [70] T. Rose, *An Approach to the Evaluation of Blast Loads on Finite and Semi-Infinite Structures*. PhD thesis, Cranfield University, 2001.
- [71] A. Remennikov, "Blast effects analysis for commercial buildings in urban setting," in *18th Australasian Conference on the Mechanics of Structures and Materials (ACMSM)*, 2004.
- [72] A. Remennikov and T. Rose, "Modelling blast loads on buildings in complex city geometries," *Computers and Structures*, vol. 83, no. 27, pp. 2197–2205, 2005.
- [73] P. Smith, T. Rose, and J. Green, "The effect of arrays of suburban buildings in providing shielding from blast," in *Proceedings of the 11th International Symposium on Interaction of the Effects of Munitions with Structures*, (Mannheim, Germany), 2003.
- [74] W. Smith, T. Rose, and S. Ng, "The influence of areal density on the shielding and channelling of blast by buildings," in *18th International Symposium on Military Aspects of Blast and Shock*, (Bad Reichenhall, Germany), 2004.

- [75] Y. Shi, H. Hao, and Z. X. Li, “Numerical simulation of blast wave interaction with structure columns,” *Shock Waves*, vol. 17, no. 1-2, pp. 113–133, 2007.
- [76] P. Smith, “Blast Walls for Structural Protection Against High Explosive Threats: A Review,” *International Journal of Protective Structures*, vol. 1, no. 1, pp. 67–84, 2010.
- [77] M. Beyer, “Blast loads behind vertical walls,” in *22nd Explosives Safety Seminar, DoD Explosives Safety Board*, (Anaheim CA, USA), 1986.
- [78] M. D. Goel and V. A. Matsagar, “Blast-Resistant Design of Structures,” *Practice Periodical on Structural Design & Construction*, vol. 19, no. 2, pp. 1–9, 2014.
- [79] I. Sochet, S. Eveillard, J. Y. Vinçont, P. F. Piserchia, and X. Rocourt, “Influence of the geometry of protective barriers on the propagation of shock waves,” *Shock Waves*, vol. 27, no. 2, pp. 1–11, 2016.
- [80] R. Löhner and J. Baum, “An assessment of architecturally appealing, semi-open shock mitigation devices,” *Engineering Computations*, vol. 29, no. 1, pp. 19–30, 2012.
- [81] J. Niollet, S. Chung Kim Yuen, and G. Nurick, “A Study to Assess the Use of Cylindrical Bars as Blast Barriers,” *International Journal of Protective Structures*, vol. 6, no. 2, pp. 263–286, 2015.
- [82] A. Chaudhuri, A. Hadjadj, O. Sadot, and G. Ben-Dor, “Study of Shock-Wave Mitigation through Solid Obstacles,” in *28th International Symposium on Shock Waves*, 2012.
- [83] R. Zong, H. Hao, and Y. Shi, “Development of a New Fence Type Blast Wall for Blast Protection: Numerical Analysis,” *International Journal of Structural Stability and Dynamics*, vol. 17, no. 6, pp. 1–29, 2017.
- [84] N. Gebbeken, T. Döge, and M. Larcher, “Safety and Security of Urban Areas through Innovative Architectural and Structural Concepts,” in *Future Security*, pp. 153–164, Berlin, Heidelberg: Springer, 2012.
- [85] N. Gebbeken and T. Döge, “Explosion Protection - Architectural Design, Urban Planning and Landscape Panning,” *International Journal of Protective Structures*, vol. 1, no. 1, pp. 1–21, 2010.

- [86] P. Smith, T. Rose, and M. Brittle, "Analysis of a generic cityscape using an adaptive mesh CFD code," in *Proceedings of the 12th International Symposium on Interaction of the Effects of Munitions with Structures*, (New Orleans, USA), 2005.
- [87] M. Mensinger and S. Trometer, "Simulation von Detonationsszenarien im urbanen Umfeld," in *Donaubauer (Hg.): Geoinformationssysteme*, pp. 150–164, 2014.
- [88] R. C. Ripley, F. Zhang, C. T. Cloney, S. McClennan, and N. McCormick, "A Modern Blast Solver Strategy and Its Urban Application," tech. rep., 2016.
- [89] I. G. Cullis, N. Nikiforakis, P. Frankl, P. Blakely, P. Bennett, and P. Greenwood, "Simulating geometrically complex blast scenarios," *Defence Technology*, vol. 12, no. 2, pp. 134–146, 2016.
- [90] M. Larcher and F. Casadei, "Explosions in Complex Geometries - A Comparison of Several Approaches," *International Journal of Protective Structures*, vol. 1, no. 2, pp. 169–196, 2010.
- [91] T. Ma, X. Xu, and J. Ning, "Research on propagation laws of explosion shock wave inside metro station," *Journal of Loss Prevention in the Process Industries*, vol. 46, pp. 54–68, 2017.
- [92] O. Hansen, P. Hinze, D. Engel, and S. Davis, "Using computational fluid dynamics (CFD) for blast wave predictions," *Journal of Loss Prevention in the Process Industries*, vol. 23, no. 6, pp. 885–906, 2010.
- [93] B. Julien, I. Sochet, and T. Vaillant, "Impact of the volume of rooms on shock wave propagation within a multi-chamber system," *Shock Waves*, vol. 26, no. 2, pp. 87–108, 2016.
- [94] F. Rigas and S. Sklavounos, "Experimentally validated 3-D simulation of shock waves generated by dense explosives in confined complex geometries," *Journal of Hazardous Materials*, vol. 121, no. 1-3, pp. 23–30, 2005.
- [95] G. A. Sod, "A survey of several finite difference methods for systems of nonlinear hyperbolic conservation laws," *Journal of Computational Physics*, vol. 27, no. 1, pp. 1–31, 1978.
- [96] M. Sun and K. Takayama, "A note on numerical simulation of vortical structures in shock diffraction," *Shock Waves*, vol. 13, no. 1, pp. 25–32, 2003.

- [97] M. K. Quinn and K. Kontis, “A Combined Study on Shock Diffraction,” in *5th Symposium on Integrating CFD and Experiments in Aerodynamics*, 2012.
- [98] F. Gnani, K. H. Lo, H. Zare-Behtash, and K. Kontis, “Experimental investigation on shock wave diffraction over sharp and curved splitters,” *Acta Astronautica*, vol. 99, no. 1, pp. 143–152, 2014.
- [99] M. van Dyke and S. Widnall, *An Album of Fluid Motion*. Stanford: Parabolic Press, 1982.
- [100] M. Brittle, *Blast Propagation in a Geometrically Complex Environment - Thesis (M.Sc.)*. Cranfield University, 2004.
- [101] A. M. Khokhlov, “Fully Threaded Tree Algorithms for Adaptive Refinement Fluid Dynamics Simulations,” *Journal of Computational Physics*, vol. 143, no. 2, pp. 519–543, 1998.
- [102] D. DeZeeuw and K. G. Powell, “An Adaptively Refined Cartesian Mesh Solver for the Euler Equations,” *Journal of Computational Physics*, vol. 104, no. 1, pp. 56–68, 1993.
- [103] R. Keppens, M. Nool, G. Tóth, and J. P. Goedbloed, “Adaptive mesh refinement for conservative systems: Multi-dimensional efficiency evaluation,” *Computer Physics Communications*, vol. 153, no. 3, pp. 317–339, 2003.
- [104] B. van der Holst and R. Keppens, “Hybrid block-AMR in cartesian and curvilinear coordinates: MHD applications,” *Journal of Computational Physics*, vol. 226, no. 1, pp. 925–946, 2007.
- [105] P. MacNeice, K. M. Olson, C. Mobarry, R. De Fainchtein, and C. Packer, “PARAMESH: A parallel adaptive mesh refinement community toolkit,” *Computer Physics Communications*, vol. 126, no. 3, pp. 330–354, 2000.
- [106] M. J. Berger and J. Olinger, “Adaptive mesh refinement for hyperbolic partial differential equations,” *Journal of Computational Physics*, vol. 53, no. 3, pp. 484–512, 1984.
- [107] M. J. Berger and P. Colella, “Local Adaptive Mesh Refinement for Shock Hydrodynamics,” *Journal of Computational Physics*, vol. 82, no. 1, pp. 64–84, 1989.
- [108] J. J. Quirk, *An adaptive grid algorithm for computational shock hydrodynamics*. PhD thesis, Cranfield Institute of Technology, 1991.

- [109] J. J. Quirk and U. Hanebutte, “A parallel adaptive mesh refinement algorithm,” tech. rep., NASA Langley Research Center, 1993.
- [110] J. J. Quirk, “A Cartesian Grid Approach with Heirarchical Refinement for Compressible Flows,” tech. rep., NASA Langley Research Center, 1994.
- [111] J. J. Quirk, “A parallel adaptive grid algorithm for computational shock hydrodynamics,” *Applied Numerical Mathematics*, vol. 20, no. 4, pp. 427–453, 1996.
- [112] C. Pantano, R. Deiterding, D. Hill, and D. Pullin, “A low numerical dissipation patch-based adaptive mesh refinement method for large-eddy simulation of compressible flows,” *Journal of Computational Physics*, vol. 221, no. 1, pp. 63–87, 2007.
- [113] J. Bell, M. Berger, J. Saltzman, and M. Welcome, “Three-Dimensional Adaptive Mesh Refinement for Hyperbolic Conservation Laws,” *SIAM Journal on Scientific Computing*, vol. 15, no. 1, pp. 127–138, 1994.
- [114] W. C. Skamarock and J. B. Klemp, “Adaptive Grid Refinement for Two-Dimensional and Three-Dimensional Nonhydrostatic Atmospheric Flow,” *Monthly Weather Review*, vol. 121, no. 3, pp. 788–804, 1993.
- [115] R. Walder and D. Folini, “A-MAZE: A Code Package to Compute 3D Magnetic Flows, 3D NLTE Radiative Transfer, and Synthetic Spectra,” in *ASP Conference Series*, vol. 24, p. 281, 2000.
- [116] M. E. Hubbard and N. Nikiforakis, “A Three-Dimensional, Adaptive, Godunov-Type Model for Global Atmospheric Flows,” *Monthly Weather Review*, vol. 131, no. 8, pp. 1848–1864, 2003.
- [117] R. Löhner, “An adaptive finite element scheme for transient problems in CFD,” *Computer Methods in Applied Mechanics and Engineering*, vol. 61, no. 3, pp. 323–338, 1987.
- [118] O. Roussel and M. Errera, “Adaptive mesh refinement: A wavelet point of view,” in *European Congress on Computational Methods in Applied Sciences and Engineering*, 2000.
- [119] W. Chen, F. Lien, and M. Leschziner, “Local mesh refinement within a multi-block structured-grid scheme for general flows,” *Computer Methods in Applied Mechanics and Engineering*, vol. 144, no. 3-4, pp. 327–369, 1997.

- [120] M. J. Berger, “Data Structures for Adaptive Grid Generation,” *SIAM Journal on Scientific and Statistical Computing*, vol. 7, no. 3, pp. 904–916, 1986.
- [121] M. Berger and I. Rigoutsos, “An algorithm for point clustering and grid generation,” *IEEE Transactions on Systems, Man, and Cybernetics*, vol. 21, no. 5, pp. 1278–1286, 1991.
- [122] O. E. Livne, “Clustering on Single Refinement Level: Berger-Rigoustos Algorithm,” tech. rep., Scientific Computing and Imaging Institute, University of Utah, 2006.
- [123] O. E. Livne, “Minimum and Maximum Patch Size Clustering on a Single Refinement Level,” Tech. Rep. UUSCI-2006-002, Scientific Computing and Imaging Institute, University of Utah, 2006.
- [124] O. E. Livne, “Efficient Update of Persistent Patches in the Berger Rigoutsos Algorithm,” Tech. Rep. UUSCI-2006-003, Scientific Computing and Imaging Institute, University of Utah, 2006.
- [125] H. Friedel, R. Grauer, and C. Marliani, “Adaptive Mesh Refinement for Singular Current Sheets in Incompressible Magnetohydrodynamic Flows,” *Journal of Computational Physics*, vol. 134, no. 1, pp. 190–198, 1997.
- [126] B. T. N. Gunney, A. M. Wissink, and D. A. Hysom, “Parallel clustering algorithms for structured AMR,” *Journal of Parallel and Distributed Computing*, vol. 66, no. 11, pp. 1419–1430, 2006.
- [127] B. T. Gunney and R. W. Anderson, “Advances in patch-based adaptive mesh refinement scalability,” *Journal of Parallel and Distributed Computing*, vol. 89, pp. 65–84, 2016.
- [128] J. Luitjens and M. Berzins, “Scalable parallel regridding algorithms for block-structured adaptive mesh refinement,” *Concurrency Computation: Practice and Experience*, vol. 23, no. 13, pp. 1522–1537, 2011.
- [129] C. A. Rendleman, V. E. Beckner, M. Lijewski, W. Crutchfield, and J. B. Bell, “Parallelization of structured, hierarchical adaptive mesh refinement algorithms,” *Computing and Visualization in Science*, vol. 3, no. 3, pp. 147–157, 2000.
- [130] A. M. Wissink, D. Hysom, and R. D. Hornung, “Enhancing scalability of parallel structured AMR calculations,” in *Proceedings of the 17th annual international conference on Supercomputing - ICS '03*, p. 336, 2003.

- [131] A. M. Wissink, R. D. Hornung, S. R. Kohn, S. S. Smith, and N. Elliott, "Large scale parallel structured AMR calculations using the SAMRAI framework," in *Proceedings of the 2001 ACM/IEEE conference on Supercomputing*, p. 6, 2001.
- [132] B. Worthen and T. C. Henderson, "Scalable Parallel AMR for the Uintah Multi-Physics Code," in *Petascale Computing: Algorithms and Applications*, pp. 67–82, Chapman and Hall, 2007.
- [133] A. Mignone, C. Zanni, P. Tzeferacos, B. van Straalen, P. Colella, and G. Bodo, "The Pluto Code for Adaptive Mesh Computations in Astrophysical Fluid Dynamics," *The Astrophysical Journal Supplement Series*, vol. 198, no. 1, p. 7, 2012.
- [134] B. Fryxell, K. Olson, P. Ricker, F. X. Timmes, M. Zingale, D. Q. Lamb, P. M. A. C. Neice, R. Rosner, J. W. Truran, and H. Tufo, "FLASH : An Adaptive Mesh Hydrodynamics Code for Modeling Astrophysical Thermonuclear Flashes," *The Astrophysical Journal Supplement Series*, vol. 131, pp. 273–334, 2000.
- [135] M. Dumbser, O. Zanotti, A. Hidalgo, and D. S. Balsara, "ADER-WENO finite volume schemes with space-time adaptive mesh refinement," *Journal of Computational Physics*, vol. 248, pp. 257–286, 2013.
- [136] M. Nguyen-Dinh, N. Lardjane, C. Duchenne, and O. Gainville, "Direct simulations of outdoor blast wave propagation from source to receiver," *Shock Waves*, vol. 27, no. 4, pp. 593–614, 2017.
- [137] M. D. Goel, V. A. Matsagar, A. Gupta, and S. Marburg, "An Abridged Review of Blast Wave Parameters," *Defence Science Journal*, vol. 62, no. 5, pp. 300–306, 2012.
- [138] T. A. Rose, *Air3d version 9 users' guide*. Engineering Systems Department, Cranfield University, 2006.
- [139] C. Catlin, M. Ivings, M. Myatt, and D. Ingram, "Explosion Hazard Assessment: A Study of the Feasibility and Benefits of Extending Current HSE Methodology to take Account of Blast Sheltering HSL/2001/04," tech. rep., Fire and Explosion Group, Health & Safety Laboratory, 2001.
- [140] "The Economic Effects of Terrorism on London - Experiences of Firms in London's Business Community," tech. rep., 2005.

- [141] P. Grossi, “Damage and Insured Losses from the 2001 World Trade Center Attacks,” *Peace Economics, Peace Science and Public Policy Property*, vol. 15, no. 2, 2009.
- [142] “Reference Manual to Mitigate Potential Terrorist Attacks Against Buildings - FEMA-426,” tech. rep., Department for Homeland Security, USA, 2011.
- [143] M. Hardwick, J. Hall, J. Tatom, and R. Baker, “Approved Methods and Algorithms for DoD Risk-Based Explosives Siting,” tech. rep., U.S. Department of Defense, 2009.
- [144] J. Stapczynski, “Blast Injuries,” *Annals of Emergency Medicine*, vol. 11, no. 12, pp. 687–694, 1982.
- [145] P. Smith and T. Rose, “Blast loading and building robustness,” *Progress in Structural Engineering and Materials*, vol. 4, no. 2, pp. 213–223, 2002.
- [146] D. Cormie, G. Mays, and P. Smith, *Blast effects on buildings*. Thomas Telford, second ed., 2009.
- [147] “Glazing Hazard Guide,” tech. rep., Security Facilities Executive Special Services Group - Explosion Protection, Cabinet Office, London, 1997.
- [148] S. Glasstone and P. J. Dolan, *The effects of nuclear weapons*. United States Department of Energy, 1977.
- [149] “Explosions and Blast Injuries : A Primer for Clinicians,” tech. rep., Department of Health & Human Services, USA, 2015.
- [150] E. Ahlers, “Fragment hazard study,” in *Minutes of the 11th Explosives Safety Seminar, Vol. 1*, (Washington, DC), Armed Services Explosives Safety Board, 1969.
- [151] W. Baker, P. Westine, J. Kulesz, J. Wilbeck, and P. Cox, “A Manual for the Prediction of Blast and Fragment Loading on Structures,” Tech. Rep. August, DOE/TIC 11268, US Department of Energy, Washington, DC, 1981.
- [152] W. Baker, “Workbook for predicting pressure wave and fragment effects of exploding propellant tanks and gas storage vessels,” Tech. Rep. September, NASA Lewis Research Centre, Cleveland, OH, 1975.
- [153] L. Dixon, J. Arlington, S. Carroll, D. Lakdawalla, R. Reville, and D. Adamson, “Issues and Options for Government Intervention in the Market for Terrorism Insurance,” tech. rep., RAND Corporation, 2004.

- [154] H. H. Willis, T. LaTourrette, T. K. Kelly, S. Hickey, and S. Neill, "Terrorism Risk Modeling for Intelligence Analysis and Infrastructure Protection," tech. rep., RAND Center for Terrorism Risk Management Policy, 2007.
- [155] "Assessing Terrorism Risk 15 Years After 9/11." <http://www.air-worldwide.com/Publications/AIR-Currents/2016/Assessing-Terrorism-Risk-15-Years-After-9/11/>. Accessed May 2017.
- [156] C. Wilkinson, "Terrorism Risk: A Reemergent Threat," *Insurance Information Institute*, no. 212, 2010.
- [157] E. M. Stoltz, K. J. Clutter, and F. Hudson, "Modeling property value loss in a city due to terrorist bombings," *IEEE Systems Journal*, vol. 3, no. 2, pp. 221–230, 2009.
- [158] H. H. Willis, "Guiding resource allocations based on terrorism risk," *Risk Analysis*, vol. 27, no. 3, pp. 597–606, 2007.
- [159] "OpenStreetMap." <https://www.openstreetmap.org>. Accessed June 2017.
- [160] "The AIR Model for Terrorism," tech. rep., AIR Worldwide, 2016.
- [161] "General Insurance Stress Test 2015 Scenario Specification, Guidelines and Instructions," tech. rep., Prudential Regulation Authority, 2015.
- [162] "Commercial Property - Keeping Insurance Valuations True During both Boom and Bust," tech. rep., Zurich, 2014.
- [163] M. Bedford, R. Harris, A. King, and A. Hawkeswood, "Occupier Density Study," Tech. Rep. September, British Council for Offices, 2013.
- [164] M. Gill, *Crime at Work Vol 1: Studies in Security and Crime Prevention*. Springer, 2016.
- [165] S. Mallonee, "Physical injuries and fatalities resulting from the Oklahoma City bombing," *JAMA: The Journal of the American Medical Association*, vol. 276, no. 5, pp. 382–387, 1996.
- [166] P. D. Smith, S. A. Forth, and T. A. Rose, *A computational tool for the evaluation of blast-structure interactions*. Engineering Systems Department, Cranfield University, 2006.
- [167] G. Whalen, *Blast Propagation in an Urban Environment - M.Sc. Project Report*. 1998.

- [168] B. Rogg, D. Hermann, and G. Adomeit, "Shock-induced flow in regular arrays of cylinders and packed beds," *International Journal of Heat and Mass Transfer*, vol. 28, no. 12, pp. 2285–2298, 1985.
- [169] H. H. Shi and K. Yamamura, "The interaction between shock waves and solid spheres arrays in a shock tube," *Acta Mechanica Sinica*, vol. 20, no. 3, pp. 219–227, 2004.
- [170] S. Seeraj and B. W. Skews, "Dual-element directional shock wave attenuators," *Experimental Thermal and Fluid Science*, vol. 33, no. 3, pp. 503–516, 2009.
- [171] S. Berger, O. Sadot, and G. Ben-Dor, "Experimental investigation on the shock-wave load attenuation by geometrical means," *Shock Waves*, vol. 20, no. 1, pp. 29–40, 2010.